Title
Evolutionary dynamics in microbial colonies

Author
Gralka, Matti

Publication Date
2018

Peer reviewed|Thesis/dissertation

Evolutionary dynamics in microbial colonies

By

Matti Gralka

A dissertation submitted in partial satisfaction of the

requirements for the degree of

Doctor of Philosophy

in

Physics

in the

Graduate Division

of the

University of California, Berkeley

Committee in charge:

Professor Oskar Hallatschek, Chair
Professor Hernan Garcia
Professor Jasper Rine

Spring 2018

Advisor: Oskar Hallatschek Matti Gralka

Evolutionary dynamics in microbial colonies

Abstract

Traditionally, evolutionary biology has mostly taken a retrospective view, looking backwards in time to infer past evolutionary dynamics. Over the past 30 years, evolution experiments in the laboratory have become a valuable complementary technique to study evolution in real time. Microbial populations in shaken flasks are an ideal model system to do this, because their short generation times and easy reproducibility allow for the study of dozens to hundreds of replicates. Our understanding of microbial evolution in these simple laboratory environments has dramatically improved in recent years.

Microbial populations in the wild face vastly more complex conditions: they grow as spatially structured communities called microbial biofilms, often consisting of interacting mixtures of different species fulfilling different purposes, subject to various, potentially self-generated, biophysicochemical gradients of, e.g., oxygen or nutrients, which are in turn altered by the physical structure of the community. In short, natural population are subject to a vast variety of ecological interactions, and it has remained unclear how much can be learned from well-mixed liquid culture experiments about how ecology affects evolution in more complex scenarios.

In this dissertation, I approach this question using one of the simplest possible ecological aspects: the fact that most populations grow in spatially structured communities. Using microbial colonies as an experimental model system, I examine the effect of spatial structure on evolutionary dynamics in a variety of ways. First, Chapters 2-4 investigate the fates of neutral mutations and the dynamics of beneficial mutations in microbial colonies to find that both the neutral diversity resulting from spontaneous mutations and the strength of adaptation is increased in colonies compared to microbial populations grown in shaken flasks. The second half of the thesis is concerned with the effects of environmental heterogeneity on evolutionary dynamics. In Chapter 5, randomly disordered environments are used to examine the competition of selection and extrinsic noise in a model system for spontaneous beneficial and deleterious mutations. In these experiments, extrinsic noise can almost entirely overpower selection such that beneficial variants cannot leverage their advantage to further their evolutionary success. Chapter 6 discusses the effects of gradients on the emergence of antibiotic resistance and how convective flow can shape the trade-off between selection for resistance and the efficacy of treatment.

Overall, the results presented in this thesis suggest that spatial structure can have a momentous influence on the evolutionary dynamics of many dense cellular populations like biofilms and tumors: not only do the dynamics of adaptation change quantitatively in spatially structured populations, but qualitatively different patterns of evolutionary dynamics emerge that cannot arise in well-mixed population. Environmental heterogeneity can also have a strong influence on the speed and the direction of adaptation: whereas random heterogeneity in the environment prevents the spread of beneficial variants, the presence of antibiotic gradients can facilitate the rapid emergence of resistance. This work thus offers a glimpse into the profound and complex ways in which ecology can impact evolution even in simple model systems.

To my family.

Contents

Citations to previously published works

Chapter 2 appears in its entirety as

> Fusco, D., Gralka, M., Anderson, A., Kayser, J., & Hallatschek, O. (2016). Excess of mutational jackpot events in growing populations due to gene surfing. *Nature Communications*, 7, 1–9. https://doi.org/10.1101/053405

Chapter 3 appears in its entirety as

> Gralka, M., Stiewe, F., Farrell, F., Möbius, W., Waclaw, B., & Hallatschek, O. (2016). Allele surfing promotes microbial adaptation from standing variation. *Ecology Letters*, 19(8), 889–898. https://doi.org/10.1111/ele.12625

Chapter 4 appears in its entirety as

> Farrell, F. D., Gralka, M., Hallatschek, O., & Waclaw, B. (2017). Mechanical interactions in bacterial colonies and the surfing probability of beneficial mutations. *Journal of the Royal Society Interface*, 14(131). https://doi.org/10.1098/rsif.2017.0073

Chapter 5 will be submitted in its entirety as

> Gralka, M. & Hallatschek, O. (2018). Environmental heterogeneity reduces the efficacy of selection.

Chapter 6 appears in its entirety as

> Gralka, M., Fusco, D., Martis, S., & Hallatschek, O. (2017). Convection shapes the trade-off between antibiotic efficacy and the selection for resistance in spatial gradients. *Physical Biology*, 14(4). https://doi.org/10.1088/1478-3975/aa7bb3

Acknowledgments

This dissertation would not have been possible without the help of many people. First and foremost, I want to thank my advisor, Oskar Hallatschek. By inviting me to join his lab at Berkeley he took a leap of faith, and I cannot thank him enough for it. During my five years at Berkeley, he has been a great mentor full of ideas. He was supportive every step of the way and always had an open door. I hope our paths will continue to cross. My committee members Jasper Rine and Hernan Garcia kept track of my progress, gave helpful suggestions and always had kind words of encouragement and support.

The work in this thesis is the result of intense collaboration. Within the Hallatschek lab, I had the good fortune of working closely with Diana Fusco, Carl Schreck, Jona Kayser, Stephen Martis, Wolfram Moebius, and QinQin Yu. My first project built on the work of Fabian Stiewe in Göttingen, and heavily benefited from fantastic simulations performed by Fred Farrell and Bartek Waclaw. Other lab members helped immensely during various stages of my PhD by providing scientific advice and moral support. Jona Kayser was the perfect office and lab mate and a constant source of enthusiasm, Ben Good taught me many things about population genetics, and Jayson Paulose endured a constant barrage of questions about KPZ, percolation, and the like. Thank you also to Morgan Delarue, Jörn Hartung, Pawel Gniewek, Daniel Weissman, Marie-Cecilia Duvernoy, Yuya Karita, and all members of the lab for many great lunch, coffee, and bar conversations.

When I arrived at Berkeley I had no experience in the lab, and I thank many people for all their help and never rolling their eyes at me over my many questions, especially Ellen Goodall, Anne Dodson, Ryan Janke and the rest of the Martin and Rine labs, and Mary Wahl. Arezou Razavi, Anne Takizawa and Joelle Miles were always helpful in solving administrative questions. Hector Nolla and Mary West gave advice on experiments and helped with equipment.

Two summer schools were among the highlights of my time at Berkeley: the MBL Physiology course in Woods Hole, and the Quantitative Biology Course at the KITP in Santa Barbara. I thank the organizers, the faculty and the students for teaching me many things, not least among those that it is okay to fail, and allowing us students to take a step back and rekindle our fascination with science that is sometimes dimmed by the gray day-to-day of the lab. Through the intense course periods, I have found many friends and met many like-minded scientists.

Many people in the lab have become good friends, as have Holly and Magnus, Leila, Aaditya and the Friday night crew, Ben and Hannah, Scott, the members of the various combos in UC Jazz that I was fortunate to be a part of, and the team at Berkeley Animal Care services. Others never went away, despite my dreadful ability of keeping in touch, especially Danny, Paul, Julia T., Julia F., Paul S., Linda, and Jens. Thank you for your continued friendship. Most importantly, I thank my family. My parents and grandparents for their unconditional love, unending support and raising me to be the person I am today. My future family-in-law, who have welcomed me in their midst with such open arms. Finally, Marie, the love of my life, for bringing so much joy and love into my life and giving me a place to call home.

1 Introduction

From some unknown initial life form, evolution has created all of the biological diversity we see today in one colossal, billion years-long process. The study of evolution has traditionally been a retrospective undertaking, inferring past evolutionary dynamics with its multitude of speciation and extinction events over millions of years, often based on morphological similarities and differences. With the advent of modern sequencing technology, the evolutionary relationships between all species can be unveiled in ever-increasing detail[1]. It is in this sense that "nothing in biology makes sense except in the light of evolution"[2], because the conceptual framework of evolution helps us make sense of the biological diversity we see.

It is tempting to view Darwin's realization that "one species does change into another"[3] through the lens of a biologically inexperienced physicist as a real-life simulation with a simple set of instructions: taking the current biological diversity and environmental variables as input, evolution adds in a few mutations, some stochasticity, and natural selection, and outputs a new state of biological diversity with species that are better adapted (in some sense) to their environment. The environment itself may also change over time, partly due to the biological species that inhabit it, and so the black box evolution feeds back on itself as it churns. When framed this way, the allure of evolution from a physics perspective may be that in principle, it appears to have a "solution", i.e., if only we understood all the underlying processes well enough, we would be able to predict how evolution should proceed. But what exactly do we mean by "predicting evolution"?

At its core, evolution is about the change of heritable traits over time, from one generation to the next. These traits, or *phenotypes*, can be as varied as the eye color of a person, the height of a tree, or the growth rate of a bacterium. Traits are determined by genes which can come in several versions or *alleles*. Each gene

corresponds to a small piece of the genome, which is stored on long molecules of DNA, consisting of millions or billions of basic structural units called nucleotides, in every cell. During every cell division, whether of a single-celled bacterium or in the human body, the genetic material on the DNA is replicated. However, this process is not perfect: mutations can occur from errors during each DNA replication, such as switching one nucleotide for another, or removing or inserting stretches of DNA. These errors are fundamentally the result of thermal fluctuations, and thus individual errors cannot be predicted. The resulting genetic changes are heritable: a cell receiving a mutated copy of a gene will replicate this version of the gene when it divides. Some mutations can be outright lethal, others are detrimental to varying degrees, and very few are beneficial; most, however, are neutral, i.e., have no obvious effect [4]. To complicate matters further, the effect of a given mutation is specific to the environment and individual it arises in. For instance, the effect of a mutation in a bacterium may depend on the detailed genetic make-up of the individual, but also environmental factors like ambient temperature, nutrient availability, or the presence of other bacteria. Thus, there is generally little hope to be able to predict evolution at the single nucleotide level [5].

However, a detailed insight into sequence evolution may not always be necessary or even desired. After all, when trying to predict evolution, one often thinks of the practical implications such as how long one has to wait for a bacterial population or a tumor to develop drug resistance [6,7], or how to select a vaccine against next year's prevalent *influenza* virus [8]. In other words, what one would typically like to predict is the phenotypic evolution of a relatively small number of traits on the scale of hundreds to thousands of generations, and perhaps some coarse-grained genetic signature of it. This is akin to the theory of statistical mechanics, where the collective behavior is the result of the random dynamics of individual particles, whose positions and momenta we know only in terms of their probability distribution.

Similarly, a theory of phenotypic evolution will not predict a specific evolutionary outcome, but instead it can only assign probabilities to different evolutionary trajectories. This is because despite the mainstream description of evolution through natural selection implying that the best-adapted, or "fittest", individual will invariably win out in the end, this is by no means the case. Instead, in a population of constant size, allele frequencies can change stochastically from generation to the next due to the inherent randomness in each individual's reproductive success. These fluctuations, called genetic drift, are the reason the ultimate fate of a mutant allele in the population is stochastic: its lineage can either go extinct when it leaves no offspring in the following generation, or it can be successful and sweep to fixation, i.e,, take over the population. Genetic drift is more impactful in smaller population where a small difference in the number of offspring corresponds to a relatively large frequency change. Thus, a neutral mutation can fix in small populations by pure chance through genetic drift, whereas its fixation is much less likely in a large population, where a mutation can essentially only fix if it confers a selective, or "fitness", advantage, which increases the *average* reproductive success of an allele relative to the rest of the population. Even with a fitness advantage, however,

the probability for a single mutation to fix in a large population is still only approximately equal to its fitness advantage, typically on the order of a few percent[4]. Thus, fixation is a rare occurrence for all but the most overwhelmingly beneficial mutations.

Beyond an individual's fitness, evolutionary trajectories are often confounded by ecological interactions between individuals of the same or different species and their environment. Classical examples in the wild range from the continual evasion of their host's immune system by viruses[9] to the adaptation of Darwin's finches to different islands[10]. To study in more controlled environments how ecology shapes evolution, experimental evolution of a wide range of species, from microbes[11] to rotifers[12], flies[13] and fish[14], in the laboratory has been an invaluable tool, complementary to studies of evolution in the wild. Microbial model systems have been especially prolific in this regard; we introduce some commonly used experimental systems and classical results of experimental evolution in microbes in the next section.

Many evolution experiments in microbes have been performed in shaken culture flasks to minimize the effects of ecological interactions and, especially, spatial structure. In the present work, we instead focus explicitly on the effects of spatial growth on the evolution in microbial populations. That spatial population structure can influence evolution is of course not a new idea. After all, Darwin's ideas about evolution were originally inspired by differences between finches from neighboring islands[3]; today, speciation is thought to require at least a modicum of geographical separation[15]. As we will show in this work, spatial structure can fundamentally impact the evolutionary dynamics in many regards, such as the fate of spontaneous mutations arising during the growth process. In addition, evolution can be shaped by the emergence of niches or external factors such as flow or spatial heterogeneity that are unique to populations growing in space. Developing a quantitative understanding of how evolutionary dynamics is shaped by spatial growth, flow, and spatial heterogeneity is a major theme of this thesis.

1.1 Experimental evolution and microbial model systems

If we are to make predictions about evolutionary trajectories or probabilities of specific evolutionary outcomes, we need repeatable, well-controlled experiments to test them. What requirements should we have of an ideal model system? Since evolutionary change occurs over the course of many generations, a model organism should have a short generation time if we are to ever to complete meaningful evolution experiments in the laboratory in a reasonable time frame. To ask quantitative questions about evolution the model system should be easy to handle for many generations and populations in parallel. Finally, to explore the space of possible evolutionary trajectories and measure their relative probabilities, we would like to be able to store a copy and "replay the tape" of evolution[16], restarting the evolution experiment at will from earlier time points. Microbial populations have generation times on the order of 1h, are easily grown in liquid or on

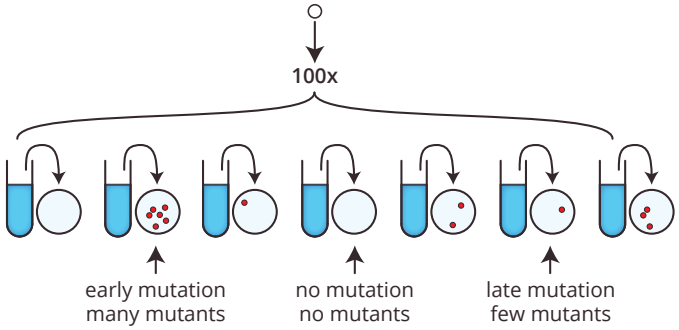

Figure 1.1: Principle of the Luria-Delbrück experiments: many replicate populations are inoculated with single cells, grown up to some final population size and plated onto agar plates containing phage, where only resistant cells can grow colonies. The number of colonies follows a very broad probability distribution because early mutations have exponentially more offspring than late ones.

solid media, and survive freezing and storage indefinitely, and have therefore been employed for evolution experiments in the laboratory for more than 30 years[17,18].

Long before becoming a model system for studying evolution, microbes have played an important role in science, medicine, and industry. Their existence and role in disease had been hypothesized in different cultures as early as the 6th century BC, and the use of microbes in primitive forms of biotechnology, such as in beer and wine brewing[19], bread baking[20], and cheese making[21], predates their discovery by several millenia. That microbes are also the causative agents of disease was finally shown in the 1880s, and starting with the discovery of antibiotics in 1929, bacterial infection were beginning to lose much of their scare. Today, that scare is returning due to the rising incidence of antibiotic-resistant bacterial infections, which present a massive public health concern[22]. In addition, bacteria involved in infections, but also healthy body functions, evolve within the human host[23–28]. Thus, in addition to being a model system for more basic questions about evolutionary dynamics in general, microbial evolution is an important field of study in its own right.

One of the earliest and simplest quantitative evolution experiments in microbes was conducted by Luria and Delbrück who in 1943 set out to settle the question whether bacteria develop resistance to phage, a virus infecting bacteria, when faced with it (acquired immunity), or whether resistance to phage was conferred through mutations arising spontaneously during each cell division[29]. Growing liquid cultures from single cells and then spreading the resulting culture on plates covered with a phage, they found a huge variance in the number of colonies on the plates, indicating that resistance was indeed the consequence of spontaneous mutation (see Fig. 1.1). This large variance can be understood intuitively by considering a growth process from a single cell without death. For a mutation to be present in more than 1/2 of the final population, it has to occur during the first cell division (after which there are two cells). To be present in more than 1/4 of

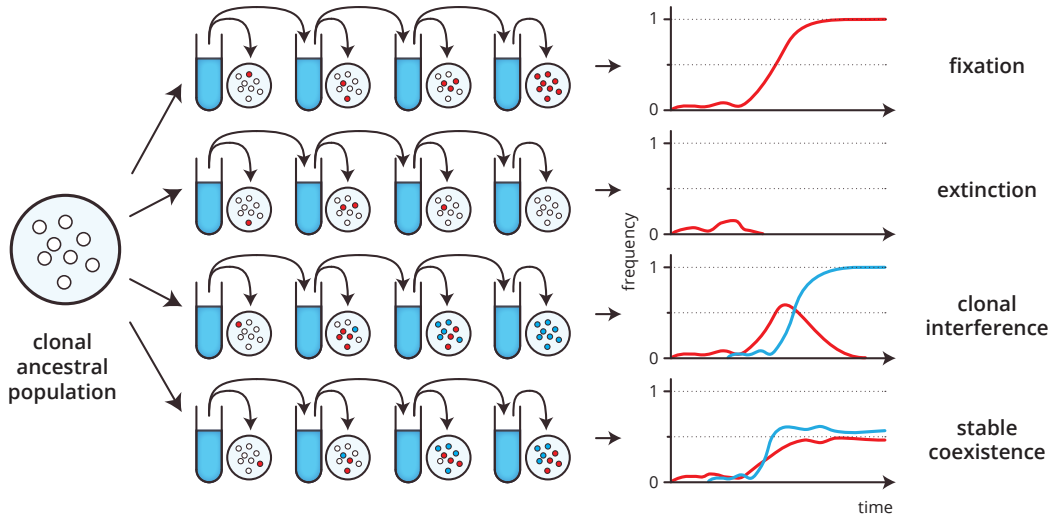

Figure 1.2: Sketch of a prototypical evolution experiment in microbes. Several replicate populations are inoculated from an ancestral clone and passaged over many generations. Periodically, the populations are assayed for phenotypes (such as by plating on agar, where mutants are shown schematically here as colored colonies) or sequenced. Thus, different evolutionary trajectories can be uncovered, such as fixation, extinction, clonal interference, and stable coexistence.

the population, the mutation must occur when there are 4 cells, and so on. Thus, to be at frequency greater x, a mutation has to occur when there are fewer than $1/x$ cells, which agrees with the analytical result[30]. In other words, early mutations give rise to many mutants, or large clones, whereas late mutations give rise to only a few. This heuristic argument suggests that the $1/x$ distribution should be observed for mutant clone sizes in any population growing without death. Indeed, it has recently been used to interpret signatures of (neutral) genetic diversity in cancers[31], although its exact applicability and interpretation is under debate[32–34]. In particular, since tumors grow as compact spatially structured populations, the distribution of clone sizes may look very different; we return to this question in Chapter 2.

The Luria-Delbrück experiment forms the basis for microbial evolution experiments. Lenski's Long-Term Evolution Experiment (LTEE) in *E. coli*, the longest-running such experiment with more than 60000 generations so far, is essentially a series of Luria-Delbrück experiments[35]. The LTEE was designed to limit ecological interactions, such as through spatial structure or cross-feeding, as best as possible: 12 replicate population started from a single clone are grown in 10ml of media containing only a low concentration of glucose in constantly shaken 50ml flasks (see Fig. 1.2 for a schematic). Every day, a small sample of the each population is transferred into fresh media. Every 500 generations, samples are frozen down, providing a fossil record of the whole experiment.

The LTEE has provided a lot of insight into the vast space of possible outcomes during long-term evolution (see Fig. 1.2). Over time, cell size increased[36], as did mutation rate in some, but not all, populations[37]. Population fitness, defined as the population averaged growth rate relative to the ancestor, increased at first rapidly due to individual beneficial mutations sweeping to fixation in the population. During the later stages of the experiment, fitness increase slowed down as the strongest available beneficial mutations already fixed and novel beneficial mutations arose on different genetic backgrounds simultaneously and competed for fixation ("clonal interference")[35,38]. More complex evolutionary outcomes emerged in a few of the replicate populations in the LTEE, such as the stable coexistence of two or more subpopulations[39,40] (Fig. 1.2), or the ability to metabolize citrate, a carbon source that could not be utilized by the ancestor[41]. Overall, however, it remained difficult to track particular mutant lineages unless they were accompanied by an easily observable phenotypic marker such distinct colony morphologies[40]. In addition, the LTEE consists of only a dozen parallel populations, and while it has answered many exploratory questions about what is possible during long-term evolution, its statistical power is limited.

To quantify evolutionary dynamics and test theoretical predictions with higher throughput and greater statistical power, many more replicate populations and an easier readout of the experiment are desirable. Two concurrent technological innovations in the past 10 years have afforded great progress in this regard.

Firstly, the emergence of affordable genome sequencing has allowed for the large scale assessment of genetic diversity and dynamics of mutant clones *in vivo* and *in vitro* in populations as diverse as tumors[31,42,43], influenza[44,45], antibiotic-resistant bacteria[46,47], and human immune B cells[48]. In the LTEE, high-throughput sequencing has allowed for the tracking of individual mutant lineages in the population[49], opening a window into the black box of genotypic evolution. Through genetic barcoding, whereby a clonal lineage can be "tagged" with a short identifying sequence, it has become possible to track hundreds of thousands of lineages at frequencies far below what is accessible through whole genome sequencing, allowing an even deeper look into evolutionary dynamics[50,51].

Secondly, advances in liquid handling through (semi-)automatic pipetting robots have enabled the parallel handling and real-time observation of hundreds of replicate populations in a 96-well plate format in microbes as diverse as *Salmonella enterica*[52], *Caulobacter crescentus*[53], and *Saccharomyces cerevisiae* (budding yeast)[54–57]. This way, the probabilities of different evolutionary trajectories in the face of a challenge chosen by the experimenter, such as increasing antibiotic or salt concentration[58–60], can be quantified and used to inform and test mathematical models of evolutionary dynamics[61]. Massive parallelization also allows for the comparison of evolutionary dynamics in different scenarios, such as with or without sex[62,63] and population subdivision[64], or at different population sizes[55] or ploidy (copy number of chromosomes)[65,66]. Budding yeast has emerged as a particularly useful model system for this, since it exists as both haploid and diploid, and it can reproduce both sexually or asexually.

Evolution experiments in microbial liquid culture have dramatically furthered our understanding of the evolutionary dynamics at the genomic level and how it depends on the spectrum of available mutations and the genotypes they arise on. The statistical power that comes from high-throughput experiments has allowed for the detailed testing of evolutionary theory. However, in order to understand genome evolution, evolutionary studies are often performed in deliberately simplified model environments where ecological interactions are reduced as much as possible. In the next section, we discuss how a simple ecological feature, the spatial structure of the population, can be studied in microbial populations.

1.2 Space – the final frontier (in evolution)

Evolution experiments in microbial populations are often performed in liquid culture without any spatial structure. By contrast, microbial populations in the wild often live attached to surfaces or liquid-air interfaces in so-called biofilms[67,68]. Biofilms are densely populated microbial communities, often encased in a matrix of extracellular polymeric substances (EPS), that can colonize almost any surface. As a result of their spatial structure, life in biofilms is characterized by spatial and temporal variations and strong gradients of, e.g., nutrients and oxygen[69]. Biofilms fulfill important roles in many ecosystems such as intertidal marine systems[70] or soil[71], but they are also involved in a number of medical and technological contexts, such as dental plaque[72], antibiotic-resistant infections[73], and the clogging of medical equipment and industrial pipes[74]. Given the ubiquity in Nature and the practical relevance of microbial biofilms, it is perhaps counter-intuitive that microbial evolution experiments are typically performed in populations of bacteria and yeast growing in liquid culture, shaken or not, and that there are surprisingly few experimental evolution studies in biofilms[75]. While it is convenient to focus on planktonic populations from an experimenter's point of view because they are arguably simpler and easier to handle than biofilms, it also means there remain many open questions regarding the interplay of ecology and evolution in biofilms: How do gradients of nutrients, oxygen, light, and other factors that are direct consequences to their spatial organization influence their evolutionary dynamics? What is the effect of spatial structure on the evolution and maintenance of cooperation and the fate of spontaneous mutations? How do multiple species assemble and interact within a biofilm[76]? And since cells are relatively closely packed in biofilms, what role do mechanical interactions play during all this[77]? In addition to the practical importance of biofilms, answers to these questions have broader relevance because biofilms can also serve as model systems for studying the interplay between evolution and ecology in other spatially organized populations, such as tumors[78,79] and invasive species undergoing range expansions[80,81].

Some of the earliest studies of biofilm evolution were performed with *P. fluorescens* growing in unshaken flasks[82]. An initially clonal population reproducibly diversifies into three stably coexisting variants, named smooth (S), wrinkly spreader (WS) and fuzzy spreader (FS) for their colony morphology when grown on agar

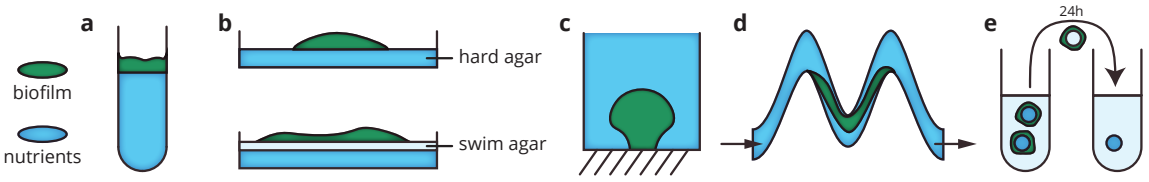

Figure 1.3: Common experimental setup for studying evolution in biofilms. a) stable microcosm without mixing, nutrients well-mixed; b) growth on agar plates, potentially allowing for swimming motility (soft agar), nutrient from below; c) submerged biofilm, nutrient from above; d) growth in microfluidic tubes with flow, constant nutrient inflow; e) bead transfer: beads contain nutrient, daily transfer of exhausted beads into fresh media. Each experimental setup allows the experimenter to probe different ecological aspects in biofilms, such as flow, motility, and nutrient or oxygen gradients.

plates. Importantly, each variant occupies a unique niche afforded by spatial structure: S inhabits the liquid phase, while WS occupies the liquid air interface and FS grows colonies at the bottom of the microcosm. If instead the flasks are shaken, the population does not diversify. Rapid diversification has been shown to be a general consequence of the niches created by the inherent heterogeneity of nutrients, oxygen, etc. in biofilms[83–87]. Thus, evolutionary dynamics can strongly depend on the degree of spatial structure of the population.

Other model systems, such as biofilms grown on beads, on agar plates, or in microfluidic devices (see Fig. 1.3) have illuminated how environmental factors that are especially prominent in biofilms mediate ecological interactions and impact evolutionary dynamics. For instance, cell adhesion, to other cells and to the substrate, and motility can create selection pressures that are unique to spatially structured populations and play important roles in cross-feeding, public goods exchange and the exclusion of "cheater" genotypes[87–92], especially in the presence of flow[90,93]. Similarly, the emergence of high levels of antibiotic resistance is dramatically sped up in antibiotic gradients through the presence of spatial regions of intermediate concentration[94,95].

In this work, we focus on microbial biofilms, or "colonies", grown on hard agar plates, where even cells possessing the molecular machinery needed for motility in liquid, such as flagella, cannot swim. Since cell motion and thus colony expansion on hard agar is only possible through cell growth and division and mechanically pushing one's neighbors across the agar surface, the effects of spatial structure on evolutionary dynamics are particularly strong in microbial colonies. This allows us to unravel the underlying physical principles of evolution in populations with strong spatial structure that can then be applied to understand evolutionary dynamics in more complex scenarios.

One such principle is that, since diffusion is the only driving force of chemical exchange on hard agar plates, there is a strong nutrient gradient across the edge of the colony. Consequently, growth is localized to

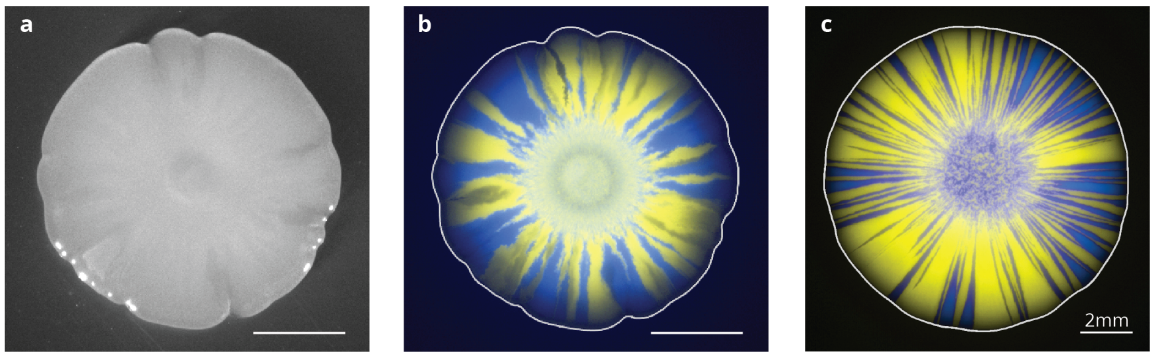

Figure 1.4: Examples of microbial colonies growth from a droplet containing a mixture of yellow and blue fluorescent cells. (a) Under white light illumination, the colony has little discernible structure. (b) Viewing the same colony under fluorescent light reveals that the population has visibly demixed from a mixed inoculum into clonal sectors composed entirely of one of the two strains. The shape and number of sectors depends on the microbial species (a&b, *E. coli* K-12, fluorescently labeled using plasmids; c, *S. cerevisiae* W303, labeled by chromosomal integration of YFP and RFP (false-colored blue)). The scale bar is 2mm.

a thin band of cells, called the growth layer, around the perimeter of the colony where the nutrient concentration is high enough to sustain growth. Cells inside the growth layer divide and thus drive the expansion of the colony, whereas cells in the bulk of the population, outside the growth layer, lack nutrients to grow and enter a quiescent state. Because the expansion of the population in a colony is driven by a small number of cells at the front of the population, microbial colonies have also been used as a model system for macroscopic range expansions, such as the human migration out of Africa[96–99] or the range expansions of plants[100,101], beetles[102,103], voles[104], butterflies[105], and toads[106,107], in which a small subpopulation of "founders" at the edge of the species range first colonize new territory.

The small population size of founders implies that random fluctuations in offspring numbers can have a large effect, i.e., genetic drift is strong at the front of these populations. This enables neutral and even slightly deleterious alleles to establish at the front and "surf" on the expansion wave[108]. In microbial colonies, allele surfing has been demonstrated experimentally, as follows[80]. Two microbial strains, isogenic except for the expression of different fluorescent proteins, are mixed in a test tube and inoculated as a small droplet on an agar plate. The microbes first concentrate at the rim of the droplet like a coffee stain[109]. Initially, all cells grow, until cells far from the front deplete their locally available nutrients and the growth layer establishes. After a few days of growth, the droplet has grown into a roughly circular colony, featureless when viewed under white light. When illuminated under a fluorescence microscope, however, one observes that the initially mixed droplet has demixed into a small number of clearly delineated sectors of either color (Fig. 1.4). Mixing the strains at a skewed ratio reveals that each sector is clonal, i.e., it emanates from a single cell in the

inoculation droplet. Fig. 1.4 also highlights an important experimental advantage of microbial colonies over liquid cultures: the fact that we can employ fluorescence microscopy to resolve the whole spatio-temporal dynamics of individual clones in colonies. Thus, by working with fluorescently marked variants, we can extract the same information about their lineage dynamics from a single fluorescence micrograph that would require whole-genome or barcode sequencing and subsequent lineage reconstruction at many different time points in well-mixed experiments.

The number of sectors in the colonies in Fig. 1.4 is much smaller than the number of cells in the ancestral population, which means that most cells do not form a sector. Success and failure to form a sector in a microbial colony thus serve as operational equivalents of extinction and fixation in well-mixed populations. However, managing to establish a clonal sector is not equivalent to fixation, and failure to establish a sector is not equivalent to extinction. This is because, while a clone failing to form a sector may have lost contact to the growing front, it can start expanding again if it were randomly sampled from the population and transferred to an empty plate. Thus, evolutionary success in colonies is perhaps best defined as the "chance to be sampled", which we can plausibly assume is proportional to a clone's frequency in the population. Since sectoring clones are much larger than clones that do not form sectors, the establishment of sectors is integral to a lineage's evolutionary success defined in this way.

As seen in Fig. 1.4, the number of sectors can depend on the microbial species: colonies of the rod-like bacterium *E. coli* and the round yeast *S. cerevisiae* exhibit quite different sectoring patterns, despite identical experimental procedure. This suggests that evolutionary dynamics in microbial colonies is influenced by microscopic details of the growth process. In particular, the morphology of the colony front dictates where cells proliferate and how they move during colony growth. Thus, whereas the dynamics of a clonal lineage in a well-mixed population depends only on its fitness advantage and the strength of genetic drift (via the population size), the future of a lineage in a colony depends also on its location within the colony and how the colony grows around it[110], A quantitative understanding of lineage dynamics in colonies and their dependence on microscopic details is lacking: How do the shape and roughness of the front influence the appearance and number of sectors, and how do both cell-scale properties such as cell shape, adhesion properties, or growth rate influence colony morphology and thus evolutionary dynamics? What are the effects on colony growth patterns of environmental parameters like temperature, chemical composition, and physical properties of the growth medium? How does the probability of an individual mutant cell to form a sector depend on its fitness relative to its neighbors?

In order to make progress towards of a predictive understanding of evolutionary dynamics in microbial colonies, we will investigate some of these questions in the following chapters. Our experiments are supported by simulations and theory that guide the interpretation of experimental results. We employ two different classes of mathematical models that we introduce in the following two sections: firstly, we describe

simple models for the growth and emergent shape of microbial colonies, and secondly, we review models of evolutionary dynamics, first in well-mixed populations as a null model, and then in spatially expanding populations.

1.3 Growth and shape of microbial colonies

The morphology of microbial colonies has been an important identifying feature since the early beginnings of microbiology[113,114], and how colony patterns form has intrigued generations of scientists[115]. As seen in Fig. 1.5, depending on the species and environmental conditions, colonies can be smooth (*S. cerevisiae*, panel a), rough (*E. coli*, b), or have a more complex morphology with wrinkles, branches, vortices, or rings (panels c-e). Even small changes in genotype, nutrient or agar concentration can have a dramatic impact on colony morphology (panels d&e). Mathematical models of growing colonies abound; in the following, we concentrate on phenomenological models for compact and roughly circular colonies such as those in Fig. 1.5a&b, and refer to the literature for models of more complex morphologies[111,116–120].

1.3.1 Traveling wave model of colony growth

The simplest mathematical model for the spread of a population in space is the Fisher wave. The population is described by the number $n(x,t)$ of individuals in a series of subpopulations called demes, invading previously unoccupied territory. Individuals proliferate at a rate depending on the local density, and migrate between neighboring demes. In the continuum limit, the time evolution of $n(x,t)$ is described by the Fisher-Kolmogorov-Petrovsky-Piscounov (FKPP) equation[121–123]

$$\partial_t n(x,t) = D\partial_x^2 n + k_0 n f(n), \tag{1.1}$$

where D parametrizes the strength of (short-ranged) migration and k_0 is the per-capita growth rate. The function $f(n)$ summarized the effects of ecology such as nutrient limitation. For instance, the population cannot grow indefinitely; growth halts when the density reaches the *carrying capacity* K, which corresponds to the maximal density that is sustainable with the given resources. The most common choice for $f(n)$ satisfying this criterion is $f(n) = (1 - n/K)$[121]. The resulting wave is called a "pulled" wave because a small number of individuals at the tip of the wave effectively create the forwards motion of the wave. Another prominent choice, $f(n) = (1-n/K)(1+Bn/K)$, describes scenarios where the population needs a minimum size to strive, a situation dubbed the Allee effect[124,125]. Such scenarios can arise for number of reasons, such as increased mating success or cooperative hunting or protection. Since the growth rate is maximal at intermediate population densities (see Fig. 1.6), the resulting wave is called a "pushed" wave because individ-

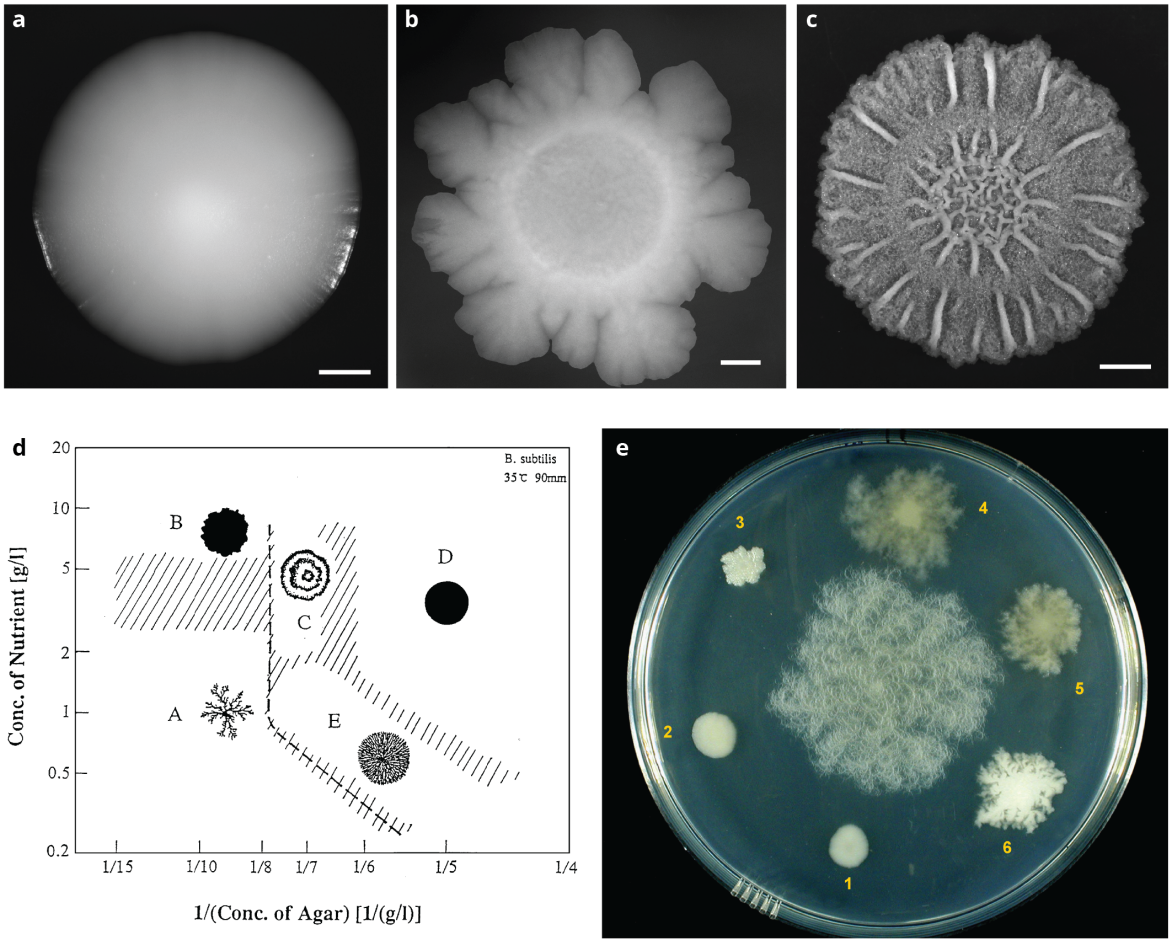

Figure 1.5: Examples of different colony morphologies. (a) Budding yeast *S. cerevisiae* on YPD grown at 30°C for 4 days has a smooth morphology. (b) *E. coli* colonies of strain REL606 grown on LB at 37°C for 3 days are characterized by a rough front. (c) Colonies of *B. subtilis* strain NCIB 3610 grown on Msgg at 30° for 3 days exhibits wrinkles. Image taken by QinQin Yu. Scale bars in panels a-c are 2mm. (d) "Phase" diagram for the diversity of colony morphologies of a wild-type strain of *B. subtilis* at 35°C on media containing different amounts of agar and nutrients. Colonies such as the one shown in panel c) correspond to type B. Reprinted with permission from Ref. 111. (e) Colonies of *Bacillus mycoides* wild type (center colony) and mutants (surrounding colonies) grown on 1.5% agar medium for two days at 25°C show that very closely related organisms can have vastly different colony morphologies. Reprinted from Ref. 112, originally published by BioMed Central.

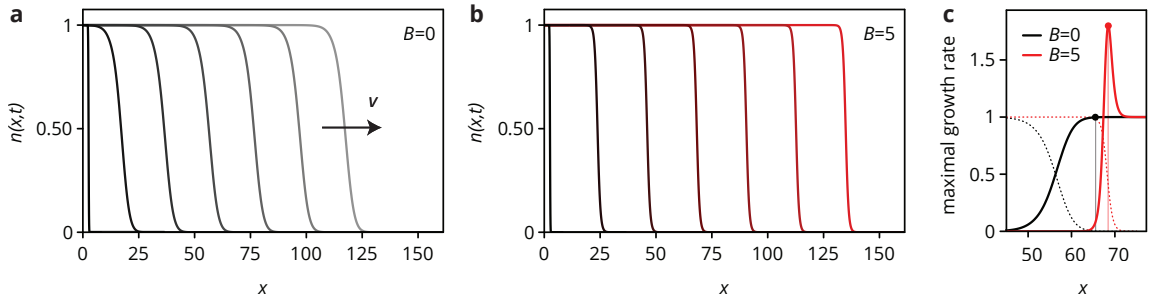

Figure 1.6: Numerical solutions to the FKPP equation without (a) and with (b) the Allee effect. Traces of $\rho(x,t)$ are shown for constant time increments. The population expands as a traveling wave with a transition region of width λ. For $B = 0$ (a, no Allee effect), $\lambda \sim \sqrt{D/k_0}$, while a strong Allee effect (b, $B = 5$) creates steeper wave profiles. (c) Without an Allee effect (black lines), the maximal per-capita growth rate is reached at when the population density (dots) is low. By contrast, the maximal growth rate is highest intermediate population density for $B > 0$ (red lines).

uals at the tip of the wave are pushed by the population towards the bulk of the population. In principle, $f(n)$ can also incorporate the effect of heterogeneous environments, such as nutrient or antibiotic gradients, on the expansion of the population. This is discussed in more detail in Chapter 6.

Numerical solutions to eq. (1.1) for both pulled and pushed waves, presented in Fig. 1.6, show that after a short initial transient, the front of the population expands away from the initial habitat at a constant speed v, with a population profile transitioning from the maximum density to zero over a relatively short transient region of width $\lambda \sim \sqrt{D/k_0}$. To find the speed of the expansion analytically, we seek traveling wave solutions to eq. (1.1) of the form $n(x,t) = n(z = x - vt)$. In the co-moving frame, $n(z)$ is then the solution to

$$0 = D\partial_z^2 n + v\partial_z n + k_0 n(1 - n/K). \tag{1.2}$$

At the tip of the traveling population wave, where the first pioneers migrate into virgin territory, the population density will be low, such that the nonlinearity in the growth term can be neglected. The density of the tip of the wave front thus falls off exponentially over the distance λ, whence the wave speed v for pulled waves can be found to be $v_F = 2\sqrt{k_0 D}$ for biologically relevant initial conditions. The wave speed of pushed waves is larger than v_F and depends on the strength of cooperation B[126].

The spread of the FKPP wave is driven by pioneers at the tip of the wave entering previously uninhabited territory. Eq. (1.1) is completely deterministic, even for very small ρ, but when and where those pioneers first arrive is a stochastic process, and thus at low density, the discreteness of individuals becomes important. The arguably simplest way to incorporate this discreteness into the Fisher wave framework is to introduce a phenomenological cut-off in the growth rate when the population density falls below a cut-off density

ϵ[127]. A more formal way to model the fluctuations at the tip of the wave consists in adding to eq. 1.1 a noise term proportional to $\sqrt{n(x,t)}\xi(t)$ with Brownian noise $\xi(t)$, resulting in the stochastic sFKPP equation. The square-root dependence of the strength of fluctuations on the local density n is a result of the Binomial sampling of the current population for the next generation, with mean and variance proportional to $n(x,t)$ when the density is low[128]. Both the phenomenological theory and the stochastic FKPP equation predict a reduction in the front speed of pulled waves that remains sizable even for relatively large carrying capacity, in excellent agreement with simulations[127,128]. A strong Allee effect reduces the importance of small number fluctuations at low population density because the expansion is driven by growth at intermediate population density[129].

1.3.2 Beyond one-dimensional Fisher waves

The FKPP equation 1.1 can easily be extended to higher dimensions, making it an attractive null model for the spread of microbial colonies[130]. Similarly to the one-dimensional case, the radially symmetric FKPP equation in two dimensions predicts the wave-like spread of the population with an asymptotic wave speed v_F and an active zone of width λ[123]. In reality, microbial colonies cannot be accurately described as Fisher waves. Firstly, as we show in Appendix A, the colony expansion speed is not generally proportional to the square root of the growth rate. In addition, there is no reason to assume that individual cells at the front are free to migrate; instead, their motion is generated in large part by the forces created by their neighbors which push them forward. Thus, the diffusion "constant" should depend on the local density, especially in organisms producing a lubricating film[116]. Finally, and most importantly, the population predicted by the FKPP equation is essentially a smooth circular disk, whereas microbial colonies are never perfectly round, as seen in Fig. 1.5. Even colonies of budding yeast (Fig. 1.5a), which seem smooth to the naked eye, are characterized by microscopic bulges spanning dozens of cells, as we will show in Chapters 3 and 4.

More realistic models for colony growth can be constructed by including nonlinear diffusion and an explicit computation of the underlying nutrient concentration field $\rho(x,t)$ into a set of partial differential equations[116,131] of the general form

$$\partial_t n(x,t) = \partial_x \left[D_n(n)\partial_x n\right] + k_0 f_\rho(\rho) n, \tag{1.3}$$

$$\partial_t \rho(x,t) = D_\rho \partial_x^2 \rho - f_\rho(\rho) n, \tag{1.4}$$

where $D_n(n)$ and D_ρ are (non-linear) diffusion coefficients for cells and nutrients, respectively, and $f_\rho(\rho)$ encapsulates the nutrient uptake efficiency of the cells. Non-linear reaction-diffusion equations of this type produce a rich phenomenology of colony morphologies, including branches and concentric ring structures observed in experiments, but they can typically only be solved numerically[116]. Thankfully, to study the effects

of colony growth patterns on evolutionary dynamics, we do not need a full description of the whole bulk of the population; a more realistic model for the rough front of colonies suffices.

1.3.3 Models of rough interfaces

The mathematical description of rough interfaces has a long history in statistical mechanics[132]. What we mean by "rough" is that the interfaces we study are subject of stochastic fluctuations that shape how the interface evolves over time. Examples of rough fronts in this sense include the interface of a fluid pushed through porous media, the fronts of forest fires and plant invasions, the edges of magnetic domains, and, of course, microbial colonies[132]. The goal is to characterize the interface in terms of a set of characteristic exponents that are universal, i.e., do not depend on microscopic details, for a large class of interfaces; two interfaces with the same characteristic exponents are said to be in the same *universality class*, implying that they share some fundamental properties such as certain symmetries. In the case of microbial colonies, the hope is that we can distill the expansion of a colony into a set of growth rules that give rise to a set of exponents that can be measured in experiments. To do this, we first discuss how to describe rough interfaces mathematically before reviewing simple evolution equations of rough interfaces.

1.3.4 Scaling concepts

It is convenient to study the front of a colony growing in a box; the characteristic exponents extend to radially growing colonies. Through cell division and cell-cell pushing, the colony will expand with an average speed v to an average "height" (radius) $\overline{h}(t) = vt$. We can characterize the roughness of the colony by quantifying the deviations from a flat front, i.e., by the variance $w^2(L,t)$ of the interface height around its mean

$$w^2(L,t) = \frac{1}{L}\int_0^L \left[h(x,t) - \overline{h}(t)\right]^2 \,\mathrm{d}x. \tag{1.5}$$

In Fig. 1.7, we simulate colony growth using a particularly simple algorithm where we will fill a box of width L by dropping in particles at random positions; new particles then "diffuse" around the neighborhood of where they first landed to find a local minimum. This algorithm, called random deposition with surface relaxation[133], generates a rough interface whose width increases initially as

$$w(L,t) \sim t^{\beta} \tag{1.6}$$

until a characteristic time t_x. The exponent β is called the growth exponent; it is the first in series of several

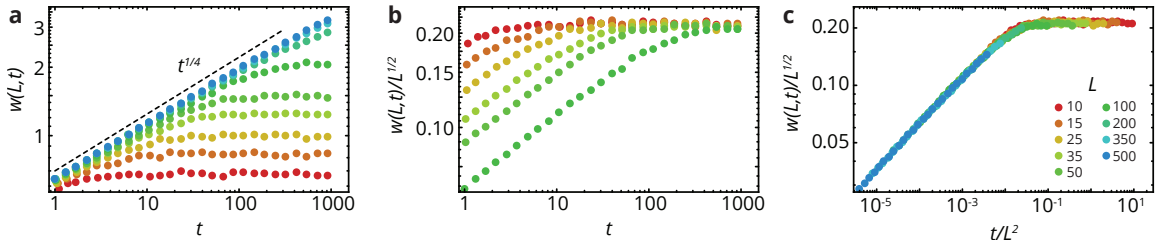

Figure 1.7: Rescaling procedure. (a) Average height over time from simulations of random deposition with surface relaxation performed for different system sizes L ($L = 10 \ldots 500$ from red to blue, see (c) for legend). (b) Rescaling the saturation width by L^α ($\alpha = 1/2$ in this example, only curves that showed clear saturation in (a) were included). (c) Rescaling time by L^z collapses all data on a master curve given by eq. (1.8).

exponents we will encounter. Running the simulation for times much longer than t_x, the interface width eventually saturates at a value that depends on the box width as

$$w_{\text{sat}}(L) \sim L^\alpha, \tag{1.7}$$

where α is called the roughness exponent. This saturation can be understood as follows: Initially, there are no correlations between different position, but as the box begins to fill and new particles organize themselves on an already roughened interface, the configuration of the interface itself induces correlations between different parts of the interface. We call the distance $\ell_\perp$ over which one region of the interface can affect incoming particles the correlation length. $\ell_\perp$ grows over time but cannot grow larger than the box width L. Hence, we can identify the crossover time t_x as the time when the correlations along the interface have reached system size L. This defines the dynamic exponent z through $t_x \sim L^z$. Since t_x is the time at which correlations span the whole system and therefore the interface width has saturated, it follows that $t_x^\beta \sim L^\alpha$. Hence, the exponents z, α, and β are coupled through the relation $z = \frac{\alpha}{\beta}$. The dynamical exponent z allows us to describe the effective average "speed" at which correlations spread laterally along the interface: Thus, in a rough microbial colony, two points along the front a distance $\ell_\perp$ apart can be correlated if the colony has grown at least a distance $\ell_\parallel \sim \ell_\perp^{1/z}$ radially.

Using the exponents α and z, we can write the interface width in its scaling form[134]

$$w(L,t) = L^\alpha f\left(\frac{t}{L^z}\right), \tag{1.8}$$

where the scaling function $f(u)$ obeys

$$f(u) \propto \begin{cases} u^{\beta}, & u \ll 1, \\ 1, & u \gg 1. \end{cases} \tag{1.9}$$

Eq. (1.8) can serve as a recipe for estimating the exponents α and z, as demonstrated in Fig. 1.7. First, we measure the roughness as function of time in systems of different size. According to eq.s (1.6) and (1.7), the initial increase in roughness will be independent of the system size, until it saturates at different values w_{sat}. Thus, we can first normalize the time-dependent roughness by L^{α} until the saturated widths overlap and then rescale time with L^{z} until all curves fall onto a master curve, given by eq.(1.8).

The exponent α has been measured directly for microbial colonies; across several microbial species, values around $\alpha \approx 0.8 \pm 0.1$ have been measured[135–137] (see also Chapter 5), although $\alpha \approx 0.5$ has also been observed[136] (see also Chapter 4). No values for β have been reported in the literature for microbial colonies. Perhaps the closest system in which the dynamic scaling of interfaces has been investigated are confluent monolayers of epithelial cells, where $\alpha \approx 0.75$ and either $\beta \approx 0.33$ or $\beta \approx 0.7$ were found, depending on the growth media[138–141]. How can we explain these exponents?

1.3.5 Edwards-Wilkinson equation

The simplest model involving stochastic growth and the effect of local diffusion, e.g., through cells division and motion of cells along the colony front, can be written as

$$\partial_t h = v + \nu \partial_x^2 h + \eta(x,t). \tag{1.10}$$

Here, ν is a parameter specifying the strength of the effective surface tension generated by random cell motion along the interface, and η encapsulates the noise associated with the growth process; we take it to be Gaussian, uncorrelated noise. Eq. (1.10) was first proposed by Edwards and Wilkinson[142] and can be more generally derived by a careful consideration of the symmetries of the system[132]. Since it is linear, analytical solutions for the roughness[142] and the full distribution of the interface height around its mean can be computed through Fourier transform techniques[143]. To compute the values of the exponents α and z, it is enough to leverage eq. (1.8) which implies that if we rescale space as $x \to bx$, the width as $w \to b^{\alpha} w$, and time as $t \to b^{z} t$, we should obtain the same differential equation for the rescaled interface. Applied to eq. (1.10), this gives

$$\partial_t h = \nu b^{z-2} \partial_x^2 h + b^{-1/2+z/2-\alpha} \eta, \tag{1.11}$$

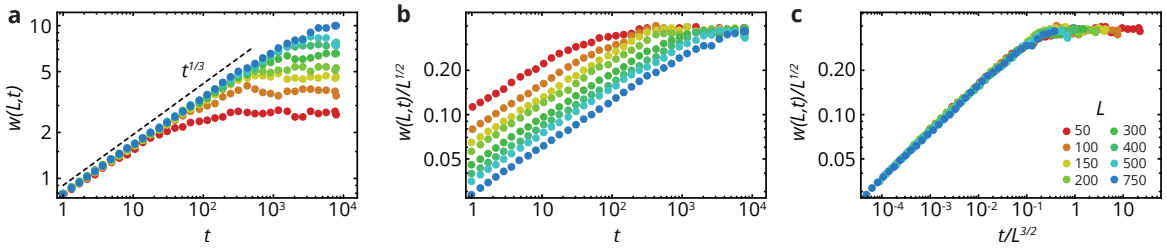

Figure 1.8: (a) Average height over time from Eden model simulations for different system sizes L ($L = 50 \ldots 750$ from red to blue, see (c) for legend). (b) As in Fig. 1.7, we rescale the saturation width by L^{α} with $\alpha = 1/2$. (c) Rescaling time by L^{z} with $z = 3/2$ collapses all data on a master curve. These exponents indicate that the Eden model is in the KPZ universality class.

Enforcing invariance under this transformation we obtain the exponents

$$\alpha = \frac{1}{2},\ \beta = \frac{1}{4},\ z = 2. \tag{1.12}$$

These exponent define the EW universality class. The exponent α implies $w_{sat}^2 \sim L$, i.e., we can regard the saturated interface as a standard diffusive random walk.

1.3.6 Eden model

The EW exponents can readily be observed in simulations such as ballistic deposition with surface relaxation (Fig. 1.7), but they differ strongly from experimental values of α and z measured in microbial colonies and other systems. But perhaps this difference is not unexpected; after all, colonies do not grow by deposition and diffusion of cells, but through cell division at the front. Therefore, a more realistic model is one where a population grows by division of any cell that is not fully surrounded by other cells. This model can most easily be simulated on a square lattice, where each lattice site is either filled or empty. Each filled site with empty neighbors has equal probability of being chosen to "reproduce", i.e., to fill one of its empty neighbors, chosen at random [*]. This algorithm is called the Eden model[144], and we will use various extensions of this model repeatedly in the following chapters.

The most important difference between the Eden model and random deposition with diffusion is that

[*]For simulations, it is convenient to keep a list of all sites that have empty neighbors and delete sites off this list if they lose contact with the front. For very large systems, even this simplification becomes time-consuming, and memory can become a constraint because the whole lattice is kept in memory at all time. As an alternative, one may only keep the front in memory, including the possible neighbors for each site in the list; after every simulation step, all sites that lost their last empty neighbor in the last step are written into a file.

new particles in the Eden model are added locally *normal* to the front, whereas in the random deposition with surface relaxation model new particles are always added from above. It is perhaps not so surprising that the Eden model gives exponents that are different from those predicted by the EW equation with $\alpha \approx 0.5$, $\beta \approx 0.33$, and $z \approx 1.5$ (see Fig. 1.8).

1.3.7 KPZ equation

To explain these exponents, we must extend our model to include growth normal to the interface. Geometrically, normal growth at an angle $\partial_x h$, projected onto the direction of propagation, yields a contribution to the front speed proportional to $\left(1 + |\partial_x h|^2\right)^{-1/2}$. Expanding to first order gives $F(\partial_x h) \sim (\partial_x h)^2$, and we arrive at the so-called Kardar-Parisi-Zhang (KPZ) equation

$$\partial_t h = v + \frac{\lambda}{2}(\partial_x h)^2 + \nu \partial_x^2 h + \sqrt{D}\eta. \tag{1.13}$$

Because of the nonlinearity, the KPZ equation is considerable more difficult to solve than eq. (1.10). Its full solution has only recently been found[145], although many analytical results were already available before, such as for the distribution of the height around the mean[146] or the distribution of the maximum height[147]. The characteristic exponents

$$\alpha = \frac{1}{2},\ \beta = \frac{1}{3},\ z = \frac{3}{2} \tag{1.14}$$

can be found through a number of ways, including scaling arguments and renormalization group calculations[132,148,149].

1.3.8 Experimental observations & deviations from KPZ

The KPZ exponents are found in a number of different simulation schemes, including the Eden model[144], and have been observed experimentally in the slow combustion of paper[150–152], progressing convection fronts in liquid crystals[153,154], the forced imbibition of liquid in porous media for strong forcing[155], the roughness of "coffee-stain effect" depositions of spheres through evaporation[109], and the fronts of some bacterial colonies[136,156]. By contrast, many other experiments have obtained exponents that are inconsistent with the KPZ universality class and typically larger than $\alpha = 1/2$ and $\beta = 1/3$. Examples include epithelial cell monolayers[138–141], coffee-stains of non-spherical objects[109], liquid imbibition into porous media[155,157,158], invasion of clover into rye[159], wetting[160–162] or burning[163] of paper, flux fronts in superconducting thin films[164], two-phase viscous flow in porous media[165], and, again, bacterial colonies[135–137] (see also Chapter 5).

If the membership in a universality class ought to be independent of microscopic details, then how can we explain these deviations from KPZ dynamics? Several extensions of the KPZ equation have been sug-

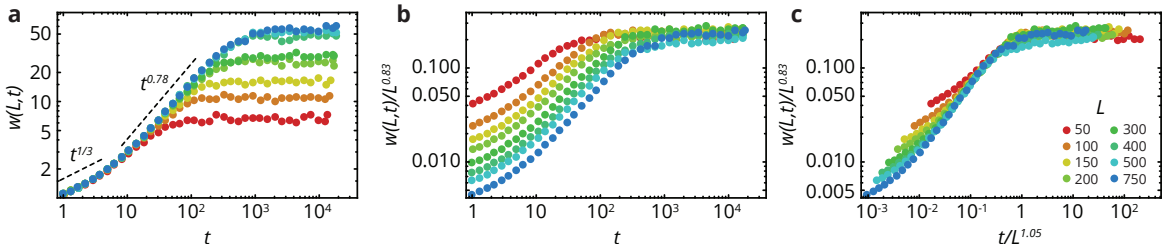

Figure 1.9: (a) Average height over time from Eden model simulations with obstacles for different system sizes L ($L = 50 \ldots 750$ from red to blue, see (c) for legend), close to the critical obstacle density $\rho_c(L)$ for each L. After an initial transient displaying KPZ scaling, another exponent $\beta \approx 0.78$ is found. (b) Rescaling the saturation width by L^α with $\alpha = 0.83$. (c) Rescaling time by L^z with $z = 1.05$ collapses all data on a master curve. The exponents $\alpha = 0.83$, $\beta = 0.78$, $z = 1.05$ are consistent with the quenched Edwards-Wilkinson (qEW) universality class.

gested to explain these differences. For instance, substituting the Gaussian noise $\eta(x,t)$ in eq. (1.13) by a spatio-temporally correlated noise gives exponents that exceed the KPZ predicted values[132,166]. Alternatively, instead of time-dependent (annealed) noise $\eta(x,t)$, we can consider *quenched* noise $\eta(x,h(x,t))$ which depends only on the interface position $h(x,t)$ and not explicitly on time. The quenched noise represents disorder in the environment that the interface grows in. This quenched disorder can be included in the KPZ equation as

$$\partial_t h = F + \frac{\lambda}{2}(\partial_x h)^2 + \nu \partial_x^2 h + \sqrt{D}\eta(x,h(x,t)), \tag{1.15}$$

where F can be understood as a pushing force driving the interface motion. We will study quenched noise and its effects on evolutionary dynamics in microbial colonies in great detail in Chapter 5. Here, we describe only the basic phenomenology of interfaces in disordered environments.

An important consequence of quenched noise is the emergence of a phase transition depending on F. If F is smaller than a characteristic force F_c, the interface becomes stationary ("pinned"). On the other hand, if $F \gg F_c$ the interface moves essentially unhindered through the environment with velocity v. In the latter case, we can simply write $\eta(x,h(x,t)) \to \eta(x,h(x,t)-vt) \sim \eta(x,t)$ to recover KPZ dynamics for $F \gg F_c$.

Two new universality classes emerge for interfaces with quenched noise, with characteristic exponents summarized in Table 1.1, depending on whether the nonlinearity dominates ($\lambda \to \infty$, quenched KPZ class) or vanishes ($\lambda \to 0$, quenched EW class)[167] as F approaches F_c. The corresponding exponents are summarized in Table 1.1; importantly, the predicted exponents are higher than in the KPZ universality class. As an example, anticipating a result from Chapter 5, Fig. 1.9 shows the result of colonies grown with the Eden model in a disordered environment created by making some lattice sites unavailable for growth. The resulting colony interfaces fall in the quenched EW universality class.

Exponent	α	β	z	Reference
EW	1/2	1/4	2	142
KPZ	1/2	1/3	3/2	148
quenched EW				
pinned ($F < F_c$)	0.92	0.88	1.07	167, 168
critical ($F \to F_c^+$)	0.92	0.87	1.07	167, 168
moving ($F \gg F_c$ or $l \gg \xi$)	1/2	1/4	2	167, 168
quenched KPZ				
pinned ($F < F_c$)	0.63	0.63	1	161, 168
critical ($F \to F_c^+$)	0.75	0.75	1	168
moving ($F \gg F_c$ or $l \gg \xi$)	1/2	1/3	3/2	168

Table 1.1: A selection of characteristic exponents for some universality classes. In the universality classes with quenched noise, $\xi \sim f^{-\nu}$ is the correlation length, with $\nu_{qEW} \approx 1.75$ and $\nu_{qKPZ} \approx 1.33$, and $f = |F - F_c|$ is the reduced force.

Overall, not all microbial colonies fall into the same universality class, and their front roughness statistics may depends on several different factors. Temporal correlation created by a minimum duration of the cell cycle may lead to higher exponents than expected from KPZ. In addition, if cells do not separate completely after cell division, this can lead to a phenomenon called chaining where cells grow in the same direction for several generations; this could plausibly introduce long-range spatial correlations. Indeed, colony fronts of *B. subtilis* were consistent with KPZ statistics if cells were septating (separating after division) properly, but exhibited a larger roughness exponent $\alpha \approx 0.8$ for chaining mutants[136]. Alternatively, some microbial colonies may fall into a quenched universality class, because the motion of individual bacteria in the colony may be hindered by other cells adherent to the agar surface or each other, or because the surface itself exhibits microscopic roughness which can function as quenched noise; this may explain why some colonies exhibit KPZ statistics on some length scales but not others (see Chapters 4 and 6).

A quantitative understanding of colony growth is the first step to modeling evolutionary dynamics in microbial colonies. Before introducing existing models of evolution in expanding colonies, it is instructive to briefly discuss a basic model of population genetics in well-mixed populations.

1.4 Modeling evolutionary dynamics

1.4.1 Evolutionary dynamics in well-mixed populations

A first step to understanding evolutionary dynamics in microbial evolution experiments like the LTEE is to track the dynamics of mutations in the population. In the LTEE, on average $N \approx 10^6$ cells are transferred daily into fresh media where they grow exponentially for $\Delta t \approx 7$ generations before exhausting their nutrients. Consider the case where the population is composed of two alleles, the wild type and a mutant type with selective advantage s, defined by its growth that is (1+s) times the wild type's, at relative frequency f in the population. The mutant's higher growth rate translates to an average increase in frequency during the growth process by a factor

$$\frac{f2^{(1+s)\Delta t}}{f2^{(1+s)\Delta t} + (1-f)2^{\Delta t}}. \tag{1.16}$$

The composition of the population after each transfer can be modeled as a Binomial sample of the population of the previous growth cycle. If f changes only little from one transfer to the next, we can then describe the evolution of the frequency f by

$$\partial_t f = sf(1-f) + \sqrt{\frac{f(1-f)}{N}}\eta(t), \tag{1.17}$$

where $\eta(t)$ is standard Brownian noise. Since eq. (1.17) is an ordinary stochastic differential equation, it can be cast into a partial differential (Fokker-Planck) equation for the probability $P(f, t|f_0, t_0)$

$$\frac{\partial P}{\partial t} = \frac{\partial^2}{\partial f^2}\left(\frac{f(1-f)}{2N}P\right) + \frac{\partial}{\partial f}\left(sf(1-f)P\right). \tag{1.18}$$

This equation is well-known in population genetics as the continuum limit (with slight variations in the definition of N) of various classical discrete processes like the Wright-Fisher model or the Moran model[169,170].

Eq. (1.18) can be used to find of the lineage dynamics of a spontaneous mutation, conferring a fitness effect s to a single mutant individual, entering the population at frequency $f_0 = 1/N$. Its frequency f will fluctuate in the population until one of two things happens: either the mutant lineage goes extinct ($f = 0$), or it fixes ($f = 1$). The probability $u = P(1, t \to \infty|1/N, t_0)$ that the mutant lineage ultimately fixes in the population determines the rate at which mutations accumulate in the population and is therefore a key quantity in population genetics. To compute u, we can make use of the Kolmogoroff backward equation for $P(f, t|f_0, t_0)$ corresponding to eq. (1.18), which conditions on the initial condition $f_0(t_0)$ instead of

the final condition $f(t)$, given by

$$\frac{\partial P}{\partial t_0} = \frac{f_0(1-f_0)}{2N}\frac{\partial^2 P}{\partial f_0^2} + s f_0(1-f_0)\frac{\partial P}{\partial f_0}. \tag{1.19}$$

Since the population size is constant and the population homogeneous until a mutation occurs, the time when a single mutation entered the population should not impact its probability of fixation. Hence, we seek a solution $P(1, t \to \infty | f_0)$ independent of t_0 (and t). Setting $\partial_{t_0} P = 0$ in eq. (1.19) and solving with the boundary conditions $p(1, t \to \infty|0) = 0$ (no fixation without mutants) and $p(1, t \to \infty|1) = 1$ (guaranteed fixation of mutant is already fixed) gives

$$u = \frac{1 - e^{-2Nsf_0}}{1 - e^{-2Ns}}. \tag{1.20}$$

Without a fitness difference, the fixation probability $u = f_0$, as one would expect by symmetry. For small s, we recover the result quoted in the introduction[171]

$$u = 2s. \tag{1.21}$$

Our simple model describes only the dynamics of a single mutation with a simple fitness effect, and the generalization to many mutations is not straightforward. The naive hope that multiple mutation will have the same fitness effect and will fluctuate independently in the population is not generally valid[17]. Instead, microbial evolution experiments over the past 30 years have uncovered highly complex dynamics of multiple coexisting lineages that have inspired a large body of theoretical studies. Firstly, each mutation generally has an effect sampled from a distribution of fitness effects (DFE), the shape of which has been studied theoretically[172,173] and inferred experimentally[51,55,174]. Secondly, the effect of a given mutation may depend not only on external parameters such as the available nutrients or the ambient temperature, but also on the genetic background it arises on (*epistasis*), its frequency in the population (frequency-dependent selection), or the presence of other genotypes in the population[17]. Mutations also need not have a direct fitness effect, but can instead increase or decrease the mutation rate[37,49,175] or facilitate future evolutionary trajectories[41,176]. Finally, many mutant lineages exist contemporaneously in large microbial populations, and mutations have to arise on lineages already characterized by a high fitness in order to be successful, an effect called clonal interference (Fig. 1.2)[177]. This effect also allows neutral mutations to fix not through direct selection, but by "hitchhiking" on a background that is on the way to fixation[178]. Here, we ignore these complications and instead aim to understand the evolutionary dynamics of single mutations with a fitness effect in spatially structured populations.

1.4.2 Evolutionary dynamics in spatially structured populations

Stochastic FKPP equation

In section 1.3.1, we used the Fisher wave as a model for the spatial expansion of a microbial colony. Originally, however, Fisher had a different scenario in mind: he was modeling the spread of a beneficial allele with fitness advantage s through an initially homogeneous one-dimensional population[121]. The time evolution of local frequency $f(x,t)$ of the beneficial allele in the population is given by

$$\partial_t f = D\partial_x^2 f + sf(1-f) + b\sqrt{f(1-f)}\xi(t), \tag{1.22}$$

where we have added a noise term with strength b encapsulating genetic drift[179]. Alternatively, eq. (1.22) arises as a generalization of eq. (1.17), which describes the dynamics of a beneficial allele in a well-mixed population, to a spatial model through the addition of a diffusion term. This interpretation identifies eq. (1.22) as the continuum limit of a series of connected well-mixed subpopulation (demes) with migration between them and has inspired the use of 96 well plates to emulate spatial expansions to study the effects of cooperation in microbes[180,181]. Since eq. (1.22) has the same mathematical structure as eq. (1.1), all previous results on the Fisher wave carry over. In particular, if selection is strong relative to genetic drift ($s > 1/b^2D$) the beneficial allele spreads through the population with the familiar Fisher wave speed $v_F = 2\sqrt{Ds}$.

As noted in Section 1.3.2, the FKPP equation can in principle be extended to model the dynamics of mutations in two dimensions, but it becomes very difficult to make analytical progress[130]. However, since most of the dynamics occurs very close to the front, we can coarse-grain the front of a two-dimensional population into a one-dimensional subpopulation in the co-moving frame of the expanding population. This one-dimensional population is then described by eq. (1.22), and the full two-dimensional dynamics is obtained by "stitching together" the one-dimensional subpopulations. This approach indeed reproduces aspects of evolutionary dynamics observed in microbial colonies (Fig. 1.4)[179,182,183].

In contrast to the Langevin equation (1.17) governing the dynamics of a mutant allele in a well-mixed population, eq. (1.22) cannot be easily written as a Fokker-Planck equation and it is therefore much more difficult to work with. However, it can be used to explain formation of neutral sectors in microbial experiments. Considering the spatial heterozygosity, defined as $H(t,x) = \langle f(x,t)(1-f(x,t))\rangle$, which measures the probability of sampling two individuals of different types a distance x apart. From eq. (1.22), it can be shown that $H(t,0)$, quantifying the degree of mixing *within* a deme, goes to zero as $t^{-1/2}$ [179], i.e., all demes are eventually filled with only a single type. This is in agreement with the experimental observation that sectors are homogeneous and separated by sharp boundaries.

Unfortunately, eq. (1.22) cannot be solved directly for $s \neq 0$ because the hierarchy of moment equations

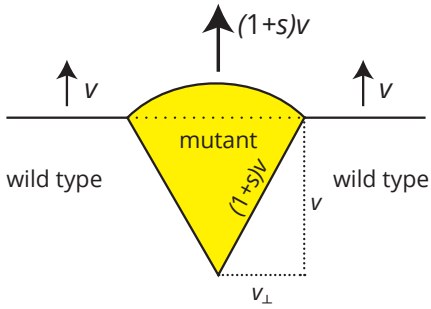

Figure 1.10: Geometrical derivation of the selection drift $v_\perp$. The wild type interface expands at speed v, whereas the mutant interface expands at speed $(1+s)v$. In order to keep a stable boundary between mutants and wild type, the sector expands into wild-type territory with speed $v_\perp = \sqrt{s(2+s)}v$.

does not close as a consequence of presence of both the diffusion term and the nonlinearity $sf(1-f)$. However, since sectors are separated by sharp boundaries after some time, it is tempting to model only the sector boundaries explicitly. To do this, we can average over the noise term to obtain a simple diffusion equation for the mean frequency $F(x,t)$ of the mutant allele. This implies that as long as the sector width $w(t) \gg 0$, it undergoes Brownian motion. In other words, the two sector boundaries can be modeled as two annihilating one-dimensional standard random walks.

Random-walk model for sector boundaries

Keeping track only of the sector boundaries simplifies the analysis significantly, as a selective difference between the two types can simply be modeled by a drift $v_\perp$ that drives the boundaries together (for $s<0$) or apart ($s>0$). The sector width w at time t is then described by the Langevin equation[184]

$$\partial_t w = v_\perp + \sqrt{4D}\eta(t), \tag{1.23}$$

where the diffusion coefficient D quantifies the strength of the sector boundary fluctuations. The boundary fluctuations play the role of genetic drift in microbial colonies, since they encapsulate the randomness of cell division and motion at the boundary and thus stochastically shape the frequency of neutral mutants. The deterministic velocity $v_\perp$ captures the selective (dis-)advantage of the sector and is given by

$$v_\perp = \sqrt{(2+s)}sv, \tag{1.24}$$

The square-root dependence of $v_\perp$ on s follows immediately from geometric consideration[130] (see Fig. 1.10). The mean sector shape for a mutant of initial width w_0 is thus

$$\langle w \rangle = w_0 + \sqrt{(2+s)s} \times vt \tag{1.25}$$

Thus, we can extract the selective advantage of a beneficial sector directly from its shape.

Note that by modeling only the sector boundaries, we have reduced the non-linear partial differential equation with multiplicative noise, eq. (1.22), into a linear ordinary differential equation with additive noise. This means that the Langevin dynamics of the sector boundaries, eq. (1.23), can again be cast into a Fokker-Planck equation for $P(w,t)$. Exactly like in the well-mixed scenario, this allows us the Kolmogoroff backwards equation corresponding to eq. (1.23) to find to compute the establishment probability u as

$$u = \frac{1 - e^{-v_\perp w_0/D}}{1 - e^{-v_\perp L/D}}. \tag{1.26}$$

The mathematical structure of eq. (1.26) is identical to eq. (1.20) for well-mixed populations. Hence, it predicts $u \sim \sqrt{2s}/D$ for a small sector, i.e, u scales with the square root of s rather than linearly in s as in the well-mixed case. This represents a qualitative departure of the evolutionary dynamics in range expansions from those in well-mixed populations.

The random-walk model can also be applied to radial colonies by describing the sector boundaries in terms of their angular width. By switching to angular coordinates, the diffusion coefficient and the selection drift become dependent on the radius, as $D(r) = D/r^2$ and $v_\perp = \sqrt{s(2+s)}v/r$. This means that the sector boundary fluctuations become weaker as the colony grows, explaining why colonies grown from a mixture of two neutral strains demix into a finite number of sectors. By contrast, only one neutral sector survives when the colony is grown in the linear geometry[184]. Computing the establishment probability is more involved for radial populations because $u(s)$ depends on the initial radius. Hence, for radial expansions, one has to first solve for the full probability density $P(w,r)$ and then use first-passage time techniques to find $u(s)$[182]. However, we find $u(s) \sim \sqrt{s}$ in the radial geometry, as well.

Scaling approach to random walks

Computing the establishment probability using the full arsenal of diffusion theory is a rather cumbersome endeavor that will yield analytical results in only a handful of special cases. For instance, we cannot easily generalize the approach of section 1.4.2 to colonies with rough fronts because the model explicitly assumes that the population can be decomposed, depending on growth geometry, into a series of flat/concentric one-dimensional populations. In addition, the sector boundaries in rough colonies of *E. coli* have been observed

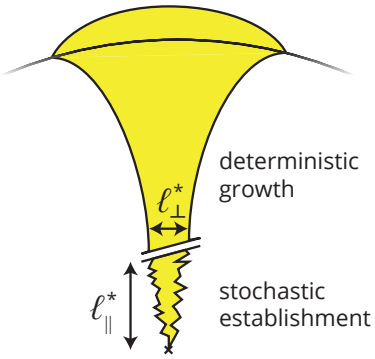

Figure 1.11: Using scaling arguments of fluctuating sector boundaries to compute the establishment probability of beneficial mutations: in sectors wider than $\ell_\perp^*$, selection is stronger than genetic drift and ensures continued survival of the sector. To reach this size, the sector boundaries fluctuate roughly neutrally for a time $\ell_\parallel^*$.

to be not diffusive, but super-diffusive random walks, with fluctuations $\ell_\perp$ around the radial direction that scale with the time-like coordinate $\ell_\parallel$ as $\ell_\perp \sim \ell_\parallel^\zeta$ with $\zeta = 0.65 \pm 0.05$[80]. Not only does this invalidate our description of the sector boundaries as standard (diffusive) random walks, for which $\zeta = 1/2$, it also places these colonies in the KPZ universality class, for which $\zeta = 1/z = 2/3$[185,186].

If we want to describe evolutionary dynamics in rough colonies but do not have access to familiar diffusion techniques, how can we proceed? As an example, let us anticipate a result from Chapter 3 and use scaling arguments to compute the establishment probability of a beneficial mutation in microbial colonies. In order to establish, a clone has to reach a characteristic width $l_\perp^*$ that is large enough to be "safe" from extinction through random genetic drift, such that selection will deterministically drive the clone to fixation. At this sector width, genetic drift and selection are equally strong: for wider sectors, selection dominates, while for narrower sector, drift is the dominant contribution. Comparing with eq. (1.23), this corresponds to $\ell_\perp^* \sim v^\perp \ell_\parallel^* \sim \sqrt{D\langle\eta^2\rangle}\ell_\parallel^*$, where $\ell_\parallel^*$ is the associated "time" at which the width $\ell_\perp^*$ is first reached. Thus, we have

$$D(l_\parallel^*)^\zeta \sim v_\perp(s) l_\parallel^*, \tag{1.27}$$

and we find the characteristic width $l_\perp^* \sim v_\perp^{\zeta/(\zeta-1)}$.

Since the sector starts small before it establishes upon reaching size $l_\perp^*$, it has to fluctuate neutrally to this size before selection can take over. But any individual clone in a subpopulation of width $l_\perp^*$ has equal chance to neutrally drift to size $l_\perp^*$. Hence, the fixation probability is simply $u \sim 1/l_\perp^*$, and we arrive at the result

$$u(s) \sim s^{-\zeta/2(\zeta-1)}, \tag{1.28}$$

which reproduces the scaling of $u \sim s^{1/2}$ for $\zeta = 1/2$ found through the backwards equation (1.26). For $\zeta = 2/3$ associated with KPZ-like fronts we obtain instead $u(s) \sim s$. This agrees well with the experimental measurements presented in Chapter 3. Note that although this scaling is identical to the classical result in well-mixed culture, eq. (1.21), its origin is very different.

In summary, scaling arguments are an extremely valuable tool for describing evolutionary dynamics. Even when analytical solutions are available, scaling arguments often encapsulate all the necessary information and can be more useful than exact, but opaque analytical results. In addition to the establishment probability in Chapter 3, we will find the size distribution of mutant clones in microbial colonies using similar scaling arguments as the ones presented here in Chapters 2 and 5.

1.5 Organization of this thesis

In this thesis, we will approach some of the questions raised in this introductory chapter about evolutionary dynamics in microbial colonies, and more generally, in spatially structured populations. To do so, we focus on creating a solid basis of quantitative experimental results on lineage dynamics in microbial colonies, such as the clone sizes of spontaneous mutations (Chapter 2) and the establishment probability of beneficial mutants (Chapters 3 & 4). In these chapters, the theory of rough interfaces will enable us to make important scaling predictions that we verify with Eden model simulations. Chapter 5 explores the effect of environmental heterogeneity on the efficacy of selection as an example of a uniquely spatial ecological effect; here, we will extend the Eden model to include quenched environmental disorder and use the results on quenched universality classes summarized in this chapter to characterize the resulting colonies. Finally, using simulations and analytical theory based on the FKPP equation introduced above, we discuss the role of flow and environmental gradients on the emergence of drug resistance in Chapter 6.

References

[1] D. R. Maddison and K.-S. Schulz. The Tree of Life Web Project, 2007.

[2] T. G. Dobzhansky. *Genetics and the Origin of Species*, volume 11. Columbia university press, 1937.

[3] C. Darwin. *On the origin of species, 1859*. Routledge, 2004.

[4] A. Eyre-Walker and P. D. Keightley. The distribution of fitness effects of new mutations. *Nature Reviews Genetics*, 8(8):610, 2007.

[5] M. Lässig, V. Mustonen, and A. M. Walczak. Predicting evolution. *Nature Ecology & Evolution*, 1 (3):0077, 2017. doi: 10.1038/s41559-017-0077.

[6] S. A. Frank. *Dynamics of cancer: incidence, inheritance, and evolution*. Princeton University Press, 2007.

[7] N. Woodford and M. J. Ellington. The emergence of antibiotic resistance by mutation. *Clinical Microbiology and Infectious Diseases*, 13:5–18, 2007. doi: 10.1111/j.1469-0691.2006.01492.x.

[8] M. Łuksza and M. Lässig. A predictive fitness model for influenza. *Nature*, 507(7490):57–61, 2014. doi: 10.1038/nature13087.

[9] J. K. Taubenberger and J. C. Kash. Influenza virus evolution, host adaptation, and pandemic formation. *Cell host & microbe*, 7(6):440–451, 2010.

[10] P. R. Grant. *Ecology and evolution of Darwin's finches*. Princeton University Press, 1999.

[11] E. Kussell. Evolution in Microbes. *Annual Review of Biophysics*, 42(1):493–514, 2013. doi: 10.1146/annurev-biophys-083012-130320.

[12] L. Becks and A. F. Agrawal. Higher rates of sex evolve in spatially heterogeneous environments. *Nature*, 468(7320):89, 2010.

[13] S. Yeaman, Y. Chen, and M. C. Whitlock. No effect of environmental heterogeneity on the maintenance of genetic variation in wing shape in drosophila melanogaster. *Evolution*, 64(12):3398–3408, 2010.

[14] D. J. Kemp, D. N. Reznick, G. F. Grether, and J. A. Endler. Predicting the direction of ornament evolution in trinidadian guppies (poecilia reticulata). *Proceedings of the Royal Society of London B: Biological Sciences*, page rspb20091226, 2009.

[15] J. A. Endler. *Geographic variation, speciation, and clines*. Number 10. Princeton University Press, 1977.

[16] J. Beatty. Replaying life's tape. *The Journal of philosophy*, 103(7):336–362, 2006.

[17] J. E. Barrick and R. E. Lenski. Genome dynamics during experimental evolution. *Nature reviews. Genetics*, 14(12):827–39, 2013. doi: 10.1038/nrg3564.

[18] E. R. Jerison and M. M. Desai. Genomic Investigations of Evolutionary Dynamics and Epistasis in Microbial Evolution Experiments. *Current Opinion in Genetics & Development*, 35:33–39, 2015. doi: 10.1002/aur.1474.Replication.

[19] N. A. Bokulich and C. W. Bamforth. The microbiology of malting and brewing. *Microbiology and Molecular Biology Reviews*, 77(2):157–172, 2013.

[20] A. Mondal and A. Datta. Bread baking–a review. *Journal of Food Engineering*, 86(4):465–474, 2008.

[21] B. E. Wolfe and R. J. Dutton. Fermented foods as experimentally tractable microbial ecosystems. *Cell*, 161(1):49–55, 2015.

[22] *Antimicrobial resistance: global report on surveillance*. World Health Organization, 2014.

[23] T. D. Lieberman, J.-B. Michel, M. Aingaran, G. Potter-Bynoe, D. Roux, M. R. Davis Jr, D. Skurnik, N. Leiby, J. J. LiPuma, J. B. Goldberg, et al. Parallel bacterial evolution within multiple patients identifies candidate pathogenicity genes. *Nature genetics*, 43(12):1275, 2011.

[24] T. D. Lieberman, K. B. Flett, I. Yelin, T. R. Martin, A. J. McAdam, G. P. Priebe, and R. Kishony. Genetic variation of a bacterial pathogen within individuals with cystic fibrosis provides a record of selective pressures. *Nature genetics*, 46(1):82, 2014.

[25] L. Yang, L. Jelsbak, R. L. Marvig, S. Damkiær, C. T. Workman, M. H. Rau, S. K. Hansen, A. Folkesson, H. K. Johansen, O. Ciofu, et al. Evolutionary dynamics of bacteria in a human host environment. *Proceedings of the National Academy of Sciences*, 108(18):7481–7486, 2011.

[26] M. M. Mwangi, S. W. Wu, Y. Zhou, K. Sieradzki, H. de Lencastre, P. Richardson, D. Bruce, E. Rubin, E. Myers, E. D. Siggia, et al. Tracking the in vivo evolution of multidrug resistance in staphylococcus

aureus by whole-genome sequencing. *Proceedings of the National Academy of Sciences*, 104(22):9451–9456, 2007.

[27] S. Zhao, T. D. Lieberman, M. Poyet, M. Groussin, S. M. Gibbons, R. J. Xavier, and E. J. Alm. Adaptive evolution within the gut microbiome of individual people. *bioRxiv*, page 208009, 2017.

[28] N. R. Garud, B. H. Good, O. Hallatschek, and K. S. Pollard. Evolutionary dynamics of bacteria in the gut microbiome within and across hosts. *bioRxiv*, page 210955, 2017.

[29] S. E. Luria and M. Delbrück. Mutations of Bacteria from Virus Sensitivity to Virus Resistance. *Genetics*, 28(6):491–511, nov 1943.

[30] D. A. Kessler and H. Levine. Large population solution of the stochastic Luria-Delbruck evolution model. *Proceedings of the National Academy of Sciences of the United States of America*, 110(29): 11682–7, jul 2013. doi: 10.1073/pnas.1309667110.

[31] M. J. Williams, B. Werner, C. P. Barnes, T. A. Graham, and A. Sottoriva. Identification of neutral tumor evolution across cancer types. *Nature Genetics*, 48(3):238–244, 2016. doi: 10.1038/ng.3489.

[32] D. Fusco, M. Gralka, A. Anderson, J. Kayser, and O. Hallatschek. Excess of mutational jackpot events in growing populations due to gene surfing. *Nature Communications*, 7:1–9, 2016. doi: 10.1101/053405.

[33] H.-Y. Wang, Y. Chen, D. Tong, S. Ling, Z. Hu, Y. Tao, X. Lu, and C.-I. Wu. Is the evolution in tumors darwinian or non-darwinian? *National Science Review*, 5(1):15–17, 2017.

[34] M. J. Williams, B. Werner, C. P. Barnes, T. A. Graham, and A. Sottoriva. Reply: Is the evolution of tumors darwinian or non-darwinian? *National Science Review*, 2018.

[35] R. E. Lenski, M. R. Rose, S. C. Simpson, and S. C. Tadler. Long-Term Experimental Evolution in Escherichia coli. I . Adaptation and Divergence During 2,000 Generations. *The American naturalist*, 138(6):1315–1341, 1991.

[36] R. E. Lenski and M. Travisano. Dynamics of adaptation and diversification: a 10,000-generation experiment with bacterial populations. *Proceedings of the National Academy of Sciences of the United States of America*, 91(15):6808–6814, 1994. doi: 10.1073/pnas.91.15.6808.

[37] P. D. Sniegowski, P. J. Gerrish, and R. E. Lenski. Evolution of high mutation rates in experimental populations of E . coli. *Nature*, 387:703–705, 1997. doi: 10.1128/AEM.02595-09.

[38] M. J. Wiser, N. Ribeck, and R. E. Lenski. Long-term dynamics of adaptation in asexual populations. *Science*, page 1243357, 2013.

[39] M. D. Herron and M. Doebeli. Parallel Evolutionary Dynamics of Adaptive Diversification in Escherichia coli. *PLoS Biology*, 11(2), 2013. doi: 10.1371/journal.pbio.1001490.

[40] J. Plucain, T. Hindre, M. Le Gac, O. Tenaillon, S. Cruveillier, C. Medigue, N. Leiby, W. R. Harcombe, C. J. Marx, R. E. Lenski, and D. Schneider. Epistasis and Allele Specificity in the Emergence of a Stable Polymorphism in Escherichia coli. *Science*, 343(January):160–164, 2014.

[41] Z. D. Blount, C. Z. Borland, and R. E. Lenski. Historical contingency and the evolution of a key innovation in an experimental population of Escherichia coli. *Proceedings of the National Academy of Sciences of the United States of America*, 105(23):7899–7906, 2008. doi: 10.1073/pnas.0803151105.

[42] M. Greaves and C. C. Maley. Clonal evolution in cancer. *Nature*, 481(7381):306, 2012.

[43] S. Ling, Z. Hu, Z. Yang, F. Yang, Y. Li, Q. Chen, Q. Gong, D. Wu, W. Li, X. Tian, C. Hao, E. A. Hungate, V. T. Daniel, R. R. Hudson, W.-h. Li, X. Lu, S. Ling, Z. Hu, Z. Yang, F. Yang, Y. Li, P. Lin, K. Chen, L. Dong, and L. Cao. Extremely high genetic diversity in a single tumor points to prevalence of non-Darwinian cell evolution. *Proceedings of the National Academy of Sciences*, 113(5):E663–E663, 2016. doi: 10.1073/pnas.1600151113.

[44] E. Ghedin, N. A. Sengamalay, M. Shumway, J. Zaborsky, T. Feldblyum, V. Subbu, D. J. Spiro, J. Sitz, H. Koo, P. Bolotov, et al. Large-scale sequencing of human influenza reveals the dynamic nature of viral genome evolution. *Nature*, 437(7062):1162, 2005.

[45] R. A. Neher and T. Bedford. nextflu: Real-time tracking of seasonal influenza virus evolution in humans. *Bioinformatics*, 31(21):3546–3548, 2015. doi: 10.1093/bioinformatics/btv381.

[46] S. B. Levy and B. Marshall. Antibacterial resistance worldwide: causes, challenges and responses. *Nature medicine*, 10(12s):S122, 2004.

[47] J. Davies and D. Davies. Origins and evolution of antibiotic resistance. *Microbiology and molecular biology reviews*, 74(3):417–433, 2010.

[48] H.-X. Liao, R. Lynch, T. Zhou, F. Gao, S. M. Alam, S. D. Boyd, A. Z. Fire, K. M. Roskin, C. A. Schramm, Z. Zhang, et al. Co-evolution of a broadly neutralizing hiv-1 antibody and founder virus. *Nature*, 496(7446):469, 2013.

[49] B. H. Good, M. J. McDonald, J. E. Barrick, R. E. Lenski, and M. M. Desai. The dynamics of molecular evolution over 60,000 generations. *Nature*, 551(7678):45, 2017.

[50] J. R. Blundell and S. F. Levy. Beyond genome sequencing: Lineage tracking with barcodes to study the dynamics of evolution, infection, and cancer. *Genomics*, 104(6):1–14, 2014. doi: 10.1016/j.ygeno.2014.09.005.

[51] S. F. Levy, J. R. Blundell, S. Venkataram, D. A. Petrov, S. Fisher, G. Sherlock, Q. Biology, S. Brook, C. Biology, and S. Brook. Quantitative evolutionary dynamics using high-resolution lineage tracking. *Nature*, 519(7542):181–186, 2015. doi: 10.1038/nature14279.Quantitative.

[52] A. I. Nilsson, S. Koskiniemi, S. Eriksson, E. Kugelberg, J. C. D. Hinton, and D. I. Andersson. Bacterial genome size reduction by experimental evolution. *Proceedings of the National Academy of Sciences USA*, 102(34):12112–12116, 2005. doi: 10.1073/pnas.0503654102.

[53] M. Ackermann, A. Schauerte, S. C. Stearns, and U. Jenal. Experimental evolution of aging in a bacterium. *BMC Evolutionary Biology*, 7:1–10, 2007. doi: 10.1186/1471-2148-7-126.

[54] M. J. Dunham, H. Badrane, T. Ferea, J. Adams, P. O. Brown, F. Rosenzweig, and D. Botstein. Characteristic genome rearrangements in experimental evolution of Saccharomyces cerevisiae. *Proceedings of the National Academy of Sciences*, 99(25):16144–16149, 2002. doi: 10.1073/pnas.242624799.

[55] M. M. Desai, D. S. Fisher, and A. W. Murray. The speed of evolution and maintenance of variation in asexual populations. *Current biology : CB*, 17(5):385–94, mar 2007. doi: 10.1016/j.cub.2007.01.072.

[56] G. I. Lang, D. Botstein, and M. M. Desai. Genetic variation and the fate of beneficial mutations in asexual populations. *Genetics*, 188(3):647–61, jul 2011. doi: 10.1534/genetics.111.128942.

[57] G. I. Lang, D. P. Rice, M. J. Hickman, E. Sodergren, G. M. Weinstock, D. Botstein, and M. M. Desai. Pervasive genetic hitchhiking and clonal interference in forty evolving yeast populations. *Nature*, 500 (7464):571–4, 2013. doi: 10.1038/nature12344.

[58] E. Toprak, A. Veres, J.-B. Michel, R. Chait, D. L. Hartl, and R. Kishony. Evolutionary paths to antibiotic resistance under dynamically sustained drug selection. *Nature genetics*, 44(1):101–5, jan 2012. doi: 10.1038/ng.1034.

[59] H. A. Lindsey, J. Gallie, S. Taylor, and B. Kerr. Evolutionary rescue from extinction is contingent on a lower rate of environmental change. *Nature*, 494(7438):463–7, feb 2013. doi: 10.1038/nature11879.

[60] G. Bell and A. Gonzalez. Evolutionary rescue can prevent extinction following environmental change. *Ecology letters*, 12(9):942–8, sep 2009. doi: 10.1111/j.1461-0248.2009.01350.x.

[61] M. M. Desai. Statistical questions in experimental evolution. *Journal of Statistical Mechanics: Theory and Experiment*, 2013(01):P01003, jan 2013. doi: 10.1088/1742-5468/2013/01/P01003.

[62] M. J. McDonald, D. P. Rice, and M. M. Desai. Sex speeds adaptation by altering the dynamics of molecular evolution. *Nature*, 531(7593):233–236, 2016. doi: 10.1038/nature17143.

[63] K. Kosheleva and M. M. Desai. Recombination Alters the Dynamics of Adaptation on Standing Variation in Laboratory Yeast Populations. *Molecular Biology and Evolution*, 35(1):180–201, 2018. doi: 10.1093/molbev/msx278.

[64] S. Kryazhimskiy, D. P. Rice, and M. M. Desai. Population subdivision and adaptation in asexual populations of saccharomyces cerevisiae. *Evolution*, 66(6):1931–1941, 2012. doi: 10.1111/j.1558-5646.2011.01569.x.

[65] A. C. Gerstein, L. Cleathero, M. Mandegar, and S. Otto. Haploids adapt faster than diploids across a range of environments. *Journal of evolutionary biology*, 24(3):531–540, 2011.

[66] A. M. Selmecki, Y. E. Maruvka, P. A. Richmond, M. Guillet, N. Shoresh, A. L. Sorenson, S. De, R. Kishony, F. Michor, R. Dowell, et al. Polyploidy can drive rapid adaptation in yeast. *Nature*, 519 (7543):349, 2015.

[67] J. W. Costerton, Z. Lewandowski, D. E. Caldwell, D. R. Korber, and H. M. Lappin-Scott. Microbial biofilms. *Annual review of microbiology*, 49:711–45, 1995. doi: 10.1146/annurev.mi.49.100195.003431.

[68] L. Hall-Stoodley, J. William Costerton, and P. Stoodley. Bacterial biofilms: from the natural environment to infectious diseases. *Nature Reviews Microbiology*, 2(2):95–108, 2004. doi: 10.1038/nrmicro821.

[69] J. W. Wimpenny and S. L. Kinniment. Biochemical reactions and the establishment of gradients within biofilms. *Microbial biofilms. Plant and Microbial Biotechnology Research Series*, 5:99–117, 1995.

[70] A. W. Decho. Microbial biofilms in intertidal systems: An overview. *Continental Shelf Research*, 20 (10-11):1257–1273, 2000. doi: 10.1016/S0278-4343(00)00022-4.

[71] P. Lavelle, T. Decaëns, M. Aubert, S. Barot, M. Blouin, F. Bureau, P. Margerie, P. Mora, and J. P. Rossi. Soil invertebrates andecosystem services. *European Journal of Soil Biology*, 42(SUPPL. 1), 2006. doi: 10.1016/j.ejsobi.2006.10.002.

[72] J. L. M. Welch, B. J. Rossetti, C. W. Rieken, F. E. Dewhirst, and G. G. Borisy. Biogeography of a human oral microbiome at the micron scale. *Proceedings of the National Academy of Sciences*, 113(6): E791–E800, 2016.

[73] J. Costerton, P. Stewart, and E. Greenberg. Bacterial biofilms: a common cause of persistent infections. *Science, 1999*, 284(May):1318–1322, 1999. doi: 10.1126/science.284.5418.1318.

[74] J. W. Costerton. Overview of microbial biofilms. *Journal of Industrial Microbiology*, 15(3):137–140, 1995. doi: 10.1007/BF01569816.

[75] H. P. Steenackers, I. Parijs, K. R. Foster, and J. Vanderleyden. Experimental evolution in biofilm populations. *FEMS microbiology reviews*, 40(3):373–397, 2016.

[76] S. Elias and E. Banin. Multi-species biofilms: living with friendly neighbors. *FEMS microbiology reviews*, 36(5):990–1004, 2012.

[77] A. Persat, C. D. Nadell, M. K. Kim, F. Ingremeau, A. Siryaporn, K. Drescher, N. S. Wingreen, B. L. Bassler, Z. Gitai, and H. A. Stone. The mechanical world of bacteria. *Cell*, 161(5):988–997, 2015. doi: 10.1016/j.cell.2015.05.005.

[78] G. Lambert, L. Estévez-Salmeron, S. Oh, D. Liao, B. M. Emerson, T. D. Tlsty, and R. H. Austin. An analogy between the evolution of drug resistance in bacterial communities and malignant tissues. *Nature Reviews Cancer*, 11(5):375, 2011.

[79] E. A. Martens, R. Kostadinov, C. C. Maley, and O. Hallatschek. Spatial structure increases the waiting time for cancer. *New Journal of Physics*, 13:1–25, 2011. doi: 10.1088/1367-2630/13/11/115014.

[80] O. Hallatschek, P. Hersen, S. Ramanathan, and D. R. Nelson. Genetic drift at expanding frontiers promotes gene segregation. *Proceedings of the National Academy of Sciences*, 104(50):19926–19930, 2007.

[81] L. Excoffier, M. Foll, and R. J. Petit. Genetic Consequences of Range Expansions. *Annual Review of Ecology, Evolution, and Systematics*, 40(1):481–501, dec 2009. doi: 10.1146/annurev.ecolsys.39.110707.173414.

[82] P. B. Rainey and M. Travisano. Adaptive radiation in a heterogeneous environment. *Nature*, 394 (6688):69–72, 1998. doi: 10.1038/27900.

[83] M. G. Habets, D. E. Rozen, R. F. Hoekstra, and J. De Visser. The effect of population structure on the adaptive radiation of microbial populations evolving in spatially structured environments. *Ecology letters*, 9(9):1041–1048, 2006.

[84] R. Korona, C. H. Nakatsu, L. J. Forney, and R. E. Lenski. Evidence for multiple adaptive peaks from populations of bacteria evolving in a structured habitat. *Proceedings of the National Academy of Sciences*, 91(19):9037–9041, 1994.

[85] L. Perfeito, M. I. Pereira, P. R. A. Campos, and I. Gordo. The effect of spatial structure on adaptation in Escherichia coli. *Biology Letters*, 4(1):57–59, 2008. doi: 10.1098/rsbl.2007.0481.

[86] C. Saint-Ruf, M. Garfa-Traoré, V. Collin, C. Cordier, C. Franceschi, and I. Matic. Massive diversification in aging colonies of escherichia coli. *Journal of bacteriology*, 196(17):3059–3073, 2014.

[87] S. R. Poltak and V. S. Cooper. Ecological succession in long-term experimentally evolved biofilms produces synergistic communities. *ISME Journal*, 5(3):369–378, 2011. doi: 10.1038/ismej.2010.136.

[88] J. Schluter, C. D. Nadell, B. L. Bassler, and K. R. Foster. Adhesion as a weapon in microbial competition. *ISME Journal*, 9(1):139–149, 2015. doi: 10.1038/ismej.2014.174.

[89] D. van Ditmarsch, K. E. Boyle, H. Sakhtah, J. E. Oyler, C. D. Nadell, E. Déziel, L. E. P. Dietrich, and J. B. Xavier. Convergent evolution of hyperswarming leads to impaired biofilm formation in pathogenic bacteria. *Cell reports*, 4(4):697–708, aug 2013. doi: 10.1016/j.celrep.2013.07.026.

[90] K. Drescher, C. D. Nadell, H. A. Stone, N. S. Wingreen, and B. L. Bassler. Solutions to the Public Goods Dilemma in Bacterial Biofilms. *Current biology*, 24:1–6, dec 2014. doi: 10.1016/j.cub.2013.10.030.

[91] F. Goldschmidt, R. R. Regoes, and D. R. Johnson. Successive range expansion promotes diversity and accelerates evolution in spatially structured microbial populations. *The ISME journal*, 11(9):2112, 2017.

[92] J. Yan, C. D. Nadell, H. A. Stone, N. S. Wingreen, and B. L. Bassler. Extracellular-matrix-mediated osmotic pressure drives Vibrio cholerae biofilm expansion and cheater exclusion. *Nature Communications*, 8:327, 2018. doi: 10.1038/s41467-017-00401-1.

[93] K. Drescher, Y. Shen, B. L. Bassler, and H. A. Stone. Biofilm streamers cause catastrophic disruption of flow with consequences for environmental and medical systems. *Proceedings of the National Academy of Sciences*, 110(11):4345–4350, 2013. doi: 10.1073/pnas.1300321110.

[94] Q. Zhang, G. Lambert, D. Liao, H. Kim, K. Robin, C.-k. Tung, N. Pourmand, and R. H. Austin. Acceleration of Emergence of Bacterial Antibiotic Resistance in Connected Microenvironments. *Science*, 333(September):1764–1767, 2011.

[95] M. Baym, T. D. Lieberman, E. D. Kelsic, R. Chait, R. Gross, I. Yelin, and R. Kishony. Spatiotemporal microbial evolution on antibiotic landscapes. *Science*, 353(6304):1147 LP – 1151, 2016. doi: 10.1126/science.aag0822.

[96] N. A. Rosenberg, J. K. Pritchard, J. L. Weber, H. M. Cann, K. K. Kidd, L. A. Zhivotovsky, and M. W. Feldman. Genetic structure of human populations. *science*, 298(5602):2381–2385, 2002.

[97] S. Ramachandran, O. Deshpande, C. C. Roseman, N. A. Rosenberg, M. W. Feldman, and L. L. Cavalli-Sforza. Support from the relationship of genetic and geographic distance in human populations for a serial founder effect originating in Africa. *Proceedings of the National Academy of Sciences*, 102(44):15942–15947, 2005. doi: 10.1073/pnas.0507611102.

[98] N. Ray, M. Currat, P. Berthier, and L. Excoffier. Recovering the geographic origin of early modern humans by realistic and spatially explicit simulations. *Genome Research*, 15:1161–1167, 2005. doi: 10.1101/gr.3708505.against.

[99] S. J. Armitage, S. A. Jasim, A. E. Marks, A. G. Parker, V. I. Usik, and H.-P. Uerpmann. The southern route "out of Africa": evidence for an early expansion of modern humans into Arabia. *Science*, 331 (6016):453–456, 2011.

[100] L. R. P. C and M. A. McGeoch. Rapid range expansion and community reorganization in response to warming. *Global Change Biology*, 14(12):2950–2962, 2008.

[101] R. I. Colautti and S. C. H. Barrett. Rapid Adaptation to Climate Facilitates Range Expansion of an Invasive Plant. *Science*, 342(6156):364–366, 2013. doi: 10.1126/science.1242121.

[102] A. L. Carroll, S. W. Taylor, J. Régnière, and L. Safranyik. Effects of Climate Change on Range Expansion by the Mountain Pine Beetle in British Columbia. *Methods*, 30(BC-X-399):223–232, 2003. doi: InformationReportBC-X-399.

[103] T. J. Cudmore, N. Björklund, A. L. Carroll, and B. Staffan Lindgren. Climate change and range expansion of an aggressive bark beetle: Evidence of higher beetle reproduction in naïve host tree populations. *Journal of Applied Ecology*, 47(5):1036–1043, 2010. doi: 10.1111/j.1365-2664.2010.01848.x.

[104] T. A. White, S. E. Perkins, G. Heckel, and J. B. Searle. Adaptive evolution during an ongoing range expansion: The invasive bank vole (Myodes glareolus) in Ireland. *Molecular Ecology*, 22(11):2971–2985, 2013. doi: 10.1111/mec.12343.

[105] R. M. Pateman, J. K. Hill, D. B. Roy, R. Fox, and C. D. Thomas. Temperature-dependent alterations in host use drive rapid range expansion in a butterfly. *Science*, 336(6084):1028–1030, 2012.

[106] B. L. Phillips, G. P. Brown, M. Grennlees, J. P. Webb, and R. Shine. Rapid expansion of the cane toad (Bufo marinus) invasion front in tropical Australia. *Austral Ecology*, 32:169–176, 2007. doi: 10.1111/j.1442-9993.2007.01664.x.

[107] I. Van Bocxlaer, S. P. Loader, K. Roelants, S. D. Biju, M. Menegon, and F. Bossuyt. Gradual Adaptation Toward a Range-Expansion Phenotype Initiated the Global Radiation of Toads. *Science*, 327: 679–682, 2010. doi: 10.1126/science.1157880.

[108] L. Excoffier and N. Ray. Surfing during population expansions promotes genetic revolutions and structuration. *Trends in ecology & evolution*, 23(7):347–351, 2008.

[109] P. J. Yunker, M. A. Lohr, T. Still, A. Borodin, D. J. Durian, and A. G. Yodh. Effects of particle shape on growth dynamics at edges of evaporating drops of colloidal suspensions. *Physical Review Letters*, 110(3):1–5, 2013. doi: 10.1103/PhysRevLett.110.035501.

[110] W. Kim, F. Racimo, J. Schluter, S. B. Levy, and K. R. Foster. Importance of positioning for microbial evolution. *Proceedings of the National Academy of Sciences*, 111(16):E1639–E1647, 2014. doi: 10.1073/pnas.1323632111.

[111] M. Matsushita and H. Fujikawa. Diffusion-limited growth in bacterial colony formation. *Physica A: Statistical Mechanics and its Applications*, 168(1):498–506, 1990. doi: 10.1016/0378-4371(90)90402-E.

[112] C. Di Franco, E. Beccari, T. Santini, G. Pisaneschi, and G. Tecce. Colony shape as a genetic trait in the pattern-forming Bacillus mycoides. *BMC Microbiology*, 2:1–15, 2002. doi: 10.1186/1471-2180-2-33.

[113] J. McFadyean. The morphology of the actinomyces. *British Medical Journal*, 1(1485):1339, 1889.

[114] G. W. Fuller and G. A. Johnson. On the differentiation and classification of water bacteria. *The Journal of experimental medicine*, 4(5-6):609, 1899.

[115] M. Wheelis et al. *Principles of modern microbiology*. Jones & Bartlett Publishers, 2011.

[116] I. Golding, Y. Kozlovsky, I. Cohen, and E. Ben-Jacob. Studies of bacterial branching growth using reaction–diffusion models for colonial development. *Physica A: Statistical Mechanics and its Applications*, 260(3-4):510–554, 1998.

[117] A. M. Lacasta, I. R. Cantalapiedra, C. E. Auguet, A. Peñaranda, and L. Ramírez-Piscina. Modeling of spatiotemporal patterns in bacterial colonies. *Physical review. E, Statistical physics, plasmas, fluids, and related interdisciplinary topics*, 59(6):7036–7041, 1999. doi: 10.1103/PhysRevE.59.7036.

[118] M. Mimura, H. Sakaguchi, and M. Matsushita. Reaction-diffusion modelling of bacterial colony patterns. *Physica A: Statistical Mechanics and its Applications*, 282(1):283–303, 2000. doi: 10.1016/S0378-4371(00)00085-6.

[119] J. Dockery and I. Klapper. Finger formation in biofilm layers. *SIAM Journal on Applied Mathematics*, 62(3):853–869, 2001.

[120] X. Wang, H. A. Stone, and R. Golestanian. Shape of the growing front of biofilms. *New Journal of Physics*, 19(12):125007, 2017. doi: 10.1088/1367-2630/aa983f.

[121] R. A. Fisher. The wave of advance of advantageous genes. *Annals of Human Genetics*, 7(4):355–369, 1937.

[122] A. N. Kolmogorov. A study of the equation of diffusion with increase in the quantity of matter, and its application to a biological problem. *Moscow Univ. Bull. Math.*, 1:1–25, 1937.

[123] J. D. Murray. Mathematical biology. i, volume 17 of interdisciplinary applied mathematics, 2002.

[124] W. C. Allee et al. Animal aggregations. 1931.

[125] W. C. Allee, O. Park, A. E. Emerson, T. Park, K. P. Schmidt, et al. Principles of animal ecology. Technical report, WB Saunders Philadelphia, 1949.

[126] G. Birzu, O. Hallatschek, and K. S. Korolev. Neither pulled nor pushed: Genetic drift and front wandering uncover a new class of reaction-diffusion waves. *arXiv preprint arXiv:1709.01601*, 2017.

[127] E. Brunet and B. Derrida. Shift in the velocity of a front due to a cutoff. *Physical Review E*, 56(3):2597–2604, 1997.

[128] O. Hallatschek. The noisy edge of traveling waves. *Proceedings of the National Academy of Sciences of the United States of America*, 108(5):1783–7, feb 2011. doi: 10.1073/pnas.1013529108.

[129] O. Hallatschek and D. R. Nelson. Gene surfing in expanding populations. *Theoretical population biology*, 73(1):158–70, feb 2008. doi: 10.1016/j.tpb.2007.08.008.

[130] K. S. Korolev, M. J. I. Müller, N. Karahan, A. W. Murray, O. Hallatschek, and D. R. Nelson. Selective sweeps in growing microbial colonies. *Physical biology*, 9(2):026008, jan 2012. doi: 10.1088/1478-3975/9/2/026008.

[131] S. Kitsunezaki. Interface dynamics for bacterial colony formation. *Journal of the Physical Society of Japan*, 66(5):1544–1550, 1997.

[132] A.-L. Barabási and H. E. Stanley. *Fractal concepts in surface growth*. Cambridge university press, 1995.

[133] F. Family. Scaling of rough surfaces: effects of surface diffusion. *Journal of Physics A: mathematical and general*, 19(8):L441, 1986.

[134] F. Family and T. Vicsek. Scaling of the active zone in the Eden process on percolation networks and the ballistic deposition model. *Journal of Physics A: Mathematical and General*, 18(2):L75–L81, 1985. doi: 10.1088/0305-4470/18/2/005.

[135] J. A. Bonachela, C. D. Nadell, J. B. Xavier, and S. A. Levin. Universality in Bacterial Colonies. *Journal of Statistical Physics*, 144(2):303–315, 2011. doi: 10.1007/s10955-011-0179-x.

[136] J.-i. Wakita, H. Itoh, T. Matsuyama, and M. Matsushita. Self-affinity for the growing interface of bacterial colonies. *Journal of the Physical Society of Japan*, 66(1):67–72, 1997.

[137] T. Vicsek, M. Cserzo, and V. K. Horváth. Self-affine growth of bacterial colonies. *Physica A: Statistical Mechanics and its Applications*, 167(2):315–321, 1990. doi: 10.1016/0378-4371(90)90116-A.

[138] N. E. Muzzio, M. A. Pasquale, M. A. Huergo, A. E. Bolzán, P. H. González, and A. J. Arvia. Spatio-temporal morphology changes in and quenching effects on the 2D spreading dynamics of cell colonies in both plain and methylcellulose-containing culture media. *Journal of Biological Physics*, 42(3):477–502, 2016. doi: 10.1007/s10867-016-9418-3.

[139] M. A. C. Huergo, N. E. Muzzio, M. A. Pasquale, P. H. P. González, A. E. Bolzán, and A. J. Arvia. Dynamic scaling analysis of two-dimensional cell colony fronts in a gel medium: A biological system approaching a quenched Kardar-Parisi-Zhang universality. *Physical Review E - Statistical, Nonlinear, and Soft Matter Physics*, 90(2):1–6, 2014. doi: 10.1103/PhysRevE.90.022706.

[140] M. A. Huergo, M. A. Pasquale, A. E. Bolzán, A. J. Arvia, and P. H. González. Morphology and dynamic scaling analysis of cell colonies with linear growth fronts. *Physical Review E - Statistical, Nonlinear, and Soft Matter Physics*, 82(3), 2010. doi: 10.1103/PhysRevE.82.031903.

[141] M. A. Huergo, M. A. Pasquale, P. H. González, A. E. Bolzán, and A. J. Arvia. Dynamics and morphology characteristics of cell colonies with radially spreading growth fronts. *Physical Review E - Statistical, Nonlinear, and Soft Matter Physics*, 84(2), 2011. doi: 10.1103/PhysRevE.84.021917.

[142] S. F. Edwards and D. R. Wilkinson. The Surface Statistics of a Granular Aggregate. *Proceedings of the Royal Society A: Mathematical, Physical and Engineering Sciences*, 381(1780):17–31, 1982. doi: 10.1098/rspa.1982.0056.

[143] T. Antal and Z. Rácz. Dynamic scaling of the width distribution in Edwards-Wilkinson type models of interface dynamics. *Physical Review E - Statistical Physics, Plasmas, Fluids, and Related Interdisciplinary Topics*, 54(3):2256–2260, 1996. doi: 10.1103/PhysRevE.54.2256.

[144] M. Eden. A two-dimensional growth process. *Dynamics of fractal surfaces*, 4:223–239, 1961.

[145] M. Hairer. Solving the kpz equation. *arXiv preprint arXiv:1109.6811*, 2011.

[146] M. Prähofer and H. Spohn. Universal Distributions for Growth Processes in 1+1 Dimensions and Random Matrices. *Physical Review Letters*, 84(21):4882–4885, 2000. doi: 10.1103/PhysRevLett.84.4882.

[147] S. N. Majumdar and A. Comtet. Airy distribution function: from the area under a brownian excursion to the maximal height of fluctuating interfaces. *Journal of Statistical Physics*, 119(3-4):777–826, 2005.

[148] M. Kardar, G. Parisi, and Y.-C. Zhang. Dynamic scaling of growing interfaces. *Physical Review Letters*, 56(9):889–892, 1986.

[149] D. Forster, D. R. Nelson, and M. J. Stephen. Large-distance and long-time properties of a randomly stirred fluid. *Physical Review A*, 16(2):732, 1977.

[150] M. Myllys, J. Maunuksela, M. Alava, T. Ala-Nissila, J. Merikoski, and J. Timonen. Kinetic roughening in slow combustion of paper. *Physical review. E, Statistical, nonlinear, and soft matter physics*, 79(8):1515, 1997. doi: 10.1103/PhysRevE.64.036101.

[151] J. Maunuksela, M. Myllys, O.-P. Kaehkoenen, J. Timonen, N. Provatas, M. J. Alava, and T. Ala-Nissila. Kinetic Roughening in Slow Combustion of Paper. *Phys. Rev. Lett*, 80(25):9007, 1998.

[152] L. Miettinen, M. Myllys, J. Merikoski, and J. Timonen. Experimental determination of KPZ height-fluctuation distributions. *European Physical Journal B*, 46(1):55–60, 2005. doi: 10.1140/epjb/e2005-00235-y.

[153] K. A. Takeuchi and M. Sano. Universal fluctuations of growing interfaces: Evidence in turbulent liquid crystals. *Physical Review Letters*, 104(23):1–4, 2010. doi: 10.1103/PhysRevLett.104.230601.

[154] K. A. Takeuchi, M. Sano, T. Sasamoto, and H. Spohn. Growing interfaces uncover universal fluctuations behind scale invariance. *Scientific Reports*, 1:1–5, 2011. doi: 10.1038/srep00034.

[155] S. Atis, A. K. Dubey, D. Salin, L. Talon, P. Le Doussal, and K. J. Wiese. Experimental Evidence for Three Universality Classes for Reaction Fronts in Disordered Flows. *Physical Review Letters*, 114(23): 1–5, 2015. doi: 10.1103/PhysRevLett.114.234502.

[156] F. F. Farrell, M. Gralka, O. Hallatschek, and B. Waclaw. Mechanical interactions in bacterial colonies and the surfing probability of beneficial mutations. *J. R. Soc. Interface*, 14(20170073), 2017. doi: https://doi.org/10.1101/100099.

[157] R. Albert, A. L. Barabási, N. Carle, and A. Dougherty. Driven interfaces in disordered media: Determination of universality classes from experimental data. *Physical Review Letters*, 81(14):2926–2929, 1998. doi: 10.1103/PhysRevLett.81.2926.

[158] S. He, G. Kahanda, and P.-z. Wong. Roughness of Wetting Fluid Invasion Fronts in Porous Media Shanjin. *Physical Review Letters*, 69(13):2013–2016, 1992. doi: 10.1103/PhysRevLett.70.694.

[159] A. J. Allstadt, J. A. Newman, J. A. Walter, G. Korniss, and T. Caraco. Spatial Competition: Roughening of an Experimental Interface. *Scientific Reports*, 6(July):1–10, 2016. doi: 10.1038/srep29908.

[160] V. K. Horvath and H. E. Stanley. Temporal scaling of interfaces propagating in porous media. *Physical Review E*, 52(5):5166–5169, 1995. doi: 10.1103/PhysRevE.52.5166.

[161] S. V. Buldyrev, A.-L. Barabasi, F. Caserta, S. Havlin, H. E. Stanley, and T. Vicsek. Anomalous Interface Roughening in Porous Media: Experiment and Model. *Physical Review A*, 45(12):R8315, 1992.

[162] S. V. Buldyrev, A. Barabhi, S. Havlinasb, J. Kertkf, H. E. Stanley, and H. S. Xeniasa. Anomalous interface roughening in 3D porous media: experiment and model. *Physica A*, 191:220–226, 1992.

[163] J. Zhang, Y. C. Zhang, P. Alstrøm, and M. T. Levinsen. Modeling forest fire by a paper-burning experiment, a realization of the interface growth mechanism. *Physica A: Statistical Mechanics and its Applications*, 189(3-4):383–389, 1992. doi: 10.1016/0378-4371(92)90050-Z.

[164] R. Surdeanu, R. J. Wijngaarden, E. Visser, J. M. Huijbregtse, J. H. Rector, B. Dam, and R. Griessen. Kinetic roughening of penetrating flux fronts in high- TcThin film superconductors. *Physical Review Letters*, 83(10):2054–2057, 1999. doi: 10.1103/PhysRevLett.83.2054.

[165] V. K. Horvath, F. Family, and T. Vicsek. Dynamic scaling of the interface in two-phase viscous flows in porous media. *Journal of Physics A: Mathematical and General*, 24:24–29, 1991.

[166] E. Medina, T. Hwa, M. Kardar, and Y.-C. Zhang. Burgers equation with correlated noise: Renormalization-group analysis and applications to directed polymers and interface growth. *Physical Review A*, 39(6):3053, 1989.

[167] L. A. N. Amaral, A. L. Barabási, H. A. Makse, and H. E. Stanley. Scaling properties of driven interfaces in disordered media. *Physical Review E*, 52(4):4087–4104, 1995. doi: 10.1103/PhysRevE.52.4087.

[168] H. A. Makse and L. A. N. Amaral. Scaling Behavior of Driven Interfaces above the Depinning Transition. *Europhysics Letters (EPL)*, 31(7):379–384, 1995. doi: 10.1209/0295-5075/31/7/007.

[169] J. F. Crow, M. Kimura, et al. An introduction to population genetics theory. *An introduction to population genetics theory.*, 1970.

[170] R. Der, C. L. Epstein, and J. B. Plotkin. Generalized population models and the nature of genetic drift. *Theoretical population biology*, 80(2):80–99, 2011.

[171] J. B. S. Haldane. A Mathematical Theory of Natural and Artificial Selection, Part V: Selection and Mutation. *Mathematical Proceedings of the Cambridge Philosophical Society*, 23(07):838, 1927. doi: 10.1017/S0305004100015644.

[172] D. P. Rice, B. H. Good, and M. M. Desai. The evolutionarily stable distribution of fitness effects. *Genetics*, 200(1):321–9, 2015. doi: 10.1534/genetics.114.173815.

[173] B. H. Good and M. M. Desai. Fluctuations in fitness distributions and the effects of weak linked selection on sequence evolution. *Theoretical Population Biology*, 85(1):86–102, 2013. doi: 10.1016/j.tpb.2013.01.005.

[174] A. Eyre-Walker and P. D. Keightley. The distribution of fitness effects of new mutations. *Nature Reviews Genetics*, 8(8):610–618, 2007. doi: 10.1038/nrg2146.

[175] B. H. Good and M. M. Desai. Evolution of mutation rates in rapidly adapting asexual populations. *Genetics*, 204(3):1249–1266, 2016. doi: 10.1534/genetics.116.193565.

[176] A. G. Knudson. Two genetic hits (more or less) to cancer. *Nature Reviews Cancer*, 1(2):157, 2001.

[177] P. J. Gerrish and R. E. Lenski. The fate of competing beneficial mutations in an asexual population. *Genetica*, 102:127, 1998.

[178] R. A. Neher. Genetic draft, selective interference, and population genetics of rapid adaptation. *Annual review of Ecology, evolution, and Systematics*, 44:195–215, 2013.

[179] K. S. Korolev, M. Avlund, O. Hallatschek, and D. R. Nelson. Genetic demixing and evolution in linear stepping stone models. *Reviews of modern physics*, 82(2):1691–1718, jun 2010. doi: 10.1103/RevModPhys.82.1691.

[180] M. S. Datta, K. S. Korolev, I. Cvijovic, C. Dudley, and J. Gore. Range expansion promotes cooperation in an experimental microbial metapopulation. *Proceedings of the National Academy of Sciences*, 110(18):7354–7359, 2013. doi: 10.1073/pnas.1217517110.

[181] S. R. Gandhi, E. A. Yurtsev, K. S. Korolev, and J. Gore. Range expansions transition from pulled to pushed waves as growth becomes more cooperative in an experimental microbial population. *Proceedings of the National Academy of Sciences*, 113(25):201521056, 2016. doi: 10.1073/pnas.1521056113.

[182] M. O. Lavrentovich, K. S. Korolev, and D. R. Nelson. Radial domany-kinzel models with mutation and selection. *Physical Review E*, 87(1):012103, 2013.

[183] K. S. Korolev, J. B. Xavier, D. R. Nelson, and K. R. Foster. A quantitative test of population genetics using spatiogenetic patterns in bacterial colonies. *The American Naturalist*, 178(4):538–552, 2011.

[184] O. Hallatschek and D. R. Nelson. Life at the front of an expanding population. *Evolution*, 64(1):193–206, 2010.

[185] S. Roux, A. Hansen, and E. L. Hinrichsen. A direct mapping between eden growth model and directed polymers in random media. *Journal of Physics A: Mathematical and General*, 24(6):L295, 1991.

[186] Y. Saito and H. Müller-Krumbhaar. Critical phenomena in morphology transitions of growth models with competition. *Physical review letters*, 74(21):4325, 1995.

2

Excess of mutational jackpot events in expanding populations revealed by spatial Luria-Delbrück experiments

The genetic diversity of growing cellular populations, such as biofilms, solid tumors or developing embryos, is thought to be dominated by rare, exceptionally large mutant clones. Yet, the emergence of these mutational jackpot events is only understood in well-mixed populations, where they stem from mutations that arise during the first few cell divisions. To study jackpot events in spatially structured populations, we track mutant clones in microbial populations using fluorescence microscopy and population sequencing. High-frequency mutations are found to be massively enriched in microbial colonies compared to well-shaken liquid cultures, as a result of late-occurring mutations surfing at the edge of range expansions. Thus, jackpot events can be generated not only when mutations arise early but also when they occur at favorable locations, which exacerbates their role in adaptation and disease. In particular, because spatial competition with the wild type keeps most mutant clones in a quiescent state, strong selection pressures that kill the wild type promote drug resistance.

2.1 Introduction

One of the hallmarks of spontaneous mutations in growing populations is the emergence of mutational jackpot events - large mutant clones arising from mutations that by chance occur early in the development of a cellular population so that their progenitors benefit from prolonged growth. Due to their sheer size, these jackpot events, first discovered by Luria and Delbrück[1], are thought to have momentous roles in short-term evolutionary processes, including the adaptation from standing variation[2–4], evolutionary rescue[5], drug resistance evolution[6–10], and the somatic evolution of genetic diseases[11,12]. However, because the emergence of jackpot events has been understood only in uniformly growing populations[1,10,13], it is currently impossible to predict their impact on the evolution of many naturally structured populations.

The original Luria-Delbrück experiment studied mutant clones arising in well-mixed microbial populations, and detected the sizes of resistant clones by counting single colonies on selective plates. Here, we generalize the assay in two ways, (i) by studying mutant clones arising in spatially structured populations and (ii) by using a combination of next-generation sequencing and fluorescence microscopy techniques to accurately detect size and structure of high-frequency clones.

We find that high-frequency mutations are massively enriched in microbial colonies compared to well-shaken liquid cultures, as a result of late-occurring mutations surfing at the edge of range expansions[14–16]. We provide a mathematical theory that explains the observed excess of jackpot events and predicts their role in promoting rare evolutionary outcomes. In particular, we show that resistant clones generated by surfing can become unleashed under high selection pressures, and thus represent a drug resistance hazard for high-dose drug treatments. In this context, our theory offers an innovative explanation for the phenomenon of "competitive release", initially observed in ecology[17–19], and more recently in tumors[20], where the craved resource is space rather than nutrients.

2.2 Results

2.2.1 Generalized Luria-Delbrück experiments

To measure the size of mutational jackpot events, we employed population sequencing with low error rates (see Methods), which returned frequencies of new mutations at many genomic sites simultaneously and independently of their phenotypic effect. Specifically, we sequenced populations of a mutator strain of *E. coli* cultured in well-mixed liquid medium, where growth is uniform, and as colonies on solid agar medium, where most growth occurs at the colony edge (see Methods)[21,22]. By growing from a small number of initial cells to a similar final size, all populations went through a comparable number of cell divisions (between 1×10^9 and 7×10^9, Supplementary Table 1). Counting the observed frequencies of Single Nucleotide

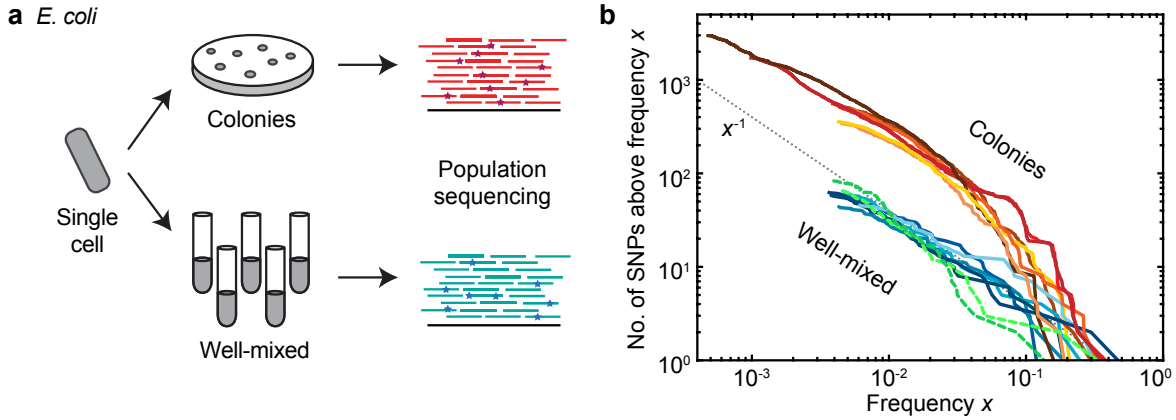

Figure 2.1: Population sequencing reveals an excess of jackpot events in spatially-growing populations. (**a**) Starting from few cells of a mutator strain of the bacterium *E. coli* (*mutT* deletion, Methods), we grew 6 colonies and 6 liquid cultures up to an average population size of 3×10^9 cells and sequenced each population at a coverage of at least 1000$\times$ (Supplementary Table 1). The number of SNPs that occur at a frequency higher than x is displayed in panel (**b**) (solid lines: colonies in warm colors, well-mixed in cold colors; dashed lines: well-mixed on plates). We found about 10 times more mutants above a frequency of 1% in colonies than in well-mixed population, even when the latter were grown on plates (Methods). The dotted black line is the fit to the well-mixed data with a mutation rate of $\mu = 0.4$ per genome per replication.

Polymorphisms (SNPs) in the populations, we obtained the number of sites in the genomes where the clonal sub-population carrying the derived mutation had a frequency larger than a given frequency value x, shown in Fig. 2.1b. Our deep sequencing procedure allowed us to detect all clones that have frequencies larger than about 10^{-3} (Methods), yielding about 600 such high-frequency events in each colony, which characterize the statistics of jackpot events.

Populations of the same size and mutation rate are expected to experience the same total number of mutational events, on average, independently of the mode of growth (liquid versus solid medium). Yet, Fig. 2.1 shows that colonies had approximately ten times more mutant clones above frequencies of 1% – corresponding to clones of at least 10^7 cells – than well-mixed populations. This difference cannot be explained by variation in final population size, since some well-mixed populations had a larger final size than some colonies (Supplementary Table 1, Supplementary Fig. 1).

To test whether the discrepancy was caused by different mutation rates in liquid culture and on agar plates, we also sequenced "plated well-mixed" populations whose growth was kept uniform by regularly spreading the cells across the plate (see Methods). The resulting distribution of SNPs is consistent with the well-mixed populations in liquid culture (green dashed and blue solid lines in Fig. 2.1b), confirming that the mutation rate is not significantly affected by the mode of growth (see also Supplementary Methods and

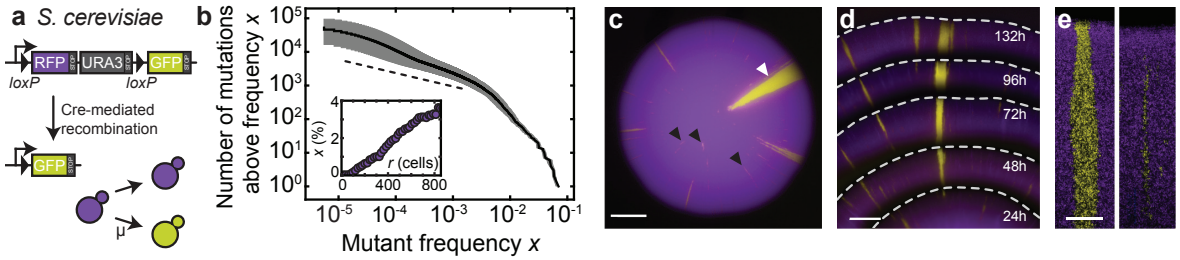

Figure 2.2: Gene surfing promotes the occurrence of mutational jackpot events in colonies. (**a**) An engineered strain of *S. cerevisiae* that stochastically switches from RFP (purple) to GFP (yellow) at a rate of 1.6×10^{-3} per cell division, enables us to visualize high frequency jackpot events as they arise during colony growth (panel **c**, scale bar corresponds to 1mm). (**b**) Image analysis (see *Methods*) of mutant clones in 343 colonies reveals a shoulder-like distribution of clone sizes, roughly consistent with our predictions for idealized two-dimensional populations (dashed line, see also Methods). The inset shows the median mutant frequency as a function of radius. Error bars are smaller than symbols. (**d**, scale bar corresponds to 0.5mm) Monitoring the spatial distribution of mutants using fluorescence time-lapse microscopy (see also Supplementary Movie 1) reveals that mutant clones come either as sectors [21] with actively growing front regions (**e**, left, scale bar equal to 0.2mm; **c**, white arrow) or as "bubbles" (**e**, right; **c**, black arrows), which are non-growing mutant clones that have lost contact with the expanding edge.

Supplementary Table 2). Thus, we conclude that the observed difference in the clone size distribution must be a consequence of the non-uniform growth in colonies, which results in a surprising number of mutations at high frequency.

2.2.2 Fluorescence microscopy reveals spatial structure of clones

To reveal the nature of the high-frequency clones in colonies, we monitored the spatial distribution of mutant clones using separate fluorescent marker experiments. We employed a genetically engineered budding yeast strain capable of switching from a red-fluorescing state to a green-fluorescing state at a rate of about 1.6×10^{-3} per replication [23]. This heritable, non-reversible switch is mediated by the stochastic expression of Cre recombinase (see Fig. 2.2a and Methods for details). As shown in Fig. 2.2c, the resulting colonies exhibited both elongated speckles (dark arrows), which we termed "bubbles", as well as previously described spoke-like sectors (white arrow) [21]. Importantly, image analysis of the clone area obtained from 343 colonies yielded a histogram consistent with the shoulder-like distribution obtained from our sequencing approach (Fig. 2.2b and Methods). Thus, both the fluorescent data from just one "engineered" site and the sequencing data covering many genomic sites seem to reflect the same mechanism shaping the clone size distribution.

The fluorescence data, moreover, revealed where clones emerge and how they grow. Time-lapse movies showed that most high-frequency clones first arise near the front of the growing colony (Fig. 2.2e, Supple-

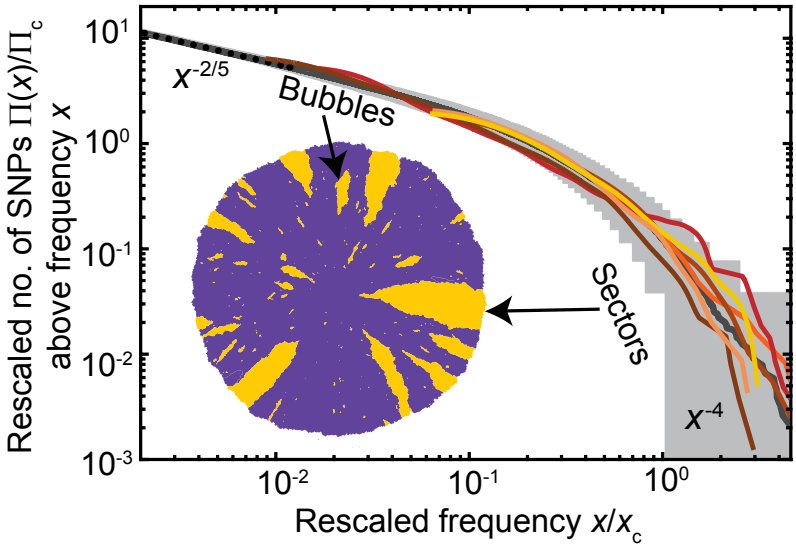

Figure 2.3: Simulations of range expansions reproduce the measured distribution of clone sizes. The clone size distribution obtained from our meta-population simulations (gray solid line) exhibits two predictable power-law tails that characterize bubbles (dotted line) and sectors, respectively (Methods). The experimental mutant spectra (colored lines) collapse onto this theory line upon scaling the two axes by the frequency of the largest bubble x_c and the probability Π_c of observing a clone larger than x_c, respectively (shaded area represent the 95% confidence interval, see Methods for details).

mentary Movie 1). The resulting clonal patches grow with the advancing frontier until they lose contact to the front, whereupon they become trapped as bubbles in the non-growing bulk of the population. Rarely, clones are able to "surf" at the front until the end of the experiment and give rise to sectors. Such allele surfing is a characteristic feature of range expansions[14,16,24] and has been demonstrated to be pervasive in microbial communities[21,25–27].

2.2.3 Gene surfing theory explains mutational jackpot events

To understand how gene surfing generates clones of different sizes, we studied their emergence in range expansion simulations. Specifically, colony growth was implemented by the random addition of new demes to the advancing frontier. The newly added deems inherited their ancestral genotype unless they mutated, which occurred at a fixed rate (Methods; Supplementary Movie 2). Interestingly, this simple meta-population model generated a clone size distribution that accurately reproduced the measured one, as can be seen in Fig. 2.3. Our simulation results, covering over four orders of magnitude, also reveal that the distribution crosses over between two power law distributions with distinct exponents. Analysis of the clone shapes pro-

Scenario	z	Low frequency	High frequency
Well-mixed	0	x^{-1}	
2D flat front	2	$x^{-1/3}$	x^{-3}
3D flat front	2	$x^{-1/2}$	x^{-2}
2D rough front*	3/2	$x^{-2/5}$	x^{-4}
3D rough front	1.61	$x^{-0.55}$	$x^{-2.3}$

Table 2.1: Predictions for the asymptotic behavior of the clone size distribution. The dynamical exponent z summarizes the statistical properties of the sector and bubble boundaries. The low-frequency regime corresponds to bubbles, the high-frequency regime to sectors. The well-mixed scenario, where bubbles and sectors are not distinct, corresponds to $D = \infty$ and is characterized by a single power-law regime. The experimental scenario presented here is well-described by the case of two-dimensional rough fronts (*), where $z = 3/2$ is given by KPZ interface growth dynamics[30].

duced in our simulations shows that the power law regimes of low and high frequencies characterize bubbles and sectors, respectively.

The effect of gene surfing is not limited to two-dimensional growth: Simulations of spherically growing meta-populations (Fig. 2.4b), such as those used to model solid tumors[28,29], still result in mutant spectra with two distinct power law regimes corresponding to bubble and sectors, respectively.

The power law exponents can be derived analytically by treating the boundaries of the mutant clones as annihilating random walks. The statistical properties of these random walks determine the relationship between the length $L_{\parallel}$ of clones parallel to the growth direction and the corresponding perpendicular length $L_{\perp}$ (see Fig. 2.4a). For instance, purely diffusive clone boundaries, which occur when the population front is completely flat, result in $L_{\parallel} \sim L_{\perp}^2$; more generally, $L_{\parallel} \sim L_{\perp}^z$, where the dynamical exponent z depends on the details of how the population grows (dimensionality, roughness of the growing front). The Kardar-Parisi-Zhang interface growth model[30], which has been found consistent with bacterial growth patterns[21], predicts $z_{2D} = 3/2$ (exact) and $z_{3D} = 1.63$ (numerical)[31]. By computing the area enclosed between two annihilating random walks, which are unbiased in the neutral case, one can determine the power law exponent for bubbles (Methods). The power law exponent for sectors follows from the one for bubbles via an exact scaling relationship (Methods). The results for different scenarios are summarized in Table 2.1.

Importantly, our scaling arguments predict that the clone size distributions obtained for different population sizes and mutation rates should collapse onto one master curve when the clones frequencies are measured in terms of the characteristic frequency of the largest occurring bubble x_c, and the clone number in terms of the average probability for a new mutation to establish a sector, Π_c. Indeed, after rescaling, our

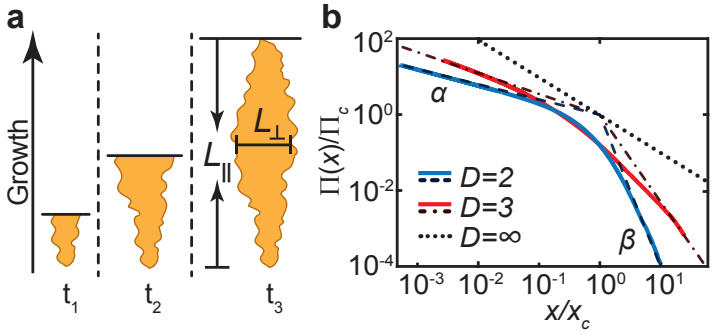

Figure 2.4: Fractal properties of clone boundaries control the size distribution of bubbles. (**a**) Sketch of the stochastic growth of a bubble, which is bounded by two annihilating random walks. (**b**) Rescaled clone size distribution from simulations in two and three dimensions approach the predicted asymptotic power-law behavior for bubbles, $x^{-\alpha}$, and sectors, $x^{-\beta}$, in the limit of small and large frequencies, respectively (dashed lines: asymptotic theory predictions). The values of the exponents are reported in Table 2.1.

sequencing data show remarkable agreement with the master curve obtained from our simulations (Fig. 2.3, Supplementary Methods, Supplementary Table 3, and Supplementary Fig. 2).

2.2.4 Role of jackpot events in the evolution of drug resistance

One of the striking features of the clone size distribution under range expansion is the excess of high frequency mutations over the well-mixed expectation. The primary consequence of more jackpot events is that, typically, the total number of mutants will be much larger in a spatially growing population compared to an equally large well-mixed population. This can be understood from the following simple mathematical argument.

If mutations arise at a low rate μ per cell division as the population is growing to a final size N, one expects μN mutational events to occur. In each generation, the frequency of mutants in the population increases by μ, on average. In a well-mixed, uniformly grown population, the number of generation is $\log_2 N$, and hence the expected total number of mutants in this case is proportional to $\mu N \log_2 N$. In a range expansion, only cells near the edge of the colony have access to sufficient nutrients, leading to the formation of a layer of growing cells of width λ (in units of cell diameters). Since a length λ is added per generation to the radius of the colony, we can estimate that $R/\lambda \propto N^{1/2}/\lambda$ generations elapse at the frontier during the growth process. Hence, the final total number of mutants created during a range expansion is proportional to $\mu N^{3/2}/\lambda$, which for large N is much larger than in a uniformly grown population of the same size. Note that, as in the classic Luria-Delbrück case, the mean is usually not a useful quantity because it is dominated by very rare, large events. Nevertheless, both the typical and the mean number of mutations exceed the well-

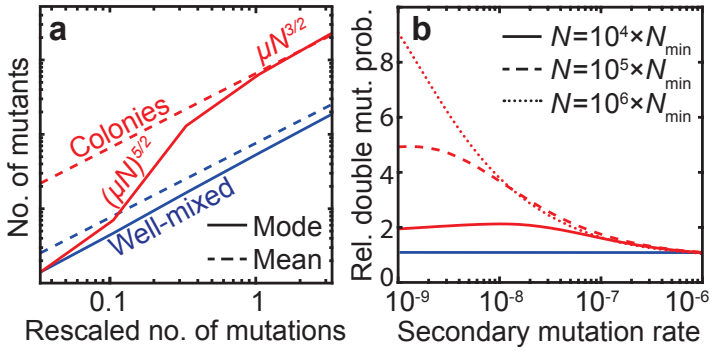

Figure 2.5: Gene surfing theory predicts an excess of jackpot events and its consequences. (**a**) Sampling the experimental clone size distribution Π, we found that the typical (mode, solid line) and the mean (dashed line) number of mutants as a function of the rescaled number of mutations $\mu N \Pi_c$, which corresponds to the number of mutations establishing into sectors, is higher in range expansions (red) than in equally large uniformly grown populations (blue). (**b**) The excess of large-frequency clones promotes multi-step evolutionary processes, such as the emergence of double mutants. The relative probability (compared to the well-mixed expectation) of producing a double mutant is always higher in a colony, especially when the secondary mutation rate is low. Here, $N_{\min} = x_{\min} N$ (Methods), which in our *E. coli* colonies corresponds to $N_{\min} \approx 10^5$.

mixed expectations, as our stochastic analysis shows (Fig. 2.5, Supplementary Note 1 and Supplementary Fig. 3).

Jackpot events can be key in acquiring complex phenotypes, such as drug resistance or the onset of cancer, which often require the accumulation of multiple mutations[11,32]. Range expansions may promote the acquisition of secondary mutations because the pool of individuals carrying the first (driver) mutation is, both on average and typically, larger than in uniformly grown populations (Fig. 2.5a). As shown in Fig. 2.5b, the probability of secondary mutations can be almost an order of magnitude larger in spatial populations compared to well-mixed ones, especially when mutation rates are low (Supplementary Note 2).

2.2.5 Drugs can trigger competitive release of mutant clones

Evolutionary dynamics is influenced by mutational jackpot events not only because of their size but also because of their particular spatial structure. The emergence of sectors, which sporadically arise from neutral mutations, is strongly suppressed when mutants carry a cost (Fig. 2.6a, Supplementary Note 3 and Supplementary Fig. 4), commonly observed for drug resistance in the absence of antibiotics[33]: Deleterious mutants can surf only briefly before they are overtaken by faster-growing wild-type cells and fall behind the growing frontier.

In the absence of antibiotics, then, costly resistant clones are expected to reside in bubbles, encased by

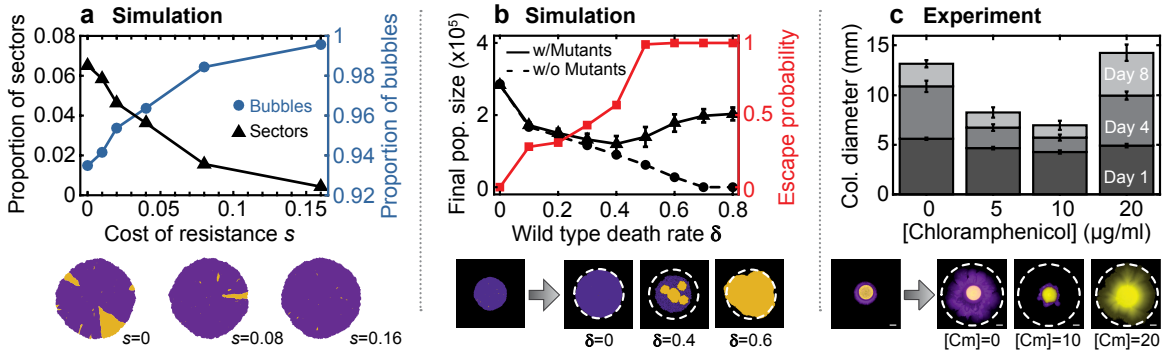

Figure 2.6: High drug concentration treatments can promote the spreading of resistance by unleashing mutants that are otherwise trapped within the colony bulk by competitive release. (**a**) When the mutants carry a cost s in the absence of antibiotics, the fraction of mutants trapped in bubbles is increased and sectors become increasingly rare. (**b**) Starting with (i) colonies pre-grown with $s = 0.4$ (black triangles, solid lines) or (ii) resistance-free control colonies (black circles, dashed lines) as initial condition, we simulated the effects of treatment with antibiotics at varying concentrations by tuning the death rate δ of the wild type (Methods). After 140 generations, resistance-free colonies showed decreasing population size up to complete eradication for $\delta > 0.7$, as expected. In contrast, colonies with resistant bubbles exhibited an initial decrease in population size followed by a steady increase for $\delta > 0.4$ (error bars represent standard deviations over 100 simulations). Visualization of the simulated colonies showed that in this range of death rates, the previously encapsulated mutants escape the surrounding wild type (red squares) and can then grow indefinitely (Supplementary Movie 3). A high dose of antibiotics may thus not only fail to eradicate the population, but even promote the spreading of resistance. This effect can be reproduced in conceptual experiments with *E. coli*, shown in (**c**), which demonstrate that high antibiotic concentrations can release trapped mutant clones. A droplet of resistant cells (yellow) embedded in a larger droplet of susceptible cells (purple) was inoculated at different antibiotic concentrations (Methods). After 8 days of growth intermediate antibiotic concentrations exhibited the least amount of total population growth. The highest drug concentrations eradicated the wild type and thus allowed the resistant mutants to spread freely. Error bars represent standard deviations over 16 replicates and scale bars correspond to 2 mm.

an expanding wild-type population. Upon a sudden environmental change, however, e.g., by a strong antibiotic attack killing the susceptible wild-type, the trapped mutants may become unleashed, regrowing and thus rescuing the population from extinction. This evolutionary rescue is brought about by a particular kind of competitive release, in which the indispensable resource is space. Competition in this case is extreme: trapped clones are not only at a disadvantage, but they have no chance of escaping unless the surrounding wild type vanishes. Consistently with this idea, we expect minimal net population growth and successful containment of resistant cells at intermediate drug concentrations, sufficiently strong to slow down proliferation of the wild-type without eradicating it. Indeed, when we implemented drug treatment as a tunable death rate for wild-type cells (Fig. 2.6b, Supplementary Movie 3, Methods), our simulations showed the

smallest net population growth for intermediate death rates. In contrast, high death rates not only failed to eradicate the population, but promoted the spread of resistance by generating an entirely resistant population.

Our simulations provide a uniquely spatial mechanism of how excessively high drug concentrations can promote the spreading of drug resistance. This effect can be reproduced in conceptual experiments in which we embedded resistant cells within a colony of susceptible cells. We found that the resistant cells stayed trapped even at intermediate drug concentrations that severely limit the wild-type growth. For higher drug concentrations, the mutants were released and grew rapidly (Fig. 2.6c). Hence, to optimally curtail microbial growth in our particular setup, the drug concentration should indeed be set at an intermediate sweet spot.

2.3 Discussion

In combination with a generalization of the Luria-Delbrück theory, our experiments show that the process of allele surfing generates an excess of high-frequency clones: Mutations have a much higher chance of being carried by a high proportion of the population. These high-frequency clones come as growing sectors and non-growing bubbles, which are spatially encased by wild-type cells. Our theory suggests that the excess of jackpot events is not limited to microbial colonies but arises generally in populations that exhibit non-uniform growth rates in two or three dimensions.

In addition to antibiotic resistance evolution in pathogenic biofilms, an excess of jackpot events could thus be relevant also during the somatic evolution of some types of cancer[12,34,35], as growing solid tumors often exhibit less growth in necrotic core regions[36] and sectoring has been recently documented[29]. Moreover, it has been argued that jackpot events play a crucial role in the predisposition to cancer and other genetic diseases[11]. Based on the classic Luria-Delbrück theory, it was predicted that a large fraction of cancers may arise from predisposed stem-cell lineages[32]. Our results suggest that if growth is non-uniform during the development of the stem cell pool, predisposed stem-cell lines may occur even more frequently than previously hypothesized.

Our sequencing study design can be applied to test this prediction by measuring the site frequency spectrum in tumors as well as in multi-cellular organisms at different stages of their development. Some clues about large frequency clones could also be collected from visible phenotypes resulting from somatic mosaicism, such as Blaschko's lines[11]. Plants or animals with pigmentations caused by mobile elements are particularly amenable to such pattern analyses.

Our experiments, simulations, and theory not only found an excess of jackpot events but also elucidated their spatial patterns. Since drug resistance often comes at a selective cost in the absence of the drug, most resistance mutant clones are expected to be small and hidden in the bulk of the susceptible wild-type pop-

ulation. A high-dose treatment removes the wild type as the natural competitor of the resistant mutants and, consequently, triggers a competitive release of the dormant mutants. This form of competitive release is extreme in the sense that mutants stop growing entirely prior to the release, due to lack of space and nutrients. Because a broad spectrum of dormant clones is also generated in three-dimensional growth, this spatial form of competitive release can be particularly relevant in solid tumors. Indeed, the hypothesis that growth control may under certain conditions be more effective than attempts of complete eradication has been recently proposed in the context of cancer[37,38], based on mathematical modeling of exponentially growing tumors treated with a varying dose of chemotherapeutic drugs over time. A recent study[20] tested this hypothesis experimentally in a mouse model and found that prolonged chemotherapy with low doses was the most effective at keeping the tumor in check. In contrast, tumors that had regrown after an initial shrinkage following high-dose treatment did not respond to a second round of treatment, possibly indicating the emergence of resistance. Our results provide a novel mechanism, based on competition for space, that can explain these observations.

As sequencing costs continue to decrease, a growing number of studies utilizes population sequencing to draw conclusions on how cellular populations evolve. In this context, our results urge for caution when employing the classic Luria-Delbrück theory as a general theory for neutral evolution, as has been proposed in a recent meta-study of intra-tumor heterogeneity[12]. For one thing, spatial effects complicate the estimation of mutation rates and the amount of resistant tumor cells. More importantly, deviations from the classic Luria-Delbrück theory may simply indicate non-uniform growth rather than non-neutral evolution.

2.4 Methods

2.4.1 Scaling of clone size distribution in expanding populations.

We consider a population expanding from one to N individuals without death. Our goal is to characterize the probability $\Pi(x)$ that a mutation randomly introduced at the birth of one of the N cells generates a clone of frequency equal or larger than x (Fig. 2.1a). In other words, $\Pi(x)$ is the reverse cumulative distribution of the size of clone introduced by a random mutation. The derivative $-\partial_x \Pi(x)$ represents the population site frequency spectrum that can be obtained directly from population sequencing. Two extreme values of $\Pi(x)$ are known a priori: $\Pi(1/N) = 1$ because any mutation will certainly reach at least frequency $1/N$ if we ignore death. On the other hand, $\Pi(1) = 1/N$ because this requires the mutation to be introduced in the very first birth, i.e., at the root of the genealogical tree.

The behavior of $\Pi(x)$ in between these boundary points is known in the well-mixed or infinite-dimensional case, studied by Luria and Delbrück; it is a single power law $(Nx)^{-1}$ [13]. Our experiments and simulations suggest that the finite-dimensional case is characterized by two asymptotic regimes: a low-frequency regime

$(Nx)^{-\alpha}$ with exponent $\alpha < 1$, corresponding to bubbles, and a high-frequency regime $N^{-1}x^{-\beta}$ with exponent $\beta > 1$, corresponding to sectors. The N-dependent pre-factors of both regimes are fixed by the boundary conditions, and the cross-over point x_c follows from continuity (Supplementary Fig. 5). The described cross-over behavior can be captured mathematically by the scaling form

$$\Pi(x) = \Pi_c \, \chi\left(\frac{x}{x_c}\right), \tag{2.1}$$

in terms of the cross-over frequency $x_c = N^{-\frac{1-\alpha}{\beta-\alpha}}$ and a cross-over probability scale $\Pi_c = N^{-\frac{\alpha(\beta-1)}{\beta-\alpha}}$. The scaling function $\chi(\xi)$ exhibits two power law regimes

$$\chi(\xi) \sim \begin{cases} \xi^{-\alpha}, & \xi \ll 1, \\ \xi^{-\beta}, & \xi \gg 1. \end{cases} \tag{2.2}$$

Simulated clone size distributions, displayed in Fig. 2.4b, confirm the predicted scaling form. In real systems, the scaling form has a range of validity, say between some minimal and maximal frequency x_{min} and x_{max} that are set by details of the growth processes which are beyond the scope of our model. For instance, the maximal frequency $x_{\text{max}} = O(1)$ accounts for the discrete nature of growth during the first few cell divisions. Similarly, $x_{\text{min}} = O(1/N)$ may reflect mutations that are born behind the front such that our gene surfing theory does not apply.

The two power law exponents α and β are constrained by the scaling behavior of the mean frequency of mutants, as follows. For a given mutation rate μ per cell division, the expected frequency $\langle X_{\text{tot}}(t)\rangle$ of mutants at the surface of a growing D-dimensional sphere satisfies

$$\partial_t \langle X_{\text{tot}}(t)\rangle = \mu \left(1 - \langle X_{\text{tot}}\rangle\right), \tag{2.3}$$

where time is measured in units of generations at the front. Hence, as long as $\langle X_{\text{tot}}(t)\rangle \ll 1$, we have $\langle X_{\text{tot}}(t)\rangle = \mu t$. Every generation, the radius grows by λ, such that it takes the population $t = R/\lambda$ generations to grow to size $N \propto R^D$. The length λ can be interpreted as a measure for the thickness of the growth layer at the edge of the colony in units of the linear dimension of the cells. The mean frequency at radius r then is $\langle X_{\text{tot}}(r)\rangle = \mu r/\lambda$, and the population mean follows as $\overline{\langle X_{\text{tot}}\rangle} \propto (\mu/\lambda)N^{1/D}$. This implies an expected total number of mutants of

$$\overline{\langle X_{\text{tot}}\rangle} N \propto \frac{\mu}{\lambda} N^{1+1/D}. \tag{2.4}$$

As we ignore cell death, there are on average μN mutations occurring during the growth of the population. Hence, the frequency of a single clone is, on average, $\langle X \rangle \propto N^{\frac{1}{D}-1}/\lambda$, which constrains the integral over $\Pi(x)$ since $\langle X \rangle = \int_0^1 \Pi(x)$. Inserting the scaling relation, eq. (2.1), we obtain for large population $N \gg 1$

$$\langle X \rangle = \int_0^1 \Pi(x) \approx \Pi_c x_c \int_0^{x_c^{-1}} \chi(\xi) = N^{-\frac{1+(\beta-2)\alpha}{\beta-\alpha}}. \tag{2.5}$$

Here, we used that $\alpha < 1$ and $\beta > 1$ such that integral over the scaling function $\chi(\xi)$ is finite and dominated by ξ-values in the cross-over region, $\xi = O(1)$. Equation (2.5) can only hold for all N if we have the scaling relation

$$\frac{(\alpha-1)(\beta-1)}{\alpha-\beta} = \frac{1}{D} \tag{2.6}$$

Thus, computing the exponent for either the bubble or the sector regime uniquely determines the exponent of the other regime. Note that in the well-mixed case, $D \to \infty$, Eq. (2.6) correctly reproduces a single power law with $\alpha = \beta = 1$. Here, we derive the exponent for the bubble regime in two dimensions; the sector regime and higher dimensions are described in Supplementary Notes 4 and 5.

2.4.2 Bubble distribution in two dimensions.

The area A, length $L_\parallel$ and width $L_\perp$ of a bubble are determined by the statistical properties of its boundaries, which result in the general relationship $L_\parallel \sim L_\perp^z$, see Fig. 2.4a. We can relate the distribution of the area $A \sim L_\perp L_\parallel \sim L_\perp^{1+z}$ of a bubble to the distribution of the lateral bubble size $L_\perp$ through

$$\Pr(A > a) = \Pr\left(L_\perp > \ell_\perp(a) \sim a^{\frac{1}{1+z}}\right). \tag{2.7}$$

For neutral mutations, we must also have the conditional probability $\Pr(L_\perp > w_\perp | \ell_\perp) \sim \ell_\perp / w_\perp$ of reaching transverse size $w_\perp$ given an initial size $\ell_\perp$ (each front segment of size $\ell_\perp$ has the same chance of expanding up to size $w_\perp$). This implies $\Pr(L_\perp > w_\perp) w_\perp = \Pr(L_\perp > \ell_\perp)\ell_\perp$. Since the choice of $w_\perp$ is arbitrary, it must hold that $\Pr(L_\perp > \ell_\perp) \sim \ell_\perp^{-1}$ for large enough $\ell_\perp$. Combining this with Eq. (2.7) yields the distribution of clone frequencies

$$\Pr(A > a) \sim a^{-\frac{1}{1+z}} \tag{2.8}$$

for asymptotically large bubbles, i.e., $\alpha_{2D} = 1/(1+z)$. In D dimensions, $\alpha_D = [1 + z/(D-1)]^{-1}$ (Supplementary Note 5). The scaling relation in eq. (2.1) can be used to find the exponent in the sector regime β. Numerical values for the exponents in a variety of scenarios are given in Table 2.1.

2.4.3 Meta-population model simulations.

We simulated range expansions using a meta-population model based on the Eden model[39]: Space is divided into a two or three-dimensional square grid, whose voxels can be empty, wild type, or mutant type. In general, each voxel represents a sub-population, also called deme, consisting of multiple individuals, and the lattice size a is a model parameter that characterizes the spatial extend of a deme.

The grid is initialized by filling the central voxel with wild-type. In each step, we choose a voxel i that has at least one empty neighbor and one of its empty neighboring voxels j at random and copy the state of i into j. If i is wild type, we switch ("mutate") voxel j to the mutant type with probability μ. A generation corresponds to a number of steps equal to the number of voxels that have at least one empty neighbor at the beginning of the generation. Note that since mutation rate and substitution rate are the same for neutral mutations, μ represents the actual mutation rate.

To accommodate the limited number of observable SNPs in the experimental data when comparing with simulations, we sample M mutations with frequency above the minimum experimentally detectable frequency from the simulated distribution. Here M is the number of observed mutations in one experiment (Supplementary Table 1). The sampling is repeated 10,000 times, and the resulting distributions binned across frequencies. The result is shown as the gray area in Fig. 2.3, containing 95% of the sampled distributions.

To simulate the effect of intermediate antibiotic concentrations on colony growth and spreading of resistant individuals observed in experiments (Fig. 2.6c), we extended the meta-population model simulation to accommodate sudden changes in the environment and death of the wild type. Environmental changes are modeled by changing the relative growth rate of mutants, g_{mut}, and wild type, g_{wt}, at time T during the simulations, which corresponds to when the antibiotic is administered. We define the selective advantage/disadvantage s of the mutant as $s = g_{\text{mut}}/g_{\text{wt}} - 1$. Without death of the wild type, the environmental change would only be felt by the individuals at the front, in contradiction to experiment, where we frequently observe the escape of mutants from the bulk of the population. Therefore, we introduce the possibility of death: After time T, any of the n_{wt} wild type cells has a chance δ of dying each generation. In addition to the standard algorithm above, each generation then incurs δn_{wt} additional iterations, in which one wild-type voxel is deleted. More details on the algorithm are reported in the Supplementary Methods. To simulate the experimental scenario in Fig. 6, we first grow a population with deleterious mutations until time T ($\mu = 2 \cdot 10^{-4}$, $s = -0.4$), whereafter new mutations are not allowed, mutants switch to having a selective advantage ($s = 0.4$), and wild type death is switched on. Supplementary Movie 3 shows the qualitative agreement with the experimental results in identifying an intermediate death rate that minimizes colony growth.

2.4.4 *E. coli* experiments.

For the sequencing experiments, we used a K12 *E. coli* strain MG1655 where the *mutT* gene was replaced by Cm_R, conferring resistance to chloramphenicol. This strain has an elevated mutation rate for A/T→C/G transversions over wild type MG1655 by a factor of about 150 on average[40]. For the trapping experiments in Fig. 2.6, we used a pair of MG1655 strains, one expressing CFP from a plasmid, the other expressing YFP and a resistance gene to chloramphenicol.

In liquid culture, *E. coli* were grown continuously shaken at 37°C in LB (10g/L tryptone, 5g/L yeast extract, 10g/L NaCl). For plates, 2% w/v bacto agar was added to the media before autoclaving. Antibiotics were added after autoclaving to cooled media.

To prepare cells of *mutT E. coli* for sequencing, we grew them in liquid culture up to a density of 10^8 cells/ml and then (i) plated single cells for colonies and (ii) inoculated well-mixed cultures from single cells following a 10^7 dilution. 86 parallel tubes were inoculated with 100μl of the dilution and incubated well-shaken for about 10 hours (around 30 generations). Cells were harvested in log phase, judged by OD600 (Supplementary Table 1). To grow well-mixed populations on plates, 16 LB plates were inoculated with 100μl of the dilutions and incubated. Every 90 minutes, 100μl PBS was pipetted onto each plate and vigorously spread using glass beads. After approximately 20 hours, 7 plates displayed a uniform bacterial lawn. Two lawns were resuspended via vortexing. Colonies were grown for three to five days up to a diameter between 1 and 1.5cm (Supplementary Fig. 2). For five colonies (colonies 1 to 5 in Supplementary Table 1 and Supplementary Fig. 6), cells were resuspended by vortexing and the genomic DNA extracted for each population. For the last colony (colony 6), the colony was cut in four parts via a glass pipette for the center portion (IN) and a razor blade (for the remaining outer ring). The outer ring was divided into three parts: 1/8, 1/4, and the remainder of the ring (around 1/2 ring), as shown in Supplementary Fig. 6. The DNA of each portion was extracted separately (details are in Supplementary Table 1). Genomic DNA was extracted from all population following the Epicentre MasterPure DNA Purification Kit Protocol.

Illumina library preparation was performed on each sample and final libraries were used at similar concentrations in order to achieve similar coverage across samples. The average insert size of the library was approximately 200 bps. The sample libraries were then sequenced on the HiSeq 2500 at the QB3 Vincent J. Coates genomic facility at UC Berkeley using 150 paired-end reads. Because the library insert size is on average smaller than 300 bps, the two paired-end reads overlap, providing two independent calls for each base in the overlapping region[41,42]. Each sequencing lane accommodated 6 distinct samples providing, on average, a coverage of 1000X per sample. One colony (colony 5 in Supplementary Table 1) was also sequenced separately in one lane, generating a 6000X coverage for this sample.

2.4.5 Processing of sequencing data.

The reads of each sample were processed according to the following pipeline. Read quality was assessed via FastQC to check for base sequence quality, GC content bias, length distribution, and adapter contamination. Because some adapter contamination was determined, reads were filtered for library adapters and trimmed when necessary.

Paired-end reads were then merged using BBmerge (available at http://sourceforge.net/projects/bbmap), which identifies the optimal relative position of corresponding read pairs and generates a unique consensus read with combined quality scores (on average, 90% of the reads were uniquely merged and used for the subsequent analysis). The resulting sequencing error was on average lower than 10^{-6} for all samples.

BreSeq[43] was then used to map the merged reads to the reference genome of *E. coli* strain MG1655 (NCBI id: NZ_CP009685.1[44]). SNP-calling and frequency calculation was also performed via BreSeq conditioning on at least 4 independent read calls.

Genomic regions with unusually high density of SNPs were omitted. To determine whether SNPs were to be disregarded, a sliding window of 5 kbps was passed across the genome counting the number of SNPs with frequency lower than a varying threshold. For each frequency threshold i, the average number of SNPs per window n_i was recorded. If a window showed a number of SNPs with p-value lower than 0.001 (assuming a Poisson distribution with mean n_i), all the SNPs in that window were removed. This procedure takes into account that SNPs with lower frequency are more numerous and thus more densely populate the genome, while providing a more conservative approach than simply removing regions with high SNP density regardless of their frequency. The flagged regions were often shared among samples and annotated as repetitive regions in the reference genome.

Among the remaining putative mutations, SNPs present in more than 40% of the population were deemed mutations carried by the seeding cell(s) and removed. Three of the liquid cultures appeared to have been seeded by multiple cells, since they contained SNPs at frequency equal to 50%. The remaining SNPs with corresponding frequency were then used to generate the clone size distribution in Fig. 2.1 for all samples, with the exception of colony 6. The details on how we combined the SNPs from the different portions of colony 6 are reported in the Supplementary Methods.

2.4.6 *S. cerevisiae* experiments.

For the fluorescent marker experiments in budding yeast (Fig. 2.2) we used the W303 *S. cerevisiae* strain JRY10643, derived from JRY9628[23]. This strain employs the Cre-loxP recombination system to switch stochastistically from a red to a green fluorescent state at a rate $\mu = 1.6 \times 10^{-3}$ per cell division. *S. cerevisiae* were grown at 30°C in YPD (20g/L peptone, 10g/L yeast extract, 20g/L dextrose). For plates, 2% w/v bacto agar

was added to the media before autoclaving. To grow colonies from single cells, saturated overnight culture was diluted 1:10 in fresh media and grown for another 4.5 hours. The resulting culture was diluted in PBS to give about 50 cells/ ml. 100μl of this dilution were spread on YPD plates (containing roughly 20ml of YPD with 2% agar) that had been dried at room temperature for at least 24h. After drying, the plates were wrapped with parafilm and incubated at 30°C for 5 days.

2.4.7 Image analysis.

For the timelapse movie (Supplementary Movie 1), single cells of JRY10643 were inoculated on YPD plates, incubated in a stage-top incubator fitted to a Zeiss AxioZoom microscope and grown overnight. One colony was selected and imaged every 30 minutes in both the red and the green fluorescent channel. For Fig. 2.2d, a colony was imaged every 24 hours and images overlaid in Adobe Photoshop. To image sectors and bubbles on the single-cell scale, a colony was cut out from the agar plates and imaged on a Zeiss LSM700 confocal microscope, using 488nm and 555nm lasers. A z-stack was recorded and later combined by maximum intensity projection.

Colonies were imaged on a Zeiss AxioZoom v16 upright microscope. The red and green fluorescent channel were recorded separately, and exposure times were set automatically by the software for each colony and channel. To measure the mutant clone size distribution in the converting budding yeast strains, we used an automated thresholding algorithm with a locally adaptive threshold. To detect large clones, we removed small object by computing the geodesic opening of the green channel image before binarizing with a locally (50 pixel radius) adaptive threshold. For the detection of small bubbles, we computed the top hat transform of the green channel, using a 15 pixel radius disk as the structuring element, which effectively removes large elements from the image. The resulting image was then segmented using an adaptive threshold in a 15 pixel radius neighborhood. Finally, the two segmented images were overlaid and eroded by 1 pixel to obtain the final segmentation. In Fig. 2.2b, we also show the result for no erosion and 2 pixel erosion (gray area).

The imaged budding yeast colonies are not strictly two-dimensional but have a roughly conical shape. Small clones thus occupy stretched three-dimensional volumes $V \sim L_{\parallel} L_{\perp}^2$, of which only the projection can be observed under the microscope. To take this projection error into account, we consider the volume V of bubbles growing in 3D, and, assuming isotropic growth, we compute the projected area $A_{\text{proj}} \sim V/L_{\perp}$, where $L_{\perp}$ is the size of the bubble section transverse to the growth direction. Using $z_{3D} = 1.61$, this leads to

$$\Pr(A_{\text{proj}} > A) \sim A^{-0.77}, \tag{2.9}$$

which serves as an upper bound for the case where bubbles are equally extended horizontally as they are vertically. Experimentally, the best fit to the low-frequency regime of the clone size distribution in Fig. 2.2b gives

an exponent of roughly 0.61, which is consistent with bubbles that have a small degree of three-dimensionality but grow mostly in the x-y plane.

Data availability

The alignment files obtained from sequencing the *E. coli* populations are available in the Sequence Read Archive (SRA) with access code SRP078606. The rest of the data that support the findings of this study are available from the corresponding author upon request.

References

[1] S. E. Luria and M. Delbrück. Mutations of Bacteria from Virus Sensitivity to Virus Resistance. *Genetics*, 28:491–511, 1943. doi: 10.1038/nature10260.

[2] J. Hermisson and P. S. Pennings. Soft sweeps molecular population genetics of adaptation from standing genetic variation. *Genetics*, 169(4):2335–2352, 2005.

[3] R. D. Barrett and D. Schluter. Adaptation from standing genetic variation. *Trends in Ecology & Evolution*, 23(1):38 – 44, 2008.

[4] P. W. Messer and D. A. Petrov. Population genomics of rapid adaptation by soft selective sweeps. *Trends in ecology & evolution*, 28(11):659–669, 2013.

[5] G. Bell and A. Gonzalez. Evolutionary rescue can prevent extinction following environmental change. *Ecology Letters*, 12(9):942–948, 2009.

[6] A. Coldman and J. Goldie. A stochastic model for the origin and treatment of tumors containing drug-resistant cells. *Bulletin of mathematical biology*, 48(3-4):279–292, 1986.

[7] F. Michor, Y. Iwasa, and M. A. Nowak. Dynamics of cancer progression. *Nature reviews cancer*, 4 (3):197–205, 2004.

[8] H. Haeno, Y. Iwasa, and F. Michor. The evolution of two mutations during clonal expansion. *Genetics*, 177(4):2209–2221, 2007.

[9] R. Durrett and S. Moseley. Evolution of resistance and progression to disease during clonal expansion of cancer. *Theoretical population biology*, 77(1):42–48, 2010.

[10] D. A. Kessler, R. H. Austin, and H. Levine. Resistance to chemotherapy: patient variability and cellular heterogeneity. *Cancer research*, 74(17):4663–4670, 2014.

[11] S. A. Frank. Somatic mosaicism and disease. *Current Biology*, 24(12):R577–R581, 2014.

[12] M. J. Williams, B. Werner, C. P. Barnes, T. A. Graham, and A. Sottoriva. Identification of neutral tumor evolution across cancer types. *Nature genetics*, 2016.

[13] D. Lea and C. A. Coulson. The distribution of the numbers of mutants in bacterial populations. *Journal of genetics*, 49(3):264–285, 1949.

[14] C. A. Edmonds, A. S. Lillie, and L. L. Cavalli-Sforza. Mutations arising in the wave front of an expanding population. *Proceedings of the National Academy of Sciences of the United States of America*, 101(4):975–979, 2004.

[15] S. Klopfstein, M. Currat, and L. Excoffier. The fate of mutations surfing on the wave of a range expansion. *Molecular biology and evolution*, 23(3):482–490, 2006.

[16] O. Hallatschek and D. R. Nelson. Gene surfing in expanding populations. *Theoretical Population Biology*, 73:158–170, 2008.

[17] J. H. Connell. The influence of interspecific competition and other factors on the distribution of the barnacle chthamalus stellatus. *Ecology*, 42(4):710–723, 1961.

[18] R. M. Keane and M. J. Crawley. Exotic plant invasions and the enemy release hypothesis. *Trends in Ecology & Evolution*, 17(4):164–170, 2002.

[19] J. C. De Roode, R. Culleton, A. S. Bell, and A. F. Read. Competitive release of drug resistance following drug treatment of mixed plasmodium chabaudi infections. *Malaria journal*, 3(1):1, 2004.

[20] P. M. Enriquez-Navas, Y. Kam, T. Das, S. Hassan, A. Silva, P. Foroutan, E. Ruiz, G. Martinez, S. Minton, R. J. Gillies, et al. Exploiting evolutionary principles to prolong tumor control in preclinical models of breast cancer. *Science translational medicine*, 8(327):327ra24–327ra24, 2016.

[21] O. Hallatschek, P. Hersen, S. Ramanathan, and D. R. Nelson. Genetic drift at expanding frontiers promotes gene segregation. *Proceedings of the National Academy of Sciences*, 104(50):19926–19930, 2007.

[22] S. Mitri, E. Clarke, and K. R. Foster. Resource limitation drives spatial organization in microbial groups. *The ISME journal*, 2015.

[23] A. E. Dodson and J. Rine. Heritable capture of heterochromatin dynamics in saccharomyces cerevisiae. *Elife*, 4:e05007, 2015.

[24] L. Excoffier and N. Ray. Surfing during population expansions promotes genetic revolutions and structuration. *Trends in ecology & evolution*, 23(7):347–351, 2008.

[25] N. J. Buttery, C. N. Jack, B. Adu-Oppong, K. T. Snyder, C. R. Thompson, D. C. Queller, and J. E. Strassmann. Structured growth and genetic drift raise relatedness in the social amoeba dictyostelium discoideum. *Biology letters*, 8(5):794–797, 2012.

[26] C. D. Nadell, V. Bucci, K. Drescher, S. A. Levin, B. L. Bassler, and J. B. Xavier. Cutting through the complexity of cell collectives. *Proceedings of the Royal Society of London B: Biological Sciences*, 280 (1755):20122770, 2013.

[27] J. van Gestel, F. J. Weissing, O. P. Kuipers, and A. T. Kovács. Density of founder cells affects spatial pattern formation and cooperation in bacillus subtilis biofilms. *The ISME journal*, 8(10):2069–2079, 2014.

[28] B. Waclaw, I. Bozic, M. E. Pittman, R. H. Hruban, B. Vogelstein, and M. A. Nowak. A spatial model predicts that dispersal and cell turnover limit intratumour heterogeneity. *Nature*, 525(7568):261–264, 2015.

[29] S. Ling, Z. Hu, Z. Yang, F. Yang, Y. Li, P. Lin, K. Chen, L. Dong, L. Cao, Y. Tao, et al. Extremely high genetic diversity in a single tumor points to prevalence of non-darwinian cell evolution. *Proceedings of the National Academy of Sciences*, 112(47):E6496–E6505, 2015.

[30] M. Kardar, G. Parisi, and Y.-C. Zhang. Dynamic scaling of growing interfaces. *Physical Review Letters*, 56(9):889, 1986.

[31] T. Halpin-Healy and Y.-C. Zhang. Kinetic roughening phenomena, stochastic growth, directed polymers and all that. aspects of multidisciplinary statistical mechanics. *Physics reports*, 254(4):215–414, 1995.

[32] S. A. Frank and M. A. Nowak. Cell biology: Developmental predisposition to cancer. *Nature*, 422 (6931):494–494, 2003.

[33] B. R. Levin, V. Perrot, and N. Walker. Compensatory Mutations, Antibiotic Resistance and the Population Genetics of Adaptive Evolution in Bacteria. *Genetics*, 154(3):985–997, March 2000.

[34] A. Sottoriva, H. Kang, Z. Ma, T. A. Graham, M. P. Salomon, J. Zhao, P. Marjoram, K. Siegmund, M. F. Press, D. Shibata, et al. A big bang model of human colorectal tumor growth. *Nature genetics*, 47(3):209–216, 2015.

[35] M. O. Lavrentovich and D. R. Nelson. Survival probabilities at spherical frontiers. *Theoretical population biology*, 102:26–39, 2015.

[36] P. Vaupel, F. Kallinowski, and P. Okunieff. Blood flow, oxygen and nutrient supply, and metabolic microenvironment of human tumors: a review. *Cancer research*, 49(23):6449–6465, 1989.

[37] R. A. Gatenby. A change of strategy in the war on cancer. *Nature*, 459(7246):508–509, 2009.

[38] R. A. Gatenby, A. S. Silva, R. J. Gillies, and B. R. Frieden. Adaptive therapy. *Cancer research*, 69(11): 4894–903, June 2009.

[39] M. Eden. A two-dimensional growth process. *Dynamics of fractal surfaces*, 4:223–239, 1961.

[40] R. Fowler and R. Schaaper. The role of the mutt gene of escherichia coli in maintaining replication fidelity. *FEMS Microbiology Reviews*, 21(1):43–54, 1997.

[41] H. Chen-Harris, M. K. Borucki, C. Torres, T. R. Slezak, and J. E. Allen. Ultra-deep mutant spectrum profiling: improving sequencing accuracy using overlapping read pairs. *BMC genomics*, 14(1):1, 2013.

[42] J. L. Preston, A. E. Royall, M. A. Randel, K. L. Sikkink, P. C. Phillips, and E. A. Johnson. High-specificity detection of rare alleles with paired-end low error sequencing (pele-seq). *BMC genomics*, 17(1):1, 2016.

[43] D. E. Deatherage and J. E. Barrick. *Engineering and Analyzing Multicellular Systems: Methods and Protocols*, chapter Identification of Mutations in Laboratory-Evolved Microbes from Next-Generation Sequencing Data Using breseq, pages 165–188. Springer New York, New York, NY, 2014.

[44] K. Berlin, S. Koren, C.-S. Chin, J. P. Drake, J. M. Landolin, and A. M. Phillippy. Assembling large genomes with single-molecule sequencing and locality-sensitive hashing. *Nature biotechnology*, 33(6): 623–630, May 2015.

2.5 Appendix

2.5.1 Strains and growth conditions

E. coli

For the sequencing experiments, we used the K12 *E. coli* strain MG1655 where the *mutT* gene was replaced by Cm_R, conferring resistance to chloramphenicol. This strain has an elevated mutation rate for A/T→C/G transversions over wild type MG1655 by a factor of about 150 on average[1]. We also performed sequencing experiments (data not shown) with wild type MG1655 (with a functional *mutT* gene). *E. coli* were grown continuously shaken at 37°C in LB (10g/L tryptone, 5g/L yeast extract, 10g/L NaCl). For plates, 2% w/v bacto agar was added to the media before autoclaving. Antibiotics were added after autoclaving to cooled media.

S. cerevisiae

For the fluorescent marker experiments (Fig. 1, SI Fig. B3) we used the *S. cerevisiae* strain JRY10643, kindly provided by Anne Dodson and Jasper Rine. This strain was derived from JRY9628 and follows the same Cre/loxP strategy employed in Ref.[2]. In short, the gene encoding the Cre recombinase was placed under control of the *α2* promoter at the transiently unsilenced *HMLα* locus. This leads to a rare, stochastic excision of a *loxP* cassette containing an *RFP*-encoding gene. Consequently, *RFP* is switched off while expression of a *GFP*-encoding gene downstream of the cassette is switched on (see Fig. 1c). To facilitate optional selection for or against the cassette in JRY10643, the *TEF* promoter and kan^r ORF present in the cassette of the ancestral JRY9628 strain was replaced by *URA3* amplified from pUG72.

In the experiments investigating the release of internally trapped bubbles upon drug application we used strains yJHK111[3] and yMM9 (unpublished, courtesy of Melanie J. I. Müller). Both strains have a W303 background (common genotype *MATa bud4Δ::BUD4(S288C) can1-100*). yJHK111 expresses the yellow fluorescent protein ymCitrine. yMM9 expresses ymCherry and is also resistant to cycloheximide via mutation *Q37E* in the gene *CYH2* (while yJHK111 is sensitive).

S. cerevisiae were grown at 30°C in YPD (20g/L peptone, 10g/L yeast extract, 20g/L dextrose). For plates, 2% w/v bacto agar was added to the media before autoclaving.

	Liquid Culture	Colonies
Average Population Size $\pm$ s.d. (10^9)	1.5 ± 0.2	2.7 ± 0.5
Empty Plates/Total Plates	66/86	19/42
μ [95% C.I.] (10^{-10})	1.8 [1.1, 2.7]	2.9 [1.8, 4.5]

Table 2.S1: Spontaneous mutation rate to spectinomycin in *mutT* obtained by performing Luria-Delbrück experiments on liquid cultures harvested in stationary phase grown in a 96 well plate and colonies grown for 3 days. The average population size and its standard deviation are computed by counting CFUs of appropriate dilutions, and the confidence interval on the mutation rate is calculated using the binomial test implemented in R.

2.5.2 Whole-genome sequencing in *E. coli*

Estimates of mutation rate in liquid culture and colonies

To verify that the mutation rate is independent of the mode of growth, we performed Luria-Delbrück experiments using *mutT* populations grown as colonies from single cell harvested after three days, and overnight liquid cultures. The liquid cultures were inoculated with 2 to 10 cells. All populations were grown up to similar size and the precise size was measured by plating dilutions on non-selective plates. The mutation rate was estimated from the fraction of populations that exhibited no growth two days after being moved onto plates with 60ug/ml of spectinomycin. The reported spontaneous mutation rate to spectinomycin in K12 *E. coli* is about 2×10^{-10}, generated by an aminoacid substitution in a ribosome unit[4]. Because the required mutation consists in a C/G to T/A transversion[5], whose rate is not affected by the *mutT* deletion of the strain, we expect similar mutation rates as in the wild-type. Table 2.S1 shows that both growth modes generate similar mutation rates. This supports our assertion that the increased number of mutants in colonies reported in Fig. 1 cannot be explained by a different mutation rate.

Colony and culture growth for sequencing

Cells of *mutT E. coli* were cultured up to a density of 10^8 cells/ml. Part of this culture was plated on LB plates to grow single cells colonies and incubated at 37°C, while the other part was diluted 10^9 folds and resuspended in 70 parallel tubes containing 5ml of LB and incubated at 37°C in a shaker for about 10 hours (around 30 generations). The density of liquid cultures that showed growth was measured via OD600 in order to collect the cells in log-phase (Table 2.S2). Cells from four independent cultures were pelleted and the genomic DNA extracted according to the Epicentre MasterPure DNA Purification Kit Protocol.

Colonies were grown for five days up to a diameter of about 1.5cm (Fig. 2.S1). For three colonies (colonies 1, 2, and 3 in Table 2.S2 and Fig. 2.S1), the cells were separated from the agar by vortexing and the genomic

	OD 600	Population Size ($\times 10^9$)	Mean Coverage	Min. Frequency ($\times 10^{-3}$)
Well-mixed 1	0.6	3.0	722	4.29
Well-mixed 2	0.35	1.8	736	4.30
Well-mixed 3	0.25	1.3	836	4.75
Well-mixed 4	0.23	1.3	495	6.13
Colony 1	0.36	3.6	884	4.74
Colony 2	0.28	2.8	893	4.81
Colony 3	0.71	7.1	1214	3.79
Colony 3 HC	0.71	7.1	6025	0.96
Colony 4: in	0.37	3.7	1348	1.39
Colony 4: 1/8	0.08	0.8	964	0.40
Colony 4: 1/4	0.15	1.5	574	1.30
Colony 4: 1/2	0.32	3.2	1271	1.28

Table 2.S2: Summary of the sequenced populations. Well-mixed population were grown in 5ml of LB, while colonies were grown for 5 days and the OD600 measured with a 10-fold dilution. The number of cells used to extract DNA for each sample, the mean sample coverage, and the minimum observed frequency are also reported. For colony 4, the minimum observed frequency is rescaled proportionally to the portion size.

DNA extracted for each population. For the last colony (colony 4 in Table 2.S2 and Fig. 2.S1), the colony was cut in four parts via a glass pipette for the center portion (IN) and a razor blade (for the remaining outer ring). The outer ring was divided into three parts: 1/8, 1/4, and the remainder of the ring (around 1/2 ring), as shown in Fig. 2.S1. The DNA of each portion was extracted separately. Details are reported in Table 2.S2.

Library preparation and sequencing

Illumina library preparation was performed on each sample and final libraries were used at similar concentrations in order to achieve similar coverage across samples. The average insert size of the library was approximately 200 bps.

The sample libraries were then sequenced on the HiSeq 2500 at the QB3 Vincent J. Coates genomic facility at UC Berkeley using 150 paired-end reads. Because the library insert size is on average smaller than 300 bps, the two paired-end reads overlap, providing two independent calls for each base in the overlapping region, which decreases the sequencing error to below 10^{-6}. Each sequencing lane accommodated 6 distinct samples providing, on average, a coverage of 1000X per sample. One colony (colony 3 in Table 2.S2) was also sequenced separately in one lane, generating a 6000X coverage for this sample.

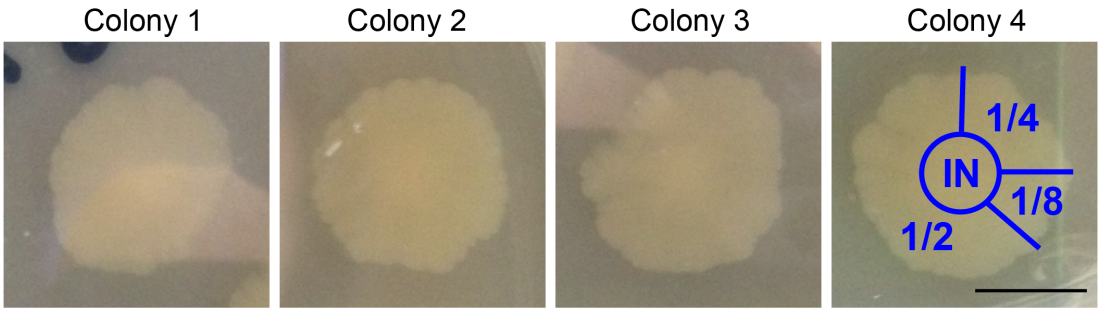

Figure 2.S1: Colonies of mutator *E. coli* used for sequencing. The scale bar corresponds to 1cm. Colony 4 was partitioned in four parts that were sequenced separately: the center (IN), and approximately one eighth (1/8), one fourth (1/4), and one half (1/2) of the outer ring.

Processing of sequencing data

The reads of each sample were processed according to the following pipeline. Read quality was assessed via FastQC to check for base sequence quality, GC content bias, length distribution, and adapter contamination. Because some adapter contamination was determined, reads were filtered for library adapters and trimmed when necessary.

Paired-end reads were then merged using Pear[6], which identifies the optimal relative position of corresponding read pairs and generates a unique consensus read with combined quality scores (on average, 90% of the reads were uniquely merged and used for the subsequent analysis). The resulting sequencing error was on average lower than 10^{-6} for all samples. Hence, the minimum observable SNP frequency in our experiments is set by the sequencing coverage and not by the sequencing error.

BreSeq[7] was then used to map the merged reads to the reference genome of *E. coli* strain MG1655 (NCBI id: NZ_CP009685.1[8]). SNP-calling and frequency calculation was also performed via BreSeq conditioning on at least 4 independent read calls.

Genomic regions with unusually high density of SNPs were omitted. To determine whether SNPs were to be disregarded, a sliding window of 5 kbps was passed across the genome counting the number of SNPs with frequency lower than a varying threshold. For each frequency threshold i, the average number of SNPs per window n_i was recorded. If a window showed a number of SNPs with p-value lower than 0.001 (assuming a Poisson distribution with mean n_i), all the SNPs in that window were removed. This procedure accounts for the fact that SNPs with lower frequency are more numerous and thus more densely populate the genome, while providing a more conservative approach than simply removing regions with high SNP density regardless of their frequency.

If a genomic region shows an average number of SNPs with frequency below i, but an unusually high

number of SNPs with frequency below j with $j > i$, this suggests that the SNPs with frequency between i and j are over-represented, which can be caused by misaligned reads or mapping issues (often leading to many false SNPs with very similar frequency. Although some SNPs in such region may represent genuine mutations, we chose to flag the whole region as problematic and remove all the corresponding SNPs. Such regions are often shared among samples and annotated as repetitive regions in the reference genome. This procedure was repeated for all samples.

Among the surviving putative mutations, SNPs present in more than 50% of the population were deemed mutations carried by the seeding cell(s) and removed. Two of the liquid cultures appear to have been seeded by multiple cells, since they contained SNPs at frequency equal to 50%. The remaining SNPs with corresponding frequency were then used to generate the clone size distribution in Figure 1 for all samples, with the exception of colony 4.

For colony 4, the clone size distribution was determined by combining the filtered SNPs from the distinct colony portions (all the fixed SNPs were fixed in all portions and thus removed). First, SNPs that were identified in two or more portions had their total frequency x_t calculated as

$$x_t = \frac{\sum_i \rho_i x_i}{\sum_i \rho_i}, \tag{2.S1}$$

where the sum runs over the different colony portions, ρ_i is the OD 600 density of portion i and x_i is the frequency of the shared SNP in portion i. SNPS that were uniquely identified in one portion of the colony and not in the others were treated in the following way. First, in each sample, the frequency of the SNP was rescaled proportionally to the size of the portion by multiplying the observed frequency by $\frac{\rho_i}{\sum_i \rho_i}$.

Secondly, we accounted for the higher resolution of portion 1/8. For each colony sample i, we defined the minimum observable frequency $\xi_i = \frac{\rho_i \min(x_i)}{\sum_i \rho_i}$, where $\min(x_i)$ is the minimum SNP frequency observed in sample i. Because of the partitioning of the colony, these frequencies satisfy the relation $\xi_{\text{in}} \sim \xi_{1/2} > \xi_{1/4} > \xi_{1/8}$ (see Table 2.S2). We then identified all the SNPs in portion 1/8 that had rescaled frequencies lower than ξ_i, where i corresponds to each of the larger three portions. If we assume that the frequency distribution of these SNPs is homogenous across the colony, we can extend their presence to the other samples in the following way. For each of the identified SNPs, a number equal to $\rho_i/\rho_{1/8}$ of inferred mutations is added to the list of mutations in portion i with frequency equal to the rescaled frequency in portion 1/8. This is repeated for all the three largest portion and, finally, the list of mutations for each portion is merged together and used to calculate the clone size distribution of colony 4 in Fig.s 1 and 2.S2.

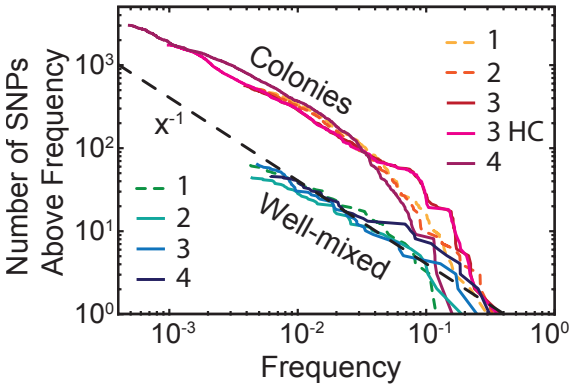

Figure 2.S2: Site frequency spectrum of each sequenced population reported in Fig. 1 where the data is labeled as in Table 2.S2 and Fig. 2.S1

Control using the wild type

To determine whether the number of SNPs detected was consistent with previously reported mutation rates, we grew and sequenced a well-mixed population and a colony of the wild type strain *E. coli* MG1655 with a functional *mutT* gene following the same protocol we used for the mutator strain. In particular, the colony was sequenced in partitions similarly to colony 4 in Fig. 2.S1. After analysis of the results, we detect only a single SNP in the well-mixed population, whose minimum detectable frequency was around 3×10^{-3}. By comparing the number of SNPs above this frequency observed in the mutator strain, we infer that the mutator strain is characterized by an approximately 100 fold increase in the mutation rate. For the colony, we detect a total of 23 SNPs combined across the different regions above frequency 3×10^{-3} compared to the 1000 SNPs found in colony 4, which suggests a 50 fold increase in mutation rate. The reported mutation rate in wild type *E. coli* is around 0.001 per genome per generation[9]. The expected mutation rate in our *mutT* deletion strain is thus roughly 0.1 per genome per generation. This number is consistent with the mutation rate inferred from fitting the well-mixed clone size distribution in Fig. 1 to the standard Luria-Delbrück expectation, which gives ≈ 0.4. Moreover, although the number of detected SNPs in the wild type is not sufficiently large to accurately compute the clone size distribution, it supports the observation that colonies produce approximately 10 times more mutations with clones above frequency 3×10^{-3} compared to equally large well-mixed populations.

Correction at low-frequencies

Even if sequencing errors can be neglected, the true and the observed frequency of a SNP can still differ because only a subsample of reads are sequenced at the SNP position. Although this is an issue across all frequencies, the relative error is much larger a low frequencies, where one extra read can have a strong impact on the reported frequency. Assuming that sampling is the only source of noise, the variance associated with a SNP with frequency x is $v(x) = x(1-x)/n$ where n is the coverage at that position[10]. The relative error on the frequency scales as $x^{-1/2}$ and is especially relevant at low frequencies. The (integrated) clone size distribution $F(x)$ can then be better approximated by

$$F(x) = \sum_i \int_x^1 \mathcal{B}[nx', nx_i]dx', \tag{2.S2}$$

where the sum runs through all SNPs and $\mathcal{B}(y', y)$ is a binomial distribution function with mean y. The clone size distributions plotted in Fig. 1 and rescaled in Fig. 2 were obtained in this way.

2.5.3 Spontaneous mutants in *S. cerevisiae*

Main experiment

The *S. cerevisiae* strain JRY10643 was used to study visually the size of mutant clones. This strain converts at a rate of $\mu \approx 1.6 \times 10^{-3}$ per generation from a red fluorescent state to a green fluorescent state. Red cells are prototrophic for uracil, while green cells are not because they have lost the *URA3* gene. To start the experiments, glycerol stock was streaked on a CSM-URA plates to select for single clones. An overnight culture was inoculated in liquid CSM-URA to prevent growth of converted cells. The saturated overnight culture was diluted 1:10 in fresh media and grown for another 4.5 hours. The resulting culture was diluted in PBS to give about 50 cells per ml. 100μl of this dilution were spread on YPD plates (containing roughly 20ml of YPD with 2% agar) that had been dried at room temperature for at least 24h. After drying, the plates were wrapped with parafilm and incubated at 30°C for 5 days. Final colonies were roughly 1cm in diameter, on average.

Imaging

Main experiment. Colonies were imaged after 5 days of growth on a Zeiss AxioZoom v16 upright microscope. The red and green fluorescent channel were recorded separately, and exposure times were set automatically by the software for each colony and channel. Note that, throughout this work, signal in the channel for the

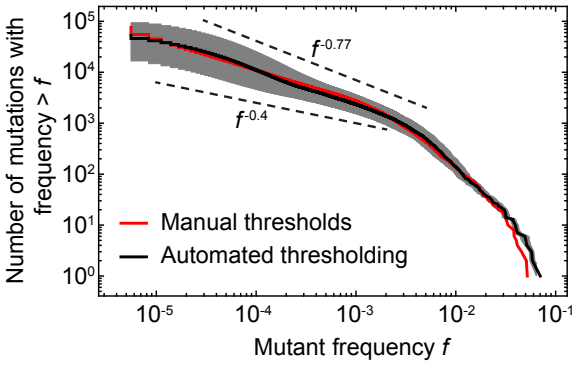

Figure 2.S3: Distribution of frequencies of mutant clones in *S. cerevisiae* colonies, measured by image analysis from 343 colonies. The red curve was obtained by manually adjusting the thresholding parameters for each image individually, while the black curve employed the automated thresholding algorithm described in Sec. 2.5.3. The gray area represents variations of the algorithm, without final erosion (top) and enhanced final erosion (bottom). The dashed line represent the expected scaling of the frequency distribution for a two-dimensional population, $x^{-0.4}$, and when accounting for 2D projection errors of three-dimensional bubbles, $x^{-0.77}$ (Methods).

fluorescent color of the "mutant" (converted JRY10643, yMM9) is pseudo-colored as yellow/orange, while the fluorescent signal of the "wild type" (unconverted JRY10643, yJHK111) is pseudo-colored as purple.

Time lapse movies. For time lapse movies, single cells were inoculated on YPD as described above. After drying, a plate was transferred to a stage-top incubator fitted to the Zeiss AxioZoom microscope and grown overnight. For SI movie 1, one colony was selected and imaged every 30 minutes in both the red and the green fluorescent channel. For Fig. 1e, several colonies were imaged at 32x magnification every two hours, keeping the front of the colony in focus. *Single-cell images.* To obtain images of bubbles and sectors on the single-cell scale, a colony from the time lapse was selected, cut out from the agar plates, and fixed on a glass slide. Confocal images were obtained using a Zeiss LSM700 microscope, using 488nm and 555nm lasers. Since the colony was strongly curved near the front, we recorded a z-stack that was later combined by maximum intensity projection.

Image analysis

To measure the mutant clone size distribution in our converting budding yeast strains, we proceeded in two ways, by manually setting the thresholding parameters for each colony individually, and using a automated thresholding algorithm.

Simple binarization schemes did not yield satisfactory results for several reasons: (i) Each colony has a different intensity profile, even after adjusting for differences in exposure time. In addition to biological

variation in gene expression of the fluorescent proteins, this is because the clone sizes varied strongly between colonies, and large clones were much brighter than smaller ones. Hence, a simple binarization with a global threshold would typically only be able to detect the largest class of clones present in a given colony. (ii) Due to the curvature of the colonies, the fluorescence signal was typically weaker near the edge of the colony than in the center. (iii) Intensity varied even within clones, making it difficult to accurately detect the edge of a clone.

Therefore, we employed a binarization scheme with a locally adaptive threshold (15 pixel radius). Both the red channel (the wild type) and the green channel (the mutants) were segmented individually, where we took into consideration not only the local mean intensity, but also the local variance. The segmented red channel was inverted and multiplied onto the segmented green channel to obtain the complete segmented image. Thus, we only counted clones if a bright spot in the green channel coincided with a dark spot in the red channel. The radius of the colony was measured independently and the final binarized image was masked with a disk of that radius. Computing the size of each segmented object, in 343 colonies, we obtain the mutant frequency distribution shown in Fig. 2.S3 (red line).

Due to the variation between colonies, it was necessary to set the thresholding parameters manually for each colony, thus making the segmentation to some degree subjective. In order to validate that our results were not skewed by the subjective choice of parameters, we devised an automated thresholding scheme, as follows. To detect large clones, we removed small object by computing the geodesic opening of the green channel image before binarizing with a locally (50 pixel radius) adaptive threshold. For the detection of small bubbles, we computed the top hat transform of the green channel, using a 15 pixel radius disk as the structuring element. This transformation effectively removes large elements from the image, leaving small objects untouched. The resulting image was then segmented using an adaptive threshold in a 15 pixel radius neighborhood. Finally, the two segmented images (for large and small objects) were overlaid to obtain the final segmentation. However, this procedure overestimated the size of mutant clones slightly, when compared to the manually thresholded result. Therefore, we eroded the segmented images by 1 and 2 pixels. The result of analyzing 343 colonies in this way is shown in Fig. 2.S3, where the black line was obtained by eroding the final segmentation by 1 pixel, and the gray background shows the variation caused by no erosion and strong erosion (2 pixels).

2.5.4 Simulations

Eden model

We simulated range expansions using a meta-population model based on the Eden model[11]. We divide space in a two-dimensional square grid, whose voxels can be empty, wild type, or mutant type. In general, each

voxel may correpond to multiple individuals and the lattice size a is a model parameter.

The grid is initialized by filling the central voxel with wild-type. At each time step,

1. a voxel i that has at least one empty neighbor is picked at random,
2. an empty neighboring voxel j is picked at random,
3. if i contains wild-type: a uniformly distributed random number u is sampled: if $u < \mu$, voxel j is filled with mutants, otherwise with wild-type; if i contains mutants, then j is always filled with mutants.

Because mutation rate and substitution rate are the same for neutral mutations, here, μ represents the actual mutation rate.

A generation is complete when the steps above are repeated for a number of iterations equal to the number of voxels that have at least one empty neighbor at the beginning of the iterations. Each generation, a number of voxels proportional to the colony circumference is added. Because the circumference grows linearly with the number of generations, the number of iterations to complete one generation also increases.

Confidence interval on clone size distribution

To compare the clone size distributions generated by the simulations with those generated by sequencing, we need to take into account that the experimental data is limited by the number of observable SNPs. The experimental clone size distribution is therefore subject to variation due to its limited sample size. To quantify this effect, we perform bootstrapping on the simulated distribution: sets of M mutations with frequency above the minimum observable experimental frequency (Table 2.S2) are sampled from the simulations and the corresponding clone size distribution is computed. Here M corresponds to the number of mutations observed in one experimental replicate. This is repeated 10,000 times in order to generate an ensemble of clone size distribution, which is then binned across frequencies. We then define the 95% confidence interval on the clone size distribution as the region containing 95% of the sampled distributions (gray area in Figure 2).

Tree-conditioned clone size distribution and Infinite Site Model

Since the clone size distribution in simulations, sequenced populations, and imaged colonies is derived from mutations that occur on one or few genealogical trees (one for sequencing, few hundreds for imaging, and few thousands for simulations), the size of the different clones are not independent, but are constrained to lie on a given tree. The individual characteristics of one specific tree can affect multiple clones and may thus give rise to a clone size distribution that is significantly different from one generated via another tree.

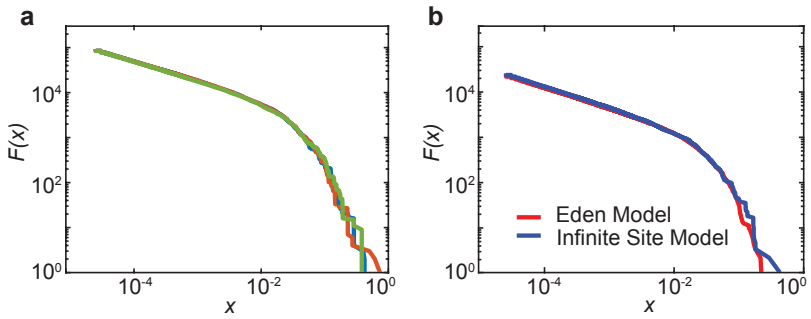

Figure 2.S4: Variation on the clone size distribution generated by tree idiosyncrasies. (**a**) Clone size distribution for three different trees generated using the Eden model and a population size of 2×10^5. (**b**) Clone size distribution generated by the standard Eden model and the Infinite Site Model on the same tree with mutation rate $\mu = 3 \times 10^{-4}$.

To test to what extent tree conditioning generates variation in the clone size distribution, we used the Eden model to generate three colonies of identical size and analyzed the complete clone size distribution. Figure 2.S4a shows that the inferred clone size distributions for the simulated trees show some variation in the sector regime, but overlap well in the bubble regime. This is in agreement with the intuition that small clones are less affected by the specific shape of the tree compared to large clones. Although tree idiosyncrasies generate some variation in the clone size distribution, the resulting noise is by far lower than that generated by subsampling (see Sect. 2.5.4), which is accounted for via bootstrapping in Fig. 2.

Conditioning on the tree, we also show that the results from the standard Eden model simulations presented in Section 2.5.4, in which mutants cannot mutate further, are consistent with an Infinite Site Model implemented on top of the Eden model, in which they can. Fig. 2.S4b shows the clone size distribution on the same tree using the standard Eden model and an infinite site model. Also in this case, the resulting variation at high frequencies is less than what is generated by subsampling.

Dynamical simulations for the effect of antibiotics on colony growth

To simulate the effect of intermediate antibiotic concentrations on colony growth and spreading of resistant individuals observed in experiments (see Fig. 4 in the main text), we adapted the Eden model simulation to accommodate sudden changes in the environment and death of the wild type.

Environmental changes are modeled by changing the relative growth rate of mutants and wild type before and after a certain time T during the simulations. The time T defines the time in which the antibiotic is administered. The relative growth rate of mutants, g_{mut}, and wild type, g_{wt}, define the selective advantage/disadvantage s of the mutant as $g_{\text{mut}}/g_{\text{wt}} - 1 = s$. Note that, if there is no death of the wild type,

the environmental changes would affect only mutant clones that have empty neighboring voxels, or new mutants that arise at the front. If the mutants initially carry a disadvantage, it is unlikely that any of them has contact with the front, meaning that *escape* of mutants can only occur via new mutants.

Therefore, since we experimentally observe the escape of pre-existing mutants, we introduce the possibility of death: after time T, any wild type cell (regardless of its neighbors) has a chance δ of dying each generation. The algorithm thus follows the following steps for each generations:

1. Count the number of cells n with at least one empty neighbor.
2. Count the total number of wild type cells n_{wt}.
3. Define $R = n$ reproductive steps and $D = d \cdot n_{\text{wt}}$ death steps.
4. During any of the $R + D$ steps,
   (a) Pick a random integer u in the $[0, R + D)$ interval.
   (b) If $u < R$ perform a reproductive step as described in section 2.5.4,
   (c) Otherwise, pick a random wild type cell and delete it.

In each generation, the algorithm ensures an average number of R births and D deaths, as desired.

To simulate the experimental scenario in Fig. 4, we first grow a population with neutral mutations until time T. After time T, new mutations are not allowed, and the wild type is ascribed a death rate δ as a proxy for the antibiotic concentrations. The Supplementary Movie 3 shows the qualitative agreement with the experimental results in identifying an intermediate death rate that corresponds to minimal colony growth.

2.5.5 Fitting of the clone size distribution from sequencing data

To estimate actual values from the empirical clone size distribution, we first determine the fitting parameters $\mu N \Pi_c$ and x_c that allow to collapse all the data one master curve $\chi(x/x_c)$ (see Appendix A). Here, (x_c, Π_c) represent the crossover between bubble and sector regime for the reverse cumulative distribution $\Pi(x)$ of clone sizes, and μN is the total number of mutations that entered the population. Because the fitting parameters depend on the population size N, which varied slightly between the colonies (see Table 2.S2), we allow the fitting parameters to vary from one colony to another.

The optimal fitting parameters are determined by minimizing the sum of least squares between the reverse cumulative clone size distribution obtained via sequencing and the master curve $\chi(x/x_c)$ derived by rescaling the results from the Eden model simulations with $x_c^{Eden} = 0.068$ and $\Pi_c^{Eden} = 0.019$ (Fig. A2 and Fig. 2.S5). Table 2.S3 summarizes the fitting parameters for each colony used to generate Fig. 2.

Colony	x_c	$\mu N\Pi_c$	$x_{\min}(10^{-4})$	$N_{\min}(10^5)$
1	0.055	303	1.2	4.3
2	0.059	238	1.8	5.0
3	0.054	333	1.1	7.8
4	0.051	435	0.71	6.4

Table 2.S3: Fitting parameters used to rescale the site frequency spectra of different colonies. When written as $F(x) = \mu N\Pi(x) = \mu N\Pi_c\chi(x/x_c)$, the site frequency spectra collapse on a single master curve in Figure 2. The minimum frequency $x_{\min}$ below which the bubble regime is expected to fail and its corresponding population size $N_{\min}$ are also reported.

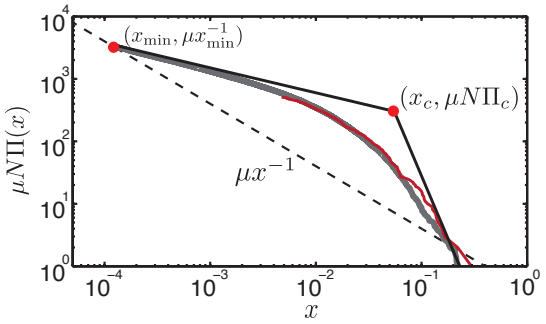

Figure 2.S5: Visualization of the fitting parameters of the site frequency spectrum obtained by sequencing colony 1. The crossover position $(x_c, \mu N\Pi_c)$ is optimized in order to have the least square deviation between the data (red) and the Eden model simulation results (gray). We find that the bubble regime intersects the well-mixed expectation (dashed black line) at frequency $x_{\min}$ below which we assume a well-mixed behavior. The same procedure is repeated for all colonies generating the parameters in Table 2.S3.

At very low frequencies, which we cannot observe via sequencing because of the limited coverage, we expect a transition from the bubble regime to a different behavior that captures finer scale dynamics (Appendix A). Although we do not attempt to characterize this regime here, we determine the minimum frequency $x_{\min}$ below which we expect the bubble scaling to fail. We define this frequency as the value at which the extrapolated bubble power-law from the sequencing site frequency spectrum of colonies intercepts the prolonged well-mixed expectation (Fig. 2.S5). Its value and the corresponding minimum population size $N_{\min} = Nx_{\min}$ is also reported in Table 2.S3. When sampling from the empirical site frequency spectrum obtained via sequencing in Figure 3, we assume that below $x_{\min}$ the clone size distribution follows a well-mixed distribution (Fig. 2.S5).

By rescaling frequency x and the number of SNPs $\mu N\Pi(x)$ above frequency x using the parameters in

Table 2.S3, we can extend the experimental clone size distribution with the Eden model simulations and our theory (Fig. 2.S5 for different population sizes and mutations rates. We can then compute the mean and the typical number of mutants, and the colony double mutant probability reported in Fig. 3 in the main text.

References

[1] R. Fowler and R. Schaaper. The role of the mutt gene of escherichia coli in maintaining replication fidelity. *FEMS Microbiology Reviews*, 21(1):43–54, 1997.

[2] A. E. Dodson and J. Rine. Heritable capture of heterochromatin dynamics in saccharomyces cerevisiae. *Elife*, 4:e05007, 2015.

[3] K. S. Korolev, M. I. J. Müller, N. Karahan, A. W. Murray, O. Hallatschek, and D. R. Nelson. Selective sweeps in growing microbial colonies. *Physical biology*, 9(2):026008, 2012.

[4] P. Anderson. Sensitivity and Resistance to Spectinomycin in Escherichia coli. *Journal of bacteriology*, 100(2):939–47, November 1969.

[5] C. D. Sigmund, M. Ettayebi, and E. A. Morgan. Antibiotic resistance mutations in 16S and 23S ribosomal RNA genes of Escherichia coli. *Nucleic acids research*, 12(11):4653–63, June 1984.

[6] J. Zhang, K. Kobert, T. Flouri, and A. Stamatakis. Pear: a fast and accurate illumina paired-end read merger. *Bioinformatics*, 30(5):614–620, 2014.

[7] D. E. Deatherage and J. E. Barrick. *Engineering and Analyzing Multicellular Systems: Methods and Protocols*, chapter Identification of Mutations in Laboratory-Evolved Microbes from Next-Generation Sequencing Data Using breseq, pages 165–188. Springer New York, New York, NY, 2014.

[8] K. Berlin, S. Koren, C.-S. Chin, J. P. Drake, J. M. Landolin, and A. M. Phillippy. Assembling large genomes with single-molecule sequencing and locality-sensitive hashing. *Nature biotechnology*, 33(6): 623–630, May 2015.

[9] H. Lee, E. Popodi, H. Tang, and P. L. Foster. Rate and molecular spectrum of spontaneous mutations in the bacterium escherichia coli as determined by whole-genome sequencing. *Proceedings of the National Academy of Sciences*, 109(41):E2774–E2783, 2012.

[10] M. Lynch. Estimation of allele frequencies from high-coverage genome-sequencing projects. *Genetics*, 182(1):295–301, May 2009.

[11] M. Eden. A two-dimensional growth process. *Dynamics of fractal surfaces*, 4:223–239, 1961.

3

Allele surfing promotes microbial adaptation from standing variation

The coupling of ecology and evolution during range expansions enables mutations to establish at expanding range margins and reach high frequencies. This phenomenon, called allele surfing, is thought to have caused revolutions in the gene pool of many species, most evidently in microbial communities. It has remained unclear, however, under which conditions allele surfing promotes or hinders adaptation. Here, using microbial experiments and simulations, we show that, starting with standing adaptive variation, range expansions generate a larger increase in mean fitness than spatially uniform population expansions. The adaptation gain results from 'soft' selective sweeps emerging from surfing beneficial mutations. The rate of these surfing events is shown to sensitively depend on the strength of genetic drift, which varies among strains and environmental conditions. More generally, allele surfing promotes the rate of adaptation per biomass produced, which could help developing biofilms and other resource-limited populations to cope with environmental challenges.

3.1 Introduction

The dynamics of adaptation has been intensely studied both theoretically and experimentally in situations where the time scales for demographic and adaptive change are vastly separated. Populations can then be

treated as either stable or as having an effective population size summarizing the effect of demographic variations on time scales much faster than the adaptive dynamics considered[1–3].

However, demographic equilibrium is frequently disrupted by, for instance, environmental changes, population growth, competition among species and local adaptation[4]. The fate of a genetic variant then both depends on and influences the demography of a dynamically changing population. Consequently, demographic and evolutionary changes can become tightly coupled[5].

Such coupling between ecology and evolution is a particularly salient feature of range expansions[6]. Many mutations occur in the bulk of a population where they have to compete for resources with their neighboring conspecifics. Mutations that, by chance, arise in a region of growing population densities have a two-fold advantage: They enjoy a growth rate advantage compared to their conspecifics in the slow-growing bulk regions, and their offspring will have a good chance to benefit from future net-growth if parent-offspring locations are correlated. These correlated founder effects, summarized by the term "allele surfing", lead to complex spatio-temporal patterns of neutral mutations and can rapidly drive mutations to high frequency by chance alone[7–10].

The importance of allele surfing has been increasingly recognized over the last 10 years[4,6,11]. Allele surfing is believed to be a ubiquitous process in populations that constantly turn over, for instance, by range expansions and contractions, local extinction or expulsion and re-colonization[12–16]. While these features are shared by many populations, they are most evident in microbial communities that frequently expand to colonize new surface regions in the environment or during infections[17,18].

Microbial experiments have shown that in the absence of selection allele surfing creates large mutant clones that are extremely unlikely to arise via neutral evolution of well-mixed populations. Characteristically, these clones take the shape of sectors with boundaries that exhibit characteristic fractal properties[19]. The random wandering of sector boundaries is a manifestation of genetic drift, as has been demonstrated experimentally in various micro-organisms, including bacteria, single-celled fungi and social slime molds, and under various demographic scenarios[19–23].

While allele surfing is well understood in the neutral case, we do not have a comprehensive picture of its adaptive potential. In particular, it is unclear how efficiently pre-existing adaptive variation[24] is selected for during range-expansions: Since allele surfing relies on enhanced genetic drift, it reduces the efficacy of selection per generation[25–27]. On the other hand, for populations of the same final size, selection has more time to act at the front of a range expansion than in a comparable well-mixed expansion, which could promote adaptation[25,28–30].

Here, we test whether allele surfing helps or hinders adaptation using microbial competition experiments to measure the efficiency of selection during growth processes. To get a sense of the range of possible evolutionary outcomes, we focus on two extreme cases: spatial range expansions and pure demographic growth

of panmictic populations. We find increased adaptation during range expansions and rationalize our quantitative results using theory and simulations.

3.2 Materials and Methods

3.2.1 Strains and Conditions

Each experiment was performed using a pair of microbial strains that are distinguished by fluorescence and a selectable marker. The fluorescent color difference allows measuring the relative abundance of each strain in competition experiments by fluorescence microscopy as well as flow cytometry. The selectable marker was used to tune the selective difference between the strains in the following way: One strain of the pair, the sensitive strain (called 'wild type'), grows slower in the presence of a drug, while the other strain, the resistant strain (called 'mutant'), is largely unaffected. Tuning the concentration of the drug in the medium thus allowed us to adjust the selective difference between both strains. Selective advantages on plates and in liquid culture were measured separately for a range of drug concentrations using the colliding colony assay[31] and flow cytometry (for *S. cerevisiae*), respectively (see Appendix C), which give consistent results (see supplementary Fig. 3.B1a). Selective differences reported throughout were obtained from linear fits.

Strains

We used *S. cerevisiae* strains with W303 backgrounds, where selective advantages were adjusted using cycloheximide. For experiments with *E. coli*, we used both DH5α and MG1655 strains, tuning fitness differences using tetracycline and chloramphenicol, respectively. Additionally, pairs of strains differing only in the fluorescent marker allowed us to perform truly neutral competition experiments (*S. cerevisiae*, *S. pombe*, *E. coli*). *S. cerevisiae* and *E. coli* strains with constitutively expressed fluorescent proteins were used to study the dynamics of cells at the front.

A detailed description of all strains and growth conditions is found in the Appendix C.

3.2.2 Main experiment

Adaptation from standing variation during two types of population expansions

For each pair of mutant and wild type, a mixed starting population of size N_i was prepared that contained an initial frequency P_i of mutants having a selective advantage s, defined as the relative difference between mutant and wild-type growth rate[31]. The population was then grown to final size N_f in two ways, through

a range expansion and, for comparison, through uniform growth, and the final mutant frequency P_f was determined. The associated increase in mean fitness ΔW follows as $\Delta W = (P_f - P_i)s$.

Uniform Growth

Mixtures of cells were grown in well-shaken liquid medium to the desired final population size and the final fraction of mutant cells was determined using flow cytometry.

Range Expansion

Colony growth was initiated by placing $2\mu l$ of the mixtures onto plates (2% w/v agar) and incubated until the desired final population size was reached. The number N_{sec} of sectors was determined by eye; the final fraction P_f was measured using image analysis (see Appendix C for details).

3.2.3 Cell-Tracking Experiments

To investigate the dynamics of cells at advancing colony fronts, we continually imaged the first few layers of most advanced cells in growing *S. cerevisiae* and *E. coli* colonies between a cover slip and an agar pad for about four hours using a Zeiss LSM700 confocal microscope. The resulting stack of images were segmented and cells were tracked as described in the Appendix C.

3.2.4 Meta-Population Model

To simulate evolutionary change during the different modes of growth, we adapted a classic meta-population model for growing microbial colonies, the Eden model[32] (Fig. 2a, Appendix A).

Range Expansion

The population spreads on a lattice and each lattice point is in one of three states: empty, wild type or mutant. Growth of the populations occurs by randomly selecting an occupied "source" site with empty neighbors and copying it into a randomly chosen empty neighbor site. A mutant is more likely to be picked than a wild-type site by a factor of $1 + s$. This process is repeated until the colony has reached the final average radius R_f and the final mutant fraction P_f is determined.

Uniform Growth

The range expansion simulation was modified such that a target site was an empty site randomly drawn from the entire lattice, rather than from the sites neighboring a given source site.

Individual-Based Simulations

To study the relevance of microscopic details on the adaptation process, we simulated a growing colony as a two-dimensional collection of sphero-cylinders (rods with hemispherical caps) of various lengths interacting mechanically (see Ref. 33 and Appendix A for details). The cells continuously grew (and divided) by consuming nutrients, whose concentration was explicitly computed.

3.3 Results

3.3.1 Adaptive Potential of Range Expansions

Our competition experiments in yeast show that when a population grows from a mixture of wild-type cells and faster growing mutant cells by a range expansion (Fig. 1a), it exhibits on average a larger final mutant frequency P_f than a well-mixed population grown to the same final population size $N_f \approx 2 \times 10^8$ (Fig. 1h). The difference in final mutant frequency between range expansion and uniform growth increases strongly with increasing selective advantage s of the mutants. For instance, for $s = 0.15$, mutants make up nearly 50% of the final population (Fig. 1d), in contrast to less than 10% mutant frequency in the well-mixed population. The discrepancy between both growth modes is even more pronounced when we plot the change $\Delta W = (P_f - P_i)s$ in mean fitness (Fig. 3.B2). Hence, adaptation from pre-existing mutations leads to a much stronger increase in mean fitness in our experiments when a given population increase occurs via the expansion of range margins rather than by a homogeneous density increase.

The spatial distribution of the mutant alleles visible in Fig. 1b-d indicates that the observed adaptation gain of range expansions hinges on the formation and growth of "sectors". These clonal regions are the footprints of surfing mutants that have locally established at the edge of the range expansion[19,25,31]. Sectors contain the vast majority of mutants in the population: If one removes the mutants that reside in sectors from the analysis, or chooses initial frequencies so low that sectors do not occur, the adaptation gain is essentially absent.

Selection has a strong impact on the shape and size of sectors: While a single mutant sector in yeast is stripe-like in the neutral case, it has a trumpet-like shape and can represent a substantial fraction of the total population when the mutants have a selective advantage (compare Figs. 1b-d). The rapid increase of sector size with selective advantage of the mutant strain is quantified in Fig. 1j. For instance, a single mutant sector

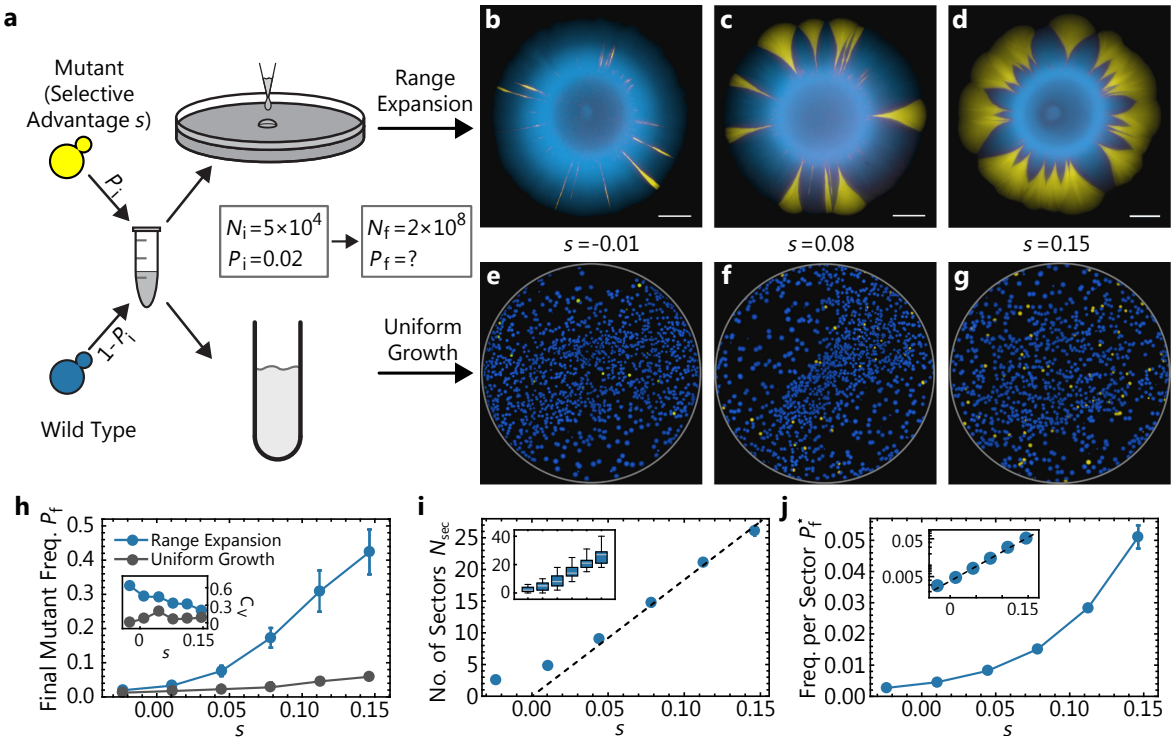

Figure 3.1: Adaptation from standing variation during a population size increase. Adaptation during the growth of a budding yeast population from an initial size N_i to N_f is studied for two demographic scenarios, Range Expansion and Uniform Growth. (a) Schematic of the experimental assay: Cultures of a wild-type and a faster-growing mutant strain are mixed at an initial mutant frequency $P_\mathrm{i} = 0.02$. Subsequently, a mixed population of initially $N_\mathrm{i} = 5 \times 10^4$ cells is grown to a final population size of $N_\mathrm{f} = 2 \times 10^8$. The growth process occurred either on agar plates ("Range Expansion") over the course of 5 days, or overnight under uniform growth conditions ("Uniform Growth"). The selective advantage s of the mutants is controlled by the concentration of cycloheximide, which inhibits the growth of the wild-type cells. The fluorescent microscopy images (b-d) show the distribution of both mutant (yellow) and wild-type (blue) cells at the end of range expansion experiments with selective advantage of $s = -0.01, 0.08,$ and 0.15, respectively. Scale bars are 2mm. (e-g) After plating the final populations of the uniform growth experiments, one obtains a distribution of single colonies with a color ratio representing the ratio of mutants to wild type. (h) Final mutant frequency and corresponding coefficient of variation (inset) as a function of selective advantage determined in range expansions (blue, 35 replicates) and under uniform growth (gray, 2 replicates). Notice that the final mutant frequency is larger for range expansions and increasingly so for larger selective differences. (i) Number of sectors N_sec at the end of range expansions as a function of selective advantage. The inset illustrates the spread of data points as a box plot. (j) Final frequency P_f^* per sector, defined as the area of a single sector normalized by the area of the entire colony, as a function of selective advantage s. The inset displays the same data using a logarithmic axis for the frequency per sector. Only sectors without contact to other sectors were selected for analysis. Error bars are standard error of the mean throughout. The measurements for (h, i, j) were all done on the same 35 replicates per data point.

with selective advantage $s = 0.15$ contains roughly 5% of the total population in our experiments. Under these conditions, a single clonal sector is like an adaptive "jackpot" event that can cause a substantial increase in the mean fitness of the population.

However, the early stages of surfing are a highly stochastic process, and therefore these jackpot events are rare. This is reflected in the rather small number of sectors (proportional to the initial frequency of mutants, see Fig. 3.B3) detected in our experiments. The colonies shown in Fig. 1b-d, for instance, were started with about 10^3 founder mutants in the inoculum, but only exhibit a handful of sectors (Fig. 3.1i). The number of sectors varies strongly between replicates (Fig. 3.1i, inset) and, if the mutants are very infrequent initially, there is a substantial chance that no sectors form (Fig. 3.B4). Importantly, while the number of sectors is generally small, it increases with selective advantage, further contributing to the adaptation gain in range expansions.

3.3.2 Towards a Minimal Model for Adaptation by Gene Surfing

The population dynamics of our colonies differs from uniform growth in numerous aspects: Cells are delivered to the plate in a droplet, which forms a ring of cells after evaporation[34]. The cells start to grow and push each other across the surface of the agar. The population grows at first exponentially, until the growth of the core of the colony slows down due to nutrient depletion behind the front. The further advancement of the front is driven by a layer of proliferating cells (the "growth layer"[19,35] at the edge of the colony (Fig. 3.B5).

While some of these complexities are specific to microbial colonies and biofilms[36], elevated growth rates at range margins combined with local dispersal are the characteristic features of range expansions. To see whether these features alone could reproduce the observed pattern of adaptation, we created a simple metapopulation model (Methods), in which the frontier advances by random draws from the demes within the range margins. This simple model has been shown to exhibit universal fractal properties of advancing interfaces[37], which have also been measured in bacterial range expansions[19].

As can be seen in Fig. 3.2, a simulation analog of Fig. 3.1, the model mirrors our experimental findings: Beneficial mutations have a higher frequency in populations that have undergone a range expansion than uniform expansion. The simulations also reproduce the stochastic formation of sectors and the qualitative dependence of sector number and size on the selective advantage. Thus, the patterns of adaptation seen in our colony experiments seem to originate from the few general features of range expansions that are incorporated in our minimal simulations.

Indeed, we now provide mathematical arguments and individual-based simulations to show how the key features of range expansions conspire to generate the observed adaptation gain; detailed mathematical derivations are provided in Appendix A.

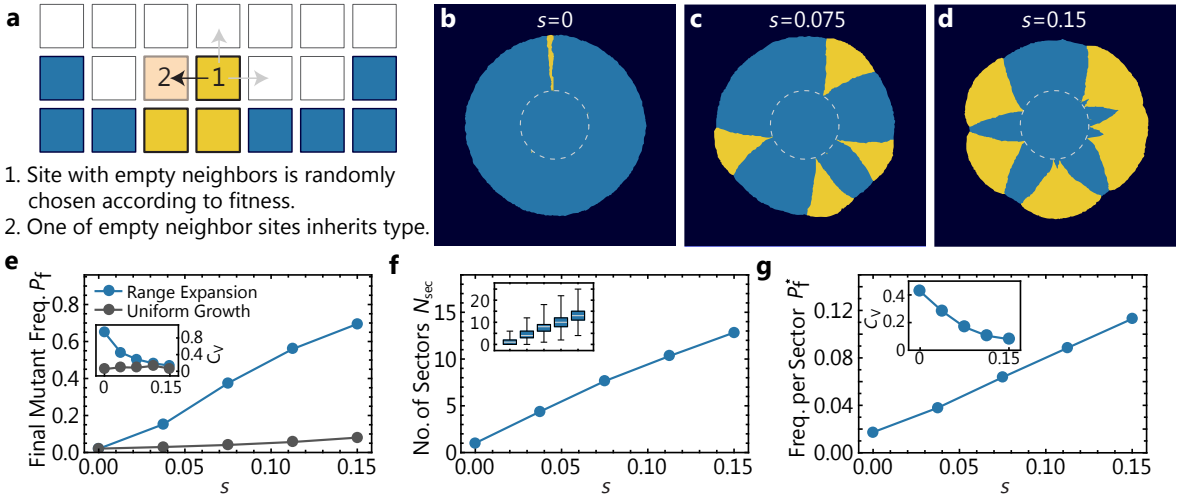

Figure 3.2: Adaptation from standing variation emerging in a meta-population model of population growth. (a) Illustration of the algorithm underlying our coarse-grained simulations (Methods). A lattice site at the population frontier is chosen and copied into an empty neighboring lattice site. The newly occupied site inherits the state of the parent site. (b-d) State of the lattice at the end of three simulations. To mimic our experiments in Fig. 1, we initiated the expanding population as an occupied disk (dashed line) of radius $R_\mathrm{i} = 550$ such that a random fraction $P_\mathrm{i} = 0.02$ of lattice sites is of the mutant type, and simulated until the final radius $R_\mathrm{f} \approx 3R_\mathrm{i}$ was reached. (e) Final mutant frequency P_f and corresponding coefficient of variation C_v (inset) as a function of selective advantage s determined in range expansions (blue, 500 simulations per condition) and corresponding simulations of uniform growth (gray, 3 simulations per condition, see Methods for algorithm) for the same parameters. Both final frequency and variation are larger for range expansions. (f) Number and standard error of mean of sectors at the end of range expansions as a function of selective advantage for the same simulations. Inset illustrates the spread of data points as a box plot. (g) Frequency per sector P_f^*, calculated from colonies with only a single sector, which were simulated using a low initial mutant fraction $P_\mathrm{i} = 0.005$.

3.3.3 Qualitative Explanation for Adaptation Gain

We shall begin with a simple, qualitative argument that demonstrates an important difference between range expansions and uniform growth. In a well-mixed population, the mutant frequency grows exponentially with time, $P_f \propto e^{sT}$. The number T of generations, however, increases only logarithmically with the final population size, $T \propto \ln N_f$, such that the mutant frequency changes by $P_f/P_i = (N_f/N_i)^s$. In our experiments, this leads to a modest relative change in mutant frequency, e.g., by a factor of 2 for a 6% beneficial mutation over the course of the growth process, which corresponds to about 12 generations. Importantly, the absolute frequency remains well below 1 when the initial frequency is small. Moreover, the final mutant frequency varies relatively little among different replicates, as quantified by the coefficient of variation (Fig. 1h inset). This is because nearly all initially present cells give rise to clones, with similar clone sizes, each corresponding to only a minute fraction of the total population.

In contrast to uniform growth, more generations need to pass to reach the same final population size N_f in a radially expanding population ($T \propto \sqrt{N_f}$ in a radially expanding population, in contrast to $T \propto \ln N_f$ in the well-mixed case). This implies that selection has more time to act during a range expansion, so that one might expect an increased final mutant frequency.

3.3.4 Adaptation Gain Depends on Sector Shape and Number

The above run-time argument captures the main reason for the adaptation gain, but it ignores two important counter-forces: (i) The efficacy of selection is reduced during a range expansion, because the frequency of a selected mutation increases only algebraically with time, in contrast to exponential sweeps in uniformly growing populations. (ii) Only few of the initially present cells give rise to expanding clones. Therefore, to fully understand the adaptive potential of range expansion we must examine the mechanism of sector expansion and formation, the latter being an inherently stochastic process caused by enhanced genetic drift at the front[19]. Ignoring any interaction between sectors and the small fraction of mutants in non-surfing clones, we can estimate the final frequency P_f of mutants by multiplying the number N_{sec} of sectors with their relative frequency P_f^* in the population,

$$P_f = P_f^* \times N_{sec}$$

While simple deterministic arguments exist to predict the frequency P_f^* of individual clones, new population genetic theory is required to predict the number N_{sec} of sectors. Remarkably, we shall see that the number of sectors is sensitive to microscopic details of the population growth process.

Final frequency P_f^* of expanding clones

The two boundaries of sectors in radial range expansions are logarithmic spirals[31]. These spirals emerge from the origin of the sector at a characteristic opening angle $\phi(s) \approx 2\sqrt{2s}$ that is set by the selective advantage s of the mutant[25]. Up to logarithmic corrections, one therefore expects a final frequency of mutant cells from a single sector to be $P_f^* \approx \phi(s)/2\pi \sim \sqrt{s}$ in large colonies (see eq. (3.A11) for the full result). This means that a single initial mutant can give rise to a macroscopically large clone of order $\sqrt{s}$. The fractional size of mutant sectors grows even faster in range expansions with straight rather than curved fronts.

Sector number N_{sec}

The establishment of beneficial mutations is generally a result of the competition between random genetic drift and the deterministic force of selection. At the coarse-grained description of clones in terms of sectors, genetic drift manifests itself in the random wandering of sector boundaries, ultimately a result of randomness in the reproduction process[19]. Balancing the random sector boundary motion with the deterministic sector expansion due to selection, we show in Appendix A (see Eq. (3.A15)) that the number of sectors is proportional to s in two dimensions. Note that although the s-dependence of the number of sectors in two-dimensions is identical to Haldane's classical result $2s$ for the establishment probability of beneficial mutations[38,39], the proportionality changes in the three-dimensional case to a predicted $s^{1.87}$ (Appendix A), which may be relevant to the evolution of solid tumors.

3.3.5 Modeling the Onset of Surfing

While our minimal model reproduces aspects of the experimental data reasonably well (see Fig. 3.A2), it cannot predict how microscopic details influence the adaptation dynamics. Microscopic details are summarized by a fit parameter, the effective deme size, which enters our expression for the number of sectors N_{sec} (Eq. (3.A19)).

To study directly how these microscopic factors influence the number of sectors, we developed an individual-based off-lattice simulation framework for microbial range expansions, where each cell is modeled explicitly as a growing elastic body of variable aspect ratio (see Methods and Appendix A). These computer simulations reveal that surfing events result from a complex competition between selection and genetic drift: The probability for an individual cell to form a sector (the surfing probability) increases with selective advantage s but the increase is much faster for colonies with a smooth front line than for colonies with strongly undulating fronts (Fig. 3.3i). The observed difference between the rough and smooth fronts can be explained intuitively as follows: If a mutant resides in a front region that is lagging behind neighboring wild-type regions, it will likely be overtaken and enclosed by the neighboring wild-type regions, despite its higher growth

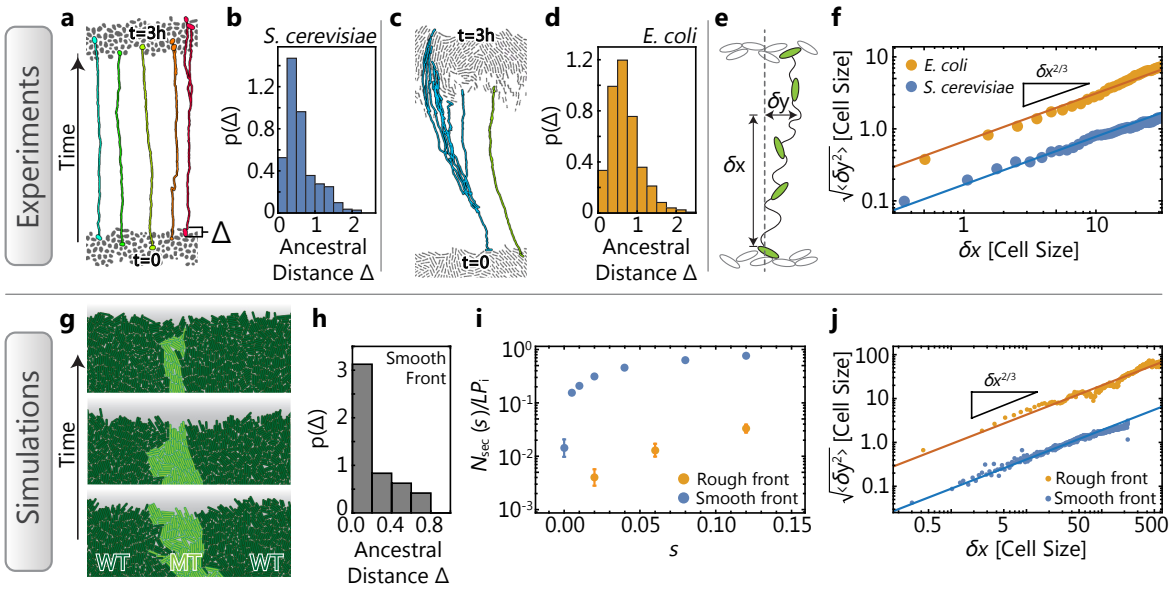

Figure 3.3: Surfing depends sensitively on location and the strength of genetic drift. Time-lapse microscopy (top row) and individual-based simulations (bottom row) reveal cell-scale dynamics at the front of expanding colonies. (a, c) Segmented micrographs of the initial front (bottom cells) and the front after three hours of growth (top cells) in *S. cerevisiae* (a) and *E. coli* (c) colonies, respectively. Colored lines track lineages backward in time (see also Figs. 3.B8-3.B10). The histograms in (b, d, h) quantify how surfing success depends on position: The probability density $p(\Delta)$ that the lineages tracked for 3 hours back in time lead to an ancestor that had a distance Δ (in unit of cell diameters) to the front. Note the pronounced peak in both experiments (b, c) and simulations (h). (e) Illustration and measurement of the random meandering of tracked lineages. We measure the lateral displacement δy (in units of cell diameters) a lineage has undergone while moving a distance δx along the direction of the front propagation, and average $\langle \delta y^2 \rangle$ over all lineages. (f) Average (root mean square) lateral displacement of lineages in expanding colonies, showing that *E. coli* lineages are fluctuating substantially more strongly than *S. cerevisiae* lineages (absolute value at a given δx). The lateral displacement in both cases follows a characteristic scaling (slope), as expected for a spatially unbiased growth process with a rough front (Appendix A). These experimental observations can be reproduced in simulations (j) of expanding rough and smooth fronts, respectively. (g) In simulations with rough fronts, surfing beneficial mutations (light green) are frequently occluded by neighboring wild-type domains (dark green). (i) As a consequence, the number of sectors are much lower for rough than smooth fronts, for identical initial mutant frequency P_i and front length L.

rate (Fig. 3.3g). Such "occlusion" events are more likely for rougher fronts, thus increasing the probability that beneficial mutations are lost by chance. In line with this explanation, we find that colonies with rougher fronts also exhibit higher levels of genetic drift, as quantified[19] by the lateral (perpendicular to the expansion direction) displacement of lineages from their origin (Fig. 3.3j). Importantly, we find that front roughness can be strongly influenced by several parameters that can vary among strains and conditions (Fig. 3.A11, Tables 3.A1, 3.A2).

Moreover, we find that only mutations that occur very close to the front line have any chance of long-term surfing (Fig. 3.3h). For our experiments, this implies that only those ancestral mutants have a chance to surf that, by chance, are in the first few cell layers of the dried inoculated droplet. The narrowness of the layer from which surfers are recruited, moreover, makes an important prediction about surfing of *de novo* mutations: Since the width λ of the growth layer where mutations occur can be much wider than the average width d of the cells in the front line, the effective mutation rate μ_{eff} of mutations occurring in the growth layer is the bare mutation rate μ reduced by a factor of $d/$, which is on the order of a few percent in most microbial colonies. Hence, the vast majority of beneficial mutations are effectively wasted in expanding populations because they occur behind the front line. Therefore, during range expansions with *de novo* mutations, a lot fewer surfing events should be observed than expected for a given mutation rate (as measured by, e.g., fluctuation analysis) and surfing probability (as measured by, e.g., the number of sectors), especially for a thick growth layer. This may contribute to the accumulation of deleterious mutations during range expansions[26].

3.3.6 Experimentally Probing the Onset of Surfing

Our individual-based model made two crucial predictions about the early stages of surfing, which we tested in a series of experiments described below.

(i) Surfing occurs only directly at the front. Control measurements show that the number of surfing events is proportional to the initial frequency (Fig. 3.B3) and not significantly sensitive to the total number of cells, as long as they form a contiguous perimeter around the initial droplet (Fig. 3.B6). These observations are consistent with the hypothesis that surfing events originate in the front region of the colony. To test whether surfers arise in the very first cell layer only, we took time-lapse movies (SI movies 1 and 2) of an advancing front at a resolution that allows us to track lineages backward in time. The resulting genealogies show that only cells at the very front remain as ancestor of future populations. We can extract histograms of ancestor distances from the front (Fig. 3.3b, d; see also Fig. 3.B10), showing that cells have to be within about one cell diameter to have any chance of giving rise to a successful lineage.

(ii) The strength of genetic drift influences surfing rates, and is highly variable. We repeated our competition experiments using pairs of *E. coli* (Methods) strains and found up to an order of magnitude

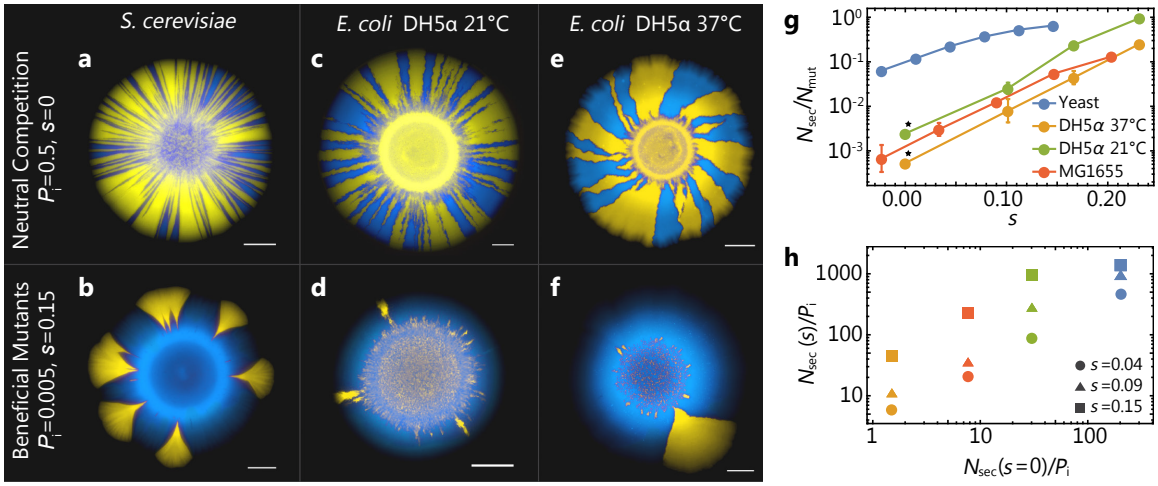

Figure 3.4: Adaptation during range expansions for different strains and conditions. (a-f) Top row: Images of colonies after neutral range expansions (Methods) with an initial mutation frequency of $P_{\mathrm{i}} = 0.5$. The number of sectors formed (panel g) and their shape (see Fig. B7) varies between *S. cerevisiae* and *E. coli* and temperature at which colonies are grown. The bottom row shows corresponding range expansions when mutants have a selective advantage of $s \approx 0.15$, at low initial mutation fraction of $P_{\mathrm{i}} = 0.005$. Scale bars are 2mm in each image. (g) The number N_{sec} of sectors normalized by the number N_{mut} of mutant cells in the outside rim of the inoculum as a function of the selective advantage of the mutants for different species, strains, and growth conditions (about 35 replicates per data point). The asterisk (*) denotes the use of the neutral strain pairing as opposed to the mutant-wild-type pair. (h) The number of sectors N_{sec} normalized by the initial fraction P_{i} against the normalized number of sectors in the neutral case shows a clear correlation between neutral dynamics and the surfing probability of advantageous mutant clones: weaker genetic drift (more sectors in neutral competitions) is indicative of a higher surfing probability. Panel (h) is obtained by interpolating data from panel (g) for the selected values of s.

differences in surfing probability, i.e., proportion of surfing mutants N_{sec}/N_{mut}, for a given selective advantage (Fig. 3.4). This underscores that the selective advantage of a mutation alone has little predictive power over the probability of surfing. The reason is that allele surfing also depends on the strength of genetic drift, which can be estimated from the number of sectors emerging in neutral competition experiments (Fig. 3.4a, c, e). Fig. 3.4g shows a clear correlation between the number of surfing beneficial mutations and the number of surfing neutral mutations, for four conditions and different fitness effects. This suggests that measuring the strength of random genetic drift is necessary to predict the efficacy of adaptation.

The difference between strains can partly be understood from time-lapse movies of the colony growth at single-cell resolution (SI movies 1 and 2). While cell motion perpendicular to the front direction is limited in yeast colonies, there is strong dynamics within the *E. coli* front. Tracking the cells through 3 hours of growth elucidates the difference in cellular dynamics, as shown in Fig. 3.3a and c. We quantify this observation by measuring the cells' lateral displacement (Fig. 3.3e-f, Appendix C), which is about an order of magnitude stronger in *E. coli* compared to budding yeast, explaining (at least part) of the difference in genetic drift. The same effect can be observed in computer simulations of the individual-based model (Fig. 3.3i, j).

While it may not seem surprising that genetic drift varies somewhat (though not an order of magnitude) between taxa due to differences in the reproductive process, we also found that the level of genetic drift varies among different growth conditions for the same species. Fig. 4c-f show the results of competition experiments between two differently labeled but otherwise identical E. coli strains (DH5α background) at two different incubation temperatures. Notice that the neutral sectoring pattern undergoes a striking change: While only few sectors can be observed at 37°C, many spoke-like sectors arise at 21°C. Importantly, surfing probabilities varied, as predicted, with observed variations in the strength of genetic drift: repeating the establishment experiments at lower temperatures shows that the number of established clones indeed increased for smaller amounts of genetic drift (Fig. 3.4g, h).

3.4 Discussion

Laboratory evolution experiments usually investigate the rate of adaptation per unit time. This is the relevant quantity when resources are abundant or replenish faster than they are consumed, as for example in a chemostat[40].

By contrast, in our experiments we have compared the adaptive outcome of two types of population expansions, range expansion and uniform growth, under the condition that both types lead to the same final population size, no matter how long it may take. Thus, we have effectively measured the rate of adaptation per cell division or, equivalently, per biomass produced. We believe this is the crucial comparison when

population growth is resource-limited, which may arguably apply not only to microbial biofilms[35,41], but also to various other types of natural populations, including tumors, and spreading pathogens[42,43].

Our experiments show that, starting from standing adaptive variation, range expansions generate a larger, often much larger, mean fitness increase in microbial communities than equivalent uniform population expansions. In essence, this results from the effective serial dilution of the pioneer population, generated by the fact that the offspring of pioneers tend to be the pioneers of the next generation. As a consequence of these spatio-temporal correlations, selection can act over more generations at the front of a range expansion than in a uniform expansion.

However, because the relevant pioneer population is small, sampling effects (genetic drift) are important: The gain in adaptation comes in partial sweeps, visible in our experiments as large "sectors", which represent successfully surfing alleles. The total adaptation gain during a range expansion depends on both the number of sectors and the size of sectors. While the shape of sectors simply reflects the selective advantage of the mutants, the stochastic number of sectors is a result of the competition between selection and (strong) genetic drift in the pioneer population.

Thus, predicting the number of sectors, and ultimately the rate of adaptation in population expansions, requires a measurement of both the strength of selection and genetic drift. In microbial experiments, the strength of genetic drift, which is related to the front roughness, can be measured by neutral mixing experiments with fluorescently labeled strains. Such measurements show that the strength of genetic drift varies by orders of magnitude among strains and conditions like growth medium or temperature, affecting surface roughness, growth layer width, or cell shape, as illustrated in Fig. 3.5. Thus, changes in the microbial growth processes can strongly influence the adaptive potential of range expansions via their impact on the strength of genetic drift. This may be important, for instance, for adaptation in developing biofilms with their complex surface properties[36,44], and could be tested in flow chamber experiments.

Our results underscore the adaptive potential of allele surfing: Although, as was found previously in the neutral case, allele surfing is a rare event that depends on enhanced genetic drift at the frontier[19], it becomes more likely as the selective advantage of the mutation increases. Nevertheless, out of the pre-existing mutant population only few mutants manage to establish and surf at the frontier. The ones that do, however, leave a strong mark on the population as a whole; driven by selection, their descendants sweep to high frequencies in the population.

In other words, allele surfing turns a population expansion into a high-paying evolutionary slot machine[45]: The expected gain in fitness is high on average but it relies on rare surfing events controlled by the competition of genetic drift and selection. Range expansions can thus lead to large evolutionary change if these jackpots events do occur. By contrast, well-mixed populations lead to a homogeneous growth of all cells, resulting in less overall change in frequencies.

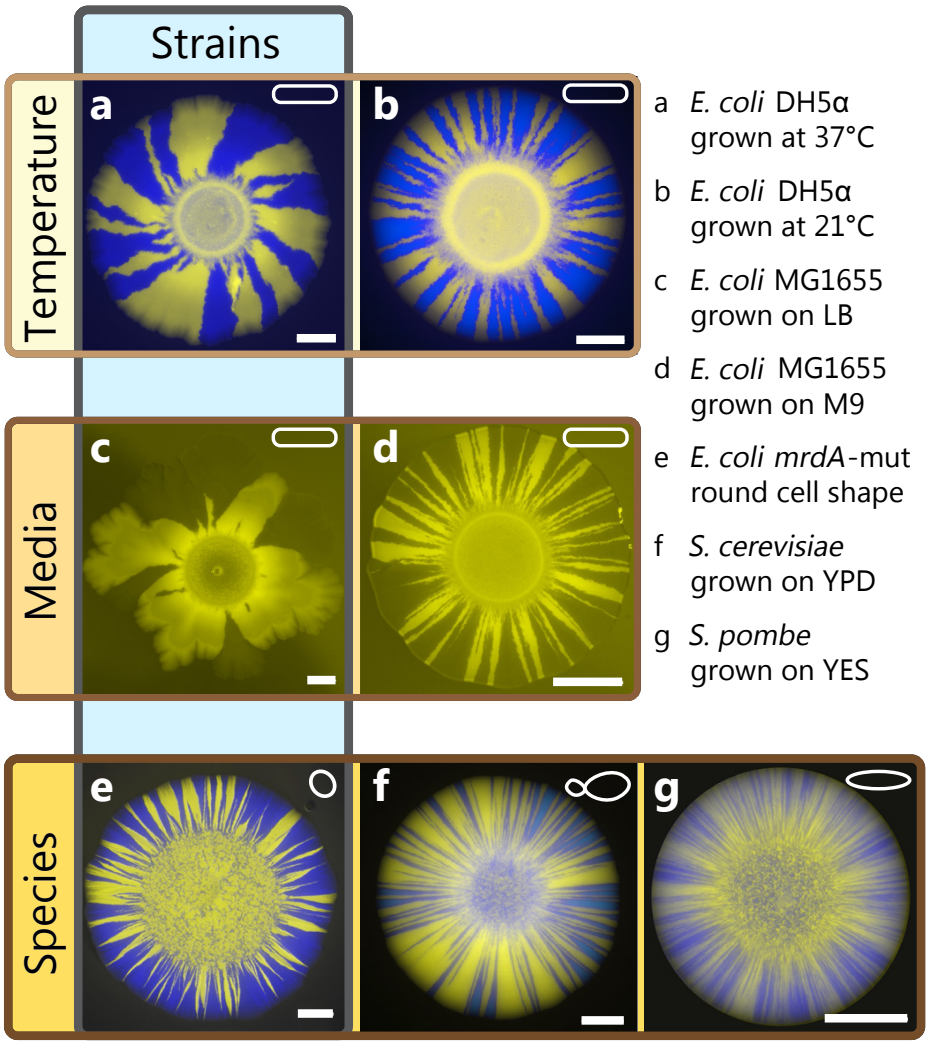

Figure 3.5: Variability of genetic drift across species, strains, and environmental conditions. Each image shows a colony of two neutral strains grown with a starting frequency $P_i = 0.5$. Colored frames indicate the main differences between images. *E. coli* colonies (a-e) exhibit fewer sectors and are less regular than yeast colonies (f-g), which produce many sectors. Environmental factors, in particular temperature (a-b) or composition of media (c-d) also influence the strength of genetic drift. Even for identical conditions, different *E. coli* strains exhibit varying morphologies and sector numbers: For example, mutations influencing cell shape (e) may leads to straighter sectors boundaries and more sectors, although cell shape alone does not accurately predict the strength of genetic drift (compare *E. coli* (a-d) and *S. pombe* (g), which are both rod-shaped). All scale bars are 2mm.

As our experiments have focused on standing genetic variation, they have ignored the impact of spontaneous mutations occurring during the population expansion. Enhanced genetic drift at expanding frontiers is expected to promote the genetic load due to new deleterious mutations[9,25,26,46], which may lead in extreme cases to a slowdown of the population expansion, for instance when "mutator" strains are involved. Thus, enjoying an adaptation increase from a range expansion may require a sufficiently low rate of deleterious mutations.

Strikingly, our expanding colonies shifted from a predominantly wild-type to a largely resistant population under quite weak selective pressures. We hypothesize that adaptation by allele surfing could be a general mechanism for efficiently shifting the balance between pre-existing types after an environmental change. Moreover, a proposed connection[47] between drug resistance in bacterial communities and malignant tissues suggests that similar effects could be at play in solid tumors that harbor standing variation prior to drug treatment.

Allele surfing may also help explain the efficient adaptation seen in some cases of species invasions, such as in cane toads, which developed longer legs in the course of the invasion of Australia[48]. Although we do expect our results to carry over to more complex scenarios, sex, death, recombination, dominance, and heterogeneities in resources and selection pressures may significantly complicate the dynamics. Key differences could arise, for instance, if mutants do not have an expansion velocity advantage, but are instead merely outcompeting the wild-type individuals within already occupied regions. In this case, we expect sectors to reach substantially lower frequencies than in our experiments.

Adaptation by gene surfing matches the pattern of a "soft" selective sweep[24,49], in which multiple adaptive alleles sweep through the population at the same time, however with a unique spatial structure. Although these sweeps can be strong, as seen in our experiments, they may be hard to identify in population genomic studies when they carry along different genomic backgrounds. However, as sequencing costs drop further and spatial sampling resolution increases, the genomic signal of these localized soft sweeps may become directly discernable.

References

[1] H. J. Muller. Some genetic aspects of sex. *The American Naturalist*, 66(703):118–138, 1932.

[2] J. F. Crow and M. Kimura. Evolution in sexual and asexual populations. *The American Naturalist*, 99(909):439–450, 1965.

[3] J. F. Crow, M. Kimura, et al. An introduction to population genetics theory. *An introduction to population genetics theory.*, 1970.

[4] L. Excoffier, M. Foll, and R. J. Petit. Genetic consequences of range expansions. *Annual Review of Ecology, Evolution, and Systematics*, 40:481–501, 2009.

[5] R. Ferriere and S. Legendre. Eco-evolutionary feedbacks, adaptive dynamics and evolutionary rescue theory. *Phil. Trans. R. Soc. B*, 368(1610):20120081, 2013.

[6] L. Excoffier and N. Ray. Surfing during population expansions promotes genetic revolutions and structuration. *Trends in ecology & evolution*, 23(7):347–351, 2008.

[7] C. A. Edmonds, A. S. Lillie, and L. L. Cavalli-Sforza. Mutations arising in the wave front of an expanding population. *Proceedings of the National Academy of Sciences of the United States of America*, 101(4):975–979, 2004.

[8] S. Klopfstein, M. Currat, and L. Excoffier. The fate of mutations surfing on the wave of a range expansion. *Molecular biology and evolution*, 23(3):482–490, 2005.

[9] J. M. Travis, T. Münkemüller, O. J. Burton, A. Best, C. Dytham, and K. Johst. Deleterious mutations can surf to high densities on the wave front of an expanding population. *Molecular biology and evolution*, 24(10):2334–2343, 2007.

[10] O. Hallatschek and D. R. Nelson. Gene surfing in expanding populations. *Theoretical population biology*, 73(1):158–170, 2008.

[11] J. M. Waters, C. I. Fraser, and G. M. Hewitt. Founder takes all: density-dependent processes structure biodiversity. *Trends in Ecology & Evolution*, 28(2):78–85, 2013.

[12] I. Hanski. Metapopulation dynamics. *Nature*, 396(6706):41–49, 1998.

[13] R. Freckleton and A. Watkinson. Large-scale spatial dynamics of plants: metapopulations, regional ensembles and patchy populations. *Journal of Ecology*, 90(3):419–434, 2002.

[14] C. R. Haag, M. Riek, J. W. Hottinger, V. I. Pajunen, and D. Ebert. Genetic diversity and genetic differentiation in daphnia metapopulations with subpopulations of known age. *Genetics*, 170(4): 1809–1820, 2005.

[15] D. R. Taylor and S. R. Keller. Historical range expansion determines the phylogenetic diversity introduced during contemporary species invasion. *Evolution*, 61(2):334–345, 2007.

[16] M. Arenas, N. Ray, M. Currat, and L. Excoffier. Consequences of range contractions and range shifts on molecular diversity. *Molecular biology and evolution*, 29(1):207–218, 2011.

[17] I. Cho and M. J. Blaser. The human microbiome: at the interface of health and disease. *Nature Reviews Genetics*, 13(4):260–270, 2012.

[18] E. K. Costello, K. Stagaman, L. Dethlefsen, B. J. Bohannan, and D. A. Relman. The application of ecological theory toward an understanding of the human microbiome. *Science*, 336(6086):1255–1262, 2012.

[19] O. Hallatschek, P. Hersen, S. Ramanathan, and D. R. Nelson. Genetic drift at expanding frontiers promotes gene segregation. *Proceedings of the National Academy of Sciences*, 104(50):19926–19930, 2007.

[20] K. S. Korolev, J. B. Xavier, D. R. Nelson, and K. R. Foster. A quantitative test of population genetics using spatiogenetic patterns in bacterial colonies. *The American Naturalist*, 178(4):538–552, 2011.

[21] C. D. Nadell, V. Bucci, K. Drescher, S. A. Levin, B. L. Bassler, and J. B. Xavier. Cutting through the complexity of cell collectives. In *Proc. R. Soc. B*, volume 280, page 20122770. The Royal Society, 2013.

[22] P. D. Freese, K. S. Korolev, J. I. Jiménez, and I. A. Chen. Genetic drift suppresses bacterial conjugation in spatially structured populations. *Biophysical journal*, 106(4):944–954, 2014.

[23] J. Van Gestel, F. J. Weissing, O. P. Kuipers, and A. T. Kovács. Density of founder cells affects spatial pattern formation and cooperation in bacillus subtilis biofilms. *The ISME journal*, 8(10):2069–2079, 2014.

[24] R. D. Barrett and D. Schluter. Adaptation from standing genetic variation. *Trends in ecology & evolution*, 23(1):38–44, 2008.

[25] O. Hallatschek and D. R. Nelson. Life at the front of an expanding population. *Evolution*, 64(1): 193–206, 2010.

[26] S. Peischl, I. Dupanloup, M. Kirkpatrick, and L. Excoffier. On the accumulation of deleterious mutations during range expansions. *Molecular ecology*, 22(24):5972–5982, 2013.

[27] S. Peischl and L. Excoffier. Expansion load: recessive mutations and the role of standing genetic variation. *Molecular Ecology*, 24(9):2084–2094, 2015.

[28] Q. Zhang, G. Lambert, D. Liao, H. Kim, K. Robin, C.-k. Tung, N. Pourmand, and R. H. Austin. Acceleration of emergence of bacterial antibiotic resistance in connected microenvironments. *Science*, 333(6050):1764–1767, 2011.

[29] P. Greulich, B. Waclaw, and R. J. Allen. Mutational pathway determines whether drug gradients accelerate evolution of drug-resistant cells. *Physical Review Letters*, 109(8):088101, 2012.

[30] R. Hermsen, J. B. Deris, and T. Hwa. On the rapidity of antibiotic resistance evolution facilitated by a concentration gradient. *Proceedings of the National Academy of Sciences*, 109(27):10775–10780, 2012.

[31] K. S. Korolev, M. J. Müller, N. Karahan, A. W. Murray, O. Hallatschek, and D. R. Nelson. Selective sweeps in growing microbial colonies. *Physical biology*, 9(2):026008, 2012.

[32] M. Eden. A two-dimensional growth process. *Dynamics of fractal surfaces*, 4:223–239, 1961.

[33] F. Farrell, O. Hallatschek, D. Marenduzzo, and B. Waclaw. Mechanically driven growth of quasi-two-dimensional microbial colonies. *Physical review letters*, 111(16):168101, 2013.

[34] R. D. Deegan, O. Bakajin, T. F. Dupont, G. Huber, S. R. Nagel, and T. A. Witten. Capillary flow as the cause of ring stains from dried liquid drops. *Nature*, 389(6653):827–829, 1997.

[35] S. Mitri, E. Clarke, and K. R. Foster. Resource limitation drives spatial organization in microbial groups. *The ISME journal*, 10(6):1471–1482, 2016.

[36] C. D. Nadell, K. R. Foster, and J. B. Xavier. Emergence of spatial structure in cell groups and the evolution of cooperation. *PLoS computational biology*, 6(3):e1000716, 2010.

[37] M. Kardar, G. Parisi, and Y.-C. Zhang. Dynamic scaling of growing interfaces. *Physical Review Letters*, 56(9):889, 1986.

[38] T. Maruyama. On the fixation probability of mutant genes in a subdivided population. *Genetics Research*, 15(2):221–225, 1970.

[39] Z. Patwa and L. M. Wahl. The fixation probability of beneficial mutations. *Journal of The Royal Society Interface*, 5(28):1279–1289, 2008.

[40] T. J. Kawecki, R. E. Lenski, D. Ebert, B. Hollis, I. Olivieri, and M. C. Whitlock. Experimental evolution. *Trends in ecology & evolution*, 27(10):547–560, 2012.

[41] P. S. Stewart and M. J. Franklin. Physiological heterogeneity in biofilms. *Nature Reviews Microbiology*, 6(3):199–210, 2008.

[42] C. E. Lee. Evolutionary genetics of invasive species. *Trends in ecology & evolution*, 17(8):386–391, 2002.

[43] S. Ling, Z. Hu, Z. Yang, F. Yang, Y. Li, P. Lin, K. Chen, L. Dong, L. Cao, Y. Tao, et al. Extremely high genetic diversity in a single tumor points to prevalence of non-darwinian cell evolution. *Proceedings of the National Academy of Sciences*, 112(47):E6496–E6505, 2015.

[44] J. B. Xavier and K. R. Foster. Cooperation and conflict in microbial biofilms. *Proceedings of the National Academy of Sciences*, 104(3):876–881, 2007.

[45] S. E. Luria and M. Delbrück. Mutations of bacteria from virus sensitivity to virus resistance. *Genetics*, 28(6):491, 1943.

[46] M. O. Lavrentovich, M. E. Wahl, D. R. Nelson, and A. W. Murray. Spatially constrained growth enhances conversional meltdown. *Biophysical journal*, 110(12):2800–2808, 2016.

[47] G. Lambert, L. Estévez-Salmeron, S. Oh, D. Liao, B. M. Emerson, T. D. Tlsty, and R. H. Austin. An analogy between the evolution of drug resistance in bacterial communities and malignant tissues. *Nature Reviews Cancer*, 11(5):375–382, 2011.

[48] B. L. Phillips, G. P. Brown, J. K. Webb, and R. Shine. Invasion and the evolution of speed in toads. *Nature*, 439(7078):803–803, 2006.

[49] P. S. Pennings and J. Hermisson. Soft sweeps ii—molecular population genetics of adaptation from recurrent mutation or migration. *Molecular biology and evolution*, 23(5):1076–1084, 2006.

3.5 Appendix A – Theory and Simulations

3.5.1 Coarse-grained simulations and analytical results

Simulation algorithm

We simulate range expansions using a metapopulation model on a lattice, similar to the Eden model. Initially, the central site of an empty lattice is filled with a single cell. In each time step, a cell with at least one empty neighboring lattice site is randomly chosen to divide into one of the empty sites in its 4-site neighborhood. If there are mutants in the colony with a selective advantage s, the algorithm first randomly chooses whether to forward the wildtype or mutant population, where the mutants are chosen with probability

$$p(\mathrm{MT}) = \frac{(1+s)N_{\mathrm{MT}}}{(1+s)N_{\mathrm{MT}} + N_{\mathrm{WT}}} = 1 - p(\mathrm{WT}), \tag{3.A1}$$

where N_{MT} and N_{WT} are the number of mutant and wild type site having empty neighbors.

Standing variation. The colony is first grown to a radius R_{i} (by running the simulation $T = \pi R_{\mathrm{i}}^2$ steps; for Fig. 2, $T = 10^6$) of only wild types. Then, filled lattice sites are randomly populated with wild types and mutants at a specified ratio P_{i}. The colony is grown a total of $8\pi R_{\mathrm{i}}^2$ time steps, i.e., to a final radius of about $2.8 \times R_{\mathrm{i}}$. This corresponds roughly to the radial increase in our experiments.

For the scaling function below, P_{i} was varied between 0.02 and 0.005 to minimize interaction between sectors. Sectors were counted by identifying all mutant clones that have at least one member with at least one empty neighboring lattice site at the end of the simulation.

De novo mutations. Instead of starting from a mixture of wild type and mutant sites, we can allow for spontaneous mutations. Populations are grown from a single individual, and every new individual has a chance μ of converting to the mutant type, having an advantage s. Here, we do not consider back mutations.

Long range jumps. To interpolate between the well-mixed and the colony case, we simulate long range jumps by following Ref.[1]. A random number Y between 0 and 1 is drawn and transformed to a jump length r by computing

$$r = \left(Y\left[L^{\mu} - C^{\mu}\right] - C^{\mu}\right)^{-1/\mu}. \tag{3.A2}$$

Here, L and C specify the maximum and minimum jump length. The new variable r is distributed as a truncated power-law with a power-law tail, i.e., $p(r) \sim r^{-\mu}$. To allow for long range jumps, we employ periodic boundary conditions. In addition, an angle φ is drawn between 0 and 2π. In every step, a random lattice site (x_i, y_i) is chosen and the jump attempted to the lattice site located closest to $(x_i + r\cos\varphi, y_i + r\sin\varphi)$; if the site is empty, it is filled, otherwise a new site is chosen. Only successful jumps forward the time variable, such that exactly one jump happens in each time step. After T_{i} steps, mutants are introduced

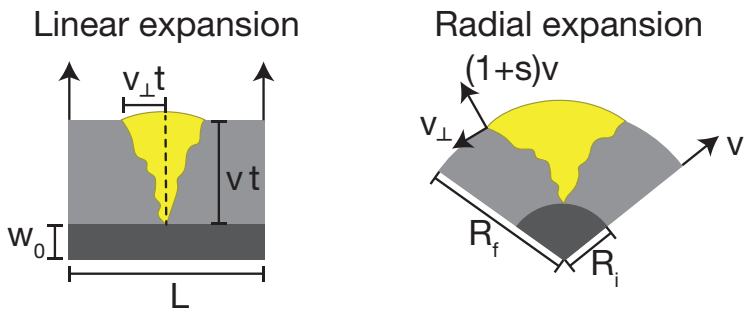

Figure 3.A1: Sketch of the expansion of a sector in a linear (left) and a radial range expansion (right). While sectors have a constant opening angle φ in a linear expansion, their boundaries form logarithmic spirals in the radial expansion case, enclosing an angle φ that increases logarithmically with the radius R_f (cf. Eq. (3.A9)).

by randomly mutating each filled lattice with a probability equal to the desired ratio of wild type to mutant cells. Thus, the initial frequency of mutants is stochastic, mimicking the situation in real experiments.

Final mutant frequency

In the following, we refine the scaling arguments given in the main text to explain the increased adaptation gain in range expansions. To reach the same final population size, a larger number of generations at the front of a range expansion is necessary, allowing selection to act for longer, compared to exponentially growing populations. Yet, selection is weaker at the advancing front in the sense that a selective advantage s does not lead to an exponential increase in frequency like it does in well-mixed populations. Nevertheless, we argue below that the former effect is in general stronger than the latter, leading to a net increase in adaptation gain.

Well-mixed population

Starting from N_i initial cells, of which a fraction P_i are mutants, the number of mutant cells $M(t)$ at time t (in generations) is $M(t) = P_i N_i 2^{(1+s)t}$. To reach final population size N_f, it takes $t = \log_2(N_f/N_i)$ generations, hence, $M(t) = P_i N_i (N_f/N_i)^{1+s}$. The final mutant frequency thus becomes

$$P_f = \frac{M(t)}{N_f} = P_i \left(\frac{N_f}{N_i}\right)^s = P_i(1+\eta)^s, \tag{3.A3}$$

where we have defined the fold change $\eta = N_f/N_i - 1$ of the total population size. The adaptation gain in a well-mixed population can be quantified through the fold change R_{WM} of the mutant frequency

$$R_{WM} = \frac{P_f}{P_i} - 1 = (1+\eta)^s - 1 \approx s \log(1+\eta) \tag{3.A4}$$

for $s \ll 1$. For small η, this reduces to $R_{WM} \approx \eta s$.

Flat front range expansion

Start from a region of (constant) height L and width w_0, containing $N_i = Lw_0$ individuals (see sketch in Fig. 3.A1, left). We assume that the width grows at speed v, and sector size increases with perpendicular velocity $v_\perp = \sqrt{s(s+2)}v$[2]. The final mutant population size is composed of the size of (roughly triangular) beneficial sectors times their number, plus the neutral contribution, i.e.,

$$M(t) = vv_\perp t^2 N_{sec} + P_i N_f, \tag{3.A5}$$

where we have ignored fluctuations of the sector boundaries as well as the typically small number of mutants in non-surfing clones. The number of generations to reach final size N_f is $t = (N_f - N_i)/vL = \eta N_i/vL$. Plugging this into $M(t)$ and dividing by N_f to find the final mutant frequency, we get

$$P_f = \frac{v_\perp \eta^2 N_i}{(1+\eta)vL^2} N_{sec} + P_i. \tag{3.A6}$$

The number of sectors can be estimated as $N_{sec} = LP_i u(s)$, where $u(s)$ is the (unknown) probability to form a sector per individual at the front, i.e., the surfing probability. Hence, we obtain the fold change $R_{FF} = P_f/P_i - 1$ in the flat front case as

$$R_{FF} = \frac{v_\perp \eta^2 N_i u(s)}{(1+\eta)vL} = \frac{\sqrt{s(2+s)}\eta^2 N_f u(s)}{(1+\eta)^2 L} \approx \frac{\sqrt{s(2+s)} N_f u(s)}{L} \tag{3.A7}$$

for $\eta \gg 1$. Thus, for a final population size much larger than the initial population size (as is the case in our experiments), the size of the adaptation gain R_{FF} depends critically on the surfing probability $u(s)$. This indicates that a purely deterministic treatment is not appropriate to understand adaptation during range expansions. Adaptation crucially hinges on sector formation. Nevertheless, for some fixed s, Eq. (3.A7) shows that in the long run, range expansions will always produce a larger adaptive outcome than exponentially growing populations as the linear scaling of R_{FF} with N_f will eventually overtake the logarithmic scaling of R_{WM}.

Radial expansions

The situation is less straightforward in a radial expansion, as the shape of sectors is influenced by both inflation and selection. Their shape and size can be understood from simple geometrical arguments [2,3], which we replicate and extend here.

Mutants grow faster into the expanding territory by a factor of $1+s$ (see sketch in Fig. 3.A1, right). This speed difference together with the requirement of continuity of the colonial edge enforces a fixed speed at which mutants expand (wild-types retract) along the colony edge. The transverse expansion speed $v_\perp = \sqrt{s(s+2)}$ (in units of the wild-type front speed) follows from equating the speed of radial growth in both compartments (1 vs. $1+s$). As a consequence of the transverse expansion of the two sector boundaries, the opening angle φ of the sector increases with radial distance according to

$$\mathrm{d}\varphi = 2v_\perp \,\mathrm{d}r/r = 2\sqrt{s(2+s)}\,\mathrm{d}r/r. \tag{3.A8}$$

Integration yields a logarithmic increase with radius,

$$\varphi(R_\mathrm{f}|R_\mathrm{i}) = \int_{R_\mathrm{i}}^{R_\mathrm{f}} \mathrm{d}\varphi = 2\sqrt{s(2+s)}\log(R_\mathrm{f}/R_\mathrm{i}), \tag{3.A9}$$

as was already shown in Ref.[3]. Assuming large sectors such that the initial period of sector formation is negligible, the final frequency of the sector is obtained by integration,

$$P_\mathrm{f}^* \approx (\pi R_\mathrm{f}^2)^{-1} \int_{R_\mathrm{i}}^{R_\mathrm{f}} \mathrm{d}r r\varphi(r) = \frac{\sqrt{s(2+s)}}{2\pi R_\mathrm{f}^2}\left(R_\mathrm{i}^2 - R_\mathrm{f}^2 + 2R_\mathrm{f}^2 \log\left(\frac{R_\mathrm{f}}{R_\mathrm{i}}\right)\right). \tag{3.A10}$$

Defining the fold change in the population size η through $N_\mathrm{f} = \pi R_\mathrm{f}^2 = (1+\eta)\pi R_\mathrm{i}^2 = (1+\eta)N_\mathrm{i}$, we get

$$P_\mathrm{f}^* \approx \frac{\sqrt{s(2+s)}}{2\pi}\left(\log(1+\eta) - \frac{\eta}{1+\eta}\right) \approx \frac{\sqrt{s(2+s)}}{2\pi}\log(1+\eta), \tag{3.A11}$$

where we have assumed $\eta \gg 1$ in the final step. We again define $N_\mathrm{sec} \equiv LP_\mathrm{i}u(s)$, where here $L = 2\pi R_\mathrm{i}$, and obtain the fold change in mutant frequency for radial expansions as

$$R_\mathrm{RE} = (P_\mathrm{f}^*/P_\mathrm{i})\,N_\mathrm{sec} = P_\mathrm{f}^* 2\pi R_\mathrm{i} u(s) \approx \sqrt{s(2+s)}\log(1+\eta)R_\mathrm{i}u(s). \tag{3.A12}$$

Comparing this to the well-mixed result we obtain

$$\frac{R_{\mathrm{RE}}}{R_{\mathrm{WM}}} \approx \sqrt{\frac{2}{s}} R_{\mathrm{i}} u(s) \tag{3.A13}$$

for $0 < s \ll 1$. As in the flat front case, the surfing probability enters in determining the adaptation gain increase of the range expansion compared to well-mixed population. The crucial difference to the flat front case lies in the fact that $R_{\mathrm{RE}}/R_{\mathrm{WM}}$ is independent of N_{f}. It is thus ultimately the number of sectors that elevates the adaptation gain in the radial range expansion over the well-mixed one. Therefore, a detailed understanding of the establishment of sectors is necessary. Previous calculations of the surfing probability in boundary-limited radial range expansions have predicted $u(s) \sim \sqrt{s}$[2], which would remove the dependence of $R_{\mathrm{RE}}/R_{\mathrm{WM}}$ on s. As we have seen in Fig. 1I, this is not the case in our experiments, where we find instead $u(s) \sim s$. This linear dependence is reminiscent of the classical Haldane result, but we show below that this similarity is fortuitous and can in reality be traced back to surface growth properties of colonies.

Validating the minimal model

Our result thus far neglects the fact that the mutant sectors have a larger area than a wild-type sector of the same opening angle because it bulges outward at the colony rim. Numerical estimates of the correction show that this contribution is not always negligible, especially for large s. To improve the calculation, one could account for the fractional area of the circular cap associated with a mutant sector of given opening angle and selective effect. In addition, the sector shape computed above is only valid far from the inoculum, where initial stochastic effects of sector formation no longer impact the shape of the sector. Lastly, in some of our experiments, sectors collide and hence cover a slightly smaller area than if they had grown undisturbed.

Nevertheless, we can compare our experimental data to the theoretical prediction. Fig. 3.A2 (left) shows the final mutant frequency P_{f}^{*} as a function of the number of sectors, for each colony, multiplied by the $\sqrt{s(2+s)}$. The averaged data (black dots), fall on a line, as predicted by Eq. (3.A12).

In addition, our results predict that the ratio $R_{\mathrm{RE}}/R_{\mathrm{WM}}$ of the adaptation gain from a range expansion and uniform growth should scale as $u(s)/\sqrt{s}$. Normalizing by the experimentally measured surfing probability $u(s) \approx N_{\mathrm{sec}}/2\pi R_{\mathrm{i}}$, we recover the predicted scaling $\sqrt{s}$, see Eq. (3.A13) and Fig. 3.A2 (right).

3.5.2 Number of surfing clones

The deterministic calculations for the adaptation gain in range expansions hinge on the likelihood of the formation of sectors. Computing the number of sectors, or "surfing clones", is a stochastic problem that involves the fluctuation statistics of growing microbial colonies. While these fluctuations are complicated to

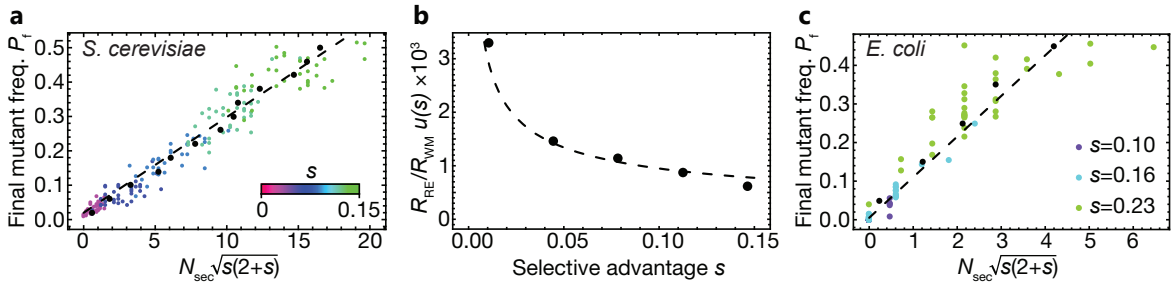

Figure 3.A2: Validating the minimal model with experimental results. (a) Final mutant frequency P_f in *S. cerevisiae* colonies, as a function of $N_{sec}\sqrt{s(2+s)}$, which exhibits the predicted linear scaling (see eq. (3.A12), dashed line). Each dot corresponds to a colony with mutant selective advantage given by the color legend. Black dots are average values over mutant frequency bins of width 0.04. (b) The ratio between R_{RE} and R_{WM}, normalized by the surfing probability of a single clone, as a function of s is consistent with the predicted $\sqrt{s}$ scaling (Eq. (3.A13), dashed line). (c) Final mutant frequency P_f in *E. coli* DH5α colonies, as a function of $N_{sec}\sqrt{s(2+s)}$. Black dots are average values over mutant frequency bins of width 0.1.

derive microscopically, their overall scaling behavior is well understood, allowing us to derive the relationship between the number of sectors, the selective advantage and the initial conditions of the population.

Linear fronts, standing variation

Consider first the case of a linear front with a small initial fraction $P_i \ll 1$ of mutant sites. As the population edge advances, the extinction and growth of a mutant sector will be dominated by genetic drift as long as the lateral size $l_\perp$ of the sector is smaller than some characteristic size $l_\perp^{(sel.)}$. Once a sector has reached this size $l_\perp^{(sel.)}$, selection takes over and it is unlikely that the sector goes extinct (at the front). Thus, we may call $l_\perp^{(sel.)}$ the establishment size for surfing. If we knew $l_\perp^{(sel.)}$ we could estimate the surfing probability by a martingale argument, as follows. Since the dynamics of a sector below size $l_\perp^{(sel.)}$ is neutral, all of the $l_\perp^{(sel.)}$ front ancestors have the same chance to generate a clone that drifts up to size $l_\perp^{(sel.)}$ or larger. Thus, we can estimate the probability $u(s)$ of a mutant clone to surf as

$$u(s) \sim \frac{1}{l_\perp^{(sel.)}}. \tag{3.A14}$$

Since we begin with a fraction of P_i initially mutated sites, we expect a number $N_{mut}u(s) \sim P_i L/l_\perp^{(sel.)}$ of successful surfing events, where L is the length of the front. Note that one has a simple linear dependence on P_i only for small $P_i l_\perp^{(sel.)} \ll 1$. For larger P_i, sectors may overlap when they are still smaller then their establishment length, leading to (predictable) deviations from the observed scaling: The actual number of

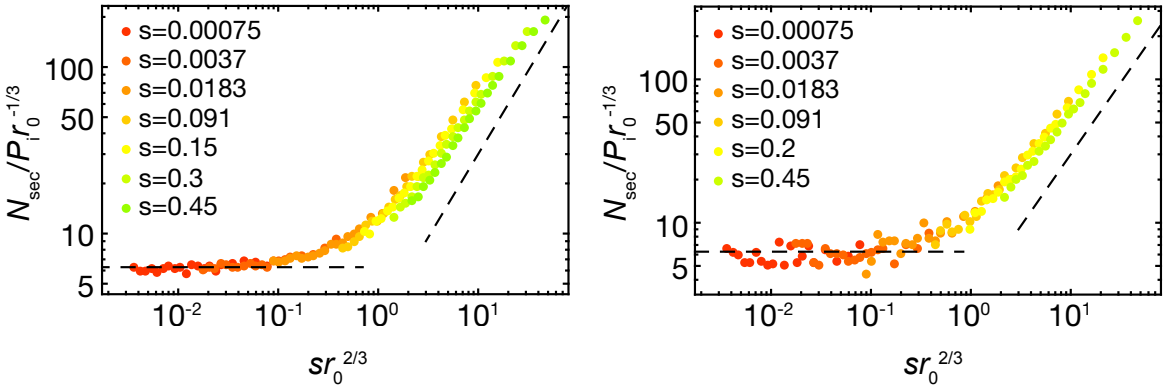

Figure 3.A3: Number of sectors in Eden simulations with standing variation follows a scaling form. Left: Scaling function starting from a droplet of radius r_0. Here, we chose the initial mutant frequency as $P_\mathrm{i} = 0.02$ like in the experiments. Lines are guide to the eye, showing the predicted constant and linear regimes. At large s, deviations from a linear scaling become visible, because sectors inevitably begin to interact. Right: Scaling function for $P_\mathrm{i} = 0.005$, this time grown from a single cell to a population of (average) radius r_0, then inserting mutants at ratio P_i, for a wide range of r_0. The scaling function is virtually indistinguishable from that for flat initial conditions. The plot legend explains the color code for the selective differences.

surfing events will be smaller than estimated.

The establishment length $l_\perp^{\mathrm{sel.}}$, and consequently the number of surfers, is controlled by a competition between selection and genetic drift. The smaller s, the larger the sector needs to become, by chance, for selection to take over genetic drift. Genetic drift in our colonies depends on the roughness properties of the colony edge: The rougher the front, the larger the stochastic evolutionary outcomes are. To estimate the establishment length $l_\perp^{\mathrm{sel.}}$, we need to invoke the universal fractal properties of Eden fronts which are in the Kardar-Parisi-Zhang (KPZ) universality class[4]. Conditional on survival, a neutral sector reaches size $l_\perp$, roughly, after a time of order $l_\perp^{3/2}$, a KPZ prediction that was confirmed in Ref.[5]. Thus, the magnitude of the speed of growth of the width of a sector due to random genetic drift scales as $v_\perp^{\mathrm{drift}} \sim l_\perp / l_\perp^{3/2} = l_\perp^{-1/2}$ (again in units of the wild-type front speed). Selection on the other hand increases a sector width linearly in time according to a constant speed $v_\perp^{\mathrm{sel.}} = \sqrt{s(s+2)}$[3]. Both speeds balance at a length scale of $l_\perp^{\mathrm{sel.}} \sim (s(s+2))^{-1}$. Genetic drift dominates ($v_\perp^{\mathrm{drift}} \gg v_\perp^{\mathrm{sel.}}$) when $l_\perp \ll l_\perp^{\mathrm{sel.}}$ and selection dominates ($v_\perp^{\mathrm{drift}} \ll v_\perp^{\mathrm{sel.}}$) for $l_\perp \gg l_\perp^{\mathrm{sel.}}$. Knowing the establishment length now allows us to predict the scaling of the number of sectors $N_{\mathrm{sec}} \sim P_\mathrm{i} L / l_\perp^{\mathrm{sel.}} \sim P_\mathrm{i} L s(s+2)$.

Radial expansion

To model a circular colony, one has to take into account the effect of "inflation"[2]: As the colony expands, the circumference increases in size. As a consequence, domain boundaries tend to move away from one another at a speed proportional to their current (front) distance, keeping the opening angle of the sector constant. Inflation enables mutations to fix even if they are neutral because, on long times, inflation is a stronger driving force than genetic drift. The speed $v_\perp^{\text{infl.}}$ of inflation of a sector of front size $l_\perp$ is such that it keeps the sector angle $l_\perp/R$ constant. Thus, we have $v_\perp^{\text{infl.}} \sim l_\perp/R$. Balancing this speed of inflation with the speed $v_\perp^{\text{drift}}$ of genetic drift yields another characteristic length $l_\perp^{\text{infl.}} \sim R^{2/3}$. This is the establishment length for a neutral sector: If a neutral sector reaches size larger than $l_\perp^{\text{infl.}}$, it will be protected by inflation from going extinct through genetic drift.

For the case with selection, we expect that if $l_\perp^{\text{infl.}} \ll l_\perp^{\text{sel.}}$, establishment will be effectively neutral as a result of the competition of drift and inflation. If on the other hand we have $l_\perp^{\text{infl.}} \gg l_\perp^{\text{sel.}}$ then surfing is controlled by the competition of drift and selection. This expectation can be summarized by the scaling form

$$N_{\text{sec}} = P_{\text{i}} R/l_\perp^{\text{infl.}} \mathcal{F}_{\text{SV}}\left(l_\perp^{\text{infl.}}/l_\perp^{\text{sel.}}\right) = P_{\text{i}} R^{1/3} \mathcal{F}_{\text{SV}}\left(sR^{2/3}\right), \tag{3.A15}$$

which depends on the initial radius R of the colony and the selective advantage s of the mutations. The scaling function $\mathcal{F}_{\text{SV}}(\xi)$ satisfies

$$\mathcal{F}_{\text{SV}}(\xi) \sim \begin{cases} \text{const. for } \xi \to 0, \\ \xi \text{ for } \xi \to \infty. \end{cases} \tag{3.A16}$$

Our analysis thus predicts that when the selection coefficient is small, the number of sectors will be roughly equal to the neutral number of sectors, scaling as the third root of the initial radius. For larger selection coefficients, on the other hand, the number of sectors will scale like the radius times the selection coefficient s. This analysis is supported by simulations, see Fig. 3.A3.

3D range expansions

The preceding discussion can be extended to the important case of three-dimensional radial range expansions, pertaining to, e.g., growing solid tumors. In 3D, a neutral surviving sector has lateral size $l_\perp$ after a time of order $l_\perp^{1.56}$ (another KPZ prediction[4]). We can estimate the surfing probability of a clone of size l_c by the probability $u(s) \sim (R/l_c)^{-2}$ that a clone from a neutral mutation reaches a solid angle l_c^{-2}. The length scale l_c again arises from the competition between drift, $v_\perp^{\text{drift}} \sim l_\perp/l_\perp^{1.56}$, and selection, $v_\perp^{\text{sel.}} \sim \sqrt{s(2+s)}$ and is given by $l_c \sim (s(2+s))^{-0.89}$. The surfing probability of a mutant with selective advantage s thus

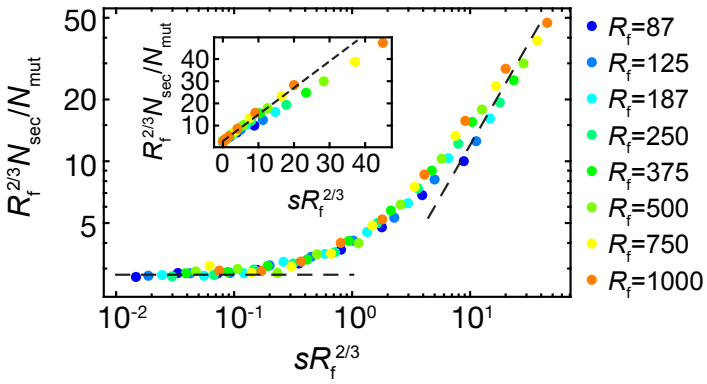

Figure 3.A4: Number of sectors for colonies with de novo mutations obeys a scaling relation, for a wide range of selective advantages s and final radius R_f (see color legend). The number of sectors N_{sec} was computed by only counting mutant clones that were both still present at the front at the end of the simulation and that were born before $R_f/2$. Because sectors inevitably have large areas for large s, we record the actual number of mutations N_{mut} in $R_f/2$ for simulations, which was set to an average of 5 to limit interactions between clones. The scaling function saturates for $\xi \to 0$ and scales as ξ for $\xi \to \infty$ (dashed lines are guides to the eye). The inset shows the same data on linear scale.

scales $u(s) \sim s^{1.79}$. Thus, weakly beneficial mutations have a particularly small changes of surfing in three-dimensional populations.

De novo mutations

So far, we have focused on the number of sectors emerging from a standing variation experiment. One may alternatively consider the situation of a colony growing from a single cell. Mutations occur at a constant rate μ per lattice site. Then, we can follow very similar scaling arguments as for standing variation to arrive at the same scaling form,

$$N_{sec} = \mu R_f \frac{R_f}{l_\perp^{infl.}} \mathcal{F}_{DN}\left(l_\perp^{infl.}/l_\perp^{sel.}\right) = \mu R_f^{4/3} \mathcal{F}_{DN}\left(sR_f^{2/3}\right), \tag{3.A17}$$

however, with a different scaling function $\mathcal{F}_{DN}(\xi)$ satisfying the same asymptotic limits,

$$\mathcal{F}_{DN}(\xi) \sim \begin{cases} \text{const. for } \xi \to 0, \\ \xi \text{ for } \xi \to \infty. \end{cases} \tag{3.A18}$$

Note that the length scale R_f appearing in these equations defines the final radius of the colony.

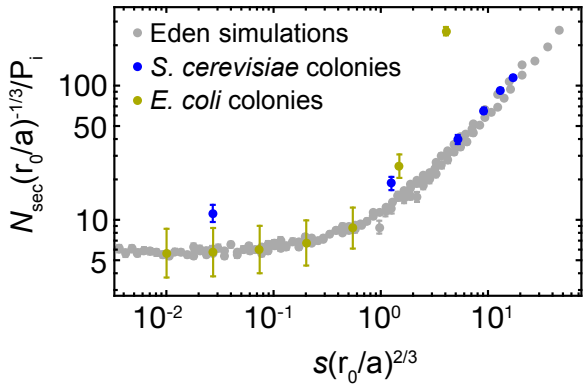

Figure 3.A5: By fitting the experimental data to the scaling relation from Fig. 3.A3, we obtain estimates for the appropriate value of a in our experiments. We find $a = 0.8\mu$m for budding yeast and $a = 12\mu$m for *E. coli*. Note that since the number of sectors in *E. coli* experiments depends roughly exponentially on s, we only fit the constant as $s \to 0$. For the *E. coli* data points, we interpolated from the experimental results to obtain values for small s.

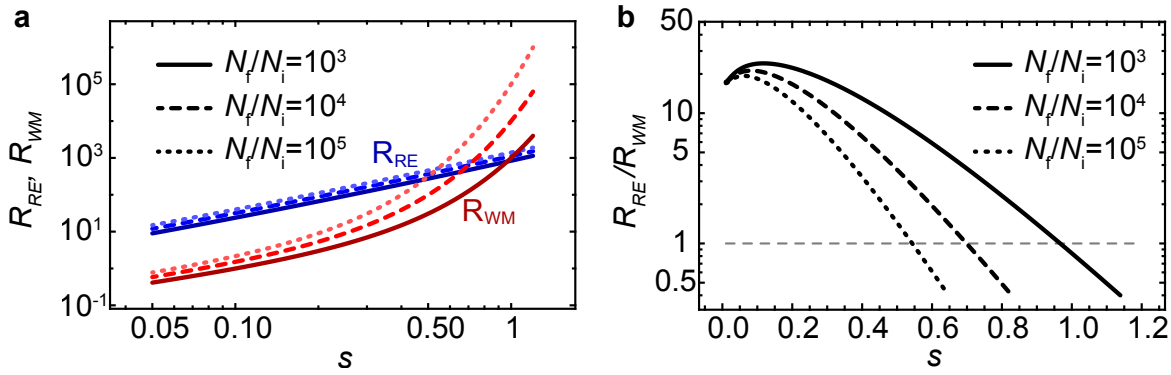

Figure 3.A6: Adaptation gain in range expansions (R_{RE}, Eq. (3.A12)) and uniformly grown (R_{WM}, Eq. (3.A4)) populations. The number of sector was computed from Eq. (3.A19) with $a = 0.8\mu$m. A prefactor of 0.05 was introduced to match the experimentally measured sector size. We find that, for a wide range of parameters, the range expansion gives rise to a higher adaptation gain. In our experimental set-up, we expect the uniformly grown population to become more efficient than the range expansion around $s = 0.7$ (dashed line in **(b)**).

3.5.3 Mapping the Eden model to colonies

The Eden model is, ultimately, a simplified lattice model that aims to capture the coarse behavior of a colony. To map Eden model predictions to an actual colony, one needs to fit the relevant phenomenological parameters. As we will see, the values of these parameters will also tell us to what extent the Eden model may be applicable.

A lattice site has a width and a length. By the rotational symmetry of a colony, we expect that we have to choose, in general different length $a_\parallel$ and $a_\perp$ for the radial and transverse width of a lattice site, respectively. The choice of these lengths leaves selection and inflation unaffected but it influences the strength of genetic drift: Conditional on survival, a neutral sector reaches size $l_\perp$, roughly, after a radial distance of order $a_\parallel(l_\perp/a_\perp)^{3/2}$, as was measured in Ref.[5]. Thus, the magnitude of the speed of growth of the width of a sector due to random genetic drift scales as $v_\perp^{\text{drift}} \sim l_\perp/[a_\parallel(l_\perp/a_\perp)^{3/2}] = (a_\perp^{3/2}/a_\parallel)l_\perp^{-1/2}$. The competition between genetic drift, selection and inflation then leads to the establishment lengths $l_\perp^{\text{sel.}} \sim (a_\perp^3/a_\parallel^2)(s(s+2))^{-1}$ and $l_\perp^{\text{infl.}} \sim (a_\perp/a_\parallel^{2/3})R^{2/3}$, respectively. Applied to an actual colony, the Eden model prediction thus takes the form

$$N_{\text{sec}} = P_{\text{i}}R/l_\perp^{\text{infl.}}\mathcal{F}_{\text{SV}}\left(l_\perp^{\text{infl.}}/l_\perp^{\text{sel.}}\right) = P_{\text{i}}(R/a)^{1/3}\mathcal{F}_{\text{SV}}\left[s(R/a)^{2/3}\right]. \tag{3.A19}$$

This result shows that we have effectively one parameter $a = a_\perp^3/a_\parallel^2$, a "microscopic" length scale, to fit the predictions of the Eden model in the case of standing variation. Nevertheless, it is useful to think of this one length scale as the ratio $a_\perp^3/a_\parallel^2$ of two length scales, because there are natural candidates for the radial and transverse length scales $a_\parallel$ and $a_\perp$. For instance, in the case of yeast, it is natural to choose the radial length to be the thickness of the growth layer and the transverse length simply as a cell diameter – there is no other transverse length scale in this problem. Then one expects $a_\perp^3/a_\parallel^2 < 5\mu$m. This explains then why the fitted microscopic length scale $a = 0.8\mu$m (see Fig. 3.A5) is smaller than a single yeast cell diameter.

In the case of *E. coli* on the other hand, we do have another transverse length scale. Time lapse movies reveal that *E. coli* colonies buckle on length scales of order $a_\perp \approx 20\mu$m. Indeed, the fitted microscopic length scale $a = 12\mu$m is much larger than a single *E. coli* cell.

Once the value of a is known, we can compare the adaptation gain in uniformly grown population and range expansions and find the parameter range for which range expansions are more efficient. Our model predicts for the case of *S. cerevisiae* (Fig. 3.A6) and our experimental parameter range ($a = 0.8\mu$m, $N_{\text{f}}/N_{\text{i}} \approx 10^4$) that range expansions are more efficient up to values of $s < 0.7$, although we do not expect our model to be accurate at such high values of s. Hence, for most experimentally accessible parameters, we expect range expansions to exhibit a higher adaptation gain than well-mixed growth.

In the case of de novo mutations, we obtain the growth layer width λ as an additional parameter, since

only mutations arising at the front are able to surf. Hence,

$$N_{\text{sec}} = \frac{\mu R_{\text{f}}}{\lambda}(R_{\text{f}}/a)^{1/3}\mathcal{F}_{\text{DN}}\left[s(R_{\text{f}}/a)^{2/3}\right]. \tag{3.A20}$$

Note that, in the de novo mutation case, one has to measure both the mutation rate, growth layer width and roughness length scale to obtain predictions from the Eden model.

Limits of the coarse-grained Eden model

Our coarse-grained lattice model is a meta-population model, meaning that each lattice site represents a subpopulation of cells. The size N_{e} of those subpopulations can be estimated once we have determined the linear dimensions $a_{\parallel}$ and $a_{\perp}$ of a lattice site (see previous paragraph). Thus, we may estimate $N_{\text{e}} \approx a_{\parallel}a_{\perp}/A_{\text{cell}}$, which amounts to 2.5 and 200 in the cases of budding yeast and *E. coli*, respectively.

The parameter N_{e} allows scrutinizing a precondition for the applicability of our coarse-grained model. If, for a given selective advantage, N_{e} is too large, we cannot assume that mutants will fix in a subpopulation with probability equal to their current ratio. This is assumed when we set the mutation rate in the Eden model equal to the mutation rate of single cells. The same assumption is made in the case of standing variation, when we assume that the initial fraction of mutant lattice sites is equal to the initial frequency of mutant cells. If subpopulations behaved like well-mixed sub-populations, for instance, we would have to require $N_{\text{e}}s \ll 1$. Note that this condition is strongly violated in our *E. coli* experiments. For $N_{\text{e}}s \gg 1$, the effective mutation rates as well as the initial frequencies would have to be multiplied by $N_{\text{e}}s$. Since, however, our populations are manifestly spatial, it is not clear how a more microscopic model would behave. Therefore, we also implemented more explicit simulations that take into account the shape and steric interaction between cells (described in detail below).

3.5.4 Analysis of long-range jumps

We extend our meta-population by allowing for long-range jumps in each step. The rationale behind introducing long-range dispersal is that well-mixed growth and colonies are natural opposites in that they feature no and strong spatial correlations and mixing. Long-range jumps allow for a breaking of spatial correlations and thus lie in between these two cases. We then also expect the adaptation efficacy to interpolate between the colony and the well-mixed case as the likelihood of long-range jumps increases.

As described in the Methods section above, we can vary the likelihood of large jumps by tuning the parameter μ. Hallatschek and Fisher[1] showed that the expansion speed of a growing population, in terms of its range, depends on the parameter $\delta = \mu - d$, where d is the spatial dimension. If $\delta > 0$, the range of

the population grows as a power-law, while for $\delta < 0$, long-range jumps are frequent and the range of the population grows as a stretched exponential.

Introducing mutants with selective advantage s at initial frequency $P_\mathrm{i} = 0.02$, we studied the influence of dispersion range on the efficiency of adaptation. The naive expectation would be that in the limit of short-ranged jumps, adaptation should be as efficient as in the classical Eden model, whereas long-range jumps increase the mixing of the population such that adaptation becomes less efficient, asymptotically becoming well-mixed.

Fig. 3.A7 shows examples of populations grown from $N_\mathrm{i} = 10^3$ to $N_\mathrm{f} = 10^6$ for different values of μ and s. We observe that the final frequency of the mutants increases with s, as expected, but does so much more strongly when μ is large. As μ increases, the populations become increasingly patchy, with mutants primarily residing in confined spatial regions. For $\mu = 5$, we even observe sectors very much like in Eden simulations. Fig. 3.A8 shows the results of 750 simulations for each set of parameters (μ, s). We see indeed that the average final frequency of mutants increases as long-range jumps become increasingly rare. Thus, long-range jumps can hinder adaptation from standing variation even in spatially structured growing population because they effectively induce mixing which allows previously trapped clones to continue to grow, allowing for fewer generation to happen at the very front (for fixed final population size).

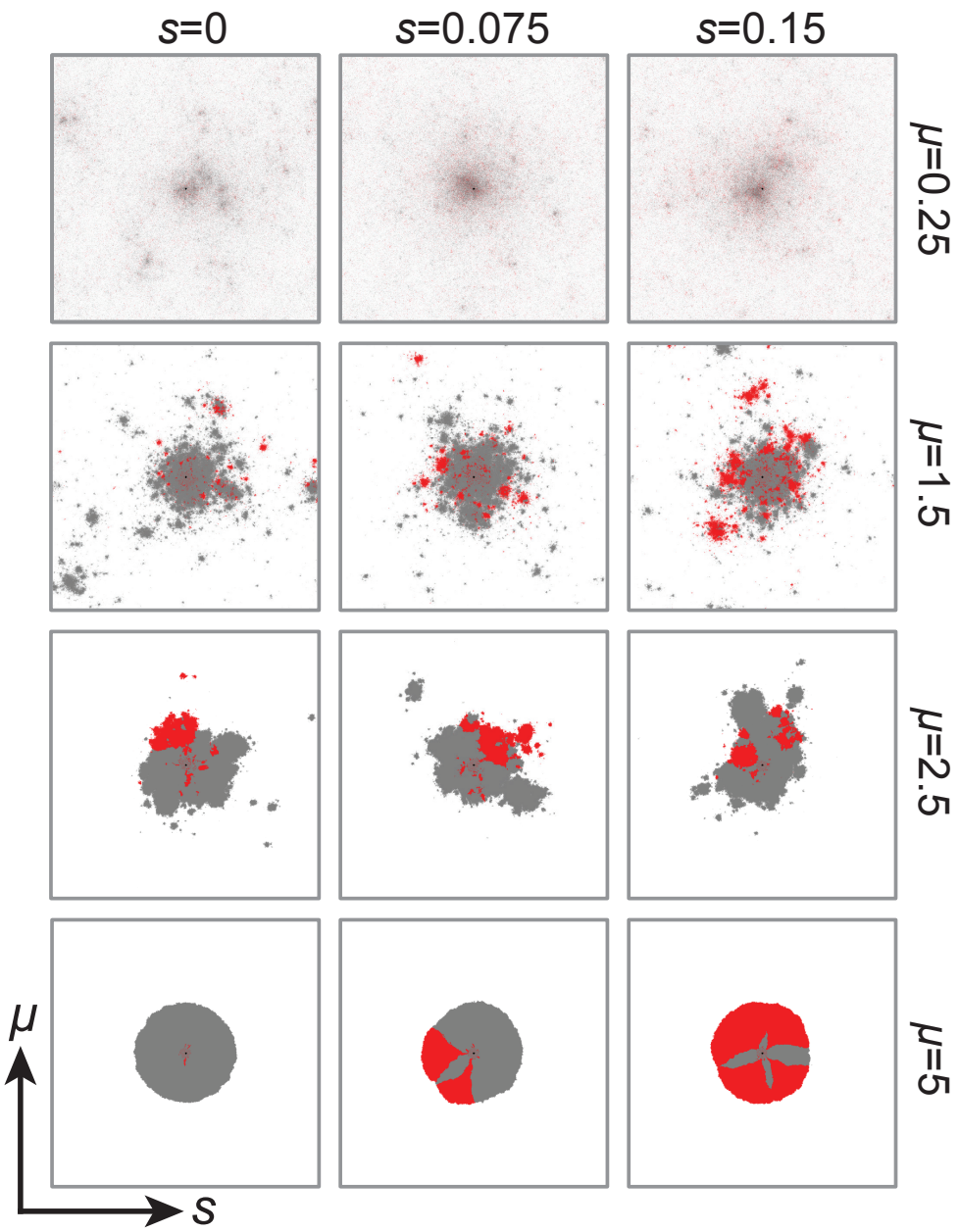

Figure 3.A7: Examples of populations undergoing range expansions with long-range dispersal. Different selective advantages s of the mutants (shown in red) over the wild type (gray) are shown as the columns. Varying the "spread" coefficient μ (rows), we obtain almost well-mixed populations for small μ (when large jumps are common), while sectors emerge for very large μ (when practically no large jumps occur). For intermediate μ, mutants accumulate in patches that resemble sectors more and more as μ increases. The larger μ, the higher the mean final mutant frequency, as shown in Fig. 3.A8.

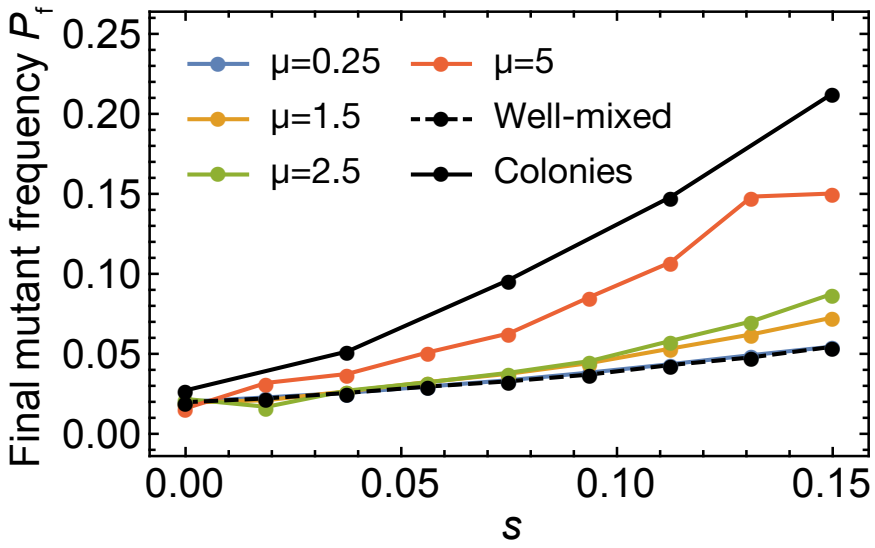

Figure 3.A8: Final mutant frequency in populations grown with varying degrees of dispersal. All populations grown from $N_\mathrm{i} = 10^3$ to $N_\mathrm{f} = 10^6$ with a starting fraction of $P_\mathrm{i} = 0.02$. Populations with long-range jumps show adaptation efficiency intermediate between well-mixed and strictly short-ranged range expansions (Eden model). For $\mu \ll \delta$, the final mutant frequency becomes indistinguishable from the well-mixed case. Results obtained by averaging over 750 simulations.

Parameter	*E. coli*-like (long) cells	Yeast-like(short) cells
Diffusion constant D $\left[\mu\mathrm{m}^2/\mathrm{h}\right]$	500	500
Initial nutrient concentration [a.u.]	1	1
Nutrient uptake rate κ [a.u./h]	1.5 or 1.8	4
Young modulus E [kPa]	100	500
Minimal division time T [min]	40	120
Cell diameter [μm]	1	4
Minimal length [μm]	2.5	0
Damping coefficient ζ [10^{16} h^{-1}]	65	65
Friction coefficients	$k_\perp = 4, k_\parallel = 0.25$	$k_\perp = k_\parallel = 1$
Width of simulation box L [μm]	340, 640	320, 640, 1280

Table 3.A1: Parameters of the off-lattice model.

3.5.5 Individual-based simulations: method and results

Model description

In order to develop a microscopic understanding of the surfing process, we used a model based on that used in Ref. [6], with a few modifications. Our model strikes a balance between computational cost, limited knowledge of the nature of mechanical interactions between cells in microbial colonies, and the reproduction of experimental observations made in this work.

All cells are modeled as sphero-cylinders of variable length l and identical radius r_0. Cells interact mechanically through Hertzian repulsion: $F = \frac{4}{3} E r_0^{1/2} h^{3/2}$ where F is the repulsive force, E is the effective Young modulus of the cell, r_0 is the radius and h is the overlap between interacting cells. The dynamics of the cells is described by the overdamped Newton equations of motion:

$$\frac{\mathrm{d}}{\mathrm{d}t}\vec{r} = \frac{K^{-1}\vec{F}}{m}, \tag{3.A21}$$

$$\frac{\mathrm{d}}{\mathrm{d}t}\varphi = \frac{\tau}{\zeta J}. \tag{3.A22}$$

Here, $\vec{r}$ is the position of the cell's center of mass, φ is the angle the cell with the x-axis, $\vec{F}$ is the total force, τ is the total torque acting on the cell, m is the mass, J is the momentum of inertia of the sphero-cylinder,

Quantity	*E. coli*-like (long) cells		Yeast-like(short) cells
	$\kappa = 1.5$	$\kappa = 1.8$	$\kappa = 4$
Thickness of the growing layer λ [μm]	31	25	95
Roughness of the growing layer σ [μm]	12	15	3.6
Speed of the growing layer [μm/h]	26	23	31
Average area $\langle A \rangle$ per cell [μm^2]	1.7	2.0	15.6
Average linear size a of cell [μm]	1.3	1.4	4.5
Thickness of the growing layer λ/a [cells]	24	18	24

Table 3.A2: Steady-state properties of the growing layer.

and ζ is the damping (friction) coefficient. The matrix K

$$K = \zeta \begin{bmatrix} k_{\parallel} n_x^2 + k_{\perp} n_y^2 & (k_{\parallel} - k_{\perp}) n_x n_y \\ (k_{\parallel} - k_{\perp}) n_x n_y & k_{\perp} n_x^2 + k_{\parallel} n_y^2 \end{bmatrix} \tag{3.A23}$$

takes into account the possible anisotropy of friction between the cell and the surface: $k_{\perp}$ is the damping coefficient in the direction perpendicular to cell's major axis, $k_{\parallel}$ is the damping coefficient in the parallel direction, and $\vec{n} = (\cos\varphi, \sin\varphi)$. For isotropic friction, $k_{\perp} = k_{\parallel}$, and the matrix K reduces to the identity matrix times the friction coefficient. To model cells which prefer to roll rather than to slide we set $k_{\perp} < k_{\parallel}$, whereas for cells that prefer to slide along the major axis it holds that $k_{\perp} > k_{\parallel}$. In particular, for "yeast-like" cells we assume isotropic friction, whereas for "*E. coli*-like" cells we set $k_{\perp} > k_{\parallel}$. This replicates experimentally observed long "chains" of aligned cells and high surface roughness of *E. coli* colonies.

Cells consume nutrients diffusing in the 2D substrate beneath the colony of cells. The concentration $c(\vec{r}, t)$ of the nutrient evolves in time as

$$\frac{\partial c}{\partial t} = D \left(\frac{\partial^2 c}{\partial x^2} + \frac{\partial^2 c}{\partial y^2} \right) - \kappa \sum_i \delta \left(\vec{r}_i - \vec{r} \right), \tag{3.A24}$$

where D is the diffusion constant, κ is the nutrient uptake rate and $\{\vec{r}_i\}$ are the positions of the cells. We assume that cells elongate at a constant rate as long as the local nutrient concentration is larger than 2% of the initial concentration, and divide when they double in length. The length of individual cells thus increases linearly in time in our model. Although this is not true for real microorganisms[7,8], deviations from linear growth are not important for the population level we are concerned with.

We model faster-growing mutants by increasing both the elongation rate and the nutrient uptake rate by $1 + s$, where s is the selective advantage of the mutant over the wild type.

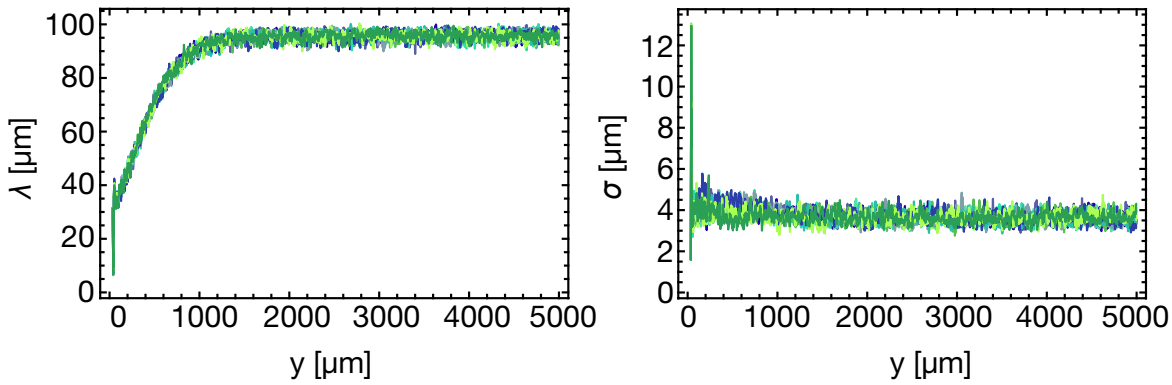

Figure 3.A9: Run-in period of off-lattice simulations. Thickness λ and roughness σ of the growing layer for "yeast-like" cells, for 10 simulation runs (different colors).

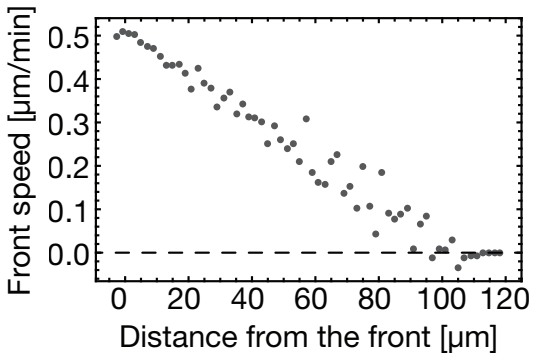

Figure 3.A10: Average speed of cells at a given distance from the colony front for simulated "yeast-like" cells.

To reduce computation time we simulate only a narrow strip of width L at the front of the colony, with periodic boundary conditions in the direction perpendicular to the direction of growth, and fix cells which lag behind the growth layer.

All parameters are listed in Table 3.A1. The assumed values have been chosen to make simulations computationally feasible while at the same time to approximately reproduce experimental observables: the average cell size, the velocity of the moving front, and the thickness of the growth layer. For example, the trade-off between speed and realism required the diffusion constant to take an unrealistically small value.

Characterization of the properties of simulated colonies

We define the growth layer as the layer at the colony front in which cells were replicating. We calculated the thickness λ of the growth layer as the average of the shortest distances between cells at the very front of the

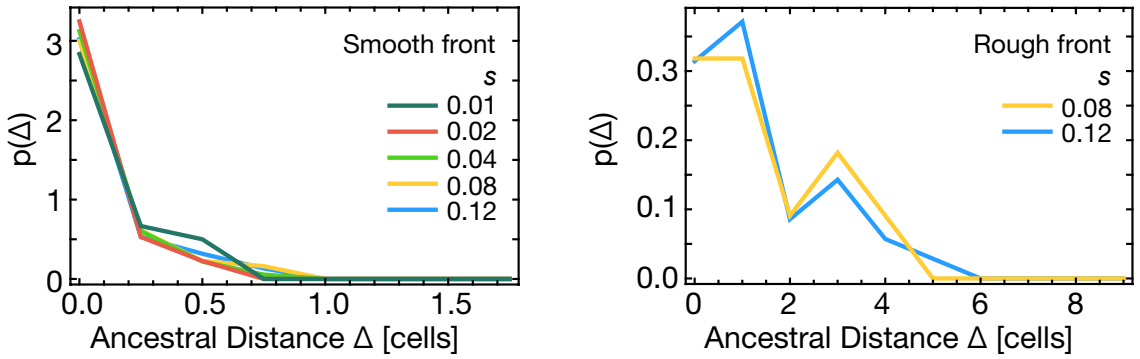

Figure 3.A11: The probability density that a lineage originated at distance Δ from the front (cell lengths) given that it fixed in the growing layer, for different selective advantages ($s = 1\%,\ 2\%,\ 4\%,\ 8\%$ and 12%). Left: "yeast-like" cells. The probability is concentrated at the very first line of cells, almost independently of selective advantage. Right: "*E. coli*-like" cells. The distribution is slightly broader but still concentrated around $\Delta = 0$.

growth layer (first line of cells) and the last layer of cells towards the bulk still exhibiting growth.

The roughness σ was defined as the square root of the mean square deviation of the front height $y(x)$, where $y(x)$ corresponds to the envelope of the front, with resolution 1μm. The speed of the front was obtained by fitting a straight line to the average position of the front $\overline{y}(t)$.

Fig. 3.A9 shows that the thickness and the roughness of the growing layer stabilize after some time. The steady-state values are given in Table 3.A2. The table also shows the average cell size determined as the area of the growing layer divided by the number of cells. This is the actual size taken by the average cell; mechanical compression due to growth causes this area to be slightly lower than the average area of an isolated spherocylinder as determined by the parameters from Table 3.A1.

We also computed the average linear cell size a as the square root of the average area, $a = \langle A \rangle^{1/2}$. This enabled us to express the thickness of the growing layer in cell lengths as λ/a. We adjusted the parameters of the model for "yeast-like" and "*E. coli*-like" cells such that λ/a was approximately the same for both types of cells.

The speed of the cells in the growing layer is a linear function of the distance from the front (Fig. 3.A10). This replicates well the experimentally observed behavior (Fig. SIE 8). We note that in our experiments cessation of growth in the center of the colony and the emergence of the growing layer may be due to the accumulation of waste rather than nutrient exhaustion. However, as demonstrated in Ref.[6], the behavior of the model is similar regardless of whether growth is limited by nutrients or waste products, and that in both cases growth becomes confined to a thin layer after an initial period of exponential growth, in agreement with what is observed experimentally.

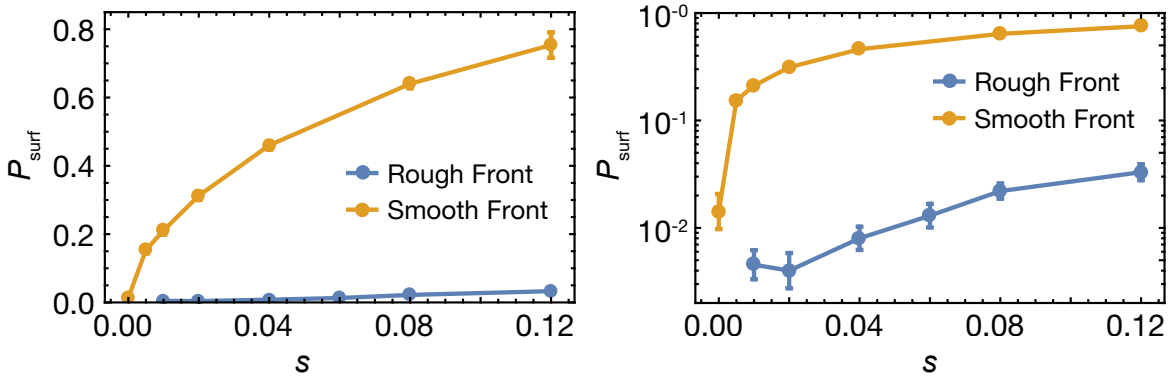

Figure 3.A12: Left: Surfing probability P_{surf} versus selective advantage s for "yeast-like" cells ("smooth front", orange) and "*E. coli*"-like cells ("rough front", blue. Here, $\kappa = 1.8$). Smooth fronts deviate from a line only by about 1 cell diameter, while rough fronts exhibit a roughness of about 10 cell diameters. Parameters and measured characteristics of the populations are given in Tables 3.A1 and 3.A2. Mutants were introduced only into the first layer of cells. The surfing probability P_{surf} decreases with increasing roughness, but increases with selective advantage. Right: the same plot with a logarithmic scale.

Surfing probability at the front and distribution of ancestor location

To determine the surfing probability P_{surf} of mutants with different selective advantages we first ran simulations in which mutant cells were randomly inserted into a steady-state growing layer. We ran between 1000 and 10000 simulations and calculated P_{surf} as the proportion of runs in which the mutant fixed in the growing layer. We also determined P_{surf} for mutants appearing at different distances from the front.

Our results show that P_{surf} is very small even for quite large selective advantage $s = 0.12$: $P_{\text{surf}} = 0.004$ for "*E. coli*-like" cells and $P_{\text{surf}} = 0.015$ for "yeasts-like" cells for parameters as in Table 3.A1. Fig. 3.A11 shows that the surfing probability quickly decreases with the distance Δ from the front of the first (founder) mutant cell.

We then ran simulations with mutants inserted only in the first line of cells. Fig. 3.A12 shows that "yeast-like" cells have a much larger P_{surf} than "*E. coli*"-like cells. Since the two cases differ in the roughness of the growing layer (c.f. Table 3.A2), we hypothesized that roughness is the main factor affecting the amount of genetic drift. To test this, we simulated "*E. coli*"-like populations with reduced roughness – this was achieved by decreasing the nutrient uptake rate (Table 3.A2). We indeed observed an increase in P_{surf}, in accordance with our hypothesis.

3.5.6 Supplementary discussion: Dynamics behind the front

In our experiments, change in local allele frequencies occurs only directly at the front, and our analysis above reflects this fact. While true for non-motile microbes, our arguments arguably extend to other cases where spatial arrangements are mostly conserved, e.g., biofilms and to some extent, solid tumors. However, our results are valid more generally, independently of whether sectoring is neutral or beneficial, as long as the front advances faster than the blurring of the sectors occurs. However, if there is mixing behind the front, any spatial inhomogeneity in local allele frequencies will eventually be blurred out.

Blurring of neutral sectors

If individuals can move randomly behind the front, existing sector boundaries will undergo diffusion and thus have a characteristic width w scaling as $w(t) \sim \sqrt{t}$. The front, however, advances at constant speed and hence the front position $r(t) \sim t$. Hence, on long time-scales, the advancement of the front is much faster than the blurring of sectors, and sector boundaries will remain sharp near the advancing front.

Beneficial sectors behind the front

After the front has passed, beneficial sector will slowly blur due to diffusion, but may also widen or shrink as the beneficial mutants compete with the wild type in the bulk. Even if the mutants exhibit a growth rate advantage at the front, there is not a priori reason to assume that the same is true in the bulk, where other characteristics than maximum growth rate may be more important. For example, a more efficient use of nutrients in poor growth environments (like the bulk of a colony) may prove to be more advantageous than the ability to outgrow one's competitors when nutrients are abundant.

References

[1] O. Hallatschek and D. S. Fisher. Acceleration of evolutionary spread by long-range dispersal. *Proceedings of the National Academy of Sciences*, 111(46):E4911–E4919, 2014.

[2] O. Hallatschek and D. R. Nelson. Life at the front of an expanding population. *Evolution*, 64(1): 193–206, 2010.

[3] K. S. Korolev, M. J. Müller, N. Karahan, A. W. Murray, O. Hallatschek, and D. R. Nelson. Selective sweeps in growing microbial colonies. *Physical biology*, 9(2):026008, 2012.

[4] M. Kardar, G. Parisi, and Y.-C. Zhang. Dynamic scaling of growing interfaces. *Physical Review Letters*, 56(9):889, 1986.

[5] O. Hallatschek, P. Hersen, S. Ramanathan, and D. R. Nelson. Genetic drift at expanding frontiers promotes gene segregation. *Proceedings of the National Academy of Sciences*, 104(50):19926–19930, 2007.

[6] F. Farrell, O. Hallatschek, D. Marenduzzo, and B. Waclaw. Mechanically driven growth of quasi-two-dimensional microbial colonies. *Physical review letters*, 111(16):168101, 2013.

[7] W. Donachie, K. Begg, and M. Vicente. Cell length, cell growth and cell division. *Nature*, 264(5584): 328, 1976.

[8] M. Osella, E. Nugent, and M. C. Lagomarsino. Concerted control of escherichia coli cell division. *Proceedings of the National Academy of Sciences*, 111(9):3431–3435, 2014.

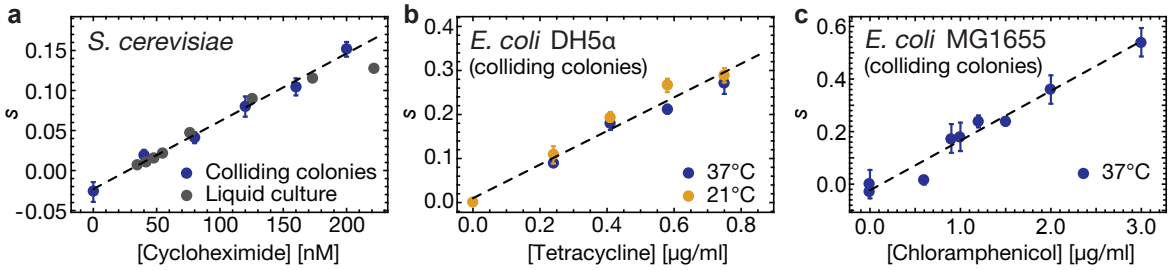

Figure 3.B1: Selective advantages s between resistant and sensitive strains as function of drug concentration for *S. cerevisiae* and *E. coli* for different assays and conditions. (a) Budding yeast strains with W303 background (yMM9 and yJHK111) used in Fig. 1. Best linear fit is shown and used throughout the paper. Liquid culture fitness measurements (3 replicates from the same initial culture per data point, gray dots) over 60 generations agree with the colliding colony result (blue dots) for a range of cycloheximide concentrations. (b) *E. coli* DH5α competition (strains eOH2 and eOH3) on plates with different concentrations of tetracycline at 37°C (blue data points) and 21°C (yellow data points) using the colliding colony assay. Temperature had no significant impact on the relative fitness of the two strains. Best fit is shown through combined data and used throughout the paper. (c) *E. coli* strain MG1655 competed against strain SJ102 at different concentrations of chloramphenicol, measured using the colliding colony assay, with linear best fit. All error bars are standard error of the mean (about 20 replicates per data condition, except for well-mixed competition).

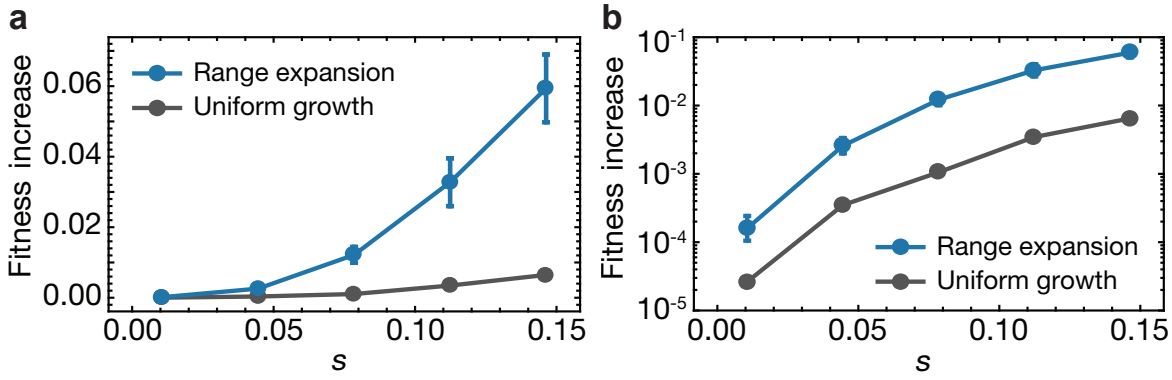

Figure 3.B2: Increase in mean fitness, defined as $\overline{\Delta W} = (P_\mathrm{f} - P_\mathrm{i})s$, computed from the final mutant frequency P_f measured in Fig. 1h, with linear (a) and logarithmic axis (b). Range expansions leads to a higher increase in mean fitness than uniform growth to the same final population size.

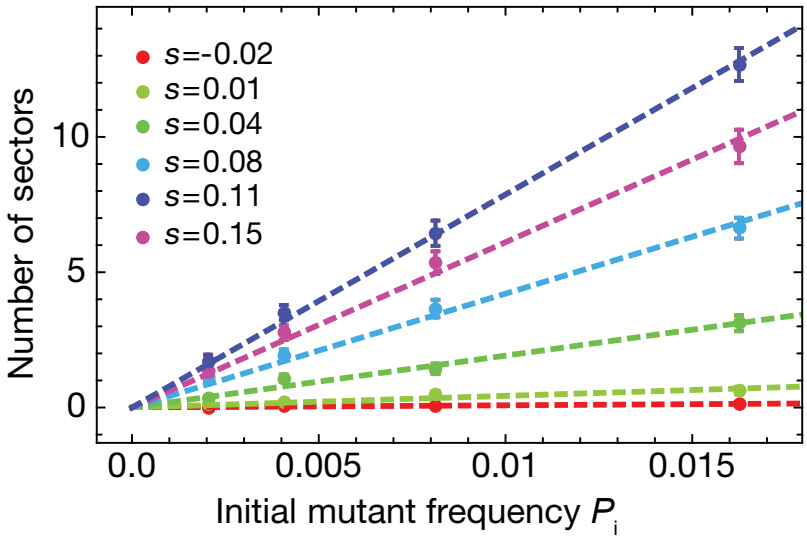

Figure 3.B3: Number of sectors N_sec counted in yeast colonies at different initial mutant frequencies P_i and selective advantages s. The proportionality of sector number and initial mutant frequency implies that sectors arise independently for small enough fractions. Points are averages from 30 colonies per condition, error bars correspond to the standard error of the mean.

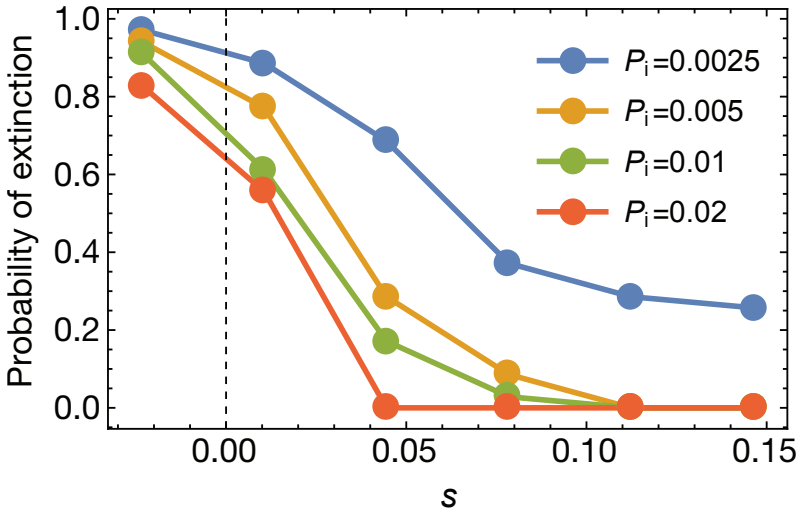

Figure 3.B4: Probability of extinction, defined as the probability of having zero sectors at the front, in yeast colonies for a variety of initial mutant frequencies P_i and selective advantages s (35 colonies from same initial culture per data point).

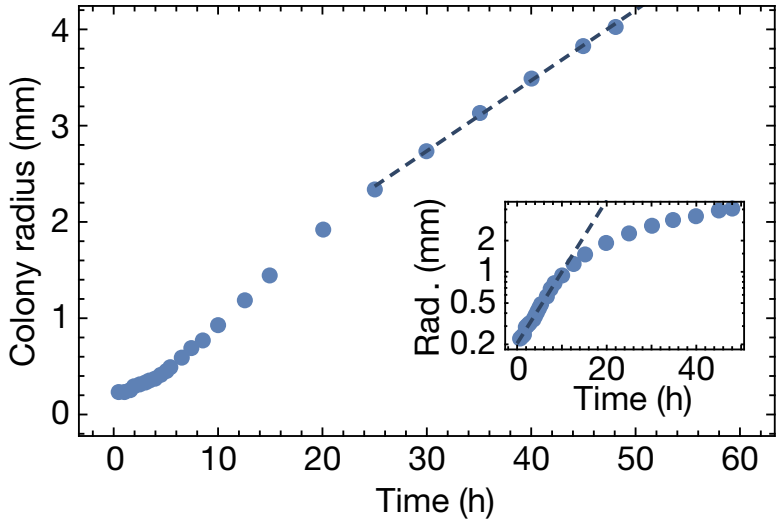

Figure 3.B5: Two regimes of yeast colony radius growth. Colony radii extracted from a time lapse movie of a growing yeast colony. Single yeast cells were inoculated onto an agar plate and grown for about 12 hours. Once microcolonies were detectable, the agar plate was transferred to a stage-top incubator and the colony was imaged in bright-field and fluorescence light every 30 minutes. Initially, the colony radius growth exponentially, indicating that the radius of the colony is not yet larger than the eventual growth layer thickness of the colony. For late times, the colony radius grows linearly in time, which can be interpreted as a growth layer of constant final thickness.

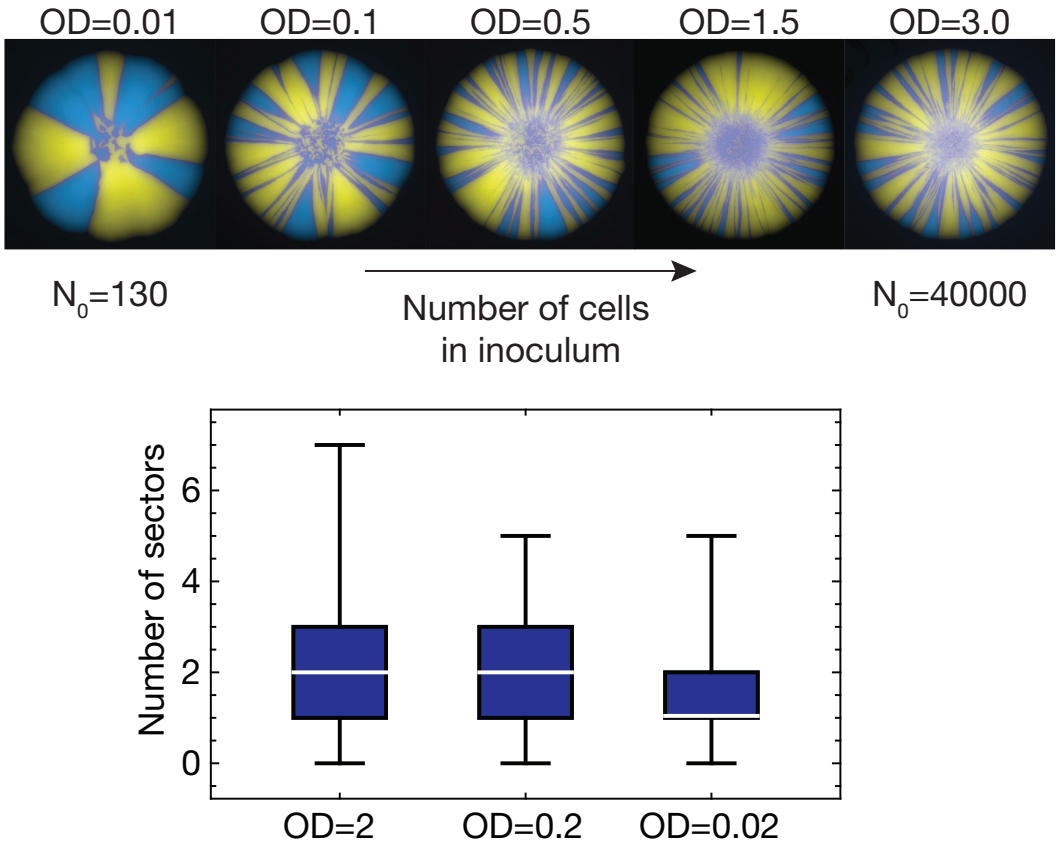

Figure 3.B6: Number of sectors for different number of cells in inoculum. Top: Example images show the change of population patterning with increasing cell number in the inoculum. Here, we mixed two selectively neutral *S. cerevisiae* strains (yJHK111 and yJHK112) at an initial ratio of $P_\mathrm{i} = 0.5$. For large cell number N_0 the population pattern does not change when increasing N_0 further. (Bottom) Number of sectors measured in standing variation assays for different inocula, for the same strains. We assayed 50 neutral colonies with an initial ratio of $P_\mathrm{i} = 0.01$ per dilution, allowing us to count individual sectors. We found no significant difference in sector numbers when diluting a typical culture (OD=2 in the figure, corresponding to about 30000 cells in a 2μl droplet) by a factor of 10 ($p > 0.05$, Mann-Whitney U-test). Dilution by another factor of 10 showed again no significant difference to the intermediate case (first 10-fold dilution), but did show a significant difference ($p < 0.05$) to the original case . Taken together we conclude that the number of sectors is not sensitive to density of the initial culture, given that the inoculum contains at least about 1000 cells in a 2μl droplet. This means that typical pipetting errors or a small change in cell densities of the culture mixtures, which we estimate to be in the range of at most 10 per cent, should have no impact on the number of sectors. The observations can be understood from Fig. 3: Only cells at the front have a chance to surf, and in our experiments, the front is imposed as an initial condition by the drying inoculum. Hence, as long as the cells in the droplet form a continuous ring of cells (such that at every point of the ring there is a defined front), the number of cells in the bulk of the inoculum plays no role in the future fate of the colony.

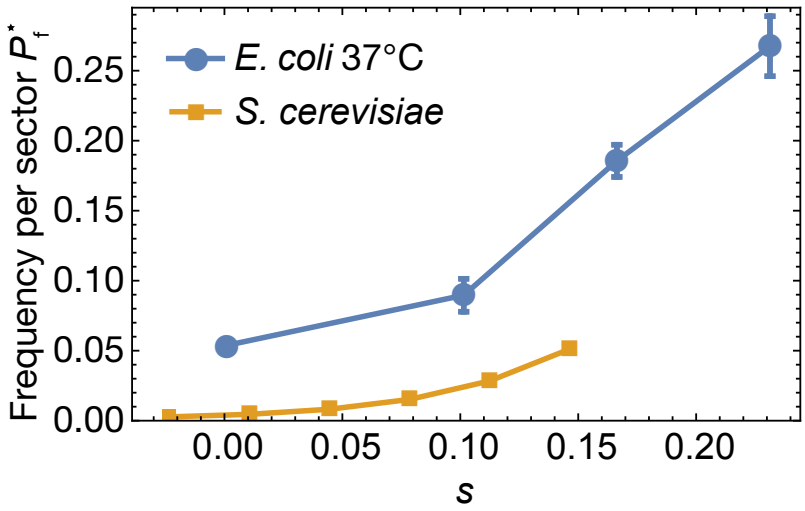

Figure 3.B7: Frequency per sector for *E. coli* DH5α grown at 37°C (blue dots, see also Fig. 4f) together with corresponding data for *S. cerevisiae* (data as in Fig. 1j). Only individual, non-interacting sectors were selected for analysis. Each individual sector is much larger in (relative) size in *E. coli* than in *S. cerevisiae* colonies. In fact, a yeast sector at the highest assayed selective advantage has a relative size comparable to a neutral *E. coli* sector. Error bars are standard errors of the mean, from about 20 sectors per selective advantage s.

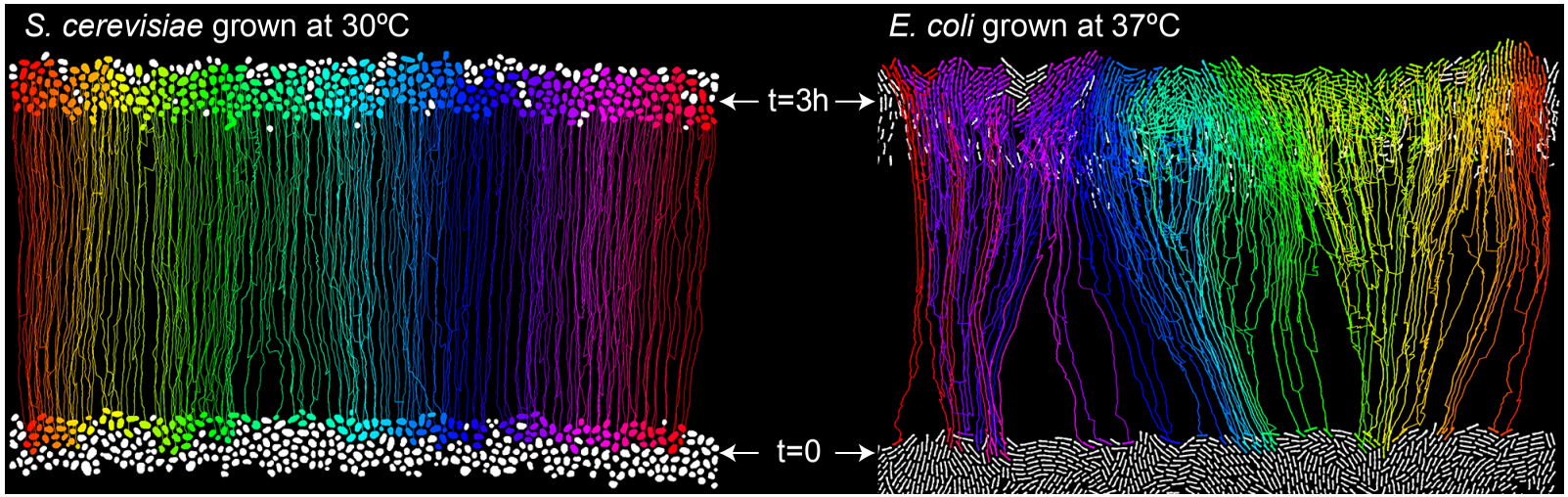

Figure 3.B8: Tracking of individual cell dynamics in *S. cerevisiae* and *E. coli* front reveal microscopic motion patterns. *S. cerevisiae* and *E. coli* fronts tracked for 3 hours (full images from Fig. 3). Shown are the front of each colony at the start of the experiment (*t=0*) and after 3 hours. All tracked lineages and cells are colored. White cells at the top could not be tracked, while white cells at the bottom have no tracked descendants at the front after 3 hours.

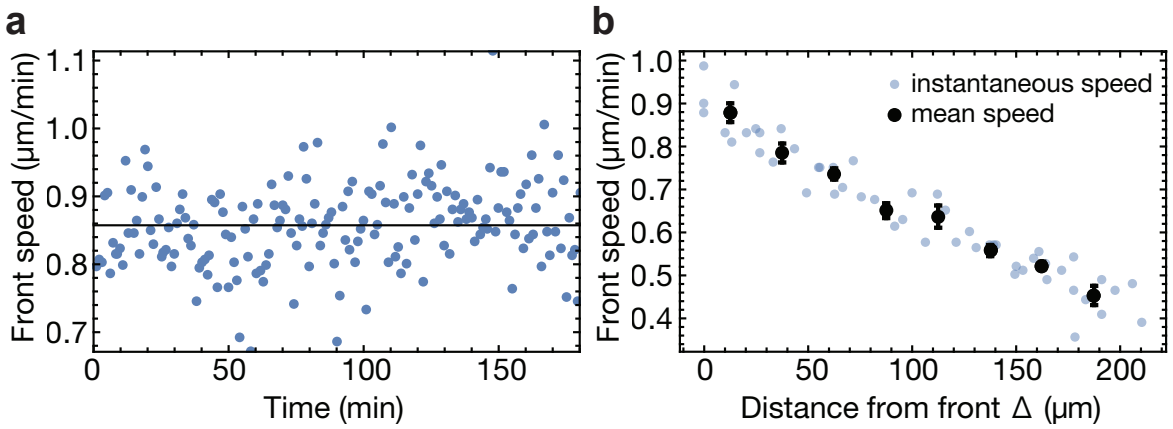

Figure 3.B9: Overall front speed and speed of individual cells at and behind the front for *S. cerevisiae*. A. Instantaneous front speed, defined as the difference in mean front position in each frame, and time average (solid line). The front speed in a *S. cerevisiae* colony is constant over at least three hours (from SI movie 1, see also Fig. 3.B5). B. Speed of individual cells as a function of distance from the front. Speed was measured by visually following 16 individual cells, initially a distance Δ behind the front, and recording their position every 30 minutes for 90 minutes. Instantaneous speed was computed by dividing the relative change in position by 30 minutes. Here, Δ is the distance from the front at the beginning of each 30 minute interval. For the mean speed, data were binned in 25μm intervals. An approximately linear decrease in speed implies near-constant growth rate at least 200μm into the bulk of the colony.

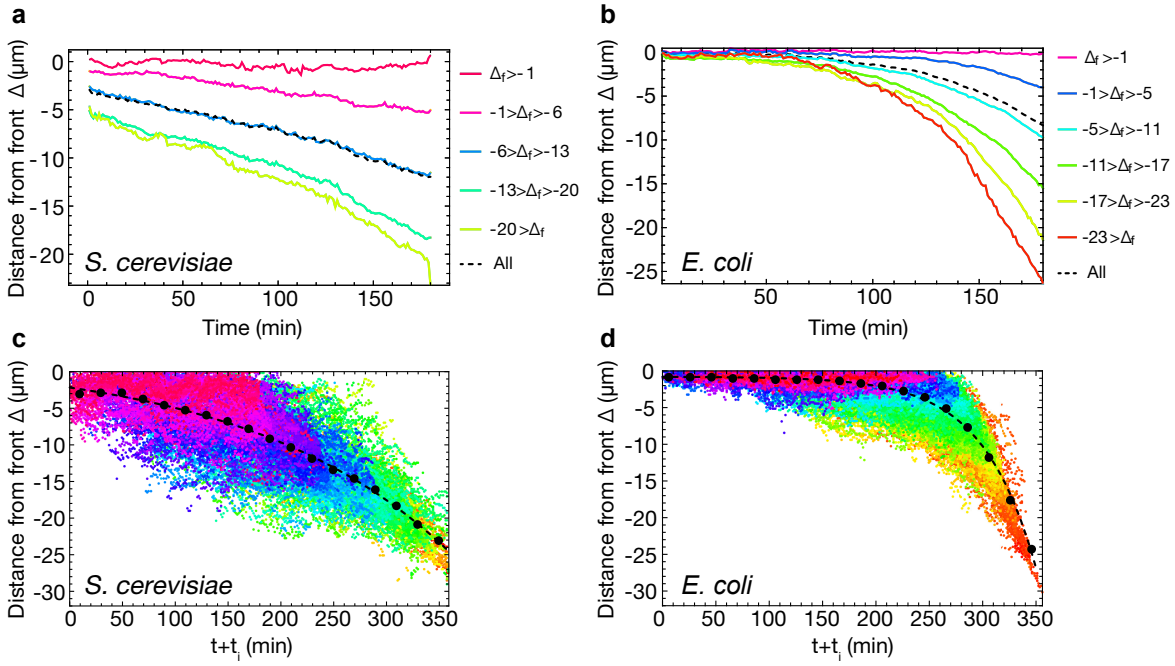

Figure 3.B10: Dynamics of lineages at and behind the front, extracted from SI movies 1 and 2, for *S. cerevisiae* and *E. coli*. Front position was recorded at every time point, and the distance to the front computed for all cells. For (a) & (b), cell trajectories were pooled together depending on their final distance Δ_f from the front at the end of the movies (see color legends). Over time, all cells falls behind the front on average, except those that remain directly at the front until the end (for these cells, $\Delta_f > -1$).

To understand the dynamics of cells falling behind the front, we assumed that exterior parameters did not change over the course of the experiment and that therefore, only time differences should matter. This would imply that at any given time, the distance from the front should determine future dynamics (except for cells directly at the front). In (c) and (d), we show the distance Δ from the front of each cells (color scheme as in (a) and (b), respectively), shifted such that the final distances Δ_f from the front of each cell's trajectory overlapped with the cell trajectory with the largest Δ_f (shown in red). Binning over intervals of 20 minutes reveals the average dynamics of cells falling behind the front (black dots): the distance Δ to the front increases exponentially (fit, dashed line) in time, independently of position, except for cell that "surf", i.e., stay at the front for the full duration of the experiment, shown in magenta. From the shifted cell trajectories, we extracted the histograms of initial distance to the front of cells, conditional on surfing. For the histograms in Fig. 3, we pooled cell trajectories with $t + t_i < 10$min and $t + t_i < 75$min for *S. cerevisiae* and *E. coli*.

3.7 Appendix C – Experimental methods

3.7.1 Strains

S. cerevisiae – competition experiments

To perform population growth experiments, we used strains yJHK111 ('wild type yellow strain',[1]), yJHK112 ('wild type red strain',[1]), and yMM9 ('red mutant strain', unpublished, courtesy of Melanie J. I. Müller). All three strains have a W303 background (common genotype *MATa bud4Δ::BUD4(S288C) can1-100*, see Table 3.C2 for details). yJHK111 expresses the yellow fluorescent protein ymCitrine, yJHK112 expresses the red fluorescent protein ymCherry. yMM9 expresses ymCherry, but is also resistant to cycloheximide (CHX) via mutation *Q37E* in gene *CYH2* (while yJHK111 and yJHK112 are sensitive). Experiments with tunable selection were performed using the pair yJHK111 and yMM9 with a variable concentration of cycloheximide in the medium. Experiments with neutral standing variation were performed using the pair yJHK111 and yJHK112. Note that, throughout this work, signal in the channel for the fluorescent color of the "mutant" (yMM9 and yJHK112) is pseudo-colored as yellow, while the fluorescent signal of the wild type (yJHK111) is pseudo-colored as blue.

S. cerevisiae – cell tracking at front

To track cells at the front, we used strain yMG10c, a convertant of yMG10, which in turn is based on strain yDM117 (W303 background, *HO::cre-EBD*, courtesy of Jasper Rine), transformed with a cassette (pMG4) based on pMEW90 (courtesy of Mary Wahl[2]). pMG4 contains a *loxP* cassette followed by *ymCitrine*, linked with *cyh2r* via ubiquitin. yMG10 was incubated with estradiol to induce auto-recombination, and streaked onto plates containing selective amounts of cycloheximide to select for the convertant yMG10c used for the time lapse movie in Fig. 3, which has genotype W303 *HO::cre-EBD SUC2::loxP-ymCitrine-ubq-cyh2r*.

S. pombe

To investigate genetic demixing from neutral standing variation in S. pombe, we used two variants of strain MJ95 (genotype *leu1-*, *ura4-*, *h-*)[3], which were obtained by replacing *mCherry* with the coding region for YFP and CFP from plasmids pOH1 and pOH2 at the *atb2* locus.

Plasmids with fluorescent markers cyan and yellow

pOH1 and pOH2 are based on the vector pTrc99A, with sequences for eCFP and Venus YFP inserted between the *Sac*I and *Xba*I sites, respectively. These plasmid are inducible by IPTG but we found the base

level of expression of the fluorescent proteins to be sufficient without inducer. For a more detailed description see Ref. 4.

E. coli – competition experiments

Population growth experiments were performed using three different backgrounds:

1. DH5α transformed with pOH1 and pOH2, resulting in eOH1 and eOH2. These strains are identical to those used in Ref. 4. For the competition experiments, we transformed eOH2 with the plasmid pACYC184 (New England Biolabs), conferring resistance to tetracycline, resulting in eOH3. Experiments with tunable selection were performed using the pair eOH1 and eOH3 (Fig. 4), adding low concentrations of tetracycline to the growth medium (in addition to ampicillin for plasmid maintenance). Experiments with neutral standing variation were performed using the pair eOH1 and eOH2 (Figs. 4 & 5).

2. Strain MG1655 (not fluorescent) and its derivative SJ102 (genotype MG 1655 *intC::λpR-YFP-Cmr*, courtesy of Ivan Matic), which constitutively expresses YFP and is resistant to chloramphenicol, allowing us to perform experiments with tunable selection (Figs. 4 & 5) by adding low concentrations of chloramphenicol to the growth medium. SJ102 was also used to study the dynamics of *E. coli* cells at the front (Fig. 3, SI movie 2).

3. A pair of JE 5713 [5] (cross between B6 [6] and KL228 [7,8]), transformed with plasmids pOH1 and pOH2, giving rise to eOH4 and eOH5, were used for competition experiments with neutral standing variation (Fig. 5). These strains have been reported as *rodA* mutants but also carry a point mutation in the gene *mrdA* (Waldemar Vollmer, private communication), causing a round cell shape.

Name	Composition	Used for...	Temperature [°C]
YPD	20g/L peptone, 10g/L yeast extract, 20g/L dextrose	*S. cerevisiae*	30
YES	5g/L yeast extract, 30g/L glucose, 225mg/L adenine, histidine, leucine, uracil, lysine hydrochloride	*S. pombe*	30
LB	10g/L tryptone, 5g/L yeast extract, 10g/L NaCl	*E. coli*	21, 37
M9	200mL/L 5× M9 salts [9], 5g/L dextrose, 2mM $MgSO_4$, 0.1 mM $CaCl_2$	*E. coli* (Fig. 5)	37

Table 3.C1: Media and growth conditions used in this study. For plates, 2% w/v bacto agar was added to the media before autoclaving. Antibiotics were added after autoclaving to cooled media.

Strain	Description	Genotype	Fluor.	Resistance	Reference	Fig(s).
S. cerevisiae						
yJHK111	YFP WT	W303 *MATa bud4Δ::BUD4(S288C) can1-100 his3::prACT1-ymCitrine-tADH1:His3MX6*	yellow	-	[1]	1,4,5
yJHK112	RFP WT	W303 *MATa bud4Δ::BUD4(S288C) can1-100 his3::prACT1-ymCherry-tADH1:His3MX6*	red	-	[1]	1,4,5
yMM9	RFP MT	W303 *MATa bud4Δ::BUD4(S288C) can1-100 his3::prACT1-ymCherry-tADH1:His3MX6 CYH2::cyh2-Q37E*	red	CHX	unpublished	1,4,5
yMG10	converter (RFP)	W303 *HO::cre-EBD SUC2::loxP-RFP-loxP-YFP-ubq-cyh2r*	red	G418, Nat	This study	-
yMG10c	converted (YFP)	W303 *HO::cre-EBD SUC2::loxP-YFP-ubq-cyh2r*	yellow	CHX, Nat	This study	3
S. pombe						
MJ95	RFP WT	*mCherry-atb2::hph, leu1-, ura4-, h-*	red	Hyg	[3]	-
MJ95-CFP	CFP WT	*CFP-atb2::hph, leu1-, ura4-, h-*	cyan	Hyg	This study	5
MJ95-YFP	YFP WT	*YFP-atb2::hph, leu1-, ura4-, h-*	yellow	Hyg	This study	5
E. coli						
eOH1	CFP WT	NEB DH5α *eCFP* (pTrc99A)	cyan	Amp	[4]	4, 5
eOH2	YFP WT	NEB DH5α *YFP* (pTrc99A)	yellow	Amp	[4]	4, 5
eOH3	YFP MT	NEB DH5α *YFP* (pTrc99A) + pACYC184	yellow	Amp, Tet	This study	4, 5
MG1655	WT	-	-	-	Laboratory stock	4, 5
SJ102	YFP MT	MG 1655 intC::λP_R-*YFP*-Cm^R	yellow	Cm	unpublished	3, 4, 5
JE5713	Round cell shape	*mrdA*-mut	-	-	[5]	-
eOH4	CFP round cells	JE5713 *eCFP* (pTrc99A)	cyan	Amp	This study	5
eOH5	YFP round cells	JE5713 *YFP* (pTrc99A)	yellow	Amp	This study	5

Table 3.C2: Strains used in this study.

3.7.2 Determining fitness differences as function of drug concentration

Liquid culture (*S. cerevisiae* only)

Single colonies were picked and grown overnight, then diluted 1:10 in fresh media, and grown for another 3 generations to ensure growth in log phase. The resulting cultures were mixed at ratio $P_{\mathrm{i}} = 0.5$ (measured by OD) and about 10000 cells inoculated into the wells of a 96 well plates with fresh YPD containing a range of antibiotics concentrations (3 replicates from the same initial culture per concentration). The plates were sealed and grown at 30°C overnight, then shaken vigorously for at least 1 minute. 10μl of the culture were diluted into PBS for analysis in the flow cytometer (Beckman-Coulter Fortessa X2). Every day, about 10000 cells were re-inoculated into fresh YPD to passage the cells for a total of 5 days, corresponding to about 60 generations. The cultures diluted in PBS were stored at $4°$C until they were analyzed using the flow cytometer at a rate of at most 10000 events per second. The resulting ratio of mutants to wild type increased exponentially with the number of generations elapsed, whence the fitness difference could be calculated from the slope of the curve in a semi-logarithmic plot.

On plates

Fitness differences were measured in separate experiments using the colliding colony assay, described briefly in the following, see also Ref. 1. Two 1μl droplets, each containing one of the two strains in log phase, are placed on agar plates about 5mm apart and incubated for at least 72 hours, until a sizable interface between the resulting colonies is formed. A circle of radius R is manually fitted to the collision interface using the Zeiss *ZEN* software and the distance l between the inoculation centers is measured. The selection coefficient s can be calculated via

$$s = \frac{1 - 2z + \sqrt{1 + 4z^2}}{2z}, \tag{3.C1}$$

where $z = R/l$. The resulting values of s were found to exhibit an approximately linear dependence on drug concentration (Fig. B1a). We used the values of s given by the linear regression in the figures in the main text (Fig. 1h, i, j, Fig. 4g, h). Following the results from Ref. 1, we assumed the same regression for fitness differences on plates and in liquid culture.

3.7.3 Adaptation from standing variation during two types of population expansions

Experiment and quantification

The experimental procedure for competition experiments from standing variation is described briefly in the main text and methods therein, see also Fig. 1a for a cartoon of the experiments. Here, we provide additional details on the experimental procedures.

All competition experiments were performed on one batch of media/plates (per experimental series) and using the same overnight cultures. For each competition experiment on plates we also carried out fitness measurements (via colliding colonies) on the same batch of plates. Final population sizes of the budding yeast colonies were measured by resuspending colonies into PBS, diluting and replating to count colony forming units, or measuring optical density and comparing with a previously obtained calibration.

To measure the frequency of yeast mutants in well-mixed liquid culture, we grew and mixed the strains as described above and grew the mixture overnight in aerated culture tubes at 30°C (2 replicates from the same initial culture per concentration). We separately checked that the competed strains had the same carrying capacity to avoid error due to the cultures entering stationary phase. The next morning, we sampled 20μl from each tube into 180μl of PBS. The mixture was then measured in a Beckman-Coulter Fortessa X20 flow cytometer at a rate of at most 10000 events per second.

To determine the number of cells in the outer rim of the inoculum, N_{mut}, in Fig. 4h, we measured the radius r_0 of the evaporated droplet (5 colonies from the same initial culture), which was easily visible under brightfield illumination. N_{mut} was then calculated as $N_{\text{mut}} = 2\pi r_0 P_{\text{i}}$. The variable $N_{\text{sec}}/N_{\text{mut}}$ in Fig. 4g hence corresponds to the probability of surfing of an individual mutant cells in the very first cell layer, assuming that the droplet rim is perfectly flat. $N_{\text{sec}}/N_{\text{mut}}$ differs from the true surfing probability (of an individual cell in the front) by a numerical factor of order 1 taking into account the irregularities of the droplet perimeter.

Image analysis

To measure the frequency of mutants in colonies, images of the colonies were taken with a Zeiss AxioZoom v16 fluorescence microscope at 3.5x zoom and analyzed using custom routines written in *Mathematica* (Wolfram Research, Inc., Mathematica, Version 10.1, Champaign, IL (2015)). Because the colonies' fluorescence typically becomes weaker near the colony boundary, we employed a local adaptive binarization scheme. Since individual images varied in intensity distribution, it was necessary to set the binarization thresholds by hand for each image such that the binarized shape corresponded well to the observed sector shapes. We ex-

[CHX]	0	40	80	120	160	200
Sectors	46	101	178	102	69	35

Table 3.C3: Number of sectors analyzed per cycloheximide concentration.

pect the error from this "subjective" choice of thresholds to be small. During binarization, the outer radius of the colony, its center, and the radius of the inner ring, stemming from the inoculation droplet, were also measured. The frequency of mutants was then calculated by measuring the area of mutants and dividing by the area of the annulus between the outer and inner radius, i.e., the fraction inside the homeland was neglected, but the emerging bulge (for larger s) was taken into account.

For the frequency per sector in Figs. 1 and B7, we selected only colonies that either only had a single sector, or colonies with few sectors that did not touch. Since the colonies used for Fig. 1 had many sectors at large s, we also used colonies from experiments with smaller P_1 (0.0025, 0.005, 0.01) to acquire enough "free-standing" sectors. The frequency was then computed as described above. Table 3.C3 gives the number of sectors analyzed for each concentration of cycloheximide.

3.7.4 Growth of *S. cerevisiae* colony from single cell

Using a Zeiss AxioZoom v16 upright microscope, we tracked the growth of a colony (strain yMG10c) by taking time-lapse movies of the fluorescence signal detected in a stage-mounted Okolab UNO-PLUS incubator at 30°C and at constant relative humidity. An agar plate in a Petri dish was inoculated with single cells and grown in the stage-top incubator until colonies were visible at the desired magnification. Then, one colony was randomly chosen and the time lapse movie was recorded for 48 hours, taking an image every 30 min. The colony radius was determined by fitting a circle to the circumference of the colony.

3.7.5 Cell tracking at the front

Experiment

For single-cell resolution time lapse movies (SI movies 1 and 2) of growing SJ102 and yMG10c, we used a Zeiss LSM700 in confocal mode with a 488nm laser. Agar plates were inoculated with fresh culture droplets (2μl), that were left to dry for several minutes. The agar around the droplet was then cut into a 2cm$\times$2cm pad and inverted onto a clean coverslip, such that the cells touched the coverslip. The coverslip with the cells was then incubated for a day to reach steady-state growth of the colony. After mounting the coverslip in a stage-top incubator, we mounted the incubator on the microscope and let it equilibrate for about 2h. Humidity

in the chamber was controlled by the addition of a water reservoir. *E. coli* cells were imaged with a 40x oil objective, *S. cerevisiae* cells with a 20x air objective. Images were taken at 1 frame per minute with a dwelling time of about 6μs/px (31s exposure per frame) for 274/228 minutes, respectively.

Analysis

For cell tracking, all frames were cleaned automatically using a median filter and contrast-adjusted. In SI movie 2, some frames were manually retouched to remove brightness fluctuations. All frames were segmented with a local adaptive binarization algorithm (same parameters for all frames) and objects touching the image boundaries were removed. Because cells far behind the front could usually not be tracked accurately, we only analyzed the first few cells layers by automatically finding the position of the front and removing segmented objects far from it.

To determine the ancestry of cells at the front, we proceeded backwards in time. An individual cell was tracked by creating a mask from its outline, dilating it, and computing the overlap with the previous frame. The cell's position in the previous frame was then determined by finding the cell with maximal overlap.

For Fig. 3, we tracked a total of 692 and 407 cells for 180 minutes in *E. coli* and *S. cerevisiae*, respectively, i.e., we shortened the original time lapse movies to 180 minutes. This was done to maximize the number of tracked cells while still maintaining information over sufficiently long time scales.

To obtain the mean square displacement in Fig. 3f, we proceeded as follows. Each tracked cell in the final frame was traced back to its ancestor 180 minutes ago. Since the front had a defined direction of motion (which we defined as the x-axis), we measured, in each time step, the position of the cell relative to its original position and computed the displacement y from the x-axis, and take the square. These operations are performed for all tracked cells, and averaging is performed over bins of x-displacements to account for cells moving by different amounts in the x-direction per frame. After averaging, the square root was taken in each x-bin, and the curves were fitted using *Mathematica*. In order to compare values for *S. cerevisiae* and *E. coli*, we divided the displacements in x and y by the effective cell sizes d, given by $d = 4.5\mu$m for *S.cerevisiae* and $d = \sqrt{3.5\mu\text{m} \times 0.7\mu\text{m}}$ for *E.coli*. The effective cell size for *E. coli* was determined by the harmonic mean of its semi-axes, which were both measured directly from the time-lapse movie, as was the cell size of *S. cerevisiae*.

Figures

Figures of the cell tracking (Figs. 3a, c and Fig. B8) were created using Adobe Photoshop by overlaying images of the segmented cells at $t = 0$ and $t = 3$h with the computed lineages. For Figs. 3a & c, an outline was added to the tracked lineages and the cells in the lineage to increase visibility.

References

[1] K. S. Korolev, M. J. Müller, N. Karahan, A. W. Murray, O. Hallatschek, and D. R. Nelson. Selective sweeps in growing microbial colonies. *Physical biology*, 9(2):026008, 2012.

[2] M. E. Wahl and A. W. Murray. Multicellularity makes cellular differentiation evolutionarily stable. *bioRxiv*, page 010728, 2014.

[3] V. Ananthanarayanan, M. Schattat, S. K. Vogel, A. Krull, N. Pavin, and I. M. Tolić-Nørrelykke. Dynein motion switches from diffusive to directed upon cortical anchoring. *Cell*, 153(7):1526–1536, 2013.

[4] O. Hallatschek, P. Hersen, S. Ramanathan, and D. R. Nelson. Genetic drift at expanding frontiers promotes gene segregation. *Proceedings of the National Academy of Sciences*, 104(50):19926–19930, 2007.

[5] URL **http://www.shigen.nig.ac.jp/ecoli/strain/nbrpStrainDetailAction.do?strainId=1235**.

[6] B. G. Spratt. Distinct penicillin binding proteins involved in the division, elongation, and shape of escherichia coli k12. *Proceedings of the National Academy of Sciences*, 72(8):2999–3003, 1975.

[7] **http://cgsc.biology.yale.edu/Strain.php?ID=4603**.

[8] B. Low. Rapid mapping of conditional and auxotrophic mutations in escherichia coli k-12. *Journal of bacteriology*, 113(2):798–812, 1973.

[9] **doi:10.1101/pdb.rec12295**.

4

Mechanical interactions in bacterial colonies and the surfing probability of beneficial mutations

Bacterial conglomerates such as biofilms and microcolonies are ubiquitous in nature and play an important role in industry and medicine. In contrast to well-mixed cultures routinely used in microbial research, bacteria in a microcolony interact mechanically with one another and with the substrate to which they are attached. Here we use a computer model of a microbial colony of rod-shaped cells to investigate how physical interactions between cells determine their motion in the colony and how this affects biological evolution. We show that the probability that a faster-growing mutant "surfs" at the colony's frontier and creates a macroscopic sector depends on physical properties of cells (shape, elasticity, friction). Although all these factors contribute to the surfing probability in seemingly different ways, their effects can be summarized by two summary statistics that characterize the front roughness and cell alignment. Our predictions are confirmed by experiments in which we measure the surfing probability for colonies of different front roughness. Our results show that physical interactions between bacterial cells play an important role in biological evolution of new traits, and suggest that these interaction may be relevant to processes such as *de novo* evolution of antibiotic resistance.

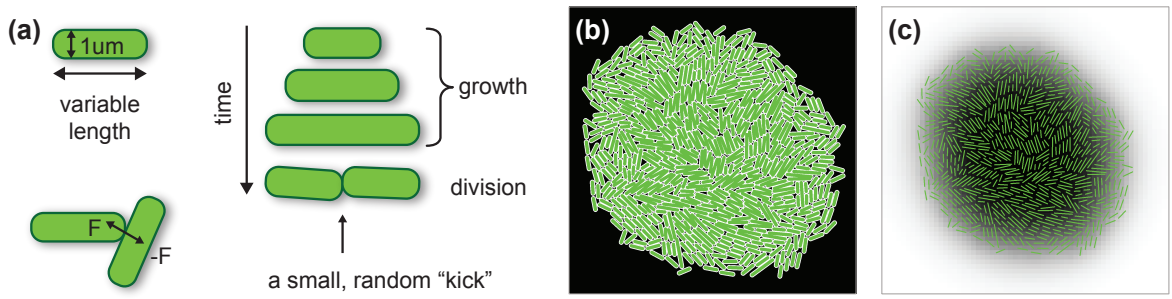

Figure 4.1: (a) Illustration of the computer algorithm. Bacteria are modelled as rods of varying length and constant diameter. When a growing rod exceeds a critical length, it splits into two smaller rods. (b) A small simulated colony. (c) The same colony with nutrient concentration shown as different shades of gray (white = maximal concentration, black = minimal); the cells are represented as thin green lines.

4.1 Introduction

Bacteria are the most numerous organisms on Earth capable of autonomous reproduction. They have colonised virtually all ecological niches and are able to survive harsh conditions intolerable for other organisms such as high salinity, low pH, extreme temperatures, or the presence of toxic elements and compounds[1]. Many bacteria are important animal or human pathogens, but some bacteria find applications in the industry as waste degraders[2] or to produce fuels and chemicals[3]. In these roles, biological evolution of microbes is usually an undesired side effect because it can disrupt industrial processes or lead to the emergence of new pathogenic[4] or antibiotic-resistant strains[5].

Experimental research on bacterial evolution has been traditionally carried out in well-stirred cultures[6,7]. However, in their natural environment bacteria often form aggregates such as microcolonies and biofilms. Such aggregates can be found on food[8], teeth (plague), on catheters or surgical implants[9], inside water distribution pipes[10], or in the lungs of people affected by cystic fibrosis[11]. Bacteria in these aggregates adhere to one another and the surface on which they live, form layers of reduced permeability to detergents and drugs, and stochastically switch to a different phenotype that is more resistant to treatment[12–14]; this causes biofilms to be notoriously difficult to remove.

An important aspect of bacteria living in dense conglomerates is that they do not only interact via chemical signaling such as quorum sensing[15] but also through mechanical forces such as when they push away or drag other bacteria when sliding past them. Computer simulations[16–19] and experiments[20–24] have indicated that such mechanical interactions play an important role in determining how microbial colonies grow and what shape they assume. However, the impact of these interactions on biological evolution only recently came into focus[25].

A particularly interesting scenario relevant to microbial evolution in microcolonies and biofilms is that of a range expansion[26] in which a population of microbes invades a new territory. If a new genetic variant arises near the invasion front, it either "surfs" on the front and spreads into the new territory, or (if unlucky) it lags behind the front and forms only a small "bubble" in the bulk of the population[27]. This stochastic process, called "gene surfing", has been extensively studied[25,28–34] but these works have not addressed the role of mechanical interactions between cells. Many of the existing models do not consider individual cells[28], assume Eden-like growth[32], or are only appropriate for diluted populations of motile cells described by reaction-diffusion equations similar to the Fisher-Kolmogorov equation[35]. On the other hand, agent-based models of biofilm growth, which have been applied to study biological evolution in growing biofilms[36–38], use very simple rules to mimic cell-cell repulsion which neglect important physical aspects of cell-cell and cell-substrate interactions such as friction.

In this work, we use a computer model of a growing microbial colony to study how gene surfing is affected by the mechanical properties of cells and their environment. In our model, non-motile bacteria grow attached to a two-dimensional permeable surface which delivers nutrients to the colony. This corresponds to a common experimental scenario in which bacteria grow on the surface of agarose gel infused with nutrients. We have previously demonstrated[17] that this model predicts a non-equilibrium phase transition between a regular (circular) and irregular (branched) shape of a radially expanding colony of microbes, and that it can be used to study biological evolution in microbial colonies[25]. Here, we use this model to show that the surfing probability of a beneficial mutation is determined by the roughness and the cellular ordering at the expanding front of the colony. We also investigate how mechanical properties of cells such as elasticity, friction, and cell shape affect these two quantities. We corroborate some of our results in experiments with microbial colonies that display varying degrees of roughness of the growing front and show that it influences the surfing probability as expected.

4.2 Computer model

We use a computer model similar to that from Refs. 17, 23, 25, with some modifications. Here we discuss only the generic algorithm; more details will be given in subsequent sections where we shall talk about the role of each of the mechanical factors.

We assume that bacteria form a monolayer as if the colony was two-dimensional and bacteria always remained attached to the substrate. This is a good approximation to what occurs at the edge of the colony and, as we shall see, is entirely justifiable because the edge is the part of the colony most relevant for biological evolution of new traits. We model cells as spherocylinders of variable length and constant diameter $d = 2r_0 = 1\mu$m (Fig. 4.1a). Cells repel each other with normal force determined by the Hertzian contact

theory: $F = (4/3)Er_0^{1/2}h^{3/2}$ where h is the overlap distance between the walls of the interacting cells, and E plays the role of the elastic modulus of the cell. The dynamics is overdamped, i.e. the linear/angular velocity is proportional to the total force/total torque acting on the cell:

$$\frac{d\vec{r}_i}{dt} = \vec{F}/(\zeta m), \tag{4.1}$$

$$\frac{d\phi_i}{dt} = \tau/(\zeta J). \tag{4.2}$$

In the above equations $\vec{r}_i$ is the position of the centre of mass of cell i, ϕ_i is the angle it makes with the x axis, $\vec{F}$ and τ are the total force and torque acting on the cell, m and J are its mass and the momentum of inertia (perpendicular to the plane of growth), and ζ is the damping (friction) coefficient. We initially assume that friction is isotropic, and explore anisotropic friction later in Sec. 4.4.3. Note that the mass m and the momentum of interia J are the proxy for cell size. These quantities are not constant because cells change their size over time, and hence m, J cannot be absorbed into the friction coefficient.

Bacteria grow by consuming nutrients that diffuse in the substrate. The limiting nutrient concentration dynamics is modelled by the diffusion equation with sinks corresponding to the bacteria consuming the nutrient:

$$\frac{\partial c}{\partial t} = D\left(\frac{\partial^2 c}{\partial x^2} + \frac{\partial^2 c}{\partial y^2}\right) - k\sum_i \delta\left(\vec{r}_i - \vec{r}\right). \tag{4.3}$$

Here $\vec{r} = (x, y)$, $c = c(\vec{r}, t)$ is the nutrient concentration at position $\vec{r}$ and time t, D is the diffusion coefficient of the nutrient, and k is the nutrient uptake rate. The initial concentration $c(\vec{r}, 0) = c_0$.

A cell elongates at a constant rate v_l as long as the local nutrient concentration is larger than a certain fraction (>1%) of the initial concentration. When a growing cell reaches a pre-determined length, it divides into two daughter cells whose lengths are half the length of the mother cell. The critical inter-cap distance $l_{\text{cap}-\text{cap}}$ at which this occurs is a random variable from a Gaussian distribution with mean ℓ_c and standard deviation $\pm 0.15\,\ell_c$. Varying ℓ_c allows us to extrapolate between quasi-spherical cells (e.g. yeasts *S. cerevisae* or the bacterium *S. aureus*) and rod-shaped cells (e.g. *E. coli* or *P. aeruginosa*), whereas the randomness of $l_{\text{cap}-\text{cap}}$ accounts for the loss of synchrony in replication that occurs after a few generations (the coefficient of variation of the time to division $\sim 0.1 - 0.2$[39–41]). The two daughter cells have the same orientation as the parent cell, plus a small random perturbation to prevent the cells from growing in a straight line.

We use two geometries in our simulations: a radially expanding colony that starts from a single bacterium (Fig. 4.2a), and a colony growing in a narrow (width L) but infinitely long vertical tube with periodic boundary conditions in the direction lateral to the expanding front (Fig. 4.2d). While the radial expansion case represents a typical experimental scenario, only relatively small colonies (10^6 cells as opposed to $> 10^8$ cells

Name	Value	Units
Nutrient diffusion constant D	50	μm^2/h
Nutrient concentration c_0	1	a.u.
Nutrient uptake rate k	1 – 3	a.u./h
Young modulus E	100	kPa
Elongation length v_l	4	μm/h
Cell diameter	1	μm
Average max. inter-cap distance l_c	4	μm
Damping coefficient ζ	500	Pa·h

Table 4.1: Default values of the parameters of the model. This gives ≈ 30min doubling time and the average length of bacterium $\approx 3\mu$m. If not indicated otherwise, all results presented have been obtained using these parameters.

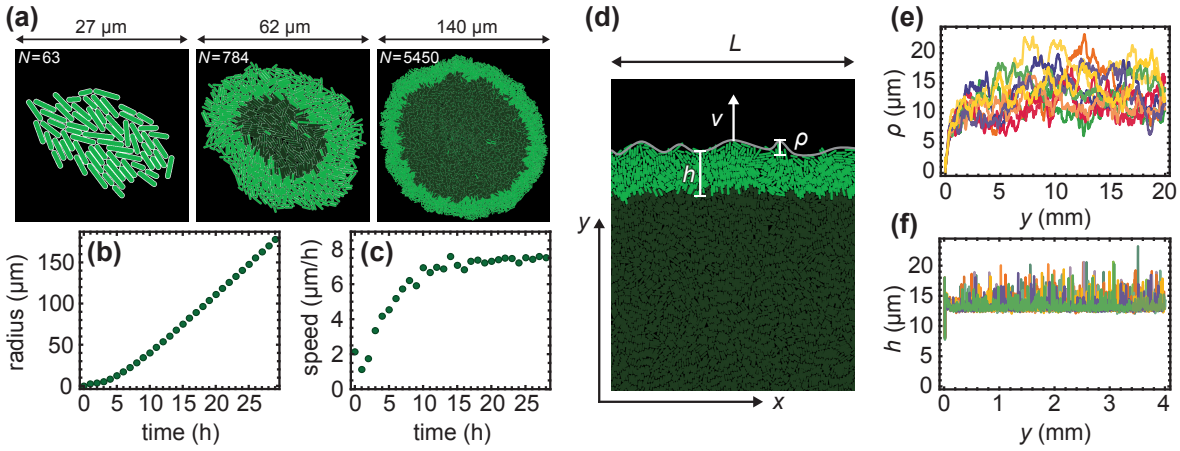

Figure 4.2: (a) Snapshots of a radially-growing simulated colony taken at different times (sizes), for $k = 2$. Growing bacteria are bright green, quiescent (non-growing) bacteria are dark green. (b) The radius of the colony increases approximately linearly in time. (c) The expansion speed tends to a constant value for long times. (d) Example configuration of cells from a simulation in a tube of width $L = 80\mu$m. The colony expands vertically. h is the thickness of the growing layer (Eq. (4.4)), ρ is the roughness of the front (Eq. (4.5)). (e, f) Roughness ρ and thickness h as functions of the position y of the front, for $L = 1280\mu$m and $k = 2.5$, and for 10 independent simulation runs (different colours).

in a real colony[25]) can be simulated in this way due to the high computational cost. The second method (growth in a tube) enables us to simulate growth for longer periods of time at the expense of confining the colony to a narrow strip and removing the curvature of the growing front. This has however little effect on the surfing probability of faster-growing mutants if the width L of the tube is sufficiently large[42].

Figure 4.1b, shows a snapshot of a small colony; the concentration of the limiting nutrient is also shown.

Table 4.1 shows default values of all parameters used in the simulation. Many of these parameters have been taken from literature data for the bacterium *E. coli*[25], but some parameters such as the damping coefficient must be estimated indirectly[17]. We note that the assumed value of the diffusion constant D is unrealistically small; the actual value for small nutrient molecules such as sugars and aminoacids would be $\sim 10^6 \mu\text{m}^2/\text{h}$, i.e., four orders of magnitude larger. Our choice of D is a compromise between realism and computational cost; we have also shown in Ref. 17 that the precise value of the diffusion coefficient is irrelevant in the parameter regime we are interested here. We also note that in reality cessation of growth in the center of the colony and the emergence of the growing layer may be due to the accumulation of waste chemicals, pH change etc., rather than nutrient exhaustion. Here we focus on the mechanical aspects of growing colonies and do not aim at reproducing the exact biochemistry of microbial cells, as long as the simulation leads to the formation of a well-defined growth layer (as observed experimentally).

4.3 Experiments

Experiments were performed as described in our previous work[25]. Here we provide a brief description of these methods.

Strains and growth conditions.

For the mixture experiments measuring surfing probability, we used pairs of microbial strains that differed in fluorescence color and a selectable marker. The selective difference between the strains was adjusted as in[25] using low doses of antibiotics. The background strains and antibiotics used were *E. coli* DH5α with tetracycline, *E. coli* MG1655 with chloramphenicol, and *S. cerevisiae* W303 with cycloheximide. Selective differences were measured using the colliding colony assay[33]. *E. coli* strains were grown on LB agar (2%) medium (10g/L tryptone, 5g/L yeast extract, 10g/L NaCl) at either 37°C or 21°C. *S. cerevisiae* experiments were performed on either YPD (20g/L peptone, 10g/L yeast extract, 20g/L glucose) or CSM (0.79g/L CSM (Sunrise media Inc.), 20 g/L glucose) at 30°C. 20g/L agar was added to media before autoclaving. Antibiotics were added after autoclaving and cooling of the media to below 60°C.

Measuring surfing probability.

For each pair of mutant and wild type, a mixed starting population was prepared that contained a low initial frequency P_i of mutants having a selective advantage s. Colony growth was initiated by placing 2μl of the mixtures onto plates and incubated until the desired final population size was reached. The initial droplet radius was measured to compute the number of cells at the droplet perimeter. The resulting colonies were

imaged with a Zeiss AxioZoom v16. The number of sectors was determined by eye. The surfing probability was calculated using Eq. (4.10).

Timelapse movies.

For single cell-scale timelapse movies, we used a Zeiss LSM700 confocal microscope with a stage-top incubator to image the first few layers of most advanced cells in growing *S. cerevisiae* and *E. coli* colonies between a coverslip and an agar pad for about four hours, taking an image every minute.

Measuring roughness.

Images of at least 10 equal-sized colonies per condition were segmented and the boundary detected. The squared radial distance δr^2 between boundary curve and the best-fit circle to the colony was measured as a function of the angle and averaged over all possible windows of length l. The resulting mean δr^2 was averaged over different colonies.

Images of moving fronts at the single-cell level from the timelapse movies were first segmented using a local adaptative threshold algorithm to identify cells. The front was found by the outlines of cells directly at the front. For all possible windows of length l, a line was fitted to the front line and the mean squared distance from the best-fit line was measured, as in Ref. 28. The resulting mean squared distance was averaged over all windows of length l and all frames.

4.4 Simulation results

4.4.1 Growth and statistical properties of the simulated colony

We now discuss the properties of our simulated colonies. When the colony is small, all bacteria grow and replicate. As the colony expands, the nutrient becomes depleted in the centre of the colony because diffusion of the nutrient cannot compensate its uptake by growing cells. This causes cessation of growth in the centre. When this happens, growth becomes restricted to a narrow layer at the edge of the colony, Fig. 4.2a, and Supplementary Video 1. The radius of the colony increases approximately linearly in time (Fig. 4.2b,c). The presence of a "growing layer" of cells and the linear growth of the colony's radius agree with what has been observed experimentally [25,43].

Statistical properties of the growing layer can be conveniently studied using the "tube-like" geometry. Figure 4.2d shows a typical configuration of cells at the colony's frontier (see also Supplementary Video 2). The growing layer can be characterized by its thickness h and roughness ρ which we calculate as follows. We first rasterize the growing front of the colony using pixels of size $1 \times 1\mu$m, and find the two edges of the

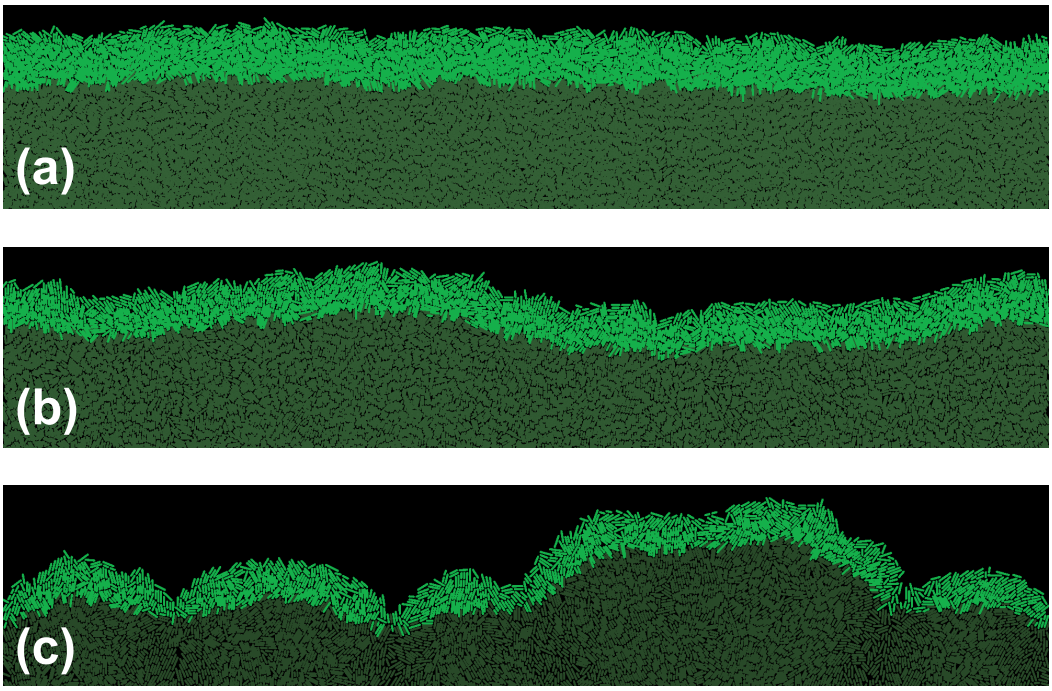

Figure 4.3: The frontier of the colony for three different nutrient uptake rates $k = 1.8$ (a), $k = 2.2$ (b) and $k = 2.6$ (c). The thickness of the growing layer (bright green) decreases only moderately ($1.64\times$) from $h = 13.5 \pm 0.1\mu$m for $k = 1.8$ to $h = 8.2 \pm 0.1\mu$m for $k = 2.6$, but this has a large impact on the front roughness which changes from $\rho = 2.1 \pm 0.2\mu$m to $\rho = 9.3 \pm 0.4\mu$m, correspondingly. For $k = 2.6$ the growing layer begins to loose continuity and splits into separate branches.

front: the upper one (the colony edge) $\{y_i^+\}$ and the lower one (the boundary between the growing and quiescent cells) $\{y_i^-\}$. We then calculate the average thickness as

$$h = \frac{1}{L}\sum_{i=1}^{L} \min_{j=1,\ldots,L} \sqrt{(i-j)^2 + (y_i^+ - y_j^-)^2}. \tag{4.4}$$

This method takes into account that the growing layer can be curved and does not have to run parallel to

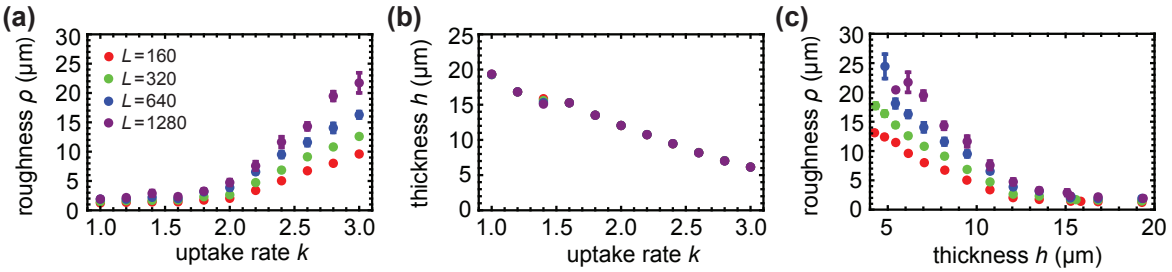

Figure 4.4: Roughness (a) and thickness (b) of the growing layer for different front lengths (tube widths) $L = 160$ (red), $L = 320$ (green), $L = 640$ (blue), and $L = 1280$ μm (purple). (a) Thickness h decreases as the nutrient uptake rate k increases. h does not depend on the length L of the front. (b) Roughness ρ increases with both k and L. (c) Roughness versus thickness; different points correspond to different k from panels (a,b).

the x axis*. Similarly, we calculate the average roughness as

$$\rho = \sqrt{\frac{1}{L}\sum_{i=1}^{L}(y_i^+ - Y^+)^2}\,, \tag{4.5}$$

where $Y^+ = (1/L)\sum_i y_i^+$. Note that all quantities (L, Y^+, y_i^+, y_i^-) are in pixels and not μm.

After a short transient the expansion velocity, the nutrient profile, and other properties of the growing layer stabilize and vary little with time (Fig. 4.2e,f). It is therefore convenient to choose a new reference frame co-moving with the leading edge of the colony. Since cells that lag behind the front do not replicate, we do not have to simulate these cells explicitly. This dramatically speeds up simulations and enables us to study stripes of the colony of width $L > 1$mm and length > 10mm.

We have shown previously[17] that the thickness of the growing layer of cells is controlled by the nutrient concentration c_0, nutrient uptake rate k, growth rate b, and elasticity E of cells. This in turn affects the roughness of the leading edge of the colony. This relation is illustrated in Fig. 4.3, where we vary the uptake rate k while keeping the remaining parameters constant.

Figure 4.4 shows that front thickness decreases and its roughness increases with increasing k; eventually, when a critical value $k_c \approx 2.5$ is crossed, the growing front splits into separate branches. This transition has been investigated in details in Ref. 17. Although this scenario can be realized experimentally[44,45], here we focus on the "smooth" regime in which colonies do not branch out and the frontier remains continuous.

*Alternatively, h can be defined as the area of the colony that contains replicating cells divided by the interface length L. Both methods produce similar results.

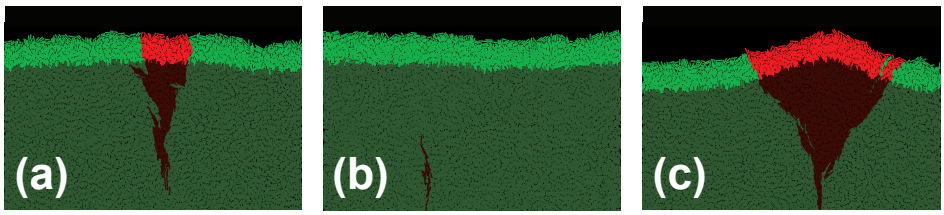

Figure 4.5: The fate of mutants. Panels (a) and (b) show different fates of a sector of fitter ($s = 0.1$) mutant cells (red) in a colony of "wild-type" cells (green). The sector can either expand (panel (a)) or collapse and become trapped in the bulk when random fluctuations cause mutant cells to lag behind the front (panel (b)). Panel (c) shows a sector with larger ($s = 0.5$) growth advantage; significantly faster growth of mutant cells leads to a "bump" at the front. In all cases $k = 1.8, L = 160\mu$m.

4.4.2 Surfing probability of a beneficial mutation

When a mutation arises at the colony's frontier, its fate can be twofold[25,28]. If cells carrying the new mutation remain in the active layer, the mutation "surfs" on the moving edge of the colony and the progeny of the mutant cell eventually forms a macroscopic "sector" (Fig. 4.5). On the other hand, if cells carrying the mutation leave the active layer, the mutation becomes trapped as a "bubble" in the bulk of the colony[27]. Due to the random nature of replication and mixing at the front, surfing is a stochastic process; a mutation remains in the active layer in the limit $t \to \infty$ with some probability P_{surf} which we shall call here the surfing probability.

Surfing is a softer version of fixation - a notion from population genetics in which a mutant takes over the population. The soft-sweep surfing probability has therefore a hard-selection-sweep counterpart, the fixation probability, which is the probability that the new mutation spreads in the population so that eventually all cells have it. Both surfing and fixation probabilities depend on the balance between selection (how well the mutant grows compared to the parent strain) and genetic drift (fluctuations in the number of organisms due to randomness in reproduction events)[46]. In Ref. 25 we showed that P_{surf} increased approximately linearly with selective advantage s – the relative difference between the growth rate of the mutant and the parent strain. Here, we study how the properties of the active layer affect P_{surf} for a fixed s.

We first run simulations in the planar-front geometry in which a random cell picked up from the growing layer of cells with probability proportional to its growth rate is replaced by a mutant cell with selective advantage $s > 0$. This can be thought of as mutations occurring with infinitely small but non-zero probability per division. The simulation finishes when either fixation (all cells in the growing layers becoming mutants) or extinction (no mutant cells in the growing layer) is achieved. Before inserting the mutant cell, the colony is simulated until the properties of the growing layer stabilize and both thickness and roughness reach steady-state values. The simulation is then repeated many times and the probability of surfing is estimated from

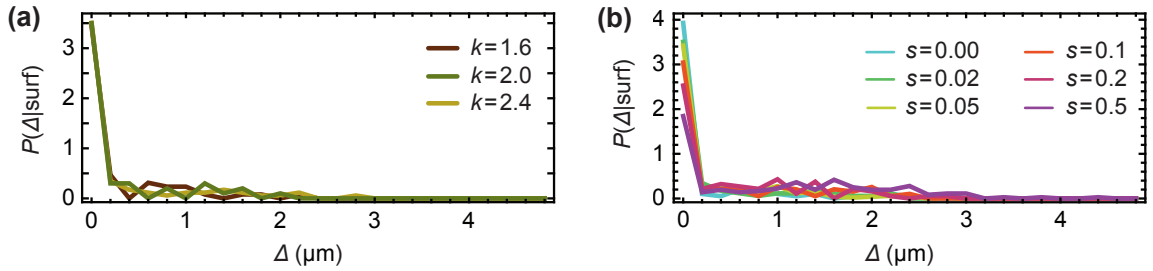

Figure 4.6: (a) $P(\Delta|\text{surf})$ for $L = 160\mu$m, selective advantage $s = 0.02$, and different $k = 1.6, 2.0, 2.4$. (b) $P(\Delta|\text{surf})$ for $L = 160\mu$m, $k = 2.0$, and different selective advantages $s = 0, 0.02, 0.05, 0.1, 0.2, 0.5$. Only mutants from the first layer of cells have a significant chance of surfing.

the proportion of runs leading to fixation of the mutant in the growing layer. Snapshots showing different fates (extinction, surfing) of mutant sectors are shown in Fig 4.5.

Surfing probability depends on the position of the cell in the growing layer.

In Ref. 25 we showed that the surfing probability strongly depends on how deeply in the growing layer a mutant was born. Here we would like to emphasize this result as it will become important later. Let Δ be the distance from the edge of the colony to the place the mutant first occurred. Figure 4.6 shows the probability density $P(\Delta|\text{surf})$ that a cell was born a distance Δ behind the colony front, *given that it went on to surf on the edge of the expanding colony*. It is evident that only cells born extremely close to the frontier have a chance to surf. Cells born farther from the frontier must get past the cells in front of them. This is unlikely to happen, even if the cell has a significant growth advantage, as the cell's growth will also tend to push forward the cells in front of it. This also justifies why we focus on two-dimensional colonies only; even though real colonies are three-dimensional, all interesting dynamics occurs at the edge of the colony which is essentially a mono-layer.

Given that surfing is restricted to the first layer of cells, and the distribution $P(\Delta|\text{surf})$ is approximately the same for all explored parameter sets (different k and s), for our purpose it would be a waste of computer time to simulate mutants that occurred deeply in the growing layer. To save the time, and to remove the effect the front thickness has on P_{surf} (thicker layer = lower overall probability), we changed the way of introducing mutants. Instead of inserting mutants anywhere in the growing layer, we henceforth inserted them only at the frontier.

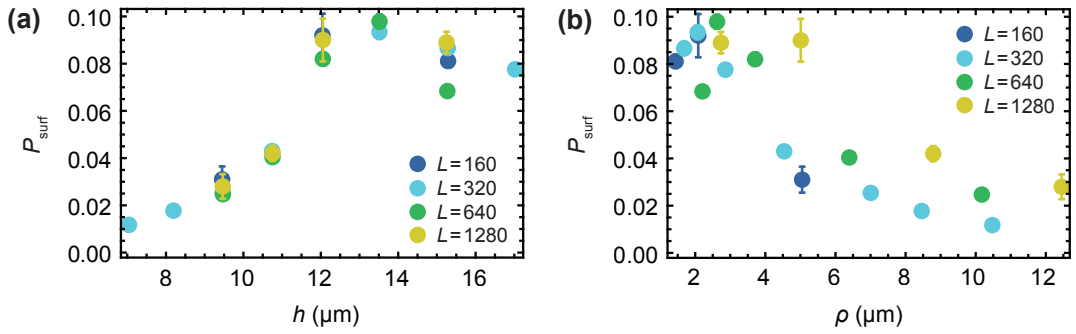

Figure 4.7: (a) P_{surf} for different thickness h of the growing layer, for $s = 0.02$ and $L = 160, 320, 640, 1280\,\mu$m (different colours). (b) the same data as a function of front roughness ρ. Between 10^3 and 10^4 simulations were performed for each data point to estimate P_{surf}.

Roughness of the front is more predictive of P_{surf} than its thickness.

Using the new method of introducing mutants (only the first layer of cells), we run simulations for $s = 0.02$ and for different widths L and nutrient uptake rates k as in Fig. 4.4. Figure 4.7 shows how the surfing probability P_{surf} varies as a function of the thickness and the roughness of the front. P_{surf} increases with increasing thickness h and decreases with increasing roughness ρ. We know from Fig. 4.4 that thickness and roughness are inversely correlated so this reciprocal behaviour is not surprising. An interesting question is whether any of the two quantities, roughness or thickness, directly affects the probability of surfing? From a statistics point of view, thickness h seems to be a better predictor of P_{surf} because data points for the same h but for different L correlate better. However, it could be that it is actually front roughness that directly (in the causal sense) affects the surfing probability and that P_{surf} and h are anti-correlated because of the relationship between h and ρ.

We performed two computer experiments to address the above question. First, we simulated a colony that had a very low and constant roughness $\rho \approx 1\mu$m, independently of front's thickness. This was achieved by introducing an external force $F_y = -gy$ acting on the centre of mass of each cell, where $g > 0$ was a "flattening factor" whose magnitude determined the strength of suppression of deviations from a flat front. P_{surf} plotted in Figure 4.8a, as a function of h for two cases: "normal", rough front ($g = 0$), and "flattened" front ($g > 0$), demonstrates that the surfing probability does not depend on h in the case of flat front.

Second, we varied roughness while keeping thickness constant. This was done by measuring front roughness in each simulation step, and switching on the external "flattening" force $F_y = -gy$ if the roughness was larger than a desired value ρ_{max}. Figure 4.8b, shows that although thickness remains the same for all data points, P_{surf} decreases with increasing roughness.

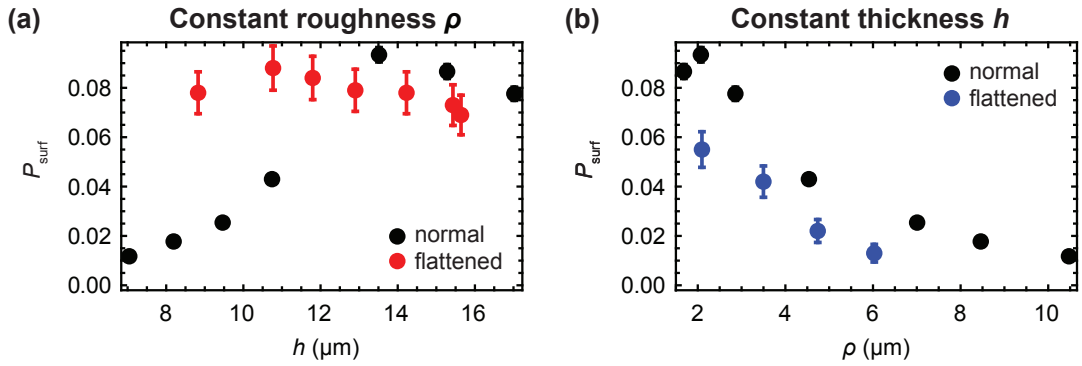

Figure 4.8: (a) P_{surf} as the function of front thickness h for the normal (black) and flattened front (red, $g = 500$), for $L = 320\mu$m. We vary the nutrient uptake rate $k = 1.6...2.8$ to simulate fronts of different thickness. The flat front has roughness ρ between 0.84 and 1.0 for all k. (b) P_{surf} for the normal (black) and flattened front (blue) as the function of roughness ρ. The flattened front has approximaly the same thickness for all data points (h between 10.0 and 10.3μm). The points correspond to maximum roughness set to $\rho_{\text{max}} = 2, 3.5, 5$, and 7, for $k = 2.6$; the actual (measured) ρ differs very little from these values.

We can conclude from this that it is the increase in the roughness, and not decreasing thickness, that lowers the surfing probability for thinner fronts (larger nutrient intake rate k). However, the data points in Fig. 4.7b, from different simulations do not collapse onto a single curve as it would be expected if average, large-scale front roughness was the only factor.

Local roughness predicts P_{surf}

According to the theory of Ref. 30, the dynamics of a mutant sector can be described by a random process similar to Brownian motion in which the sector boundaries drift away from each other with constant velocity. The velocity depends on the growth advantage s whereas the amplitude of random fluctuations in the positions of boundary walls is set by the microscopic dynamics at the front. We reasoned that these fluctuations must depend on the roughness ρ of the frontier, and that a mutant sector should be affected by front roughness when the sector is small compared to the magnitude of fluctuations. This means that local roughness $\rho(l)$, determined over the length l of the front, should be more important than the global roughness $\rho(L)$.

We calculated the local roughness as

$$\rho(l) = \frac{1}{n}\sum_{i=1}^{n}\sqrt{\frac{1}{l}\sum_{j=i}^{i+l}(y_j^+ - Y^+)^2}. \tag{4.6}$$

Here Y^+ is the average height of the interface and $\{y_i^+\}$ are the vertical coordinates (interface height) of the points at the leading edge, obtained as in Section 4.4.1. Figure 4.9 shows that P_{surf} for different L now collapse onto a single curve, for all lengths $l \approx 10 \ldots 100\mu$m over which roughness has been calculated.

Orientation of cells affects P_{surf}.

So far we have focused only on the macroscopic properties of the leading edge of the colony, completely neglecting its granular nature due to the presence of individual cells. Recall that in our model each cell is rod-shaped, and the direction in which it grows is determined by the orientation of the rod. Figure 4.10a shows that cells at the leading edge assume orientations slightly more parallel to the direction of growth (vertical) in the flattened front than in the normal simulation. A natural question is how does cellular alignment affects P_{surf}, independently of the roughness? To answer this question, we simulated a modified model, in which external torque $\tau = -\tau_{\text{max}} \sin[(\phi - \phi_{\text{preferred}}) \mod \pi]$ was applied to the cells, forcing them to align preferentially in the direction $\phi_{\text{preferred}}$. We investigated two forced alignments: $\phi_{\text{preferred}} = 0$ corresponding to cells parallel to the x axis and hence to the growing edge of the colony, and $\phi_{\text{preferred}} = \pi/2$ which corresponds to the vertical orientation of cells (perpendicular to the growing edge).

Figure 4.10b compares these two different modes with previous simulations with no external torque, for approximately the same thickness and roughness of the growing layer. It is evident that the orientation of cells strongly affects the surfing probability: horizontally-forced cells have $\sim$ 3x smaller P_{surf} compared to the normal case, which in turn has $P_{\text{surf}} \sim$ 5x smaller than vertically-forced cells.

Shorter cells have higher P_{surf} than long cells.

To check how the aspect ratio of cells affect P_{surf}, we simulated cells whose maximal length was only 2μm and the minimal separation before the spherical caps was zero, i.e., the cells became circles immediately after division. As before we selected a set of k's such that the thickness and roughness were approximately the same for all simulations. In order to make a fair comparison between "short rods" and "long rods" from previous simulations, thickness and roughness were expressed in cell lengths rather than in μm. This was done by dividing both h and ρ by the average length of a cell measured for cells from the growing layer. Figure 4.10c show that short rods have a much higher surfing probability than long rods.

In all previous simulations, even for short rods, cells remembered their orientation from before division and growth always initially occurred in that direction. To see whether this has any impact on P_{surf}, we considered a scenario in which the new direction of growth is selected randomly and does not correlate with the direction prior to division. Figure 4.10c shows that P_{surf} almost does not change regardless whether a short cell randomly changes its orientation after division or not.

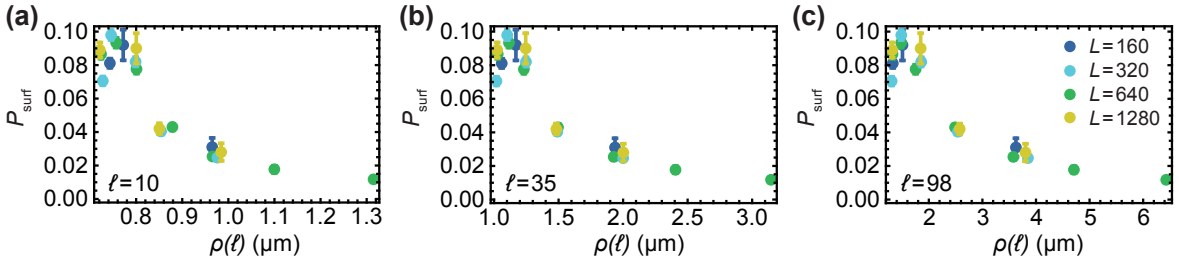

Figure 4.9: P_{surf} as the function of local roughness $\rho(l)$ of the growing layer, for different sizes $L = 160, 320, 640, 1280$ μm (as in Fig. 4.7) and $s = 0.02$. (a) $l = 10$, (b) $l = 35$, (c) $l = 98$ μm. For each l, data points for different L collapse onto a single curve.

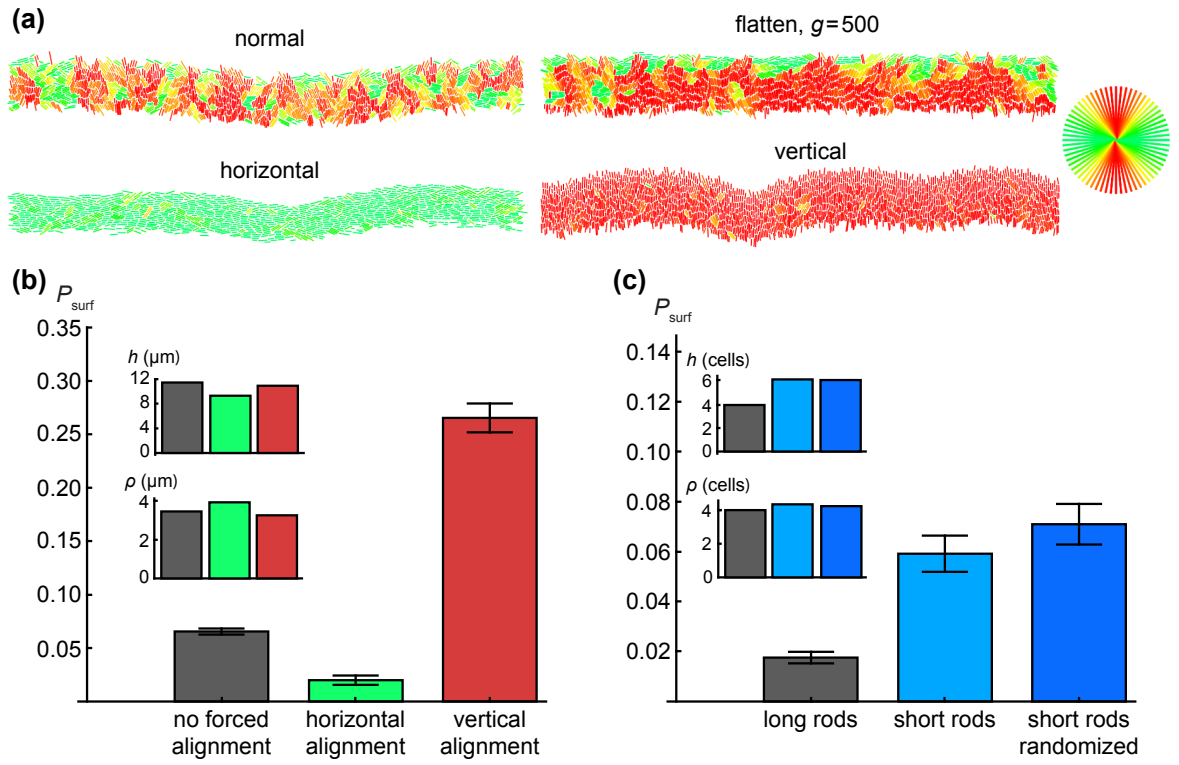

Figure 4.10: (a) Orientation of cells (colours as in the circle in the upper-right corner) in the growing layer for different models. (b, c) Comparison of fixation probabilities for different cellular alignments at the front, for approximately the same thickness and roughness, both of which were controlled by varying k. To achieve this, different k needed to be used in panels (b, c) and hence the two panels cannot be directly compared. In all cases $L = 320\mu$m, $s = 0.02$. For horizontally- and vertically-forced cells, $\tau_{\max} = 10000$. Short cells have a maximum length of 2μm; upon division, they become circles of diameter 1μm.

4.4.3 Surfing probability and the mechanical properties of bacteria

Our results from the previous section demonstrate that surfing is affected by (i) the roughness of the growing layer, (ii) the orientation of cells, (iii) the thickness of the growing layer if mutations occur inside the growing layer and not only at its edge. To show this, we varied thickness, roughness, and orientation of cells by using *ad hoc* external forces flattening out the front or forcing the cells to order in a particular way. In this section we will investigate what parameters of the model affect surfing in the absence of such artificial force fields.

Thickness of the growing layer.

If cells are prohibited to form multiple layers, as in our 2d simulations, thickness h can be determined from the parameters of the model by a simple dimensional analysis. Assuming that h is proportional to the characteristic scale over which the nutrient concentration and cell density reaches bulk values[17], we can approximate h by

$$h \approx \sqrt{\frac{E}{(\zeta/a)\phi}}(1/\beta - 1)^{3/4}, \tag{4.7}$$

where E is the elastic modulus of the bacterium (Pa), a is the average area per cell (μm^2), ζ is the friction coefficient (Pa·h), ϕ is the replication rate (h^{-1}), and $\beta < 1$ is a dimensionless ratio of the nutrient consumption rate to biomass production rate (i.e. new bacteria): $\beta = (k\rho_0)/(\phi c_0)$. Equation (4.7) shows that thickness h increases with increasing cell stiffness (larger E) and replication rate ϕ, and decreases with increasing nutrient uptake k and increasing friction ζ. The aspect ratio of the cells does not affect h in our model. Equation (4.7) suggests that the thickness of the growing layer can be conveniently controlled in an experiment by varying temperature or growth medium (which both affect the growth rate), or by varying the nutrient concentration c_0. We shall use the first two methods when discussing the experimental verification of our theory.

Orientation of cells.

A useful measure of the global alignment of cells in the colony is the order parameter $S = \langle \cos^2(\phi - \Phi) \rangle$. Here ϕ is the angle a cell makes with the x-axis and Φ is the angular coordinate of the vector normal to the front; this is to remove a trivial contribution to S due to the curvature of the front caused by roughness. According to this definition, $S = 1$ if all cells are perfectly vertically aligned (in the direction of growth), $S = 0$ if they are horizontal (parallel to the front), and $S = 1/2$ if their orientations are random. It turns out that changing the uptake rate (and hence thickness h) from $k = 1.6$ to $k = 2.8$ changes S by a small amount from $S = 0.77$ to $S = 0.70$. Here we are more interested in other factors that do not affect h.

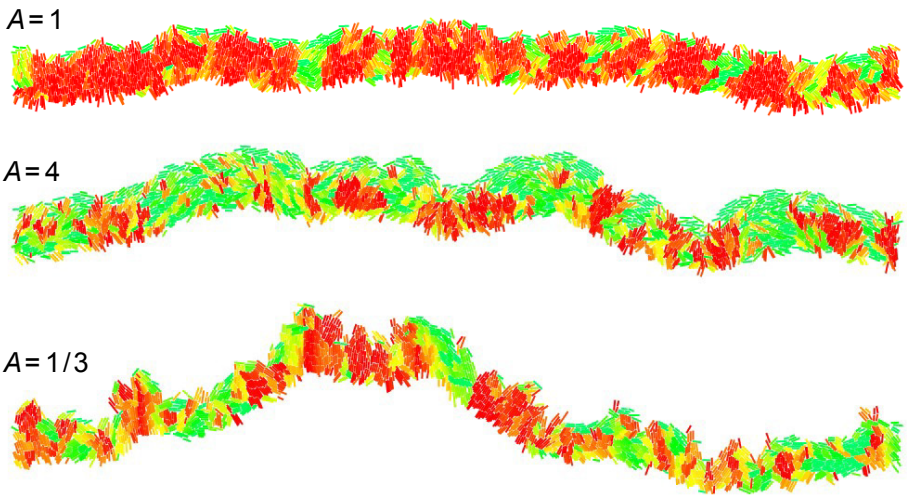

Figure 4.11: Snaphots of a growing colony with different friction anisotropy. The global order parameter $S = 0.79$ (isotropic friction $A = 1$), $S = 0.53$ (rolling rods $A = 4$), and $S = 0.63$ (sliding rods $A = 1/3$).

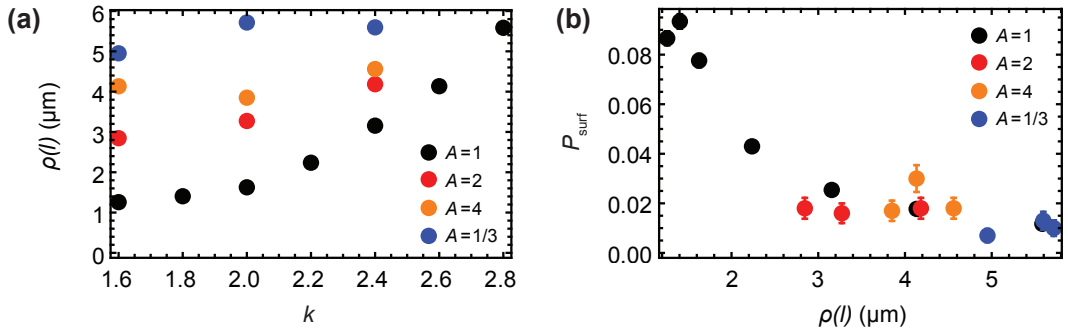

Figure 4.12: (a) Roughness ρ as the function of k, for different levels of friction anisotropy: no anisotropy (black points, $A = 1$), "rolling rods" $A = 2$ (red), $A = 4$ (orange), and "sliding rods" $A = 1/3$ (blue). (b) surfing probability versus ρ for the same parameters as in panel (a).

Friction.

One such factor is the nature of friction between cells and the substrate. So far, in all simulations the friction force was proportional to the cell's velocity, irrespective of the direction of motion. To test whether this assumption affected front roughness and the surfing probability, we ran simulations in which friction coefficients were different in the directions parallel and perpendicular to the cell's axis. We replaced Eq. (4.1)

for the dynamics of the centre of mass with the following equation:

$$\frac{d\vec{r}_i}{dt} = K^{-1}\vec{F}/m, \tag{4.8}$$

where the matrix K accounts for the anisotropy of friction:

$$K = \begin{bmatrix} \zeta_{\parallel} n_x^2 + \zeta_{\perp} n_y^2 & (\zeta_{\parallel} - \zeta_{\perp}) n_x n_y \\ (\zeta_{\parallel} - \zeta_{\perp}) n_x n_y & \zeta_{\perp} n_x^2 + \zeta_{\parallel} n_y^2 \end{bmatrix}. \tag{4.9}$$

We now have two friction coefficients: $\zeta_{\perp}$ is the coefficient in the direction perpendicular to cell's major axis $\vec{n}$, whereas $\zeta_{\parallel}$ is the coefficient in the parallel direction. For convenience, we shall assume that $\zeta_{\parallel} = A\zeta, \zeta_{\perp} = \zeta/A$ where A is the "asymmetry coefficient" and ζ is the isotropic friction coefficient, same as in previous simulations (Table 1). For isotropic friction, $A = 1$, hence $\zeta_{\perp} = \zeta_{\parallel} \equiv \zeta$ and $K = 1\zeta$, and we recover Eq. (4.1). If $A > 1$, it is easier for the rod to "roll" than to slide along the major axis. If $A < 1$ it is easier for the rod to slide.

Figure 4.11 shows images of the front for different levels of friction anisotropy. In the anisotropic "rolling rods" case ($A > 1$), cells are significantly more oriented edge-on to the colony, and the roughness is noticeably larger. In the "sliding rods" case ($A < 1$) the roughness is even larger but the orientation of cells falls between the isotropic and the "rolling rods" case. This is quantified in Fig. 4.12a, where we plotted ρ as a function of k. The same figure, panel (b), shows that, as expected, the surfing probability goes down with increasing roughness.

4.5 Comparison with experiments

We next checked whether the predicted dependence of the surfing probability on the roughness of the growing layer agree with experiments. We measured surfing probabilities of beneficial mutants with different selective advantages $s = -5 \ldots 25\%$ in colonies of *E. coli* and *S. cerevisiae* (Methods) grown at different conditions affecting the roughness of the growing layer. A small number of fluorescently labeled mutant cells was mixed with a much larger number of wild-type cells, and a small droplet of the mixture was used to inoculate a colony on a Petri dish. After a few days, colonies with a characteristic sectoring pattern emerged (Fig. 4.13). By zooming into the colony edge we confirmed that some mutants "surfed" at the front and expanded into large sectors whereas some mutants did not make it and became trapped as bubbles in the bulk of the colony (Fig. 4.13, compare with Fig. 4.5).

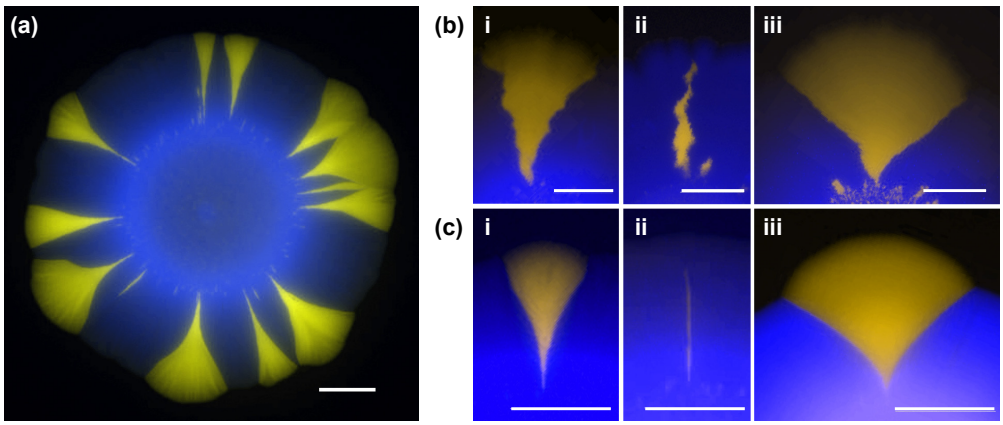

Figure 4.13: (a) An example of a *S. cerevisiae* colony with beneficial mutants (yellow) forming sectors. The mutants have a growth rate advantage of $s \approx 10\%$. (b,c) Fate of mutant cells - experimental counterpart of Fig. 4.5. Colonies of *E. coli* (b) and *S. cerevisiae* (c) were inoculated using a mixture of a majority of wild-type cells (blue, false colour) and a small number of mutant cells (yellow) with $s = 8\%$ (i and ii). Some mutant clones formed large sectors (i), while others (ii) lagged behind the front, became engulfed by wild-type cells and eventually ceased to grow ("bubbles"). A large growth advantage ($s \approx 16\%$, iii) caused the sector to "bulge out". All three phenomena are well reproduced by our simulations (c.f. Fig. 4.5). In all panels, scale bar = 2mm.

We counted the number N_{sec} of sectors and estimated the surfing probability P_{surf} from the formula[25]:

$$P_{\text{surf}} = \frac{N_{\text{sec}}}{2\pi r_0 P_{\text{i}}}, \tag{4.10}$$

where P_{i} is the initial fraction of mutant cells in the population and r_0 the initial radius of the colony (in units of cell diameters). Note this equation makes sense only if surfing is restricted to the first layer of cells; we have shown that this is true in computer simulations and we shall experimentally validate it later in this section. Fig. 4.14a shows P_{surf} for *E. coli* and *S. cerevisiae*, and for different conditions. In the limit of low selective advantage $s < 10\%$ we are interested here, the surfing probability is highest in colonies of roughly-spherical *S. cerevisiae*, which have rather smooth boundaries, and smallest for the rod-shaped bacterium *E. coli*, characterized by rough fronts. This agrees with our predictions (Fig. 4.10), however it does not yet show whether this is due to difference in the cell shape (aspect ratio, c.f. the penultimate paragraph of Sec. 4.2) or different thickness or roughness of the growing layer.

To study the connection between surfing and surface roughness, we computed the local roughness $\rho(l)$ as a function of window length l (Fig. 4.14b, cf. Eq. (4.6) and Methods) for the same colonies for which we previously calculated P_{surf} (Fig. 4.14a). In all cases, $\rho^2(l)$ showed a linear dependence on window length l after a transient at small window lengths, i.e., the colony boundary behaved like a standard random walk

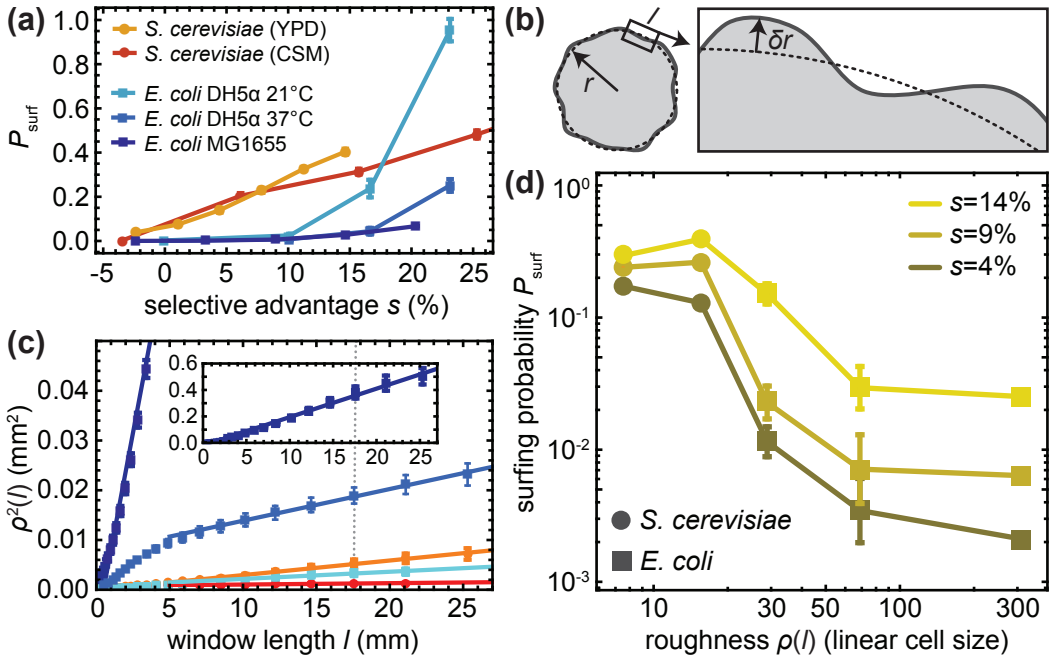

Figure 4.14: Surfing probability versus roughness in experimental colonies. In all panels squares and circles correspond to *E. coli* and *S. cerevisiae*, respectively. **(a)** Surfing probability P_{surf} for different species and growth conditions as a function of the selective advantage s. *S. cerevisiae* has a much higher P_{surf} at low s, while P_{surf} of *E. coli* strain DH5α at 21°C increases faster than linearly for large s, surpassing *S. cerevisiae* for $s > 15\%$. **(b)** Diagram illustrating how roughness $\rho(l)$ was measured (Methods). **(c)** The local roughness squared $\rho^2(l)$ for different conditions (colours as in (a), error bars are standard errors of the mean over at least 10 colonies per condition). Solid lines are linear fits to the data points. The dotted line corresponds to the window length $l = 17\text{mm}$ used to calculate roughness in panel (d). The inset shows $\rho^2(l)$ for *E. coli* MG1655 (dark blue), which has the highest roughness. **(d)** Surfing probability versus $\rho(l = 17\text{mm})$, for different s. To compare *E. coli* and *S. cerevisiae*, we normalized roughness by the linear cell size (square root of the average area), which we estimated from microscopy images to be 2 and 4.7μm, respectively.

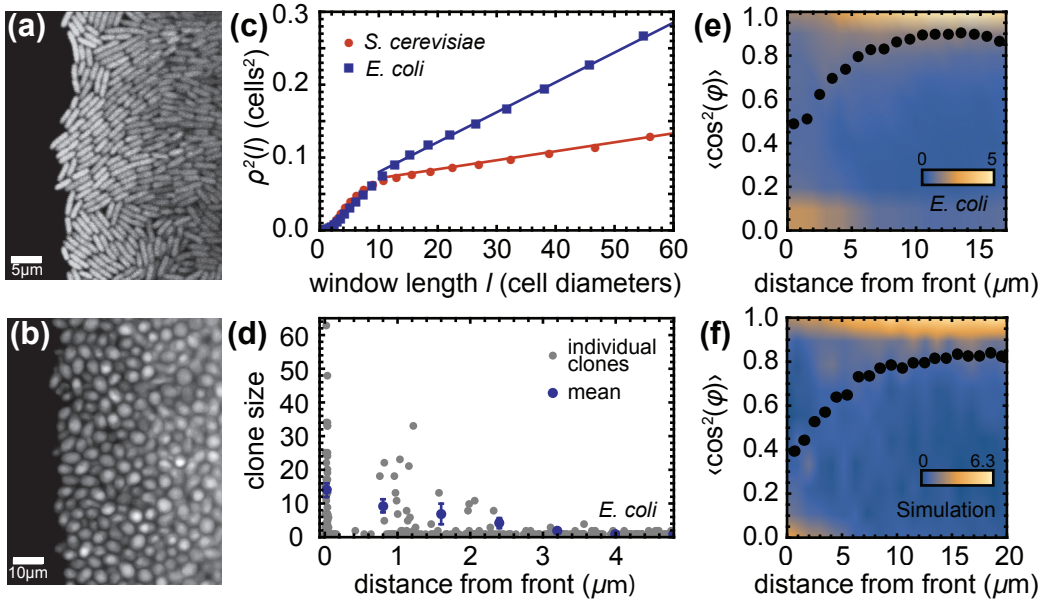

Figure 4.15: Microscopic properties of the growing layer. (a,b) Snapshot of an *E. coli* front (panel a, scalebar 5μm) and a *S. cerevisiae* front (panel b, scalebar 10μm) front. (c) Local roughness squared $\rho^2(l)$ as a function of the window size l. Dashed lines are fits to the data points. (d) The number of offspring for all initial cells near the front, for *E. coli*. Only cells within 2-3μm ($\sim$ one cell) from the edge of the colony have a significant number of offspring. (e) Probability density plot of the order parameter $\langle\cos^2\phi\rangle$ for *E. coli* as a function of the distance from the edge. Blue = low probability, yellow = high probability. The dotted line is the average order parameter versus the distance from the front. Cells are preferentially aligned with the direction of propagation, except for cells directly at the front, which are parallel to it. (f) Density plot of the order parameter for a simulated front with $k = 1.4, L = 320\mu$m.

(Fig. 4.14c).

We then tested the correlation of colony roughness with surfing probability in a similar way to what we did in computer simulations. In Fig. 4.14d, we plot the surfing probability P_{surf} as a function of colony roughness measured at one specific window length $l = 17$mm (dotted line in Fig. 4.14c), for different selective advantages s. We observe that the surfing probability of *E. coli* decreases with increasing roughness (Fig. 4.14d) for all s, in good qualitative agreement with our simulations. Similar results are obtained for different choices of the window length l for which roughness is calculated. The situation is less clear for *S. cerevisiae*; we hypothesize that this is due to roughness being too small (c.f. Fig. 4.9) to markedly affect the surfing probability.

We next examined how microscopic properties of the front (cellular orientation) correlated with macroscopic roughness. We analysed microscopic images of the fronts of *E. coli* and *S. cerevisiae* fronts (Methods,

data from Ref. 25), and measured local roughness $\rho(l)$ over sub-mm length scales l. Example snapshots in Fig. 4.15a,b show that roughness of the fronts indeed differ very much for these two microorganisms. Figure 4.15c confirms that *E. coli* has a much higher roughness compared to *S. cerevisiae*, suggesting that macroscopic roughness on the colony scale is a consequence of microscopic front roughness on the single-cell level.

To study the dynamics of surfing, we tracked *E. coli* cells over 200 minutes and measured their distance from, and orientation relative to the edge of the colony, as well as the number of offspring for all cells in the initial image. Figure 4.15d shows that cells only have an appreciable number of offspring if they are within about one cell diameter of the front. This agrees with our conclusion from simulations and justifies inserting mutants only directly at the front.

Figure 4.15e shows the order parameter $S = \left\langle \cos^2(\phi - \Phi) \right\rangle$, which measures the orientation of cells and has been defined in Sec. 4.4.3, as a function of the distance from the front. Cells near the front tend to align parallel to the front. This changes quickly behind the front, with most cells being perpendicular to the growth direction starting about 5μm behind the front. Figure 4.15f shows the distribution of S obtained from simulations; the agreement with the experimental data from Fig. 4.15e is excellent, suggesting that our model indeed captures the dynamics of the growing bacterial front reasonably well.

4.6 Conclusions

In this work we have focused on the role of mechanical interactions in microbial colonies. We first used computer simulations to show that the speed of biological evolution, measured by the probability that a new mutation "surfs" at the growing edge of a microbial colony, depends mostly on the thickness and roughness of the growing layer of cells at colony's front. Thicker fronts decrease the per-cell surfing probability because only cells from the very first layer of cells create successful progenies, and the fraction of such cells decreases with increasing front thickness. Rougher fronts also decrease the surfing probability for a similar reason; only cells at the tips of front's protrusions are successful and these tips become smaller for rougher fronts. Moreover, roughness and thickness are related; thicker front have lower roughness and vice versa. While the dependence between genetic segregation and the front thickness[47], and between thickness and roughness[48] has been known previously, in this work we have shown that it is actually the roughness of the growing layer that should be thought of as affecting the surfing probability in the causal sense. We have also linked thickness and roughness to the mechanical properties of cells for the first time. Moreover, we have discovered that the orientation of cells has also a significant effect, irrespective of front roughness, on the surfing probability. Finally, we have confirmed some of our predictions (surfing probability versus front roughness and the orientation of cells versus distance from the front) in experiments in which we varied the growth rate and the type of cells.

All three quantities, front thickness, front roughness, and cellular alignment depend in a very non-trivial way on the properties of cells and their environment: cell-surface friction (and anisotropy of thereof), elasticity of cells, their growth/nutrient uptake rate, and their shape. Many of these parameters are very difficult to control experimentally without affecting other parameters. To properly disentangle the effect of the shape of cells, friction, growth rate etc. on the surfing probability, further experiments are required in which these factors are varied independently. For example, the shape of *E. coli* can be varied by using MreB mutants [49]; while this often also affects the growth rate [50], an experiment with round *E. coli* MreB mutants could complement our results in an interesting way.

Microbial evolution is a research area that is important both from fundamental and practical viewpoints. In particular, our research shows that mechanical forces such as friction can play a significant role in biological evolution of microorganisms. To our knowledge, this article is the first that not only puts forward this idea but also provides concrete arguments in its support.

From a more practical point of view, our results are relevant to the evolution of antimicrobial resistance. It has been demonstrated that even a small bacterial population can develop *de novo* resistance to some antimicrobial drugs in less than a day [51]. This rapid evolution makes the most popular drugs - antibiotics - increasingly ineffective [52]. Since the rate of discovery of new antibiotics has steadily declined over years [53], the evolution of drug-resistant bacteria has been highlighted as one of the major challenges we will face in the coming decades. By demonstrating the role of mechanical interactions on biological evolution in microbial aggregates, our research opens up a new antimicrobial paradigm in which the physical properties of microbes could be targeted alongside standard antimicrobial therapy to reduce the probability of evolving resistance to drugs.

Data and code

All simulation/experimental data sets and code are available from Edinburgh DataShare (**`http://dx.doi.org/10.7488/ds/1702`**)

References

[1] H. G. Schlegel, C. Zaborosch, and M. Kogut. *General Microbiology*. Cambridge University Press, July 1993.

[2] D. H. Pieper and W. Reineke. Engineering bacteria for bioremediation. *Current Opinion in Biotechnology*, 11(3):262–270, June 2000. doi: 10.1016/S0958-1669(00)00094-X.

[3] W. Sabra, D. Dietz, D. Tjahjasari, and A.-P. Zeng. Biosystems analysis and engineering of microbial consortia for industrial biotechnology. *Engineering in Life Sciences*, 10(5):407–421, October 2010. doi: 10.1002/elsc.201000111.

[4] S. Chattopadhyay, S. J. Weissman, V. N. Minin, T. A. Russo, D. E. Dykhuizen, and E. V. Sokurenko. High frequency of hotspot mutations in core genes of Escherichia coli due to short-term positive selection. *Proceedings of the National Academy of Sciences*, 106(30):12412–12417, 2009.

[5] G. Koch, A. Yepes, K. U. Förstner, C. Wermser, S. T. Stengel, J. Modamio, K. Ohlsen, K. R. Foster, and D. Lopez. Evolution of Resistance to a Last-Resort Antibiotic in Staphylococcus aureus via Bacterial Competition. *Cell*, 158(5):1060–1071, August 2014. doi: 10.1016/j.cell.2014.06.046.

[6] S. F. Elena and R. E. Lenski. Evolution experiments with microorganisms: the dynamics and genetic bases of adaptation. *Nature Reviews Genetics*, 4(6):457–469, June 2003. doi: 10.1038/nrg1088.

[7] G. G. Perron, A. Gonzalez, and A. Buckling. The rate of environmental change drives adaptation to an antibiotic sink. *Journal of Evolutionary Biology*, 21(6):1724–1731, November 2008. doi: 10.1111/j.1420-9101.2008.01596.x.

[8] B. Carpentier and O. Cerf. Biofilms and their consequences, with particular reference to hygiene in the food industry. *Journal of Applied Microbiology*, 75(6):499–511, 1993. doi: 10.1111/j.1365-2672.1993.tb01587.x.

[9] J. W. Costerton, P. S. Stewart, and E. P. Greenberg. Bacterial Biofilms: A Common Cause of Persistent Infections. *Science*, 284(5418):1318–1322, May 1999. doi: 10.1126/science.284.5418.1318.

[10] D. Berry, C. Xi, and L. Raskin. Microbial ecology of drinking water distribution systems. *Current Opinion in Biotechnology*, 17(3):297–302, June 2006. doi: 10.1016/j.copbio.2006.05.007.

[11] R. L. Gibson, J. L. Burns, and B. W. Ramsey. Pathophysiology and Management of Pulmonary Infections in Cystic Fibrosis. *American Journal of Respiratory and Critical Care Medicine*, 168(8): 918–951, October 2003. doi: 10.1164/rccm.200304-505SO.

[12] P. S. Stewart and J. William Costerton. Antibiotic resistance of bacteria in biofilms. *The Lancet*, 358 (9276):135–138, 2001.

[13] E. Drenkard. Antimicrobial resistance of Pseudomonas aeruginosa biofilms. *Microbes and Infection*, 5(13):1213–1219, November 2003. doi: 10.1016/j.micinf.2003.08.009.

[14] E. B. M. Breidenstein, C. de la Fuente-Nunez, and R. E. W. Hancock. Pseudomonas aeruginosa: all roads lead to resistance. *Trends in Microbiology*, 19(8):419–426, August 2011. doi: 10.1016/j.tim.2011.04.005.

[15] P. K. Singh, A. L. Schaefer, M. R. Parsek, T. O. Moninger, M. J. Welsh, and E. P. Greenberg. Quorum-sensing signals indicate that cystic fibrosis lungs are infected with bacterial biofilms. *Nature*, 407 (6805):762–764, October 2000. doi: 10.1038/35037627.

[16] D. Boyer, W. Mather, O. Mondragon-Palomino, S. Orozco-Fuentes, T. Danino, J. Hasty, and L. S. Tsimring. Buckling instability in ordered bacterial colonies. *Physical Biology*, 8(2):026008, April 2011. doi: 10.1088/1478-3975/8/2/026008.

[17] F. D. C. Farrell, O. Hallatschek, D. Marenduzzo, and B. Waclaw. Mechanically Driven Growth of Quasi-Two-Dimensional Microbial Colonies. *Phys. Rev. Lett.*, 111(16):168101, October 2013. doi: 10.1103/PhysRevLett.111.168101.

[18] C. Giverso, M. Verani, and P. Ciarletta. Emerging morphologies in round bacterial colonies: comparing volumetric versus chemotactic expansion. *Biomechanics and Modeling in Mechanobiology*, August 2015. doi: 10.1007/s10237-015-0714-9.

[19] P. Ghosh, J. Mondal, E. Ben-Jacob, and H. Levine. Mechanically-driven phase separation in a growing bacterial colony. *Proceedings of the National Academy of Sciences*, page 201504948, 2015.

[20] D. Volfson, S. Cookson, J. Hasty, and L. S. Tsimring. Biomechanical ordering of dense cell populations. *Proc. Natl. Acad. Sci. U. S. A.*, 105(40):15346–51, October 2008. doi: 10.1073/pnas.0706805105.

[21] P.-T. Su, C.-T. Liao, J.-R. Roan, S.-H. Wang, A. Chiou, and W.-J. Syu. Bacterial Colony from Two-Dimensional Division to Three-Dimensional Development. *PLoS ONE*, 7(11):e48098, November 2012. doi: 10.1371/journal.pone.0048098.

[22] M. Asally, M. Kittisopikul, P. Rue, Y. Du, Z. Hu, T. Cagatay, A. B. Robinson, H. Lu, J. Garcia-Ojalvo, and G. M. Suel. From the Cover: Localized cell death focuses mechanical forces during 3d patterning in a biofilm. *Proceedings of the National Academy of Sciences*, 109(46):18891–18896, September 2012. doi: 10.1073/pnas.1212429109.

[23] M. A. A. Grant, B. Wacaw, R. J. Allen, and P. Cicuta. The role of mechanical forces in the planar-to-bulk transition in growing Escherichia coli microcolonies. *Journal of The Royal Society Interface*, 11 (97):20140400–20140400, June 2014. doi: 10.1098/rsif.2014.0400.

[24] E. R. Oldewurtel, N. Kouzel, L. Dewenter, K. Henseler, B. Maier, and R. Kolter. Differential interaction forces govern bacterial sorting in early biofilms. *eLife*, 4:e10811, October 2015. doi: 10.7554/eLife.10811.

[25] M. Gralka, F. Stiewe, F. Farrell, W. Möbius, B. Waclaw, and O. Hallatschek. Allele surfing promotes microbial adaptation from standing variation. *Ecology Letters*, pages n/a–n/a, June 2016. doi: 10.1111/ele.12625.

[26] S. Klopfstein, M. Currat, and L. Excoffier. The Fate of Mutations Surfing on the Wave of a Range Expansion. *Molecular Biology and Evolution*, 23(3):482–490, March 2006. doi: 10.1093/molbev/msj057.

[27] D. Fusco, M. Gralka, A. Anderson, J. Kayser, and O. Hallatschek. Excess of mutational jackpot events in growing populations due to gene surfing. *bioRxiv*, page 053405, 2016.

[28] O. Hallatschek, P. Hersen, S. Ramanathan, and D. R. Nelson. Genetic drift at expanding frontiers promotes gene segregation. *Proc. Natl. Acad. Sci. U. S. A.*, 104(50):19926–30, December 2007. doi: 10.1073/pnas.0710150104.

[29] L. Excoffier, M. Foll, and R. J. Petit. Genetic consequences of range expansions. *Annual Review of Ecology, Evolution, and Systematics*, 40:481–501, 2009.

[30] O. Hallatschek and D. R. Nelson. Life at the front of an expanding population. *Evolution*, 64(1): 193–206, January 2010. doi: 10.1111/j.1558-5646.2009.00809.x.

[31] K. D. Behrman and M. Kirkpatrick. Species range expansion by beneficial mutations. *Journal of Evolutionary Biology*, 24(3):665–675, March 2011. doi: 10.1111/j.1420-9101.2010.02195.x.

[32] A. Ali, E. Somfai, and S. Grosskinsky. Reproduction-time statistics and segregation patterns in growing populations. *Physical Review E*, 85(2):021923, February 2012. doi: 10.1103/PhysRevE.85.021923.

[33] K. S. Korolev, M. J. I. Müller, N. Karahan, A. W. Murray, O. Hallatschek, and D. R. Nelson. Selective sweeps in growing microbial colonies. *Phys. Biol.*, 9(2):026008, January 2012. doi: 10.1088/1478-3975/9/2/026008.

[34] R. Lehe, O. Hallatschek, and L. Peliti. The rate of beneficial mutations surfing on the wave of a range expansion. *PLoS Comput. Biol.*, 8(3):e1002447, January 2012. doi: 10.1371/journal.pcbi.1002447.

[35] J. D. Murray. *Mathematical Biology, Vol. 2*. Springer-Verlag, Berlin, 2003.

[36] J.-U. Kreft. Biofilms promote altruism. *Microbiology*, 150(8):2751–2760, 2004. doi: 10.1099/mic.0.26829-0.

[37] J. B. Xavier and K. R. Foster. Cooperation and conflict in microbial biofilms. *Proc. Natl. Acad. Sci.*, 104(3):876–881, January 2007. doi: 10.1073/pnas.0607651104.

[38] J. a. B. Xavier, E. Martinez-Garcia, and K. R. Foster. Social evolution of spatial patterns in bacterial biofilms: when conflict drives disorder. *Am. Nat.*, 174(1):1–12, July 2009. doi: 10.1086/599297.

[39] H. Hoffman and M. E. Frank. Synchrony of division in clonal microcolonies of Escherichia coli. *Journal of bacteriology*, 89(2):513–517, 1965.

[40] A. S. Kennard, M. Osella, A. Javer, J. Grilli, P. Nghe, S. J. Tans, P. Cicuta, and M. Cosentino Lagomarsino. Individuality and universality in the growth-division laws of single \textit{E. coli} cells. *Physical Review E*, 93(1):012408, January 2016. doi: 10.1103/PhysRevE.93.012408.

[41] S. Iyer-Biswas, C. S. Wright, J. T. Henry, K. Lo, S. Burov, Y. Lin, G. E. Crooks, S. Crosson, A. R. Dinner, and N. F. Scherer. Scaling laws governing stochastic growth and division of single bacterial cells. *Proceedings of the National Academy of Sciences*, 111(45):15912–15917, November 2014. doi: 10.1073/pnas.1403232111.

[42] M. O. Lavrentovich, K. S. Korolev, and D. R. Nelson. Radial Domany-Kinzel models with mutation and selection. *Phys. Rev. E*, 87(1):012103, January 2013. doi: 10.1103/PhysRevE.87.012103.

[43] P. D. Freese, K. S. Korolev, J. I. Jimenez, and I. A. Chen. Genetic Drift Suppresses Bacterial Conjugation in Spatially Structured Populations. *Biophysical Journal*, 106(4):944–954, February 2014. doi: 10.1016/j.bpj.2014.01.012.

[44] H. Fujikawa and M. Matsushita. Fractal Growth of Bacillus subtilis on Agar Plate. *J. Phys. Soc. Jpn*, 1989.

[45] K. Kawasaki, A. Mochizuki, M. Matsushita, T. Umeda, and N. Shigesada. Modeling spatio-temporal patterns generated by Bacillus subtilis. *J. Theor. Biol.*, 188(2):177–85, September 1997. doi: 10.1006/jtbi.1997.0462.

[46] M. A. Nowak. *Evolutionary Dynamics*. Belknap/Harvard, Camridge, Massachusetts, 2006.

[47] C. D. Nadell, K. R. Foster, and J. a. B. Xavier. Emergence of Spatial Structure in Cell Groups and the Evolution of Cooperation. *PLoS Computational Biology*, 6(3):e1000716, March 2010. doi: 10.1371/journal.pcbi.1000716.

[48] D. A. Head. Linear surface roughness growth and flow smoothening in a three-dimensional biofilm model. *arXiv preprint arXiv:1210.8103*, 2012.

[49] W. P. Smith, Y. Davit, J. M. Osborne, W. Kim, K. R. Foster, and J. M. Pitt-Francis. Cell morphology drives spatial patterning in microbial communities. *Proceedings of the National Academy of Sciences*, 114(3):E280–E286, 2017.

[50] C. N. Takacs, S. Poggio, G. Charbon, M. Pucheault, W. Vollmer, and C. Jacobs-Wagner. Mreb drives de novo rod morphogenesis in caulobacter crescentus via remodeling of the cell wall. *Journal of bacteriology*, 192(6):1671–1684, 2010.

[51] Q. Zhang, G. Lambert, D. Liao, H. Kim, K. Robin, C.-k. Tung, N. Pourmand, and R. H. Austin. Acceleration of Emergence of Bacterial Antibiotic Resistance in Connected Microenvironments. *Science*, 333(6050):1764–1767, September 2011. doi: 10.1126/science.1208747.

[52] F. Baquero and J. Blazquez. Evolution of antibiotic resistance. *Trends in Ecology & Evolution*, 12(12):482–487, December 1997. doi: 10.1016/S0169-5347(97)01223-8.

[53] B. Spellberg, R. Guidos, D. Gilbert, J. Bradley, H. W. Boucher, W. M. Scheld, J. G. Bartlett, J. Edwards, and the Infectious Diseases Society of America. The Epidemic of Antibiotic-Resistant Infections: A Call to Action for the Medical Community from the Infectious Diseases Society of America. *Clinical Infectious Diseases*, 46(2):155–164, January 2008. doi: 10.1086/524891.

5

Environmental heterogeneity reduces the efficacy of natural selection

Genetic drift, the stochasticity associated with proliferation, can be viewed as a force limiting the efficacy of natural selection: if it is strong, a spontaneous mutation can behave neutrally even if it confers a growth rate advantage. Genetic drift is particularly strong at the front of range expansions, where a small number of founding individuals at the population frontier determines the future genetic structure of the population. Evolutionary outcomes are thus intimately coupled to the dynamics at the population frontier, which in turn depends on the local environment. Environmental heterogeneities, which may favor or depress an individual's reproductive success regardless of its inherent fitness and direct its motion, may therefore be able to shape the evolutionary dynamics in such populations. To test this, we used colonies of *E. coli* with stochastic phenotype switches carrying a tunable fitness effect as a simple model system to show that strong environmental heterogeneity can dramatically impact the efficacy of selection. Our results are supported by simple simulations of expanding populations in heterogeneous environments, suggesting that the depression of selection is a generic consequence of extrinsic disorder and may also be important in other spatially expanding populations such as tumors or biofilms.

5.1 Introduction

Noise, and its competition with deterministic forces, plays an integral role in biology, such as in stochastic gene expression, cellular decision making, and cell differentiation[1]. Stochasticity is also a crucial component of evolutionary dynamics: not only do the mutations entering a population occur at random times in random individuals and at random positions in their genome, but in addition the fate of a mutation and its clonal lineage is largely stochastic and only partly determined by its effect on the individual's fitness.

The random fluctuations in the frequency of a mutant allele due to reproductive noise are called genetic drift. Genetic drift is particularly strong at the front of range expansions, a consequence of the relatively small number of individuals at the front of the expansion who contribute to future growth. The neutral diversity and adaptation in spatially expanding populations has been studied in computer simulations[2,3], in the field[4–6], and in microbial colonies[7–10]. In microbial colonies, nutrient gradients limit the number of proliferating individuals to a small region close to the colony perimeter called the growth layer. As a consequence, neutral mutation often have much larger clones compared to what is expected in well-mixed populations[8], and most mutant offspring are concentrated in a relatively small number of enormously successful lineages that "surf" on the expanding population wave. These successful lineages appear as sectors that remain in contact with the population front, while less successful lineages have lost contact with the front and appear as small patches called bubbles. The effects of mutations conferring a fitness effect during range expansions are more subtle. Deleterious mutations are predicted to remain at the population frontier for extended periods because genetic drift is strong at the front[11–14]. On the other hand, beneficial mutants can sweep to high frequency much faster in microbial colonies than in well-mixed populations[9].

The fate of spontaneous mutations in expanding microbial colonies is determined through the competition of selection and genetic drift[9,15]. Although the direct mapping is typically unknown, the strength of genetic drift in a microbial colony is fully characterized by microscopic details, e.g., cell-cell adhesion and cell shape[15], and as such can be regarded as an *intrinsic* property to the population. Most studies of evolutionary dynamics in microbial colonies so far have focused on homogeneous environments, where the intrinsic noise is the only source of stochasticity in the system.

Here, extending the successful framework of intrinsic vs. extrinsic noise of systems biology to evolution in microbial populations[16,17], we ask about the effects of *extrinsic* noise on evolutionary dynamics in microbial colonies. A simple example of an extrinsic factor that can impact evolution is environmental heterogeneity, which can alter the growth of the population and thus the evolutionary dynamics in fundamental ways. For instance, temporal and spatial gradients in antibiotic concentration vastly accelerated the emergence of resistance in recent experiments in shaken cultures[18], microfluidic devices[19] and on agar plates[20], as predicted by theory[21–25].Apart from antibiotic gradients, the effects of spatial heterogeneity on evolutionary dynam-

ics has been studied in experiments only with neutral alleles in fixed geometries, such as isolated obstacles creating "geometry-enhanced" genetic drift[26].

By contrast, little is understood about the quantitative effects of more complex environmental heterogeneities on evolutionary processes in microbial colonies. Here, we study the effects of random environmental disorder on the evolutionary dynamics in microbial populations. To this end, we employ the loss of a plasmid in *E. coli* as a model system for mutations with tunable growth rate effects whose clones can be tracked under the microscope. To study the effects of environmental disorder we grew colonies of *E. coli* on solid substrates that were either smooth or had a randomly patterned surface. We find that extrinsic noise created by environmental heterogeneity can overpower selection and reduces its efficacy to such a degree that even strongly beneficial mutations are unable to establish at rates higher than expected if they were neutral. Our results are corroborated by simple toy model simulations, suggesting that our results may generalize to other spatially growing populations, such as biofilms, tumors, and invasive species.

5.2 Results

5.2.1 Experiments

We used a strain of *E. coli* carrying a plasmid that is costly for cells to produce, resulting in a 20% growth rate disadvantage in plasmid-bearing cells compared to their plasmid-less (but otherwise isogenic) conspecifics. This strain loses the plasmid stochastically at a rate of about 5×10^{-3} per cell division (approximately independent of antibiotic concentration, see SI). The plasmid carries a gene conferring resistance to the antibiotic doxycycline (a tetracycline analog), such that the absence of the plasmid can become unfavorable when the cells are faced with increasing concentrations of the drug. Thus, by varying the amount of doxycycline in the growth media, the relative growth rates of the plasmid-bearing ("wild type") and non-bearing ("mutant") cells could be finely tuned, allowing us to treat plasmid loss as beneficial, neutral and deleterious mutations in different environments. We focus first on colonies grown on standard, "smooth", agar plates, allowing us to characterize the intrinsic noise. Afterwards, we contrast our findings with colonies grown on agar plates with a randomly patterned surface.

Homogeneous environment

We grew colonies from single cells on solid LB agar plates containing varying amounts of doxycycline ($n \geq 30$ per concentration), resulting in fitness differences s ranging from $+20\%$ to -15% (see SI Fig. 5.S2). After 3 days of growth, mutant clone appeared as dark regions in the fluorescence channel. We determined the size and number of mutant clones in the colonies and compute the frequency f_{MT} of mutants per colony as the

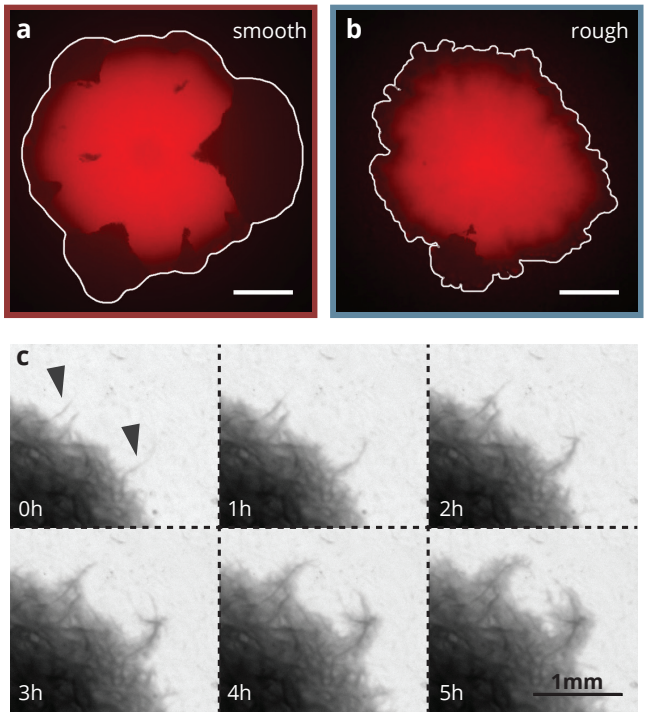

Figure 5.1: Surface roughness changes bacterial colony morphology. Colonies of *E. coli* grown from single cells harboring a plasmid containing a fluorescence gene and a resistance cassette. Loss of the plasmid leads to non-fluorescent ("mutant") sectors in the population that expand at the expense of the fluorescent ("wild-type)" population. Colony morphology depends on whether the colony grows on smooth (a) or rough (b, created by patterning the agar with filter paper) agar surfaces. (c) On rough surfaces, troughs in the surface direct growth along them, leading to locally accelerated regions that slowly widen and connect with the bulk of the population.

primary readout of our experiments, as it can serve as a proxy for the rate of adaptation of the population and thus allowed us to quantify the evolutionary dynamics in different scenarios.

When the mutants had a fitness advantage (at low doxycycline concentrations), their frequency f_{MT} increased rapidly as the population grows: for the highest advantage in our experiments, mutants made up roughly half of the total population (Fig. 5.2b). As the antibiotic concentration was increased, the mutants became first neutral and eventually deleterious at higher concentrations. In such conditions, the mutant frequency decreased approximately exponentially with the fitness cost (SI Fig. 5.S4) such that mutants made up only a small fraction of the final population.

Almost all mutants were found in sectors, clonal regions constituting a single lineage of mutants; we found 4 sectors on average at the highest mutant fitness advantage. This implies that out of millions of mutations that arose during the growth of the colony to a size of about 10^{10} cells (see SI Fig. 5.S5), the vast

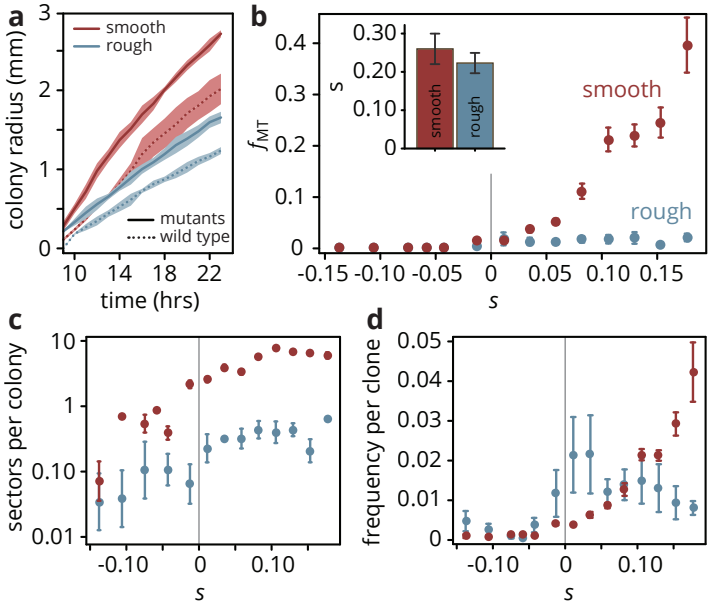

Figure 5.2: Surface roughness affected the efficacy of selection in bacterial colonies. Colonies grew more slowly on rough surfaces (a), but relative growth rate differences s were maintained (b, inset). (a) The final frequency f_{MT} after 3 days of growth for mutants of a given fitness (dis)advantage s differed strongly depending on the roughness of the surface they were grown on. On smooth plates, the mutant frequency f_{MT} increased with the selective advantage s of the mutants, whereas f_{MT} was independent of s for $s > 0$ on rough surfaces, and overall much smaller than in smooth colonies. The number of establishing sectors (c) was much smaller in rough colonies, and the average clone size (d) did not vary as strongly with s as in smooth colonies.

majority had a negligible number of offspring and had essentially no impact on the genetic make-up of the population. For our experiments, we estimated the average probability u to form a sector (the establishment probability) of a single beneficial mutation to be of order $u \sim 10^{-7}$. Thus, the success of an individual mutation in a microbial colony is an extremely rare event, even if it is strongly beneficial. The low success probability is a consequence of two processes: firstly, a mutation has to arise in the very first cell layer in order to have a large number of offspring[9] – any mutation born behind the front is quickly swept out of the growth layer by cells ahead of it. Growth layer thickness varies between different organisms and growth media; for *E. coli* on nutrient-rich media, a growth layer width of $\approx 10 - 15$ cells has been reported[9]. Likewise, any mutation that occurs during the growth in height behind the front is doomed to having only a small number of offspring before depleting its nutrients. Thus, for a typical colony height of ≈ 150 cells (see SI Fig. 5.S5), only about 1 in about 1000 mutations has any potential for success, simply because the vast majority of mutations necessarily arises in unfavorable locations. Secondly, even if the mutation arises in

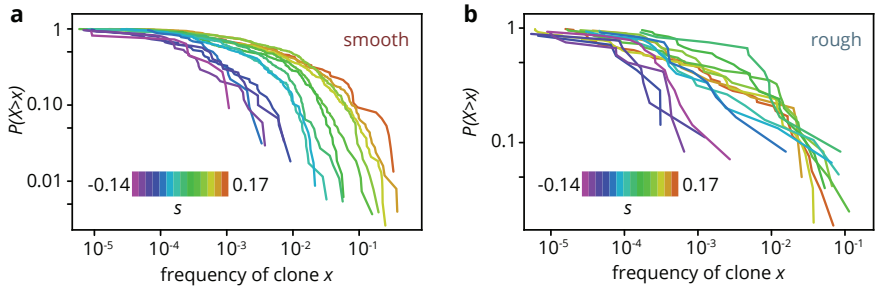

Figure 5.3: Clone size distribution $P(X > x)$ for colonies grown on smooth (a) and rough (b) substrates. Deleterious mutants are shown in magenta tones; their clones are typically small. Neutral clones are shown green; their size distribution had a broad tail. Advantageous mutations (red tones) in smooth colonies were even more broadly distributed, as large sectors establish more often. Beneficial clones in rough colonies had size distributions that were indistinguishable from the distribution for neutral mutations.

the very first layer of cells, it still has to survive genetic drift. Genetic drift in microbial colonies amounts to the random fluctuations in the sector boundaries, which are a result of the stochasticity associated with the process of cell growth and division, and subsequent cell motion due to mechanical pushing of cells on each other[7,27]. In addition, when the population is characterized by a rough front like our *E. coli* colonies, a mutation that arises inside a lagging region will have a lower chance of establishing than one that arises (by chance) in a region that is ahead. In our colonies, we estimated that about 2000 mutations per colony arose in favorable positions, each of which had an establishment probability of about 10^{-3}.

Thus, most mutations will not manage to create sectors. Since we could detect individual mutant clones under the microscope and compute their frequency x in the population, shown in Fig. 5.3a. The clone size distribution $P(X > x)$, which is related to the site frequency spectrum in population genetics, can help predict rare evolutionary outcomes such as fitness valley crossing[28] and evolutionary rescue[8], and is well understood for toy models of microbial colonies[8,29]. For neutral mutations, the clone size distribution is expected to be broad up to a shoulder indicating the typical size of the largest expected bubble. In our experiments, we indeed observed a broad shoulder-like distribution for neutral mutations, consistent with earlier experiments using population sequencing[8] (Fig. 5.3a). For beneficial mutations, the larger number of bulging sectors created an even broader distribution with maximum clone sizes of almost half the population, while the distribution for strongly deleterious mutations was cut off at small clone sizes. The clone size distribution is consistent with our initial observation that a larger selective advantage s gave rise to a larger overall mutant frequency, but it also shows that even at the largest $s \approx 0.17$, most mutant clones remained small, with more than half of the visible clones reaching frequencies of at most 1%.

Heterogeneous environment

To investigate the effect of a rough surface on colony growth and adaptation, we embedded filter paper into melted agar and removed it after cooling and drying, creating a rough agar surface characterized by troughs and elevations about 50μm high and 30μm wide. Colonies grown on rough substrates (hereafter called "rough" colonies) had a rougher front line (Fig.5.1b, SI Fig. 5.S6) than those grown on smooth substrates ("smooth" colonies). In addition, the filter paper left grooves in the agar surface that the bacteria colonized first, leading the branch-like outgrowths that grew far ahead of the rest of the population and broadened as they were incorporated into the bulk of the colony (Fig. 5.1c).

The final mutant frequency f_{MT} in rough colonies was markedly different from what we found in smooth colonies (Fig. 5.1c, blue): while the neutral frequency was roughly the same in both treatments, rough colonies showed no increase in mutant frequency as the fitness advantage s of the mutants increased, in contrast to smooth colonies, where the mutant frequency increased by a factor of 10 at the largest selective advantage $s \approx 0.16$ compared to the neutral case. This effect did not stem from an altogether elimination of selection: when colonies of mutant and wild type were grown separately on rough substrates, mutants had a fitness advantage (as measured by the radial growth rate) over the wild type consistent with the advantage they enjoyed on smooth substrates (Fig. 5.2a, inset). The insensitivity of f_{MT} to selective advantages could be broken down into a combination of two factors: the number of sectors was lower in rough colonies than in smooth colonies and constant for positive s (Fig. 5.1d), and the frequency per clone changed only little with s for $s > 0$ in rough colonies, whereas it increased exponentially with s in smooth colonies.

This discrepancy between smooth and rough colonies held also at the level of individual clones (Fig. 5.3): for all $s > 0$, the clone size distributions obtained from rough colonies were virtually indistinguishable. By contrast, negative selection tended to decrease the size of mutant clones about equally in both smooth and rough colonies. Thus, beneficial clones in rough colonies behaved effectively neutrally, whereas deleterious mutations were fully affected by their growth rate disadvantage.

Taken together, our results show that the effects of environmental disorder were two-fold: (1) it increased the strength of genetic drift, as evidenced by the lower establishment probability of beneficial mutations, and (2) it altered the expansion dynamics of established clones. To understand whether these two effects are a generic result of environmental heterogeneity we turned to simple simulations with a strongly idealized form of environmental disorder.

5.2.2 Simulations

As a simple model for spatially expanding population we employ a generalized version of the Eden model[30]. The population grows on a square lattice, initiated with a single filled site in the center. In each time step,

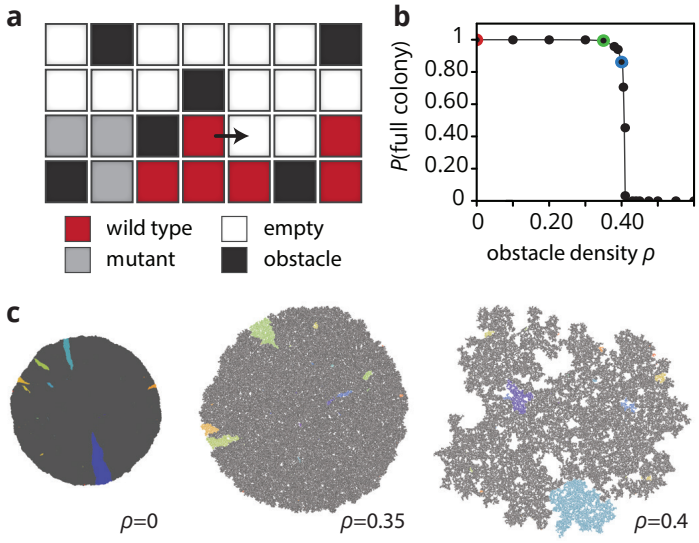

Figure 5.4: Simulating environmental disorder in a simple lattice growth model. (a) The simulation proceeds by allowing cells with empty neighbors to divide into empty space. Obstacles (black, density ρ) are distributed over the lattice to simulate environment heterogeneities. (b) If the obstacle density was larger than a critical density $\rho_c \approx 0.4$, the population was trapped and could not grow to full size. (c) Colony morphology changed depending on obstacle density and became increasing fractured as ρ approaches ρ_c. Mutant clones are shown in color.

a site with empty neighbor sites is chosen with probability proportional to its growth rate to divide into a randomly chosen empty neighbor site. With probability μ, a wild-type site acquires a single mutation, potentially conferring a fitness advantage or disadvantage s, upon division; already mutated sites do not acquire further mutations. This model is identical to that used in Ref.s 8 and 9, and its interfaces are well described by the KPZ equation, a successful model for stochastically growing interfaces[31].

To simulate environmental disorder, we first initialized the lattice with a number of "obstacles" at a density ρ. Obstacle sites were considered impassable, i.e., they were never considered eligible sites for growth; equivalent models have also been used to simulate epidemics, where the obstacles represent immune sites[32]. If the density of obstacles was too high, the obstacles formed a closed ring around the incipient colony and prevented further growth (Fig. 5.4b); thus, there is a phase transition at a critical density $\rho_c \approx 0.4$ (see also SI Fig. 5.S1). This transition is called the pinning transition of the interface in the theory of kinetic interface roughening (discussed in detail in the SI), or, equivalently, the percolation transition of the whole colony[33,34].

As the density approached the pinning transition in our simulations, the colony morphology changed, as shown in Fig. 5.4c. Without obstacles, the colonies were compact and relatively smooth. At intermediate

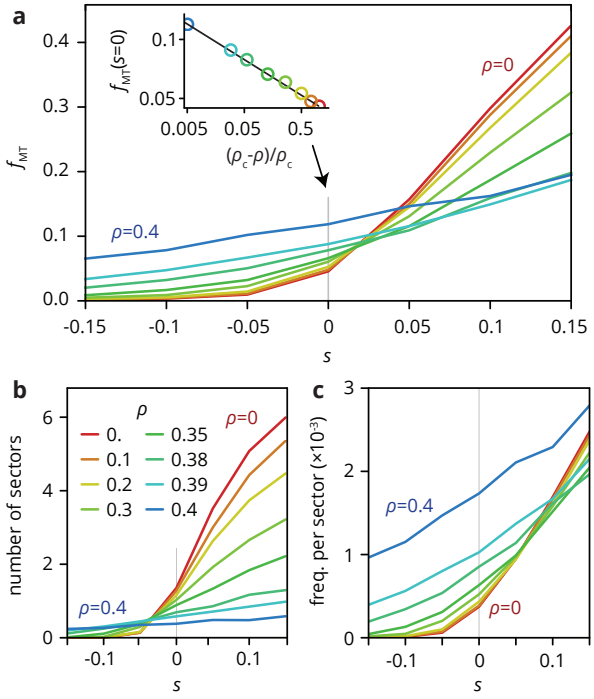

Figure 5.5: Consequences of simulated environmental disorder for the evolutionary dynamics. (a, b) Simulated colonies at $\rho = 0$ and $\rho = \rho_c$. Shown in black dots are all cells with empty neighbors. Lines connecting the ancestor (red dot) to the perimeter trace the lineages. (c) As ρ increases, the final mutant frequency f_{MT} becomes a more flat function of the fitness effect s of the mutation (see panel (e) for legend). For neutral mutations f_{MT} diverges as $f_{\mathrm{MT}} \sim |\rho - \rho_c|^{-0.18}$ (d). (e, f) The clone size distribution $P(X > x)$ measured in smooth colonies (e, $\rho = 0$) shows a strong depends on the fitness effect s of the mutants, whereas $P(X > x)$ is roughly neutral for all s in rough colonies (f, $\rho = \rho_c$).

obstacles densities, colonies were punctured by small holes and the overall density of the colony decreased. At the critical density $\rho_c \approx 0.4$ the colony was a percolation cluster[33] and had a fragmented morphology with a large number of holes and a very rough exterior (see SI Fig. 5.S1 for a quantitative analysis of the colony interfaces). In the following, we investigate how this change in colony morphology affects the evolutionary dynamics.

Consider first the final mutant frequency f_{MT} in grown colonies, shown in Fig. 5.5a. For neutral mutations, f_{MT} had a maximum at ρ_c, diverging with the distance to the critical point as $|\rho_c - \rho|^{-0.18}$ (inset). For $s \neq 0$, we found that strong environmental disorder reduced the efficacy of selection: the mutant frequency became less sensitive to the selective difference s, as beneficial mutations were less able to leverage their advantage and deleterious mutations were not purged as quickly from the population. Notably, clones remained

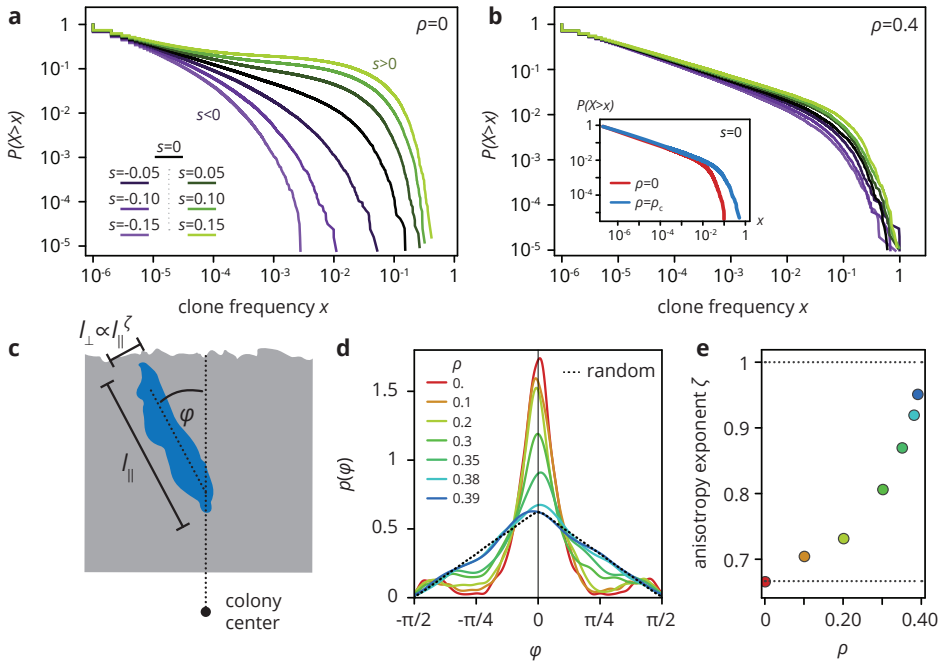

Figure 5.6: The properties of mutant clones depends on environmental disorder. The clone size distribution $P(X > x)$ measured in smooth colonies (a, $\rho = 0$) shows a strong depends on the fitness effect s of the mutants, whereas $P(X > x)$ is roughly neutral for all s in rough colonies (b, $\rho = \rho_c$). (c) Sketch of the clone angle φ and the clone length $l_{||}$ and width $l_{\perp} \sim l_{||}^{\zeta}$. (d) Clones in rough colonies tend to align less and less with the radial growth direction with increasing ρ and grow in random directions at the critical obstacle density $\rho_c = 0.4$. (e) Measuring the scaling of clone width with clone length $l_{\perp} \sim l_{||}^{\zeta}$ shows that clones are stretched without environmental disorder ($\zeta = 2/3$) and become isotropic in strong environmental disorder ($\zeta \to 1$).

spatially connected and the distinction into bubbles and sectors remained valid (Fig. 5.4c), even for high obstacles density. The number of beneficial sectors for a given selective difference s decreased with increasing environmental disorder (Fig. 5.5c), indicating a lower chance for selection to overcome the stochastic loss of the mutant clone from the front. The frequency per mutant sector was overall larger in rough colonies than in smooth ones, but less sensitive to s (Fig. 5.5d).

The effect of environmental disorder, and its impact on colony morphology, was also reflected in the size, shape and orientation of individual clones, shown in Fig. 5.6. In the absence of environmental disorder, the clone size distribution $P(X > x)$ was very broad, with a low-frequency power-law regime $x^{-2/5}$ corresponding to mutant bubbles and a steeper power-law at high frequencies characterizing sector sizes[8]. A deleterious fitness effect s of the mutations created an effective cut-off because sectors no longer formed,

whereas positive s increased the likelihood of high-frequency clones, because sectors establish more often and grow to larger frequencies when they do. Switching on strong environmental disorder, we found that the neutral clone size distribution was remarkably similar in both scenarios (Fig. 5.6b, inset). By contrast, selective differences between mutants and wild type had a much less pronounced effect on $P(X > x)$ as the strength of environmental heterogeneity increases. The clone size distribution for both beneficial and deleterious mutations thus resembled the distribution for neutral mutations, and at the critical obstacle density $\rho = \rho_c$, $P(X > x)$ became roughly independent of s, such that fitness effects associated with the mutations are effectively inconsequential at the level of individual clones. In addition, whereas mutant clones had an approximately ellipsoidal shape oriented preferentially along the radial direction in the absence of heterogeneity, they had essentially random orientations in rough colonies (Fig. 5.6c,d). Finally, the scaling of the clone width $l_\perp \sim l_\parallel^\zeta$ with its length $l_\parallel$ changed from $\zeta = 2/3$ for $\rho = 0$, consistent with previous results[8], to $\zeta \approx 0.95$ for $\rho = \rho_c$ (Fig. 5.6e), indicating roughly isotropic clones.

The clone size distribution is closely related to the site frequency spectrum in population genetics, an important tool for population genetic inference which is itself the basis for many summary statistics describing evolutionary dynamics. Fig. 5.7 gives more insight into how environmental heterogeneity shaped population genetics in our simulated colonies. Focusing on the two limiting cases, $\rho = 0$ and $\rho = \rho_c$, and neutral dynamics, we traced the lineages of all cells with empty neighbors at the colony front into a lineage tree, unveiling strongly different tree structures depending on the strength of environmental disorder (Fig. 5.7a, b). Not only were there far fewer cells at the front in rough than smooth colonies, but the lineages were characterized by much stronger fluctuations and different scaling properties (Fig. 5.7d), consistent with theoretical predictions discussed in the SI. These stronger lineage fluctuations changed the coalescence statistics of lineages in the colony: the mean pair coalescence time T_2 of two samples as a function of the distance Δx between the samples (both normalized to their maximum value) was larger without than with environmental disorder (Fig. 5.7e), indicating that two samples typically had a more recent common ancestor in disordered than in homogeneous environments, in agreement with the lineage picture shown in Fig. 5.7a and b: in the homogeneous environment, the lineage tree splits into separate branches at the origin, such that two samples coalesce quickly if they are on the same branch, but coalesce in the founder of the colony otherwise. By contrast, in the strongly disordered environment, most individual branches of the tree coalesce before reaching the origin, thus joining samples from distant regions of the tree.

To rationalize the suppression of selection by strong environmental disorder, we investigated the microscopic structure of the simulated colonies. Since mutations occur only within the growing population at the front, the properties of the front dictate the evolutionary dynamics, including the strength of selection and the size of individual clones. The standard Eden model without obstacles is characterized by growth that is locally normal to the front. The resulting colonies are compact, with an interface in the KPZ univer-

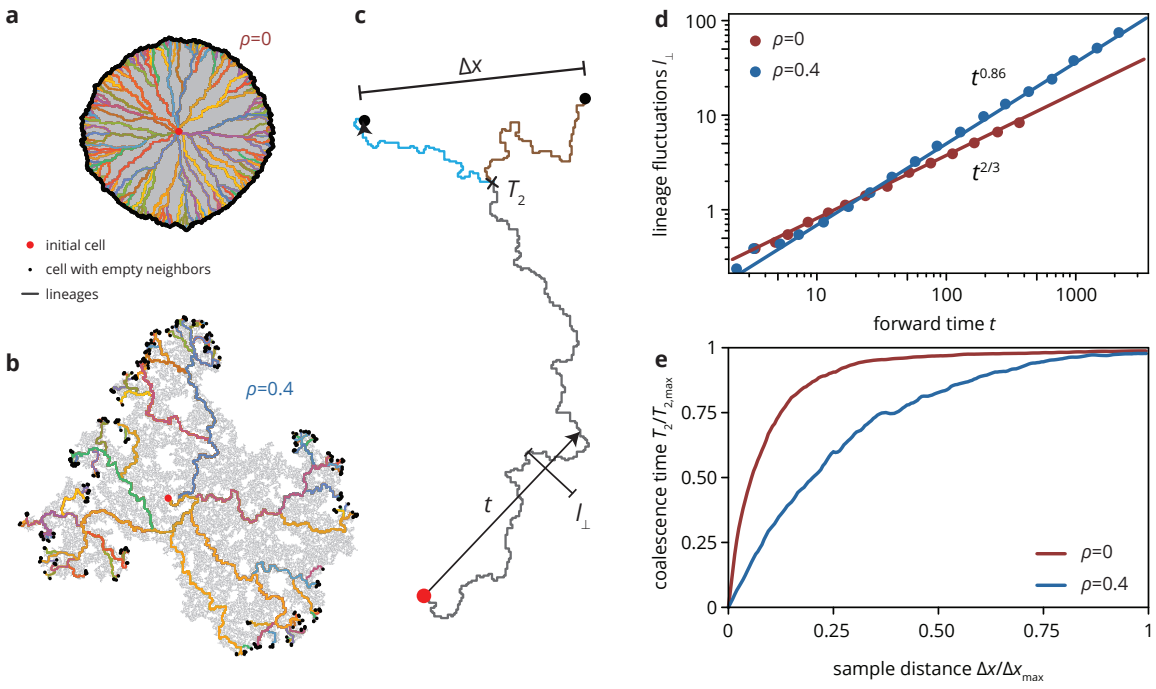

Figure 5.7: Lineage trees extracted from simulated colonies without (a) and with (b) environmental heterogeneity. (c) The lineage structure is characterized by the fluctuations $l_\perp$ of the lineages in forward time t, and the pair coalescence time T_2 (backwards in time) of two samples that are a distance Δx apart. (c) The lineage fluctuations depend on the environmental disorder: without disorder, lineage fluctuations scale as $t^{2/3}$, whereas the lineages are rougher in strong disorder, scaling as $t^{0.86}$. Strong lineage fluctuations in heterogeneous environments also impact the mean pair coalescence time of two samples a distance Δx apart by allowing lineages from distant regions of the colony to coalesce earlier than without environmental disorder (panel d).

sality class[31,35]. In the KPZ scenario, both the establishment probability of mutant sectors and details of the clone size distribution can be understood directly from the exponents characterizing the roughness of the interface[7–9].

By contrast, colonies generated by the Eden model at the critical obstacles density ρ_c are percolation clusters[33], whose interfaces fall into the quenched Edwards-Wilkinson (QEW) universality class (discussed in the SI, see SI Fig. 5.S1 and Table 5.S1). Viewing the colony as a percolation cluster implies that colony growth is dictated entirely by the local environment, as there is typically only a single accessible path through the network of obstacles at any given point[36,37]. In other words, the effective population size of growing individuals is very small, since only a few lucky individuals will be able to find these percolating paths; most individuals will get stuck in dead-ends. Hence, in order for a sector to form, the mutation must arise exactly

on such a path. However, if it does, then all newly added cells on the path will be of the mutant type. In this limit, then, sector formation is independent of the fitness of the mutants; whether a sector can form or not depends *entirely* on where the mutation arises. Similarly, the size of mutant bubbles is constrained by the network of obstacles, and whether and when the mutant bubble goes extinct depends only marginally on the fitness of its founder. This disorder-induced increase in the stochasticity of the growth process explains why selection is less efficacious in strongly disordered environments, and strongly suggests that the effect of environmental disorder on evolutionary dynamics does not depend on the details of its implementation.

5.3 Discussion

Evolution can be viewed as the result of a competition between the deterministic force of selection and various sources of randomness: firstly, intrinsic noise, which encompasses genetic drift, the nature and timing of mutations, etc., only depends on the inherent properties of the population, such as the species (including its microscopic characteristics like adhesion strength, cell shape, or growth rate) and the population size. The second source of randomness is extrinsic noise, by which we mean spatio-temporal gradients and fluctuations in environmental conditions, such as temperature, nutrient availability, or antibiotic concentration. To fully understand evolutionary dynamics, the relative strength of all three factors have to be taken into account. In evolution experiments, extrinsic noise is typically either deliberately prevented, or added in a very controlled fashion, such as periodic changes in conditions.

Here, we have studied the effects of strong extrinsic noise in the form of random environmental disorder on the fates of spontaneous mutations in microbial colonies. Our experimental observations suggest that environmental disorder can have a large impact on the evolutionary dynamics by reducing the efficacy of natural selection on spontaneous mutations. This implies that beneficial mutations are less likely to establish in a strongly disordered environment, and the rate of adaptation will therefore be reduced. Since deleterious mutations are typically more numerous than beneficial ones, environmental disorder may thus also increase the chances of an overall *decrease* in fitness, which is already more likely in range expansions than in well-mixed populations[13,14]. Thus, heterogeneities in the environment may not only slow down the process of adaptation but also lead to entirely different evolutionary outcomes. Since many mutations conferring resistance to antibiotics are often associated with a fitness cost, environmental disorder may also favor the evolution of resistance in microbial populations in this way.

Our simulations corroborated the experimental findings, suggesting that a reduced efficacy of selection can be a generic consequence of environmental heterogeneity if the extrinsic noise is strong enough to overpower selection and dictate spatial growth patterns. Nevertheless, our simulations represent a very simple toy model with a highly idealized form of environmental disorder; in reality, obstacles may not be completely

impenetrable, and a single lattice site in the simulations need not correspond to an individual cell. Indeed, we do not observe quantitative agreement between our simulations and experiments. A possible reason for this is that, since the paper used to pattern the agar surface consists of long fibers, the resulting roughness of the agar surface will feature spatial correlations, which are known to change the growth patterns of the resulting colony interface[38]. The patterns created by the paper is characterized by ridges and troughs about 50μm across, much larger than an individual cells. This may explain why deleterious mutations are efficiently purged in rough colonies, but beneficial mutations cannot translate their advantage into larger sectors: A beneficial mutation has to overcome genetic drift, and to do so, it must grow to a lateral size large enough for selection to take over[9]. However, if the characteristic length scale of the environmental disorder is smaller than this "establishment size", then the evolutionary dynamics is effectively neutral. On the other hand, a deleterious mutation born on a ridge or in a trough never grows to large enough size to "see" the disorder in the first place and thus its dynamics are unaffected by the environmental disorder.

While we have focused here on microbial populations, we expect our principal result of reduced selection efficacy by environmental heterogeneity to generalize to other dense cellular populations, such as tumors and biofilms, but also to macroscopic range expansions, as well. After all, when a population undergoes a range expansion, it will arguably not experience a completely homogeneous environments: at the very least, some areas will be more hospitable than others, but some parts of the environment may be entirely inaccessible to the population because of, e.g., rivers and lakes, a strong local competitor or predator, or lack of resources. Environmental heterogeneity is thus arguably the rule rather than the exception. Our results suggest that since range expansions in strongly heterogeneous environments can generate approximately neutral patterns of genetic diversity from mutations carrying significant fitness effects, attempts to interpret such patterns in invasive species, or generally species having undergone recent range expansions, must take into account the role the environment plays in shaping these patterns.

References

[1] G. Balázsi, A. van Oudenaarden, and J. J. Collins. Cellular decision making and biological noise: from microbes to mammals. *Cell*, 144(6):910–925, 2011.

[2] C. A. Edmonds, A. S. Lillie, and L. L. Cavalli-sforza. Mutations arising in the wave front of an expanding population. 101(4):975–979, 2004.

[3] S. Klopfstein, M. Currat, and L. Excoffier. The Fate of Mutations Surfing on the Wave of a Range Expansion. *Molecular Biology and Evolution2*, 23(3):482–490, 2006. doi: 10.1093/molbev/msj057.

[4] S. Ramachandran, O. Deshpande, C. C. Roseman, N. A. Rosenberg, M. W. Feldman, and L. L. Cavalli-Sforza. Support from the relationship of genetic and geographic distance in human populations for a serial founder effect originating in africa. *Proceedings of the National Academy of Sciences of the United States of America*, 102(44):15942–15947, 2005.

[5] T. a. White, S. E. Perkins, G. Heckel, and J. B. Searle. Adaptive evolution during an ongoing range expansion: the invasive bank vole (Myodes glareolus) in Ireland. *Molecular ecology*, 22(11):2971–85, jun 2013. doi: 10.1111/mec.12343.

[6] V. Louppe, J. Courant, and A. Herrel. Differences in mobility at the range edge of an expanding invasive population of Xenopus laevis in the West of France. *Journal of Experimental Biology*, 220: 278–283, 2017. doi: 10.1242/jeb.146589.

[7] O. Hallatschek, P. Hersen, S. Ramanathan, and D. R. Nelson. Genetic drift at expanding frontiers promotes gene segregation. *Proceedings of the National Academy of Sciences*, 104(50):19926–19930, 2007.

[8] D. Fusco, M. Gralka, J. Kayser, A. Anderson, and O. Hallatschek. Excess of mutational jackpot events in expanding populations revealed by spatial luria-delbruck experiments. *Nature communications*, 7, 2016.

[9] M. Gralka, F. Stiewe, F. Farrell, W. Moebius, B. Waclaw, and O. Hallatschek. Allele surfing promotes microbial adaptation from standing variation. *Ecology letters*, 19(8):889–898, 2016.

[10] K. S. Korolev, J. B. Xavier, D. R. Nelson, and K. R. Foster. A quantitative test of population genetics using spatiogenetic patterns in bacterial colonies. *The American Naturalist*, 178(4):538–552, 2011.

[11] J. M. J. Travis, T. Münkemüller, O. J. Burton, A. Best, C. Dytham, and K. Johst. Deleterious mutations can surf to high densities on the wave front of an expanding population. *Molecular Biology and Evolution*, 24:2334–2343, 2007. doi: 10.1093/molbev/msm167.

[12] O. J. Burton and J. M. Travis. The frequency of fitness peak shifts is increased at expanding range margins due to mutation surfing. *Genetics*, 179(2):941–950, 2008.

[13] M. O. Lavrentovich, M. E. Wahl, D. R. Nelson, and A. W. Murray. Spatially constrained growth enhances conversional meltdown. *Biophysical journal*, 110(12):2800–2808, 2016.

[14] S. Peischl, I. Dupanloup, M. Kirkpatrick, and L. Excoffier. On the accumulation of deleterious mutations during range expansions. *Molecular ecology*, 22(24):5972–82, dec 2013. doi: 10.1111/mec.12524.

[15] F. D. Farrell, M. Gralka, O. Hallatschek, and B. Waclaw. Mechanical interactions in bacterial colonies and the surfing probability of beneficial mutations. *Journal of The Royal Society Interface*, 14(131): 20170073, 2017.

[16] A. Hilfinger and J. Paulsson. Separating intrinsic from extrinsic fluctuations in dynamic biological systems. *Proceedings of the National Academy of Sciences*, 108(29):12167–12172, 2011.

[17] J. Kayser, C. F. Schreck, Q. Yu, M. Gralka, and O. Hallatschek. Emergence of evolutionary driving forces in pattern-forming microbial populations. *Philosophical Transactions of the Royal Society B: Biological Sciences*, 373(1747), 2018. doi: 10.1098/rstb.2017.0106.

[18] H. A. Lindsey, J. Gallie, S. Taylor, and B. Kerr. Evolutionary rescue from extinction is contingent on a lower rate of environmental change. *Nature*, 494(7438):463, 2013.

[19] Q. Zhang, G. Lambert, D. Liao, H. Kim, K. Robin, C.-k. Tung, N. Pourmand, and R. H. Austin. Acceleration of Emergence of Bacterial Antibiotic Resistance in Connected Microenvironments. *Science*, 333(September):1764–1767, 2011.

[20] M. Baym, T. D. Lieberman, E. D. Kelsic, R. Chait, R. Gross, I. Yelin, and R. Kishony. Spatiotemporal microbial evolution on antibiotic landscapes. *Science*, 353(6304):1147 LP – 1151, 2016. doi: 10.1126/science.aag0822.

[21] P. Greulich, B. Waclaw, and R. J. Allen. Mutational Pathway Determines Whether Drug Gradients Accelerate Evolution of Drug-Resistant Cells. *Physical Review Letters*, 109(8):088101, aug 2012. doi: 10.1103/PhysRevLett.109.088101.

[22] M. Gralka, D. Fusco, S. Martis, and O. Hallatschek. Convection shapes the trade-off between antibiotic efficacy and the selection for resistance in spatial gradients. *Physical Biology*, 14(4), 2017. doi: 10.1088/1478-3975/aa7bb3.

[23] R. Hermsen, J. B. Deris, and T. Hwa. On the rapidity of antibiotic resistance evolution facilitated by a concentration gradient. *Proceedings of the National Academy of Sciences*, 109(27):10775–10780, 2012.

[24] R. Hermsen. The adaptation rate of a quantitative trait in an environmental gradient. *Physical Biology*, 13(6):065003, 2016. doi: 10.1088/1478-3975/13/6/065003.

[25] R. Hermsen and T. Hwa. Sources and sinks: a stochastic model of evolution in heterogeneous environments. *Physical review letters*, 105(24):248104, 2010.

[26] W. Möbius, A. W. Murray, and D. R. Nelson. How obstacles perturb population fronts and alter their genetic structure. *PLoS computational biology*, 11(12):e1004615, 2015.

[27] J. Kayser, C. Schreck, M. Gralka, D. Fusco, and O. Hallatschek. Collective motion conceals fitness differences in crowded cellular populations. *bioRxiv*, page 267286, 2018. doi: 10.1101/267286.

[28] D. B. Weissman, M. M. Desai, D. S. Fisher, and M. W. Feldman. The rate at which asexual populations cross fitness valleys. *Theoretical population biology*, 75(4):286–300, jun 2009. doi: 10.1016/j.tpb.2009.02.006.

[29] J. Otwinowski and J. Krug. Clonal interference and Muller's ratchet in spatial habitats. *Physical biology*, 11(5):056003, 2014. doi: 10.1088/1478-3975/11/5/056003.

[30] M. Eden. A two-dimensional growth process. *Dynamics of fractal surfaces*, 4:223–239, 1961.

[31] M. Kardar, G. Parisi, and Y.-C. Zhang. Dynamic scaling of growing interfaces. *Physical Review Letters*, 56(9):889–892, 1986.

[32] H. J. Herrmann. Geometrical cluster growth models and kinetic gelation. *Physics Reports*, 136(3): 153–224, 1986.

[33] A. Bunde, H. J. Herrmann, A. Margolina, and H. E. Stanley. Universality classes for spreading phenomena: A new model with fixed static but continuously tunable kinetic exponents. *Physical review letters*, 55(7):653, 1985.

[34] A.-L. Barabási and H. E. Stanley. *Fractal concepts in surface growth*. Cambridge university press, 1995.

[35] F. Family and T. Vicsek. Scaling of the active zone in the eden process on percolation networks and the ballistic deposition model. *Journal of Physics A: Mathematical and General*, 18(2):L75, 1985.

[36] L. A. N. Amaral, A. L. Barabási, H. A. Makse, and H. E. Stanley. Scaling properties of driven interfaces in disordered media. *Physical Review E*, 52(4):4087–4104, 1995. doi: 10.1103/PhysRevE.52.4087.

[37] C. S. Nolle, B. Koiller, N. Martys, and M. O. Robbins. Effect of quenched disorder on moving interfaces in two dimensions. *Physica A: Statistical Mechanics and its Applications*, 205(1-3):342–354, 1994. doi: 10.1016/0378-4371(94)90512-6.

[38] E. Medina, T. Hwa, M. Kardar, and Y. C. Zhang. Burgers equation with correlated noise: Renormalization-group analysis and applications to directed polymers and interface growth. *Physical Review A*, 39(6):3053–3075, 1989. doi: 10.1103/PhysRevA.39.3053.

5.4 Supplementary information

5.4.1 Experimental methods

Strains and growth conditions

We used an *E. coli* MG1655 strain transformed with the plasmid pB10[1]. pB10 is a 65kB plasmid isolated from sewage sludge that confers resistance to several antibiotic resistance including tetracyclines and has an inserted RFP gene. Hence, cells containing pB10 ("wild type") are red fluorescent and resistant to tetracycline. The plasmid is lost sporadically[2], and the resulting cells ("mutants") are non-fluorescent and susceptible to tetracycline, but display a higher growth rate in the absence of antibiotics (characterized below). We refer to the loss of the plasmid as a "mutation" of known fitness effect and occurrence rate, both of which we characterize below.

All experiments were performed in LB at 37°C in a humidified environment. For solid media, 2% agar was added before autoclaving. Varying concentrations of doxycycline, a tetracycline that displays higher stability in agar plates than tetracycline itself, were added to freshly autoclaved media after cooling to about 60°C and poured immediately. Plates were dried in the dark for at least 24h before use.

Fitness measurements

We measured the fitness difference s between wild type and mutant cells using the colliding colonies assay[3,4]. Briefly, a mutant clone was first isolated and then grown independently of the wild type overnight. In the wild type, the plasmid was maintained by adding 10μg/ml doxycycline to the overnight culture. After growth overnight, cultures were diluted 1:10, grown for about 1.5h, and then washed twice in PBS to remove residual doxycycline. 1μl droplet of each strain were spotted on agar plates about 2mm apart. After drying, colonies were grown for 3 days and then imaged under the a Zeiss Axiozoom v16 microscope. The resulting images were used to estimate fitness differences by fitting a circle onto the mutant-wild type interface. The results are shown in Fig. 5.S2: without doxycyline, mutants have a 20-25% advantage over the wild type. Both strains have equal growth rate around ≈ 0.35ug/ml, and the mutants grow more slowly than the wild type at higher concentration of doxycycline.

For the fitness measurements in Fig. 5.2, colonies were grown from single cells on both rough and smooth plates in a temperature-controlled growth chamber and imaged overnight on a Zeiss Axiozoom v16 microscope. The resulting time lapse movies were binarized and the colony areas extracted.

Mutation rate experiment

To measure the rate of plasmid loss ("mutation rate"), we grew 48 well-mixed populations from a small number of wild-type cells for about 7 generation (i.e., from about 10 to about 1000 cells). The inoculum did not contain any mutant because the culture used to inoculate the populations contained selective amounts of tetracycline. The populations were grown either without doxycycline or at 1μg/ml doxycycline, which corresponded to the high end of concentrations used in our experiments. After 7 generations, each population was plated and the number of red (WT) and gray (MT) colonies was counted via automated image analysis. The resulting frequencies of mutants were used to infer the mutation rate by computing the maximum likelihood against simulations of the process at different mutation rates and fitness differences, as follows.

Statistical inference of mutation rate

To estimate the mutation rate, we performed maximum likelihood estimation based on probability density distributions obtained from simulations, as follows: starting from a Poisson distributed number of initial cells, 48 populations go through about 7 generations, where every wild type has a chance μ per division to produce a mutant. Mutant cells grow at a growth rate $(1+s)$ relative to the wild type. We performed 50000 simulations for each value of s and μ and computed the likelihood of each parameter combination $\theta = s, \mu$ as

$$\ell = \sum_{i=1}^{48} \ln f(x_i|\theta), \tag{5.S1}$$

where $f(x_i)$ is the probability of observing x_i under the simulation model, which we estimated from the simulation histograms. We treat s as a free parameter that we can later compare to the experimentally measured value. The precise value of s does not affect the inferred value of mu very strongly. This is because the number of generations is small in our experiment and a faster-growing mutant can gain at most a factor of four more cells than the wild type. The global maximum likelihood value μ^* is obtained for $s = 0.3$ and $s = -0.05$ for doxycycline concentrations of 0μg/ml and 1μg/ml, in good agreement with our measured values of s (see Fig. 5.S3). The error is estimated from the curvature of the likelihood as $\delta\mu \gtrsim 1/|\partial_\mu^2 \ell|_{\mu^*}$. The results are $\mu_{0\mu g/l} = 0.003 \pm 0.00055$ and $\mu_{1\mu g/l} = 0.009 \pm 0.00068$.

Main experiment and analysis

Our main experiment consists in the growth of colonies from single wild-type cells on agar plates (each containing 20ml of LB + 2% agar) containing varying concentrations of doxycycline (overall, 14 different concentrations were tested). The agar plates were either *smooth*, standard agar plates, or *rough*. Rough plates

Exponent	KPZ	This study ($\rho = 0$)	qEW	This study ($\rho = \rho_c$)
α_{loc}	1/2	0.5 ± 0.05	0.92 ± 0.04	0.9 ± 0.05
α_{G}	1/2	0.5 ± 0.05	1.23 ± 0.04	1.15 ± 0.05
β	1/3	0.3 ± 0.03	0.86 ± 0.03	0.78 ± 0.05
θ	N/A	N/A	0.24 ± 0.03	0.21 ± 0.03
ζ	2/3	0.66 ± 0.02	-	0.86 ± 0.04

Table 5.S1: Characteristic exponents for the KPZ and QEW universality classes and measured in our simulations, which are in good agreement with the literature values in Ref. 5.

were created by pouring the agar at a temperature of about 60°C and lowering filter paper (VWR Grade 410 Filter Paper, Qualitative) onto the liquid agar, where it remained until the agar had solidified. The filter paper was then removed from the hard agar surface with tweezers, resulting in a patterned agar surface.

Overnight culture of the wild type grown in LB with 10μg/l doxycycline was washed and diluted in PBS to give between 3 and 10 colonies per plate. About $n = 20 - 30$ colonies per condition were analyzed (except for smooth plates without doxycycline, where $n = 8$). After 72 hours of growth, the colonies were imaged on a Zeiss Axiozoom v16 microscope and the resulting images binarized to create a mask of the colony. Mutant clones we found manually with ImageJ. The mutant frequency per colony was then measured as the total mutant area divided by the total area of the colony.

5.4.2 Theory

Interfaces created by Eden model simulations fall into the KPZ universality class, governed by the KPZ equation for the height $h(x,t)$ [6,7]. In one dimension, starting from a line in a simulation box, the colony surface is described by

$$\partial_t h(x,t) = v_\infty + D\partial_x^2 h + \lambda \left(\partial_x h\right)^2 + \eta(x,t), \tag{5.S2}$$

where v_∞ is the final speed of front propagation and $\eta(x,t)$ is zero-mean Gaussian random noise δ-correlated in space and time describing the noise associated with the growth process. This equation generates a set of characteristic exponents that govern the roughness of the colony front and of sector boundaries. In particular, the surface height is described in terms of its root mean squared fluctuations around the mean by a Family-Viscek scaling relation [8]

$$h(t) \propto L^\alpha \mathcal{F}\left(t/L^{\alpha/\beta}\right), \tag{5.S3}$$

where

$$\mathcal{F}(x) = \begin{cases} x^{\beta}, & x \ll 1, \\ 1, & x \gg 1. \end{cases} \tag{5.S4}$$

The KPZ universality class is characterized by the roughness exponent $\alpha = 1/2$ and the temporal exponent $\beta = 1/3$; if $\lambda = 0$, the resulting universality class is called the Edwards-Wilkinson (EW) universality class characterized by $\alpha = 1/2$ and $\beta = 1/4$. The ratio $z = \alpha/\beta$ is sometimes called the dynamical exponents. It relates the size of lateral fluctuations $l_\perp$ to the time t as

$$l_\perp \sim t^{1/z}. \tag{5.S5}$$

This relationship explains the fluctuations in sector boundaries in *E. coli* colonies and Eden model simulations, and can be used to derive exponents for the site frequency spectrum and establishment probabilities in Eden model colonies[4,9,10]. In the simulation presented here, the scenario without environmental disorder is described the eq. (5.S2), explaining the site-frequency spectrum and the anisotropy exponents $\zeta = 2/3 = 1/z$ in Fig. 5.6e, and the lineage fluctuations in Fig. 5.7d.

The effect of environmental *quenched* disorder on the kinetic roughening of interfaces has been investigated in a range of experiments (see Ref. 11 for a review). Exponents obtained from experiments are in the range of $\alpha \approx 0.6 \ldots 0.9$. To model driven interface growth in disordered media, quenched environmental disorder can be included by considering a noise term $\zeta(x, h(x,t))$ that does not explicitly depend on time[12].

$$\partial_t h(x,t) = F + D\partial_x^2 h + \lambda \left(\partial_x h\right)^2 + \zeta(x, h(x,t)). \tag{5.S6}$$

Here, F is driving "force" fulfilling the same role as v_∞ in eq. (5.S2). Since the noise explicitly depends on the interface position, F cannot be transformed away and thus emerges as a new parameter that can be thought of as a force pushing the interface through the disordered media. An important consequence of quenched noise is the emergence of a critical force F_c below which the interface becomes pinned[13]. For $F > F_c$, a depinning transition takes place that is well characterized in one dimension[5]. For $F \to F_c^+$, large regions of the interface of size $\xi \sim |F_c - F|^{-\nu}$ are pinned, and the front speed increases as $|F - F_c|^{\theta}$ (see Table 5.S1).

Simulations and numerical integrations of eq. (5.S6) have characterized the pinned and moving phases and uncovered two universality classes as $F \to F_c^+$[5]: if λ diverges near the depinning transition, one speaks of the QKPZ universality class; its exponents $\alpha = \beta \approx 0.633$ in the pinned phase are understood analytically through an analogy with the directed percolation class, whereas in the moving phase $\alpha \approx \beta \approx 0.75$. If $\lambda \to 0$ instead, one speaks of the QEW universality class with $\alpha \approx 0.92$ and $\beta \approx 0.82$ in the moving phase (see also Table 5.S1); a functional renormalization group calculation gives $\alpha = 1$ and $\nu = 1/(2-\alpha)$ in one

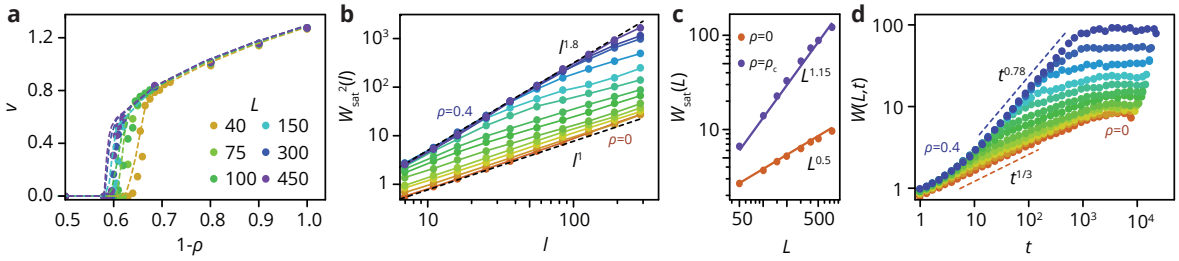

Figure 5.S1: Characterization of Eden clusters with obstacles. (a) Taking the front speed v as the order parameter, there is a phase transition at a critical obstacle density $\rho_c(L)$ depending on system size L. For an infinite system, $\rho_c \approx 0.41 \pm 0.01$. For $\rho > \rho_c$, we have $v \sim |\rho - \rho_c|^0.21$. (b) Roughness W of fully developed interfaces at $L = 400$ for varying obstacle densities, as a function of the window length l, such that $W \sim t^\alpha$. At $\rho = 0$, we find $\alpha = 1/2$, consistent with the KPZ universality class. At ρ_c, we find $\alpha_{\text{loc}} \approx 0.9$, consistent with the qEW universality class, which is known to be characterized by two roughness exponents, a local exponent (α_{loc}), and a global exponent $\alpha_G \approx 1.15 > \alpha_{\text{loc}}$ when the roughness is measured over the whole system size (see panel c). The time evolution $W(t) \sim t^\beta$ of the interface also follows dynamics consistent with KPZ ($\beta = 1/3$) and qEW ($\beta \approx 0.78$) in the limiting cases. For intermediate $0 \ll \rho \ll \rho_c$, there is a crossover from qEW at short times to KPZ dynamics at longer times, before the roughness saturates at a ρ-dependent value. For easier analysis, all simulations were performed in a box-like geometry.

dimension[14]. For $F > F_c$, there is a transition from the QKPZ/QEW universality class to the appropriate universality class with annealed noise.

As mentioned in the main text, our generalized Eden model simulations with obstacles exhibits the same pinning transition for an obstacle density $\rho \approx 0.4$. At the transition, the resulting colonies are percolation clusters on the square lattice, from whose interfaces we measure exponents that are in excellent agreement with the QEW universality class (see Table 5.S1 and Fig. 5.S1). This is consistent with the finding of Moglia et al.[15], who used a slightly more complex simulation algorithm to model the growth of cancer cell monolayers. Without obstacles, our simulations reproduce earlier findings[6] (Table 5.S1). In particular, we find $z = 3/2$ without obstacles and $z \approx 1.15$ at the critical obstacles density, which allows us to compute the scaling exponent of the sector boundaries from eq. (5.S5) as $\zeta = 1/z$. This gives $\zeta = 2/3$ and $\zeta \approx 0.86$, in excellent agreement with the lineage fluctuation exponents $\zeta = 0.66$ and $\zeta \approx 0.86$ in Fig. 5.7d.

5.4.3 Supplementary experimental results

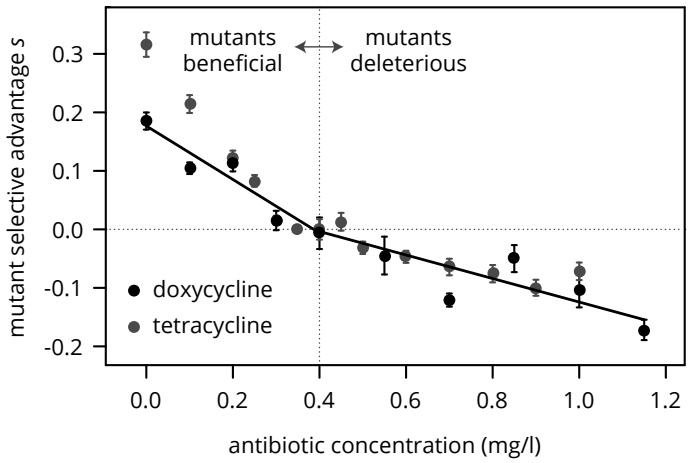

Figure 5.S2: Selective difference between mutants and wild type at different concentrations of doxycycline and tetracycline. For low antibiotic concentration, plasmid loss is beneficial such that mutants have an advantage, while the mutants become first neutral and then deleterious for higher concentrations.

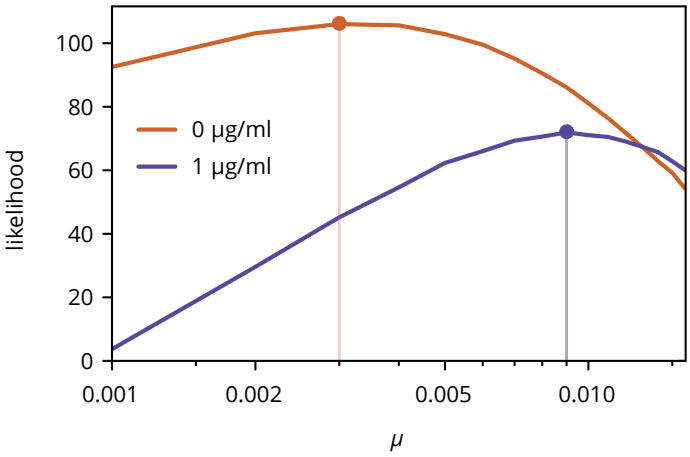

Figure 5.S3: Likelihood of mutation rate for two different concentrations of doxycycline. Only the curves with the maximum likelihood value for s are shown.

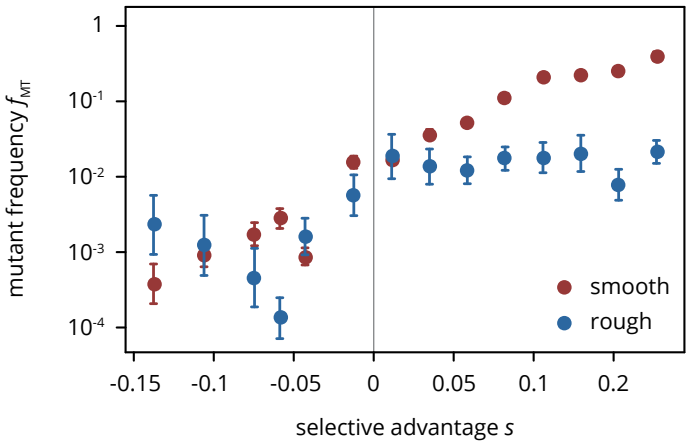

Figure 5.S4: Final frequency of mutants after 3 days of growth, on smooth (red) and rough (blue) plates. Same data as Fig. 5.2a, plotted on a semi-logarithmic scale.

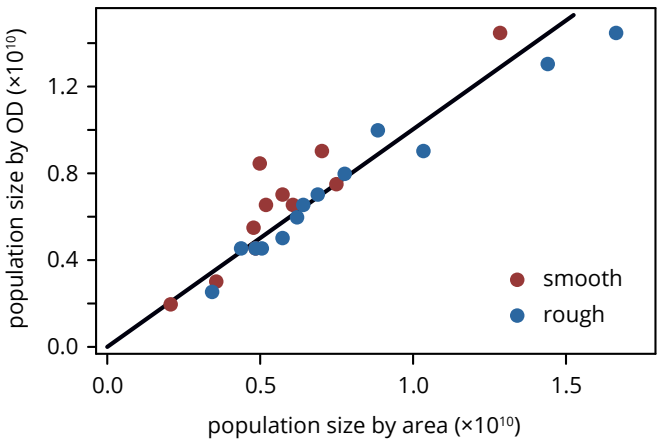

Figure 5.S5: Population size of colonies estimated by measuring colony height and area, and by resuspending and measuring the resulting optical density. The black line has slope 1.

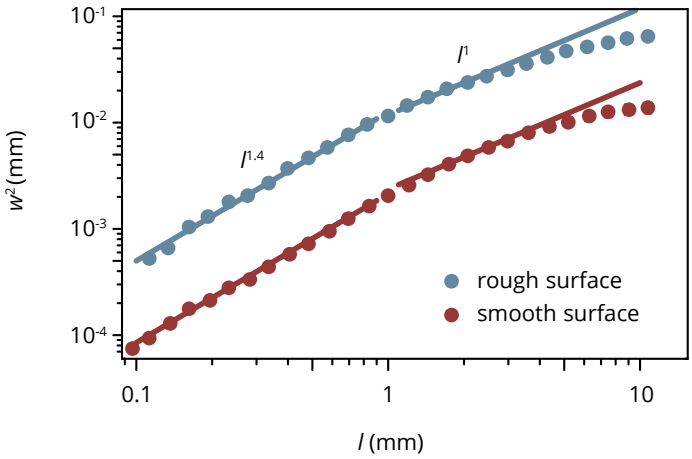

Figure 5.S6: Roughness of colonies of different media, defined as the mean square deviation from the best-fit circle. Colony boundaries were extracted and the variance w^2 of the radius fluctuations measured over different window lengths l. The KPZ universality class predict $w^2 \sim l$.

References

[1] A. Schlüter, H. Heuer, R. Szczepanowski, L. J. Forney, C. M. Thomas, A. Pühler, and E. M. Top. The 64 508 bp IncP-1 β antibiotic multiresistance plasmid pB10 isolated from a waste-water treatment plant provides evidence for recombination between members of different branches of the IncP-1 β group. *Microbiology*, 149(11):3139–3153, 2003. doi: 10.1099/mic.0.26570-0.

[2] L. De Gelder, J. M. Ponciano, P. Joyce, and E. M. Top. Stability of a promiscuous plasmid in different hosts: No guarantee for a long-term relationship. *Microbiology*, 153(2):452–463, 2007. doi: 10.1099/mic.0.2006/001784-0.

[3] K. S. Korolev, M. J. Müller, N. Karahan, A. W. Murray, O. Hallatschek, and D. R. Nelson. Selective sweeps in growing microbial colonies. *Physical biology*, 9(2):026008, 2012.

[4] M. Gralka, F. Stiewe, F. Farrell, W. Moebius, B. Waclaw, and O. Hallatschek. Allele surfing promotes microbial adaptation from standing variation. *Ecology letters*, 19(8):889–898, 2016.

[5] L. A. N. Amaral, A. L. Barabási, H. A. Makse, and H. E. Stanley. Scaling properties of driven interfaces in disordered media. *Physical Review E*, 52(4):4087–4104, 1995. doi: 10.1103/PhysRevE.52.4087.

[6] F. Family and T. Vicsek. Scaling of the active zone in the eden process on percolation networks and the ballistic deposition model. *Journal of Physics A: Mathematical and General*, 18(2):L75, 1985.

[7] M. Kardar, G. Parisi, and Y.-C. Zhang. Dynamic scaling of growing interfaces. *Physical Review Letters*, 56(9):889–892, 1986.

[8] T. Vicsek and F. Family. Dynamic scaling for aggregation of clusters. *Physical Review Letters*, 52(19): 1669, 1984.

[9] O. Hallatschek, P. Hersen, S. Ramanathan, and D. R. Nelson. Genetic drift at expanding frontiers promotes gene segregation. *Proceedings of the National Academy of Sciences*, 104(50):19926–19930, 2007.

[10] D. Fusco, M. Gralka, J. Kayser, A. Anderson, and O. Hallatschek. Excess of mutational jackpot events in expanding populations revealed by spatial luria-delbruck experiments. *Nature communications*, 7, 2016.

[11] A.-L. Barabási and H. E. Stanley. *Fractal concepts in surface growth*. Cambridge university press, 1995.

[12] D. A. Kessler, H. Levine, and Y. Tu. Interface fluctuations in random media. *Physical Review A*, 43 (8):4551, 1991.

[13] L.-H. Tang and H. Leschhorn. Pinning by directed percolation. *Physical Review A*, 45(12):R8309, 1992.

[14] T. Nattermann, S. Stepanow, L.-H. Tang, and H. Leschhorn. Dynamics of interface depinning in a disordered medium. *Journal de Physique II*, 2(8):1483–1488, 1992.

[15] B. Moglia, E. V. Albano, and N. Guisoni. Pinning-depinning transition in a stochastic growth model for the evolution of cell colony fronts in a disordered medium. *Physical Review E*, 94(5):1–13, 2016. doi: 10.1103/PhysRevE.94.052139.

6

Convection shapes the trade-off between antibiotic efficacy and the selection for resistance in spatial gradients

Since penicillin was discovered about 90 years ago, we have become used to using drugs to eradicate unwanted pathogenic cells. However, using drugs to kill bacteria, viruses or cancer cells has the serious side effect of selecting for mutant types that survive the drug attack. A key question therefore is how one could eradicate as many cells as possible for a given acceptable risk of drug resistance evolution. We address this general question in a model of drug resistance evolution in spatial drug gradients, which recent experiments and theories have suggested as key drivers of drug resistance. Importantly, our model takes into account the influence of convection, resulting for instance from blood flow. Using stochastic simulations, we study the fates of individual resistance mutations and quantify the trade-off between the killing of wild-type cells and the rise of resistance mutations: shallow gradients and convection into the antibiotic region promote wild-type death, at the cost of increasing the establishment probability of resistance mutations. We can explain these observed trends by modeling the adaptation process as a branching random walk. Our analysis reveals that the trade-off between death and adaptation depends on the relative length scales of the spatial drug gradient and random dispersal,

and the strength of convection. Our results show that convection can have a momentous effect on the rate of establishment of new mutations, and may heavily impact the efficiency of antibiotic treatment.

6.1 Introduction

The emergence of drug resistance represents one of the major clinical challenges of the current century[1–3]. Microbial pathogens quickly acquire resistance to new antibiotics[4], while solid tumors often regrow after treatment because of resistance mutations that arise during tumor growth[5]. In addition to genomic studies examining the molecular causes of resistance[6,7], the dynamics of drug resistance evolution has recently attracted wide interest[8,9], with the dual goal of understanding the emergence of resistance and developing novel strategies to prevent or control its spread[10,11]. Next-generation sequencing and high-throughput experimental techniques enable the quantitative study of resistance evolution but require the development of new theories to appropriately interpret experimental results[12].

In many realistic systems, an evolving population interacts with its surroundings and exhibits a well-defined spatial structure (for instance, in tumors and biofilms[5]). It has recently been shown that this spatial structure can strongly influence the subclonal structure and the adaptation of spatially expanding populations, both from *de novo* and pre-existing mutations[13–15]. Likewise, spatial[12,16,17] or temporal[10,18] gradients in antibiotic concentration can enable populations to reach a higher degree of resistance than in homogeneous drug concentrations, at least in part because they enable the slow accumulation of multiple mutations, each conferring a small amount of resistance.

The presence of spatial drug gradients is well documented both in the outside environment[19,20] as well as within biofilms[21] and the human body[22–24], and it has been hypothesized that the presence of spatial heterogeneities may facilitate the emergence of drug-resistant phenotypes[25]. In a microfluidic experiment, a spatial gradient indeed gave rise to a higher rate of adaptation of bacterial populations[16]. Similarly, microbes growing on soft agar plates with gradually increasing antibiotic concentrations were able to rapidly evolve resistance to high levels of antibiotics, while sudden jumps to unsustainably high concentrations dramatically slowed down adaptation[12]. These findings raise the theoretical question of how to predict the rate of emergence of drug resistance in the presence of spatial gradients.

A number of recent theoretical studies have investigated how gradients speed up the evolution of drug resistance[26–28]. Each study made critical assumptions about the nature of the gradients: Greulich et al.[27] considered a population adapting to a smooth gradient, which gradually lowers the growth rate of susceptible individuals. Hermsen et al.[26] studied resistance evolution in a series of sharp step-like increases in concentration, where a novel resistance mutations was necessary for survival in the next step (the ”staircase” model);

Hermsen [28] later proposed a generalization of the staircase model to continuous gradients. These previous studies focused on the speed of adaptation, i.e., how quickly the population evolves to tolerate high concentrations of antibiotics. In the context of the emergence of drug resistance, this observable alone ignores a crucial reality of antibiotic treatment: efficient drug treatment first and foremost aims to kill as many bacteria as possible, while limiting the rise of resistance mutation. How this apparent trade-off can be optimized to prevent the evolution of drug resistance has so far been unexplored. Moreover, many realistic growth scenarios of bacterial populations may exhibit a directed flow that drives them up or down the gradient. Examples include the gut, arteries, and urethra in the human body [29–32], but also flows in aquatic environments, like ocean and river currents [33], or flow in pipes and catheters [34]. The effect of convection on the evolution of drug resistance remains unknown.

Here, we present simulations, rationalized by a comprehensive analytical framework, of populations evolving resistance in a variety of spatial antibiotic concentration gradients and under the influence of convection. We measure the establishment probability of resistant mutants arising in a region occupied by susceptible wild type, and the drug-induced death rate of the wild type, and show how bacterial diffusion, antibiotic gradient steepness, and convection interact to affect the treatment efficiency. We find that shallow gradients and convection into the antibiotic promote wild-type death, at the cost of increasing the establishment probability of resistance mutations. Conversely, populations in steep gradients and subject to convection away from the antibiotics are less susceptible to drug-induced wild-type death but also produce fewer resistance mutants. The treatment efficiency, which quantifies the inherent trade-off between adaptation and death, is strongly modulated by gradient steepness and convection. Treatment efficiency is found to strongly depend on convection away from the antibiotic, which increases it in shallow gradients and decreases it in steep gradients.

6.2 Simulation results

We simulate a population of wild-type individuals on a lattice of L demes, each of size K, in a one-dimensional antibiotic gradient (see the sketch in Fig. 6.1 and *Methods*). Each individual can migrate into a neighboring deme, replicate, and die. The antibiotic gradient sets the death rate of the wild type, giving rise to an effective growth rate

$$s(x) = \frac{1}{2}\left[1 - \tanh(mx)\right]. \tag{6.1}$$

In the absence of antibiotics, population growth is only limited by a carrying capacity K.

Following the equilibration to the steady-state profile of the wild type, a resistant mutant is inserted into the population at position x. The resistant mutant has the same birth rate as the wild type, but it does not

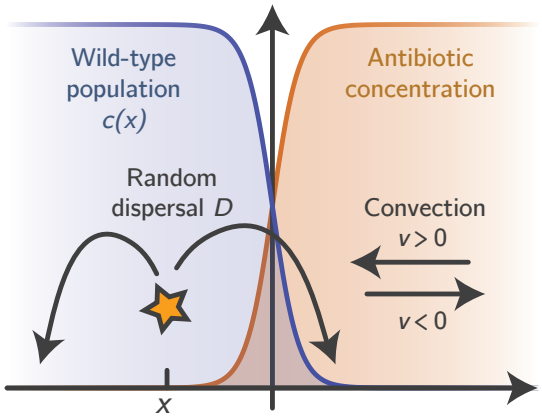

Figure 6.1: Sketch of our modeling setup. We assume that, initially, a purely wild-type population has reached a steady-state density profile (blue) in the presence of a steady-state antibiotic concentration gradient (orange). Resistance mutations occur spontaneously in randomly drawn individuals and disperse, proliferate and die until extinction or ultimate fixation. Convection can either drive the population towards the antibiotic ($v < 0$) or away from it ($v > 0$). Our goal is to analyze the fixation probability of resistance mutation for a given the rate of wild-type killing.

suffer from an increased death rate due to the antibiotics. We follow the mutant clone until it either goes extinct or reaches the far end of the simulation box, in which case we consider the mutant *established*.

In treating a bacterial infection, the optimal antibiotic strategy would eliminate as many bacteria as possible, while limiting the emergence of resistance. To quantify the treatment efficacy, we first obtain an average wild-type population profile $c(x)$ from independent simulation runs and thus compute the number B of drug-induced wild-type deaths per generation,

$$\text{total death rate } B = \sum_{i=0}^{L} c(x_i)b(x_i), \tag{6.2}$$

where $b(x_i)$ is the death rate per generation due to antibiotics in deme x_i. For simplicity, we call B the total death rate.

To quantify the emergence of resistance, we measure the local mutant establishment probability $u(x)$, i.e., the probability that a mutation that arose at position x establishes. Since the probability that a mutation occurs in the first place is proportional to the wild-type population density $c(x)$, it follows that successful mutants can only arise where both the wild-type population density and the establishment probability are high (see Fig. 6.3). A measure for how readily new resistant mutants establish is thus given by the product

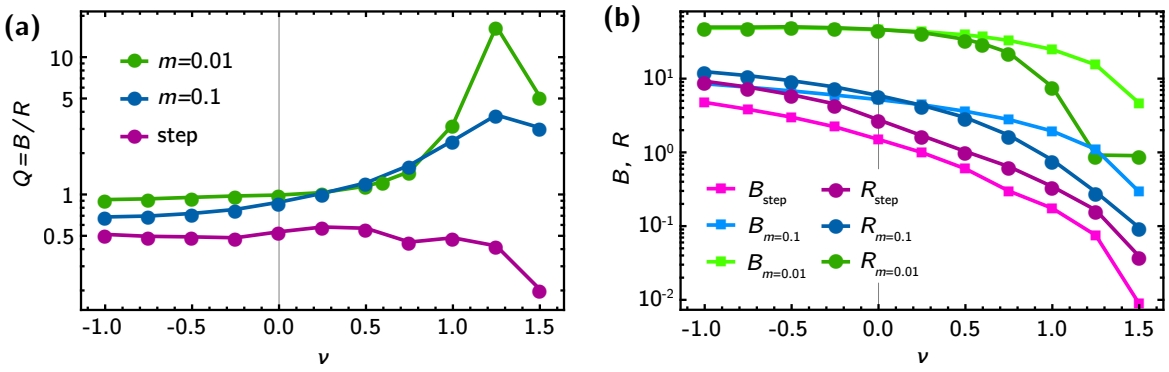

Figure 6.2: Quantifying the tradeoff between killing of wild-type cells and fixation of resistant mutants. (a) The treatment efficiency Q, defined as the number B of drug-induced deaths per generation divided by the rate of adaptation R (see eq. 6.4), for different antibiotic concentration profiles (shallow gradient, $m = 0.01$; intermediate gradient, $m = 0.1$; step-like concentration profile). Convection away from the antibiotic (positive v) can increase treatment efficiency by an order of magnitude in shallow gradients. (b) Both B and R are increased (in contrast to their ratio Q) in shallow gradients and for convection into the antibiotic.

of wild-type population density and the establishment probability, summed over all demes x_i [35]. We call this measure the rate of adaptation R,

$$\text{rate of adaptation } R = \sum_{i=0}^{L} c(x_i)u(x_i). \tag{6.3}$$

The rate of adaptation R is proportional to the rate μR of establishment, the rate at which new resistance mutations arise (at a low mutation rate μ) and establish in the population. Alternatively, the rate of adaptation R can be understood as a measure proportional to the mean establishment probability $\sum c(x_i)u(x_i)/\sum c(x_i)$, i.e., the probability that a mutation arising anywhere in the population establishes.

Finally, we define the efficiency Q of drug treatment via the amount of drug-induced wild-type death B before an adaptive mutation establishes, i.e., by $B/\mu R$. We assume mutation rates to be low such that no clonal interference occurs. Then, we can treat each mutation independently and thus define

$$\text{treatment efficiency } Q = \frac{B}{R}. \tag{6.4}$$

Fig. 6.2a shows how the treatment efficiency Q changes across gradient steepness and convection into ($v < 0$) and away from ($v > 0$) the gradient. We find that without convection ($v = 0$), and for convection toward the gradient ($v < 0$), Q is slightly higher for shallow gradients but always bounded between $Q = 0.5$

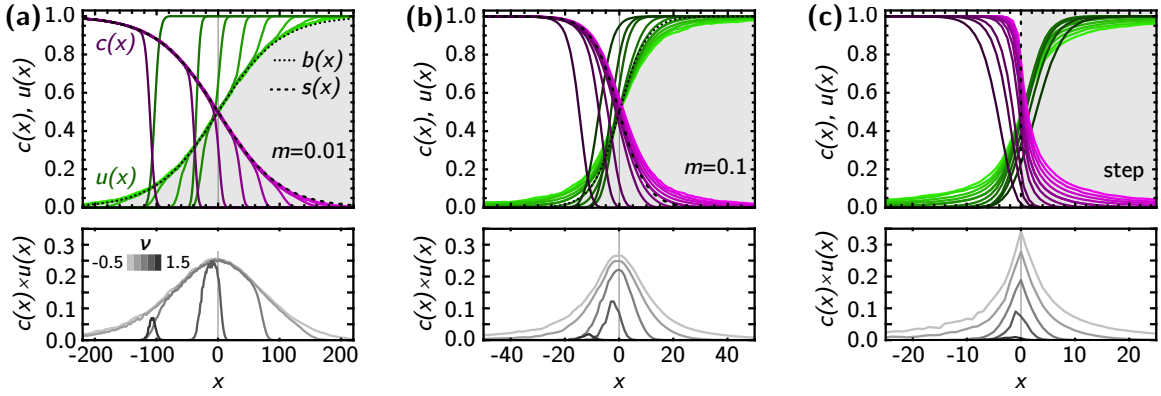

Figure 6.3: Population density $c(x)$ (magenta) and establishment probability $u(x)$ (green) for three different concentration profiles (gray background; (a) shallow gradient, $m = 0.01$; (b) intermediate gradient $m = 0.1$; (c) step) and different values of $v = -0.5$ to 1.5 (light to dark colors), from stepping stone simulations. Dotted and dashed line are the local wild-type death rate $b(x)$ and the net growth rate $s(x)$. On the right in each panel is the product $c(x)u(x)$, which identifies the region where successful mutants arise.

and $Q = 1$. However, the trend changes dramatically for positive convection away from the gradient, which boosts treatment efficiency by a factor of 10 for shallow gradients and decreases it for the step-like antibiotic profile.

Considering the rate of adaptation R and the total death rate B separately (Fig. 6.2b) illustrates the reason behind the qualitative behavior of treatment efficiency. Both R and B show similar tendencies for different gradients and convection speeds: Shallow gradients are characterized by larger values of both R and B than the step-like concentration profile. Negative convection (towards the gradient) increases both R and B by up to a factor of 5, while positive convection leads to their rapid decrease by two orders of magnitude. Remarkably, in shallow gradients the rate of adaptation R is more sensitive than the total death rate B to positive convection. The rapid decrease of R explains the increase in the treatment efficiency $Q = B/R$ for shallow gradients.

A detailed look at the population density $c(x)$ and establishment probability $u(x)$ profiles is necessary to understand the values taken by R and B. These profiles are shown in Fig. 6.3 for three different gradients (shaded areas). The population density $c(x)$ approximately tracks the net growth rate $s(x)$, while the establishment probability $u(x)$ is roughly a mirror image of the population density. In the region where the drug concentration is low and the wild-type population is dense, the mutants have no advantage over the wild type, since they compete for the same resources, and are likely to go extinct due to genetic drift. Conversely, in high drug concentration regions, the wild type cannot survive and the mutants can grow freely and establish with high probability.

Convection has a rich variety of effects on both profiles. Convection into the antibiotic (co-flow, $v < 0$) leads to broader profiles of both the wild type population density $c(x)$ and the establishment probability $u(x)$ (Fig. 6.3), while convection away (counter-flow, $v > 0$) from the antibiotic reduces both the population density and the establishment probability in the antibiotic region. For shallow gradients, we even observe an apparent cut-off in $c(x)$ (and correspondingly in $u(x)$), whose location depends on v. Consequently, co-flow increases total death rate and establishment score, while counter-flow leads to their rapid decrease.

In summary, our simulations show that both the population density profile $c(x)$ as well as the local establishment probability $u(x)$ of resistance mutants are strongly influenced by environmental parameters, in particular, by the steepness of the antibiotic gradient and the strength of convection. As a general rule of thumb, shallow gradients and convection towards increasing drug concentrations increases the rate of adaptation R, while steep gradients and convection away from the drug source decrease it. The total death rate B follows the same trend. However, subtle differences between R and B give rise to a qualitative change in behavior of the treatment efficiency $Q = B/R$, which is increased by positive convection (counter-flow) in shallow gradients and decreased in steep ones. To rationalize our results and identify the critical length scales, we now develop a mathematical model that accommodates these processes.

6.3 Theory

6.3.1 Theoretical framework

Consider a population at some density $c(x)$ in an antibiotic concentration field, which gives rise to a death rate $b(x)$ per generation, i.e., the drug-induced death rate is measured relative to the maximum growth rate a_0. We define the total (drug-induced) death rate B per generation through a continuum version of eq. 6.2 as

$$B = \int_{-\infty}^{\infty} dx\ c(x)b(x). \tag{6.5}$$

Resistance mutations arise at a rate μ, which we assume to be constant and sufficiently low such that adaptation occurs via the sequential acquisition of resistance mutations, i.e., we neglect local clonal interference. Analogously to eq. 6.3 above, we define the rate of adaptation

$$R = \int_{-\infty}^{\infty} dx\ c(x)u(x), \tag{6.6}$$

where $u(x)$ represents the probability that a beneficial mutation born at position x eventually establishes. The population density $c(x)$ can be computed using standard techniques (like deterministic reaction-diffusion equations), and we return to this question later on. The establishment probability $u(x,t)$, i.e., the probability for a mutation to survive until time t, obeys a nonlinear reaction-diffusion equation[35],

$$\partial_t u(x,t) = D\partial_x^2 u + v\partial_x u + s(x)u - a(x)u^2, \tag{6.7}$$

where $a(x)$ is the local birth rate of the mutants and $s(x) = a(x) - b(x)$ is the net growth rate (see SI section 1). Throughout this paper, we will make the assumption that the birth rate of wild-type and mutant is identical and constant, $a(x) = a_0$, and that the drug-induced death rate of the resistant mutant is zero, while the wild-type drug-induced death rate $b(x)$ ranges from 0 to a_0, i.e., we assume that the antibiotic only affects the population by increasing the death rate of the wild type. We include diffusion and convection terms to account for the random dispersal and the effects of external flow on the bacteria.

It is important at this point to note that in general the selective gradient $s(x)$ will intimately depend on various environmental factors, including competition with the wild-type population. In later sections, especially when incorporating convection (i.e., $v \neq 0$), we will take this effect into account. For now, we will assume that this function is known for given external conditions in order to gain a better intuition for the system.

6.3.2 Diffusion without convection

We will first analyze eq. 6.7 in the case without drift, i.e. $v = 0$, in order to extract the characteristic length scales of the system. We solve the extreme cases of a step-like concentration increase and a very smooth gradient analytically, and then interpolate between the two regimes using numerical solutions to eq. 6.7.

Step-like gradient

We begin by considering the simplest functional form for a selective gradient – a step:

$$s(x) = a_0\Theta(-x), \tag{6.8}$$

where $\Theta(x)$ is the Heaviside step function. Such a sharp gradient could emerge, for instance, at the boundary of different tissues or organs with different affinities to store antibiotics[36]. The equation for the fixation probability in this case is given by:

$$0 = \partial_\xi^2 u + \sigma_0\Theta(-\xi)u - u^2 \tag{6.9}$$

where we have rescaled by the diffusion length scale:

$$\xi = x/L_D, \quad L_D = \sqrt{D/a_0}. \tag{6.10}$$

In the Appendix, we solve this equation using an analogy from classical mechanics. We have that for $\xi > 0$

$$u(\xi) = \frac{1}{\sqrt{3}} \left(1 + \frac{\xi}{\sqrt{6\sqrt{3}}}\right)^{-2}, \tag{6.11}$$

implying $u \sim 1/\xi^2$ for large x. For $\xi < 0$, we obtain

$$u(\xi) = \frac{1}{2} \left\{ 3 \tanh^2 \left[\frac{1}{2}(\xi^* - \xi) \right] - 1 \right\}, \tag{6.12}$$

where $\xi^* = 2 \operatorname{arctanh} \sqrt{\frac{1}{3} + \frac{2}{3\sqrt{3}}}$.

Eq. 6.11 shows that the fixation probability decays over a characteristic length scale $L_D = \sqrt{D/a_0}$. This length scale can be roughly understood as the typical distance that a mutant individual travels through random dispersal before replicating.

Shallow gradient

Having identified the characteristic length scale over which the establishment probability decays in a step-like concentration profile, we now turn towards more realistic gradients. For simplicity, for the remainder of our calculations, we will model a shallow antibiotic gradient again as the sigmoidal function $\sigma(\xi)$ given in eq. 6.1, $\sigma(\xi) = \frac{1}{2}\left[1 - \tanh(m\xi)\right]$, such that the gradient changes over a characteristic distance $L_m = L_D/m$. Intuitively, if $L_D \gg L_m$, individuals feel sharp, step-like antibiotic transitions within their typical migration distance, and thus, we expect the results of the previous section to remain good approximations. If, conversely, individuals migrate only short distances compared to L_m, i.e., $L_m \gg L_D$, they will sample only a small region of the gradient and will not feel the differences in antibiotics concentration. To make this heuristic idea quantitative, we rescale ξ in eq. 6.7 by the new length scale L_m to obtain

$$0 = m^2 \partial_\theta^2 u + \sigma(\theta) u - u^2. \tag{6.13}$$

When $L_m \gg L_D$, i.e., $m \ll 1$, we can neglect the partial derivative in eq. 6.13, such that

$$u(\xi) = \sigma(\xi) \quad \text{(shallow gradients)}. \tag{6.14}$$

This so-called quasi-static approximation is a straight-forward extrapolation of the well-mixed result and has been used to model establishment in Ref.[27]. For $m \gg 1$, the step-like solution holds, whereas, for $m \approx 1$, no analytical solution is available; in such cases, we solve the equations numerically (see Methods).

To determine which scenario is more relevant in microbial communities, we estimate a typical m. A typical (non-motile) bacterial cell may have a diameter of $1\mu m$, swimming in a medium of viscosity comparable to that of water (with blood typically only a factor 3 larger than that[37]). Then, its diffusion constant is of order $0.1\text{-}1\mu m^2/s$. The length scale $L_D = \sqrt{D/a_0}$ for a typical birth rate of $0.5 - 2\text{hr}^{-1}$ is then between 50 and a few hundred microns. In a microfluidic experiment by Zhang et al.[16], demonstrating facilitation of adaptation through antibiotic gradients, the length scale on which the drug gradient varied was $L_m \approx 200\mu\text{m}$ so that $m \sim 1$[16].

This estimate is, however, very crude: firstly, the diffusion constant of a bacterium may not be due to thermal fluctuations but due to directed motion that only becomes approximately diffusive on long time scales[38,39]. In that case, the diffusion constant can be much larger, up to tens or even $100\mu m^2/s$. For a bacterium with a division time of 60 minutes, this leads to a expected typical length $L_D \approx 3\text{mm}$. Indeed, for motile bacteria such as those used in a recent experimental study by Baym et al.[12] with a reported spreading velocity of 40mm/hr, we find $L_D \approx 1 - 10\text{mm}$. Surely, we cannot expect homogeneous antibiotic concentration over such long length scales and indeed step-like transitions in antibiotic concentration were assumed in the study. Therefore, we expect that concentration gradients of significant sharpness should play a key role in both experimental set-ups and practically relevant systems, and hence the quasi-static approximation in eq. 6.14 should be employed with caution.

6.3.3 Wild-type population dynamics

As mentioned above, the mutants' net growth rate $s(x)$ generally depends on several environmental factors, including competition with the wild-type population. In addition, both the rate of adaptation R and the total death rate B determined in our simulations depend on the wild-type density profile $c(x)$. To provide analytical expressions for these quantities and the corresponding treatment efficiency Q, we therefore need to accommodate the coupling between wild-type and mutants. In the following, we will employ a simple logistic growth model for the wild-type population and its interaction with the mutant dynamics.

We assume that the wild-type population density $c(x,t)$ is described by the following reaction-diffusion equation:

$$\partial_t c = D\partial_x^2 c + a_{WT}(x)c\left(1 - \frac{c}{K}\right) - b_{WT}(x)c, \tag{6.15}$$

where $a_{WT}(x)$ is the local wild type birth rate, $b_{WT}(x)$ is the local antibiotic-induced death rate of the wild type. In our model, wild-type growth is limited by a logistic term $(1 - c/K)$, which models a finite amounts

of nutrients limiting the population size per deme to the carrying capacity K, while the local death rate $b_{WT}(x)$ acts on each individual independently and is therefore unaffected by the local population density. This distinguishes our model from the Fisher equation used to describe population spreading[40], where also the death rate multiplies the logistic term. Our model instead ensures that the steady-state local population density c_{SS} depends explicitly on the local death rate $b_{WT}(x)$ when the death and birth rate profiles change sufficiently slowly in space,

$$c_{SS}(x) = K\left(1 - \frac{b_{WT}(x)}{a_{WT}(x)}\right). \tag{6.16}$$

Our model, like the original Fisher equation, ignores the discrete nature of individuals, which has been shown to significantly alter the tip of the population front (see SI section 7 for a detailed discussion). Nevertheless, we expect good agreement between our model and simulations in terms of the treatment efficiency Q, whose value is not significantly affected by the details of the population profile at the tip of the wave.

For the remainder of this text, we will assume, as before, that the total growth rate $a_{WT}(x)$ is a constant, a_0, and that the presence of the antibiotic modulates selection by increasing the wild type death rate $b_{WT}(x)$. The logistic growth term makes eq. 6.15 for the wild type density $c(x)$ mathematically equivalent to eq. 6.7 for the establishment probability $u(x)$ and hence, all results carry over with minor modifications (eqs. 6.11, 6.12, and 6.14). In particular, the predicted steady-state population density $c(x)$ has a broad tail in the case of a step-like antibiotic profile, and closely follows the mirror image of the antibiotic profile if this is shallow. Note, however, that we are unable to observe the broad tail in simulations because of the discreteness effects associated with the small population size at the front (see SI section 7).

Given an explicit wild-type population profile, it is plausible to assume that the selective pressure felt by the mutants is purely due to competition with the wild type, i.e., $s_{\mathrm{MT}}(x) = 1 - c(x)$, such that the local establishment probability of the mutants is coupled to the wild type profile. This should indeed be the case if the antibiotic does not directly alter the birth and death rate of the mutants.

Hence, if $c(x)$ changes sharply, i.e., on length scales shorter than $L_D = \sqrt{D/a_0}$, we expect to see the signatures of a step-like antibiotic profile also in the behavior of $u(x)$. If, on the other hand, $c(x)$ changes slowly in space, then the quasi-static approximation may become applicable. The case of a step-like antibiotic concentration profile $s(x) = s_0\Theta(-x)$ for illustrates both scenarios (see Fig. 6.4a): for $x < 0$, $c(x)$ approaches 1 exponentially (eq. 6.12), such that $u(x)$ is well-described by the broad tail in eq. 6.11. For $x > 0$, instead $c(x)$ decays slowly and the quasi-static approximation can be used such that $u(x) \approx 1 - c(x)$. We compare the simulations with numerical and approximate analytical solutions for $c(x)$ and $u(x)$ in detail in the SI, section 7.

The solutions for $c(x)$ and $u(x)$ can then be used to compute the rate of adaptation R (eq. 6.6) and total

death rate B. Asymptotically, we find,

$$B \approx \sqrt{\frac{D}{a_0}} \times \begin{cases} \sqrt{\frac{\sqrt{12}s_0}{a_0}}, & \text{for } L_D/L_m \ll 1, \\ \frac{s_0}{2a_0 m}, & \text{for } L_D/L_m \gg 1, \end{cases} \tag{6.17}$$

and

$$R \approx \sqrt{\frac{D}{a_0}} \times \begin{cases} 1.8\sqrt{\frac{\sqrt{12}s_0}{a_0}}, & \text{for } L_D/L_m \ll 1, \\ \frac{s_0}{2a_0 m}, & \text{for } L_D/L_m \gg 1, \end{cases} \tag{6.18}$$

which agrees well with the numerical result in the two limiting cases (Fig. 6.5a). The inverse scaling of the rate of adaptation R with the gradient steepness m is also in agreement with Greulich et al.[27] in relatively steep gradients where the rate of adaptation (which is proportional to the rate of adaptation defined here) is dominated by the time until a mutation arises and establishes. Hermsen[28] also finds that the rate of adaptation increases for shallower (but still relatively steep) gradients in what is identified as the "mutation-limited" regime, where mutations are rare. However, both Hermsen and Greulich consider the establishment of many mutation (potentially simultaneously), giving rise to a second, "dispersion-limited", regime[28] in very shallow gradients, in which the mutational supply is large and the rate of adaptation is dominated by the speed with which established mutations invade previously uninhabitable territory. Since we follow the fate of individual mutations, our model operates in the mutation-limited regime exclusively, and we therefore do not expect agreement between our and their models.

6.3.4 Convection

So far, we have neglected external flows and only considered random diffusion of individuals in space. In the following, we explore the influence of convection on the population density, the establishment probability, and finally, the treatment efficiency, which, in the absence of convection, is naturally constrained to a relatively small range, see eqs. 6.17 and 6.18. When a population is subjected to convection, it will generally move in the direction of the flow, leading to either a depletion or enrichment of both mutant and wild types in the antibiotic region (unless convection is too strong, see SI section 4), depending on whether the flow is directed away (counter-flow) or towards (co-flow) the gradient, respectively. We define the direction of the flow such that a negative convection speed v points in the positive x-direction, towards the gradient (see Fig. 6.1). The corresponding equations for $c(\xi, \tau)$ and $u(\xi, \tau)$ are

$$\partial_\tau c = \partial_\xi^2 c + \nu \partial_\xi c + c\left(\sigma_{WT}(\xi) - c\right), \tag{6.19}$$

$$\partial_\tau u = \partial_\xi^2 u - \nu \partial_\xi u + u\left(1 - c - u\right), \tag{6.20}$$

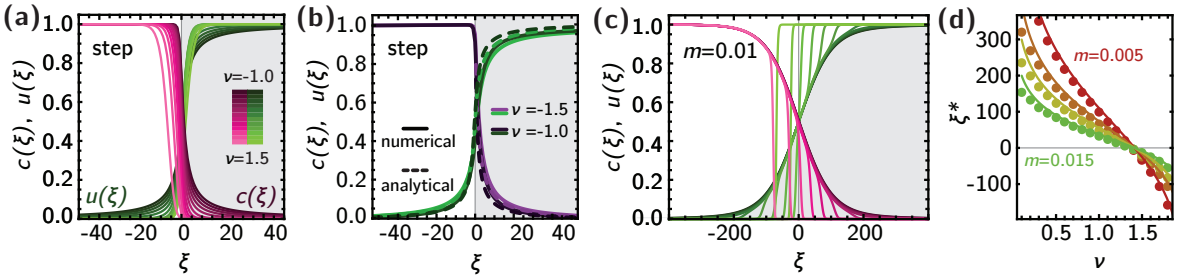

Figure 6.4: The effect of convection on population density $c(x)$ (magenta) and establishment probability $u(x)$ (green) for a step-like antibiotic concentration (a) and a very broad concentration profile ($m = 0.01$, c), for values of the convection speed ν ranging from -1 to 1.5 in steps of 0.25 (dark to light colors). Curves were obtained by numerically integrating eqs. 6.19 and 6.20 (*Methods*). For high negative convection speeds (dark colors), an analytical approximation is valid (b, SI section 5). (d) The cut-off ξ^* of the population density profile in shallow gradients found numerically (dots) agrees well with the theoretical prediction, eq. 6.22 (solid lines).

where $\nu = v/\sqrt{Da_0}$. Note the change in sign for the convection term in the equations for $u(\xi)$ and $c(\xi)$ that stems from the reverse time direction in $u(\xi, \tau)$.

Figure 6.4 shows the effect of convection on both the population density $c(\xi)$ and the establishment probability $u(\xi)$, for a step-like antibiotic profile and a shallow gradient ($m = 0.01$), obtained by first evaluating $c(\xi)$ from eq. 6.19 and then solving $u(\xi)$ from eq. 6.20 using the steady-state density profile (see *Methods*).

Consider first the step-like case. There is a strict distinction between positive and negative convection: negative convection (darker colors in Fig. 6.4a and c) tends to broaden the profiles away from the step and increase both population density and establishment probability near the step. In fact, it can be shown that for our model both profiles decay asymptotically as ν/ξ far from the step in the limit of strong negative convection (Fig. 6.4b, SI section 5). By contrast, positive convection away from the antibiotic ($\nu > 0$) reduces the wild-type population density in the antibiotic region as well as the establishment probability, giving rise to an exponential decay $c(\xi) \sim e^{-\nu\xi}$ for $\xi > 0$.

The effects of a finite gradient steepness, characterized by the length scale L_m, can be judged by rescaling eq. 6.19 by L_m, as in eq. 6.13, i.e.,

$$0 = m^2\partial_\theta^2 c + m\nu\partial_\theta c + \sigma(\theta)c - c^2. \tag{6.21}$$

For $\nu < 0$ in shallow gradients, the profiles are barely affected (see Fig. 6.4c). For $\nu > 0$, on the other hand, convection can alter the profiles strongly: As $m \to 0$, the solution to eq. 6.21 first becomes insensitive to the diffusion term and finally also to the convection term, such that the population density profile $c(\xi)$ follows

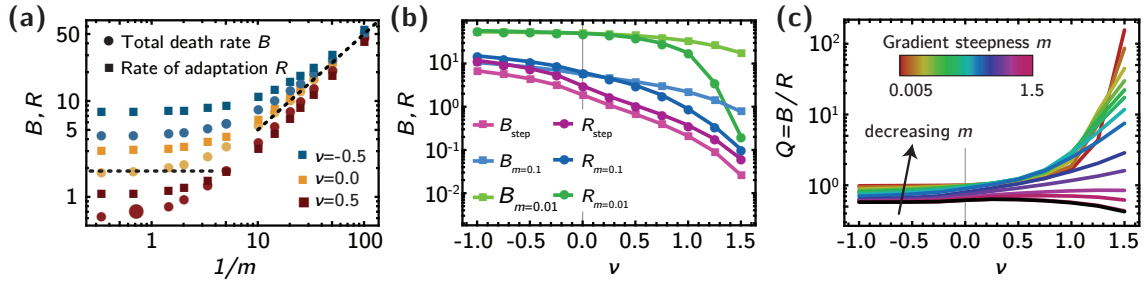

Figure 6.5: The effect of convection on the rate of adaptation R and the total death rate B in our analytical model. Panel (a) shows R and B as a function of the gradient length scale $L_m = L_D/m$. For $\nu = 0$, the total death rate B approaches the theoretical predictions, eq. 6.17. Negative/positive convection shifts both B and R up/down, respectively. Plotting B and R as a function of ν in panel (b), we recover the same trend as in stepping stone simulations: negative/positive convection increase/decrease both R and B similarly. (c) The treatment efficiency $Q = B/R$ for a step-like antibiotic profile (black) and gradients of different steepness, from shallow (purple) to steep (red).

the gradient almost perfectly until it drops steeply to zero at the cut-off position ξ^* (Fig. 6.4d, see SI section 6), given by

$$\xi^* \propto \frac{\operatorname{arctanh}(1 - \nu^2/2)}{m}. \tag{6.22}$$

This cut-off position ξ^* captures the behavior of the numerical solution very well (Fig. 6.4d). The establishment probability $u(\xi)$ mirrors $c(\xi)$ as long as $\xi^* > 0$: for $\xi < 0$, we have $u(\xi) \approx c(-\xi)$, and for $\xi > 0$, we have $u(\xi) \approx 1 - c(\xi)$. For $\xi^* < 0$, $u(\xi)$ increases very sharply from 0 to 1 at the cut-off position, leaving only a very small overlap with $c(\xi)$. Hence, the rate of adaptation R in shallow gradients becomes very small for high positive convection speeds.

Given the scaling of the population density and establishment probability profiles, we can rationalize the behavior of the total death rate B and the rate of adaptation R. As shown in Fig. 6.5a and b, both B and R increase for negative convection because $c(\xi)$ and $u(\xi)$ maintain broader profiles. In shallow gradients, B and R exhibit a plateau, since $c(\xi)$ and $u(\xi)$ are affected only weakly by negative convection (green). For positive convection, both B and R decrease rapidly by up to 2 order of magnitude for our range of parameters. In shallow gradients, the rate of adaptation R decreases faster than the total death rate B with increasing convection speed because convection affects both $c(\xi)$ and $u(\xi)$ equally, such that their overlap decreases more rapidly than $c(\xi)$ alone (see SI section 6). However, for the steepest gradients, B and R decrease at the same pace until at high convection speeds, the death rate B decreases more quickly than R because of the hard cut-off in $b(\xi)$ (Fig. 6.5).

The behavior of the treatment efficiency $Q = B/R$ (Fig 6.5c) follows directly from these considerations.

For $\nu < 0$, i.e., for convection into the antibiotic, Q changes only slightly with ν, and only in relatively steep gradients ($m \gtrsim 0.1$). This is in contrast to the case of convection away from the antibiotic: For shallow gradients, i.e., $L_m \gg L_D$, Q is approximately equal to 1 for small positive and all negative convection speeds. For strong positive convection, the rate of adaptation R becomes very small, such that Q increases rapidly (see SI Fig. S2 and SI section 6). As the step-like case is approached, i.e., for $L_m \ll L_D$, the treatment efficiency Q is *reduced* further for large positive ν, where the total death rate B decays more quickly than the rate of adaptation R.

Our numerical findings, supplemented by analytical calculations rationalize all major observations from our simulations. In particular, we find that convection can strongly alter both the total death rate B and the rate of adaptation R, but in a manner that depends on the steepness of the gradient. Although there are subtle differences between the simulated and numerical profiles of c and u (see SI section 7), our simple model reproduces even the complex phenomenology of the treatment efficiency Q, including the shift from an increase in Q in shallow gradients to a decrease in Q in steep ones.

6.4 Discussion

In order to fight an infection efficiently, an antibiotic must kill as many wild-type bacteria as possible before resistant mutants arise and survive against genetic drift. If a mutant arises in a low-concentration region, it has little advantage over the wild type and likely goes extinct. By contrast, a mutant arising in a high-concentration background will quickly establish, thus creating a resistant population that can populate regions in the antibiotic gradient inaccessible to the wild type. High population densities in high-concentration regions induce significant wild-type death, as the susceptible wild type cannot survive well in these regions. On the other hand, high population densities in high-concentration regions also maximize the number of resistance mutations that occur in a favorable environment.

We have studied this trade-off between drug-induced wild-type death and adaptation in an antibiotic gradient using simulations and analytical theory. Our simulations reveal that drug-induced death is highest when the wild-type population density is enriched in high-concentration regions, i.e., for convection towards the antibiotic, and shallow gradients. However, since each wild-type individual harbors the potential for a resistance mutation to occur, which would then have a big advantage over the wild type in the region where it occurs, the rate of establishment of resistance mutations has the same general behavior. Similarly, for strong counter-flow, the drug-induced total death rate is decreased because the wild-type population density is low in high-drug regions, which in turn limits the rate of establishment of new resistance mutations. Thus, making ad hoc predictions about the treatment efficiency is difficult. Our detailed analysis of population density $c(x)$ and establishment probability $u(x)$ profiles over a wide range of gradient steepness

and convection speeds shows that in shallow gradients, where both $c(x)$ and $u(x)$ are strongly affected by convection away from the antibiotic, treatment can become an order of magnitude more efficient than in no-flow scenarios.

Our simulations are a strongly simplified model of real populations. For instance, we have assumed that mutation establish independently, i.e., we have neglected clonal interference. Our predictions are thus strictly speaking only valid when mutations arise rarely enough that they do not interact. Typically, this condition is quantified by demanding that $\mu N_e \ll 1$, where N_e is the effective population size. In a spatial scenario, however, potentially interfering mutations can only arise in a spatial region where both the population density c and the establishment probability u are large. Thus, our results remain valid as long as $\mu \int c(x)u(x) \ll 1$. For resistance mutations with small target sizes, mutation rates can be very small, typically less than 10^{-6} [41,42], and thus our approximation may be accurate even for relatively large local populations. In addition, even when mutation rates are not small, we expect convection and spatial gradients to have the same qualitative effects on the establishment of resistance mutations, and thus our results should remain qualitatively correct in this case.

Individuals in our simulation merely occupy "space" in their specific deme; in reality, bacteria have a finite size, and a population front can advance through mere growth, even against strong counter-flow [43]. Conversely, for strong co-flow, individuals may de-adhere and be carried away from the bulk population, thus founding extant colonies that enjoy large growth rates in the absence of competition for resources. Such processes can be studied by generalizing the diffusion term in our model to a long-range dispersal term as used frequently to model epidemics [44]. Since long-range dispersal can allow individuals far from the population front to escape the bulk population, we expect it to increase the total establishment probability and thus the rate of adaptation relative to short-range dispersal as discussed here.

We have only discussed one-dimensional populations here, but real surface-bound microbial populations typically grow as two-dimensional colonies, with complex spatial patterns. The establishment of beneficial mutations in microbial colonies has recently been discussed [15,45]. Due to the particular strength of genetic drift at the front of such populations, beneficial mutations first have to reach a threshold size (depending on the strength of the selective advantage) neutrally before they become established. Once the mutant clone reaches the threshold size, the selective advantage of the mutants can deterministically drive them to fixation in the population. During the initial phase, the mutant clone is contained between boundaries with characteristic stochastic properties that are not captured in our one-dimensional model [14]. However, if the threshold size is small, the boundary fluctuations will not have a large impact on the growth of mutant clones. In such cases, we expect our results to apply also to two-dimensional populations.

The emergence of drug resistance remains a topic of significant interest, both from a scientific and a public health point of view. Considerable effort is brought forward to create novel antibiotics [46] and new therapy

strategies are developed that attempt to limit the emergence of resistance[47,48], but more research is needed to understand how resistance evolves in complex spatio-temporal settings like the spatial gradients discussed in this paper. In particular, as we have shown here, convection constitutes an important factor in shaping the adaptation to antibiotics in spatial concentration gradients and should receive more attention from both theorists and experimentalists.

References

[1] H. C. Neu. The crisis in antibiotic resistance. *Science*, 257(5073):1064–1073, 1992. doi: 10.1126/science.257.5073.1064.

[2] B. Spellberg, R. Guidos, D. Gilbert, J. Bradley, H. W. Boucher, W. M. Scheld, J. G. Bartlett, J. Edwards, and the Infectious Diseases Society of America. The epidemic of antibiotic-resistant infections: A call to action for the medical community from the infectious diseases society of america. *Clinical Infectious Diseases*, 46(2):155–164, 2008.

[3] J. Davies and D. Davies. Origins and evolution of antibiotic resistance. *Microbiology and Molecular Biology Reviews*, 74(3):417–433, 2010.

[4] S. B. Levy and B. Marshall. Antibacterial resistance worldwide: causes, challenges and responses. *Nature Medicine*, 10:S122–S129, 2004. doi: 10.1038/nm1145.

[5] G. Lambert, L. Estévez-salmeron, S. Oh, D. Liao, B. M. Emerson, T. D. Tlsty, and R. H. Austin. An analogy between the evolution of drug resistance in bacterial communities and malignant tissues. *Nature reviews. Cancer*, 11(May):375–382, 2011. doi: 10.1038/nrc3039.

[6] S. Raguz and E. Yagüe. Resistance to chemotherapy: new treatments and novel insights into an old problem. *British journal of cancer*, 99(3):387–391, 2008.

[7] J. M. Blair, M. A. Webber, A. J. Baylay, D. O. Ogbolu, and L. J. Piddock. Molecular mechanisms of antibiotic resistance. *Nature Reviews Microbiology*, 13:42–51, 2015.

[8] E. Toprak, A. Veres, J.-B. Michel, R. Chait, D. L. Hartl, and R. Kishony. Evolutionary paths to antibiotic resistance under dynamically sustained drug selection. *Nature genetics*, 44(1):101–5, jan 2012. doi: 10.1038/ng.1034.

[9] R. Allen and B. Waclaw. Antibiotic resistance: a physicist's view. *Physical biology*, 13(4):045001, 2016.

[10] J. Ramsayer, O. Kaltz, and M. E. Hochberg. Evolutionary rescue in populations of Pseudomonas fluorescens across an antibiotic gradient. *Evolutionary Applications*, 6(4):608–616, 2013. doi: 10.1111/eva.12046.

[11] R. C. MacLean, A. R. Hall, G. G. Perron, and A. Buckling. The population genetics of antibiotic resistance: integrating molecular mechanisms and treatment contexts. *Nature Reviews Genetics*, 11 (6):405–414, 2010.

[12] M. Baym, T. D. Lieberman, E. D. Kelsic, R. Chait, R. Gross, I. Yelin, and R. Kishony. Spatiotemporal microbial evolution on antibiotic landscapes. *Science*, 353(6304):1147 – 1151, 2016. doi: 10.1126/science.aag0822.

[13] S. Ling, Z. Hu, Z. Yang, F. Yang, Y. Li, Q. Chen, Q. Gong, D. Wu, W. Li, X. Tian, C. Hao, E. A. Hungate, V. T. Daniel, R. R. Hudson, W.-h. Li, X. Lu, S. Ling, Z. Hu, Z. Yang, F. Yang, Y. Li, P. Lin, K. Chen, L. Dong, and L. Cao. Extremely high genetic diversity in a single tumor points to prevalence of non-Darwinian cell evolution. *Proceedings of the National Academy of Sciences*, 113(5):E663–E663, 2016. doi: 10.1073/pnas.1600151113.

[14] D. Fusco, M. Gralka, A. Anderson, J. Kayser, and O. Hallatschek. Excess of mutational jackpot events in growing populations due to gene surfing. *Nature Communications*, 7:1–9, 2016. doi: 10.1101/053405.

[15] M. Gralka, F. Stiewe, F. Farrell, W. Möbius, B. Waclaw, and O. Hallatschek. Allele Surfing Promotes Microbial Adaptation from Standing Variation. *Ecology letters*, 19(8):889–898, 2016. doi: 10.1111/ele.12625.

[16] Q. Zhang, G. Lambert, D. Liao, H. Kim, K. Robin, C.-k. Tung, N. Pourmand, and R. H. Austin. Acceleration of emergence of bacterial antibiotic resistance in connected microenvironments. *Science*, 333(6050):1764–1767, 2011.

[17] G. Bell and A. Gonzalez. Adaptation and evolutionary rescue in metapopulations experiencing environmental deterioration. *Science (New York, N.Y.)*, 332(6035):1327–30, jun 2011. doi: 10.1126/science.1203105.

[18] G. Bell and A. Gonzalez. Evolutionary rescue can prevent extinction following environmental change. *Ecology letters*, 12(9):942–8, sep 2009. doi: 10.1111/j.1461-0248.2009.01350.x.

[19] J. L. Martinez. The role of natural environments in the evolution of resistance traits in pathogenic bacteria. *Proceedings of the Royal Society B: Biological Sciences*, 276(1667):2521–2530, 2009. doi: 10.1098/rspb.2009.0320.

[20] D. I. Andersson and D. Hughes. Microbiological effects of sublethal levels of antibiotics. *Nature reviews. Microbiology*, 12(7):465–78, jul 2014.

[21] P. S. Stewart and J. William Costerton. Antibiotic resistance of bacteria in biofilms. *The Lancet*, 358 (9276):135–138, 2001. doi: 10.1016/S0140-6736(01)05321-1.

[22] A. M. Elliott, S. E. Beming, M. D. Iseman, and C. A. Peloquin. Failure of drug penetration and acquisition of drug resistance in chronic tuberculous empyema. *Tubercle and Lung Disease*, 76(5): 463–467, 1995. doi: 10.1016/0962-8479(95)90016-0.

[23] A. Meulemans, F. Paycha, P. Hannoun, and M. Vulpillat. Measurement and clinical and pharmacokinetic implications of diffusion coefficients of antibiotics in tissues. *Antimicrobial agents and chemotherapy*, 33(8):1286–1290, 1989.

[24] A. I. Minchinton and I. F. Tannock. Drug penetration in solid tumours. *Nature Reviews Cancer*, 6 (8):583–592, 2006.

[25] T. B. Kepler and A. S. Perelson. Drug concentration heterogeneity facilitates the evolution of drug resistance. *Proceedings of the National Academy of Sciences*, 95(20):11514–11519, 1998.

[26] R. Hermsen, J. B. Deris, and T. Hwa. On the rapidity of antibiotic resistance evolution facilitated by a concentration gradient. *Proceedings of the National Academy of Sciences*, 109(27):10775–10780, 2012.

[27] P. Greulich, B. Waclaw, and R. J. Allen. Mutational pathway determines whether drug gradients accelerate evolution of drug-resistant cells. *Physical Review Letters*, 109(8):088101, 2012.

[28] R. Hermsen. The adaptation rate of a quantitative trait in an environmental gradient. *Physical Biology*, 13(6):065003, 2016. doi: 10.1088/1478-3975/13/6/065003.

[29] L. Passerini, K. Lam, J. W. Costerton, and E. G. King. Biofilms on indwelling vascular catheters. *Critical Care Medicine*, 20(5):665–673, 1992.

[30] L. Hall-Stoodley, J. William Costerton, and P. Stoodley. Bacterial biofilms: from the natural environment to infectious diseases. *Nature Reviews Microbiology*, 2(2):95–108, 2004. doi: 10.1038/nrmicro821.

[31] A. Persat, C. D. Nadell, M. K. Kim, F. Ingremeau, A. Siryaporn, K. Drescher, N. S. Wingreen, B. L. Bassler, Z. Gitai, and H. A. Stone. The mechanical world of bacteria. *Cell*, 161(5):988–997, 2015. doi: 10.1016/j.cell.2015.05.005.

[32] J. Cremer, I. Segota, C.-y. Yang, M. Arnoldini, J. T. Sauls, Z. Zhang, E. Gutierrez, A. Groisman, and T. Hwa. Effect of flow and peristaltic mixing on bacterial growth in a gut-like channel. *Proceedings of the National Academy of Sciences*, page 201601306, 2016.

[33] T. J. Battin, W. T. Sloan, S. Kjelleberg, H. Daims, I. M. Head, T. P. Curtis, and L. Eberl. Microbial landscapes: new paths to biofilm research. *Nature reviews. Microbiology*, 5(1):76–81, 2007. doi: 10.1038/nrmicro1556.

[34] D. J. Stickler. Bacterial biofilms in patients with indwelling urinary catheters. *Nature Clinical Practice Urology*, 5(11):598–608, 2008. doi: 10.1038/ncpuro1231.

[35] R. Lehe, O. Hallatschek, and L. Peliti. The rate of beneficial mutations surfing on the wave of a range expansion. *PLoS Comput Biol*, 8(3):e1002447, 2012.

[36] F. Fu, M. A. Nowak, and S. Bonhoeffer. Spatial heterogeneity in drug concentrations can facilitate the emergence of resistance to cancer therapy. *PLoS Comput Biol*, 11(3):e1004142, 2015.

[37] P. W. Rand, E. Lacombe, H. E. Hunt, and W. H. Austin. Viscosity of normal human blood under normothermic and hypothermic conditions. *J. Appl. Physiol.*, 19(1):117–122, 1964.

[38] X. L. Wu and A. Libchaber. Particle diffusion in a quasi-two-dimensional bacterial bath. *Physical Review Letters*, 84(13):3017–3020, 2000. doi: 10.1103/PhysRevLett.84.3017.

[39] M. J. Kim and K. S. Breuer. Enhanced diffusion due to motile bacteria. *Physics of Fluids*, 16(9):78–81, 2004. doi: 10.1063/1.1787527.

[40] R. A. Fisher. The wave of advance of advantageous genes. *Annals of eugenics*, 7(4):355–369, 1937.

[41] J. L. Martinez and F. Baquero. Mutation frequencies and antibiotic resistance. *Antimicrobial Agents and Chemotherapy*, 44(7):1771–1777, 2000. doi: 10.1128/AAC.44.7.1771-1777.2000.

[42] N. Woodford and M. J. Ellington. The emergence of antibiotic resistance by mutation. *Clinical Microbiology and Infection*, 13(1):5–18, 2007. doi: 10.1111/j.1469-0691.2006.01492.x.

[43] F. Tesser, J. C. H. Zeegers, H. J. H. Clercx, L. Brunsveld, and F. Toschi. Finite-size effects on bacterial population expansion under controlled fow conditions. (1), 2016.

[44] O. Hallatschek and D. S. Fisher. Acceleration of evolutionary spread by long-range dispersal. *Proceedings of the National Academy of Sciences*, 111(46):E4911–E4919, 2014.

[45] M. O. Lavrentovich, K. S. Korolev, and D. R. Nelson. Radial Domany-Kinzel models with mutation and selection. *Physical Review E*, 87(1):012103, jan 2013. doi: 10.1103/PhysRevE.87.012103.

[46] I. B. Seiple, Z. Zhang, P. Jakubec, A. Langlois-Mercier, P. M. Wright, D. T. Hog, K. Yabu, S. R. Allu, T. Fukuzaki, P. N. Carlsen, et al. A platform for the discovery of new macrolide antibiotics. *Nature*, 533(7603):338–345, 2016.

[47] P. M. Enriquez-Navas, Y. Kam, T. Das, S. Hassan, A. Silva, P. Foroutan, E. Ruiz, G. Martinez, S. Minton, R. J. Gillies, et al. Exploiting evolutionary principles to prolong tumor control in preclinical models of breast cancer. *Science translational medicine*, 8(327):327ra24–327ra24, 2016.

[48] I. K. Paterson, A. Hoyle, G. Ochoa, C. Baker-Austin, and N. G. H. Taylor. Optimising Antibiotic Usage to Treat Bacterial Infections. *Scientific Reports*, 6(November):37853, 2016. doi: 10.1038/srep37853.

6.5 Appendix

6.5.1 Methods

Individual-based simulation

We perform individual-based, stepping stone simulations where both wild-type and mutants are modeled explicitly. The population is divided into demes with carrying capacity K on a one-dimensional lattice. Wild-type and mutants replicate at a rate a_0 and migrate at rate D independently on their position. Wild-type in deme i die at a rate $b(x_i) = \frac{1}{2}[1 + \tanh(mx_i)]$. Since we assume throughout that the antibiotic leaves the mutants unaffected, mutants do not die in our simulations. Analogously to a Gillespie algorithm, in each simulation step, a birth, death or migration event is performed according to its relative rate[1,2], as follows.

- Birth. Birth events occur at a total rate equal to $a_0 \sum_i c(x_i)$, where $c(x_i)$ is the total number of individuals in deme i. For each birth event, a source individual is selected at random and replicated into a random target site between 1 and K within the same deme. Because the target site can either already be filled with an individual or be empty, this move effectively translates into logistic growth within the deme.
- Death. In our model, only the wild type can die, thus deaths have a total rate corresponding to $\sum_i b(x_i)c_{\text{wt}}(x_i)$, where $c_{\text{wt}}(x_i)$ represents the number of wild type individuals in deme i. To perform a death event, first, a deme i is picked proportionally to its relative death rate $b(x)c_{\text{wt}}(x_i)$, and then, a random wild type within the same deme selected to be removed.
- Migration. Migrations are performed at a rate $D \sum_i c(x_i)$ by picking a random individual and swapping it with a randomly selected target site from one of the two neighboring demes. As in the case of birth events, the target site can either correspond to an individual, or to an empty site.
- Time step. Time is tracked by sampling a time interval δt from an exponential distribution with rate $\sum_i [(a_0 + D)c(x_i) + b(x_i)c_{\text{wt}}(x_i)]$, as in a standard Gillespie algorithm. The total elapsed time is the sum of the sampled time intervals.
- Convection. Convection (with convection speed v) is implemented by shifting the simulation box by one deme towards or away from the wild type population, depending on whether convection is negative or positive, respectively. The shift is performed when the time since the last shift is greater than $1/|v|$.

For each simulation, we first allow the wild type to reach the steady-state profile $c(x)$. We then introduce one mutant element at position x and run the simulation until either all mutants go extinct, or mutants reach the last deme in the simulation box. No further mutations are allowed in the course of the simulations. The probability of fixation $u(x)$ is then computed as the proportion of the simulations in which a mutant introduced at x reached fixation.

Numerics

All numerical results were obtained by evaluating the differential equations using Mathematica's built-in *NDSolve* routine with the backwards differentiation (BDF) method, with a maximum step size of 1 and a domain size of 1000. Initial conditions were chosen according to the analytical approximations to the steady-state profiles given in the text. This is only done to speed up computation and increase numerical stability; starting with different initial conditions leads the same final solution. To obtain steady-state profiles, we solve the full time-dependent problems until the solution no longer changes for longer evaluation times.

To compute the establishment probability $u(x)$ in realistic wild-type population profiles $c(x)$, we first computed the steady-state population density and then used the final profile to compute the (constant in time) local death rate for the mutants $b(x) = 1 - c(x)$. The resulting numerical solutions were integrated numerically using Mathematica's built-in *NIntegrate* routine to obtain the total death rate B and the rate of adaptation R.

6.5.2 Derivation of survival probability

Suppose particles branch at rate a and disappear at rate b. Then the probability $u(0;T)$ that a particle or its offspring survive until time T satisfies

$$u(-\epsilon;T) = [1-\epsilon(a+b)]\,u(0,T) + \epsilon a\left[1-(1-u(0,T))^2\right] \tag{6.S1}$$

The first term on the right-hand side describes the case of neither disappearing nor branching. The second one accounts for the fact that when the initial particle branches then there are two particles, and the probability of survival of at least one lineage is 1 minus the square of both lineages disappearing. Using time-translation invariance $u(-\epsilon;T) = u(T+\epsilon)$, we obtain in the limit $\epsilon \to 0$

$$\partial_t u(t) = (a-b)u(t) - au^2(t). \tag{6.S2}$$

To extend this equation for spatial degrees of freedom simply account in eq. 6.S1 for the random jumps to neighboring lattice sites in a small time interval ϵ.

6.5.3 Solving the establishment probability for step-like concentration profile

The (ultimate) establishment probability of a mutation in step-like antibiotic concentration profile given by

$$\sigma(\xi) = \sigma_0\Theta(-\xi) \tag{6.S3}$$

satisfies eq. 7 in the main text, repeated here for completeness:

$$0 = \partial_\xi^2 u + \sigma_0 \Theta(-\xi) u - u^2. \tag{6.S4}$$

To solve this equation, we first treat both sides of the step independently, and then fix integration constants by invoking differentiability at $\xi = 0$.

Antibiotic-free region $\xi > 0$

The fixation probability of mutants in the region $\xi > 0$ (where $\sigma(\xi) = 0$ is determined by the following differential equation:

$$0 = \partial_\xi^2 u - u^2 \tag{6.S5}$$

with boundary conditions, $u(0) = u_0$ and $u(\infty) = 0$. We exploit a mechanical analogy to solve this equation. We write eq. 6.S5 as

$$\partial_\xi^2 u = -\partial_u V(u) \tag{6.S6}$$

with a 'potential energy' $V(u) = -u^3/3$. We can then determine the solution for $u(\xi)$ as

$$\xi = \int_{u_0}^{u(\xi)} \frac{du'}{\sqrt{-2V(u')}} \,. \tag{6.S7}$$

where the 'total energy' $E = \frac{1}{2}\left(\partial_\xi u\right)^2 + V(u) = 0$ was chosen to satisfy the boundary condition as $\xi \to \infty$. The solution thus follows as

$$u(\xi) = u_0 \left(1 + \sqrt{u_0}\xi/\sqrt{6}\right)^{-2}, \tag{6.S8}$$

implying $u \sim 1/\xi^2$ for large ξ.

Antibiotics region $\xi < 0$

In the region $\xi < 0$ the new mutations have a net growth rate $\sigma(\xi) = \sigma_0$. The fixation probability is then given as the solution of

$$\partial_\xi^2 u = -\sigma_0 u + u^2, \tag{6.S9}$$

Exploiting the same mechanical analogy, we have the integral:

$$\int_{u_0}^{u} \frac{du}{\sqrt{-\sigma_0 u^2 + 2u^3/3 + \sigma_0^3/3}} = -\xi, \tag{6.S10}$$

where we have used the condition $u(-\infty) = \sigma_0$ to set the total energy. We obtain

$$u(\xi) = \frac{\sigma_0}{2}\left\{3\tanh^2\left[\frac{\sqrt{\sigma_0}}{2}(\xi^* - \xi)\right] - 1\right\}, \tag{6.S11}$$

where $\xi^* = \frac{2}{\sqrt{\sigma_0}}\text{arctanh}\sqrt{\frac{1}{3} + \frac{2u_0}{3\sigma_0}}$.

At $\xi = 0$, u' is continuous since $u''(0)$ is finite. By imposing continuity on the derivatives from the left and right solutions, we determine $u_0 = \sigma_0/\sqrt{3}$.

6.5.4 Treatment efficiency without convection

To find an approximation for Q in the absence of convection, we can compute B and R independently.

For a shallow gradient where $c(\xi) = s_{\text{WT}}(\xi) = 1 - u(\xi)$, it follows that $B = R$ and hence $Q = 1$. For a step, B can be obtained directly by simple integration of $c(\xi)$, $B = \sqrt{2} \cdot 3^{1/4}$. To compute R, the integral for $\xi > 0$ is easily performed to yield $R^+ = \frac{2}{3}\sqrt{14/\sqrt{3} - 3}$, but for $\xi < 0$, the full solution for $c(\xi)$ cannot be easily integrated. However, $c(\xi < 0)$ is well approximated by $c(\xi) \approx 1 - (1 - \sqrt{3})e^{\xi}$. Thus, we obtain the result $R^- = B + 2(\sqrt{3} - 3)e^{\sqrt{3}B}\text{Ei}(-\sqrt{3}B)$, where $\text{Ei}(x) = -\int_{-x}^{\infty} e^{-t}/t$ is the exponential integral function. Q then evaluates to

$$Q \approx 0.581, \tag{6.S12}$$

close to the numerical value of $Q_{\text{num}} \approx 0.612$.

6.5.5 Strong convection

A population growing logistically with an homogeneous rate across demes leads to a Fisher wave with a front velocity given by $v_F = 2\sqrt{Da_0}$[3]. In the presence of a convection v, far away from the gradient the wild-type population would generate a front advancing at speed $v_F - v$. Hence, intuitively, if convection is too strong, i.e., $|v| > v_F$, the population will not be able to establish a steady-state profile.

To show this formally, we first transform eq. 17 by introducing a new variable $\psi = ue^{\nu\xi/2}$, such that the

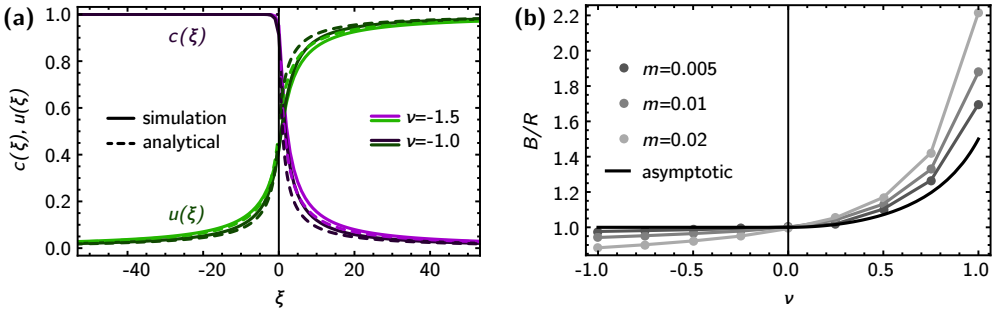

Figure 6.S1: (a) For strong negative convection, the analytical approximations to $c(\xi)$ (eq. 6.S16) and $u(\xi)$ (eq. 6.S17) matches the simulation results well. (b) Treatment efficiency Q for different gradients m, with asymptotic result, eq. 6.S27 (black).

convection term is replaced by a death term with effective death rate proportional to ν^2,

$$\begin{aligned} \partial_\tau \psi(\xi,\tau) &= \partial_\xi^2 \psi - \frac{\nu^2}{4}\psi + \sigma_0 \Theta(-\xi)\psi - \psi^2 e^{-\nu\xi/2}, \\ \psi(\xi,0) &= e^{\nu\xi/2}. \end{aligned} \tag{6.S13}$$

Around $\xi = 0$, the exponential factor is approximately equal to 1 and the nonlinearity ψ^2 can be neglected because $\psi \ll 1$. The resulting linear equation then has solutions that can be written as $\psi = \sum_k a_k(\tau) e^{ik\xi}$. Each mode then satisfies a differential equation

$$\dot{a}_k = -\omega_k a_k, \tag{6.S14}$$

with $\omega_k = k^2 + \nu^2/4 - \sigma_0$. Thus, the lowest mode $k = 0$ decays to zero as long as $\nu^2/4 - \sigma_0 > 0$, and all higher modes are suppressed by the coupling of modes through the nonlinearity[4]. Therefore, ψ, and hence $c(\xi)$, undergo an extinction transition for $\sigma_0 > 0$ when $\nu^2/4 > \sigma_0$.

6.5.6 Convection in a step-like gradient

Convection into the antibiotics

For negative v, we first solve for $c(\xi)$. For $-2 < \nu \ll 0$, we can neglect diffusion and find the equilibrium population density by solving

$$0 = \nu \partial_\xi c + \Theta(-\xi)c - c^2. \tag{6.S15}$$

The solution for $\xi > 0$ is

$$c(\xi) = \frac{1}{1 + \xi/|\nu|}. \tag{6.S16}$$

We thus uncover another characteristic length scale $L_v = X\nu = v/a_0$, which quantifies the strength of convection relative to diffusion: if $L_v \gg L_D$, convection dominates over diffusion, and vice-versa.

Far away from the antibiotics, c will always eventually reach the carrying capacity. Hence, $c(\xi \to -\infty) \to 1$, which is a fixed point of eq. 6.S15 for $x < 0$. It follows that $c(\xi < 0) \equiv 1$.

Plugging eq. 6.S16 into the equation for the establishment probability $u(\xi)$, eq. 18 in the main text, we find analytical solutions in two cases: for small but finite negative ν, the convection term and the diffusion term can both be neglected and we recover the quasi-static result $u(\xi) = 1 - c(\xi)$. For strong negative convection, $-2 < \nu \ll 0$, we can neglect only the diffusion term and integrate directly. The result is

$$\begin{aligned} u(\xi) &= \frac{1}{2 - \xi/|v|}, \qquad x < 0, \\ u(\xi) &= 1 - \frac{1}{2 + \xi/|v|}, \qquad x > 0. \end{aligned} \tag{6.S17}$$

Since $c(\xi < 0) = 1$, it is easy to see that this approximation does not yield a finite rate of adaptation for infinite domains since mutants arising far away from the antibiotics region still have a relatively high chance of establishing. In practice, the rate of adaptation is always finite because for finite ν, the decay is slightly faster that $1/\xi$. Assuming a finite domain (or a cut-off, e.g., because of a finite carrying capacity) ranging from some $-\xi_0$ to ξ_0, we can estimate both the rate of adaptation R and the total death rate B, and thus the treatment efficiency $Q = B/R$, as

$$R = \quad \nu \log[1 + \xi_0/\nu] \tag{6.S18}$$

$$B = \quad 2\nu \log[1 + \xi_0/2\nu] \tag{6.S19}$$

$$Q = \quad \frac{\log[1+\xi_0/\nu]}{2\log[1+\xi_0/2\nu]} \gtrsim \frac{1}{2} \tag{6.S20}$$

where we have assumed $\xi_0/\nu \gg 1$ in the last step. In our numerical evaluations, $\xi_0 = 500$ and $\nu < 2$, such that we have $Q \approx 0.57$.

Convection away from antibiotics

Positive convection ($\nu > 0$) away from the antibiotic limits diffusion of the wildtype into the antibiotics, thus leading to a reduced wildtype population density in the region of antibiotics. For strong convection and a step-like drug profile, the population density decays exponentially over the characteristic distance X/ν.

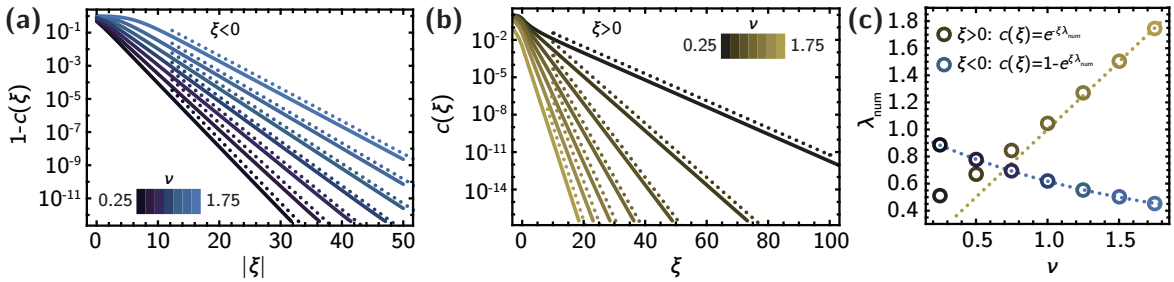

Figure 6.S2: Population density profile for a step-like antibiotic concentration gradient and positive convection $\nu > 0$. Both in the region of high antibiotic concentration $(\xi > 0)$ and no antibiotic concentration $(\xi < 0)$, the population density approaches its asymptotic value exponentially ((a) and (b), analytical results as dotted lines). Fitting the numerical curves with the analytical expressions, eqs. 6.S22 and 6.S24, we obtain the apparent exponential prefactors λ_{num}, which match well with the expressions for $\lambda_{\pm}$ given in the text.

This follows by considering the steady-state equation for $c(\xi > 0)$,

$$0 = \partial_\xi^2 c + \nu \partial_\xi c - c^2. \tag{6.S21}$$

For $\xi > 0$, $c(\xi)^2$ is positive while $c'(\xi)$ is negative; because these two terms cannot add up to zero, we cannot neglect the diffusive term. However, since we expect $c(\xi)$ to be small, we can instead neglect $c(\xi)^2$ to obtain the equation $0 = c'' + \nu c'$, such that

$$c(\xi > 0) \propto e^{-\lambda_+ \xi}, \tag{6.S22}$$

where $\lambda_+ = \nu$, which approximates the numerical solution well (Fig. 6.S2).

For $\xi < 0$, the corresponding equation reads

$$0 = \partial_\xi^2 c + \nu \partial_\xi c + c - c^2, \tag{6.S23}$$

which does not have a simple analytical solution. However, we can find by inspection that $c(\xi)$ approximately behaves as

$$1 - c(\xi < 0) \propto e^{-\lambda_- |\xi|}, \tag{6.S24}$$

where λ_- is parametrized well by $\lambda_- \approx 2/(\nu + \sqrt{\nu^2 + 4})$ (see Fig. 6.S2.

6.5.7 Shallow gradients with convection

For $\nu > 0$ and $L_m \gg L_v$, we can transform eq. 18 by defining $\psi = ce^{-\nu\xi/2}$ to obtain

$$\partial_\tau \psi(\xi,\tau) = \partial_\xi^2 \psi + \left(\sigma(\xi) - \frac{\nu^2}{4}\right)\psi - \psi^2 e^{-\nu\xi/2}. \tag{6.S25}$$

Convection only has a relatively small effect on $c(\xi)$ and $u(\xi)$, and only in the region of strong antibiotics (where $\sigma(\xi) \ll 1$), as long as $\sigma(\xi) > \nu^2/4$. For large enough ξ this will no longer be satisfied. When $\sigma(\xi) \sim \nu^2/4$, the convection term leads to a cut-off. Assuming the cut-off is faster than exponential, we can neglect the non-linearity near the cut-off and thus find a transition to negative growth rate $\partial_\tau\psi(\xi,\tau)$ for $\sigma(\xi^*) = \nu^2/4$. Solving for ξ^*, we obtain the approximate cut-off position

$$\xi^* = m^{-1}\text{arctanh}(1-\nu^2/2). \tag{6.S26}$$

Note that $\xi^* = 0$ for $\nu = \sqrt{2}$. For $\nu < \sqrt{2}$, we can estimate R and B analytically by approximating $c(\xi) \approx \sigma(\xi)\Theta(\xi - \xi^*)$ and similarly for $u(\xi)$. This leads to

$$Q = \frac{1}{2} + \frac{1}{2-\nu^2}. \tag{6.S27}$$

For $\nu < \nu^*$, this agrees well with the numerical result for shallow gradients ($m \ll 1$), as shown in Fig. 6.S1. When $\xi^* < 0$, i.e., when $\nu > \sqrt{2}$, $c(\xi)$ and $u(\xi)$ retain a small overlap, as shown in Fig. 4b in the main text. Hence, the treatment efficiency Q does not diverge at ν^*.

6.5.8 Comparing simulations and numerics

Our model for the dynamics of the population density, like the original Fisher equation, ignores the discrete nature of individuals. This has been shown to have important consequences, particularly at the tip of the population front, where the number of individuals per deme is small. A heuristic way to implement the discreteness of individuals consists in introducing a cut-off in the growth rate when the local population size becomes too small[5]. Such a cut-off alters the front profile, and the resulting correction to the expansion velocity decays only slowly with the carrying capacity K,

$$v_F^* = v_F\left(1 - \frac{\pi^2}{2\ln^2 K}\right). \tag{6.S28}$$

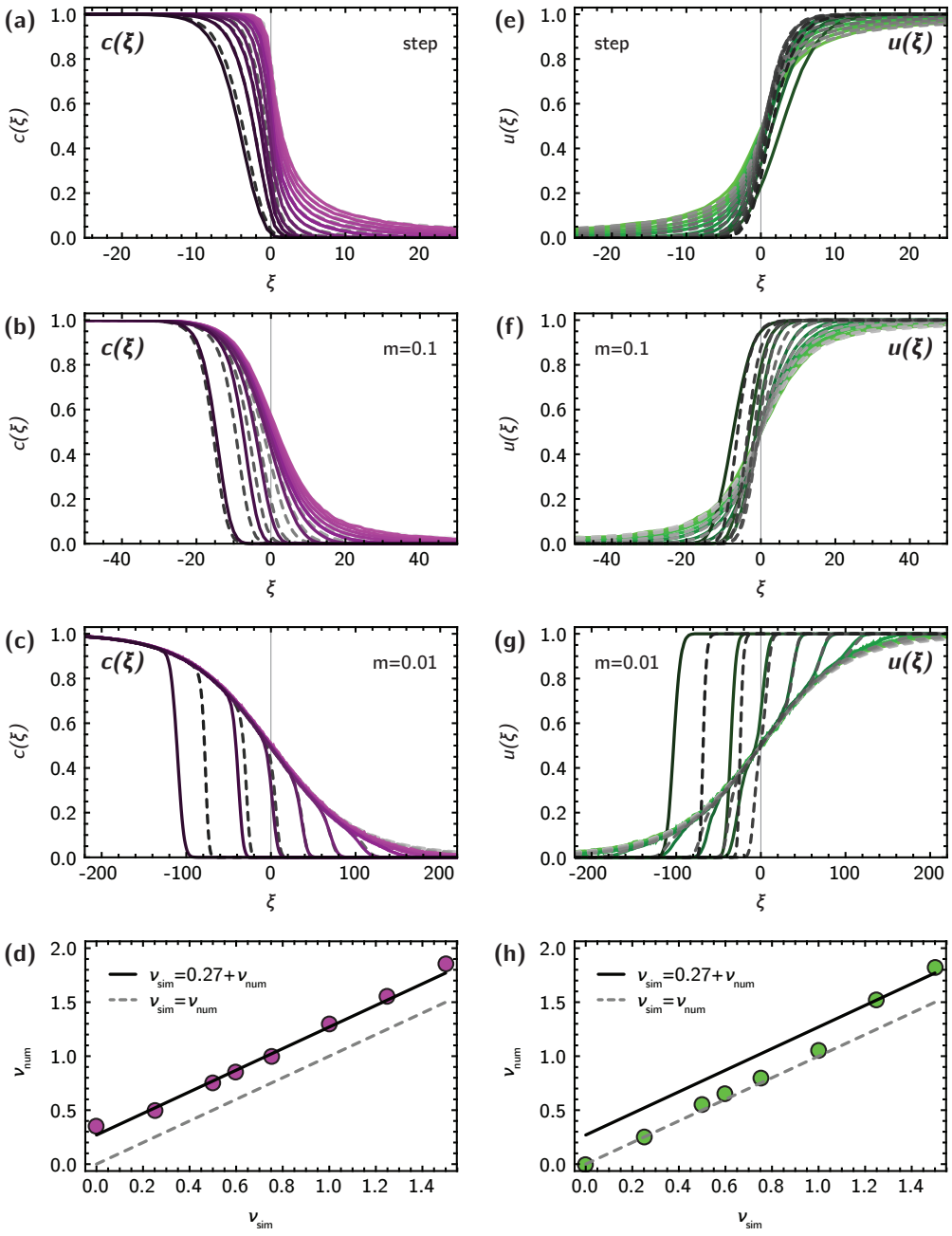

Figure 6.S3: Comparison between simulated (solid lines) and numerically evaluated (dashed gray) profiles of population density $c(\xi)$ (left column, magenta) and establishment probability $u(\xi)$ (right column, green), for three different antibiotic gradients (step-like, (a) and (e); intermediate gradient $m = 0.1$, (b) and (f); shallow gradient $m = 0.01$, (c) and (g)). Deviations between simulations and our numerical model can be traced back to a difference in effective convection speed: the population density feels a slightly higher effective convection ν_{num} (d), while the establishment probability profile reflects the actual convection speed in the simulation ν_{sim} (h) until the deviations in $c(\xi)$ become too large at high ν_{sim}.

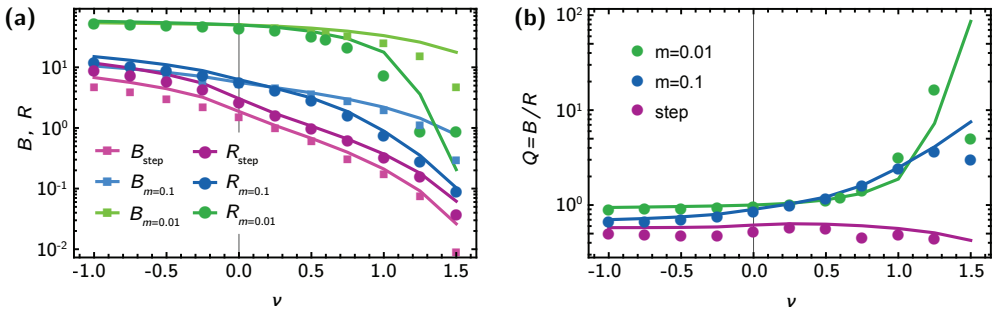

Figure 6.S4: (a) Good agreement between simulated (dots) and numerically evaluated (lines) total birth rate B and rate of adaptation R. Deviations appear mainly at high positive convection speeds $\nu \gg 0$ in shallow gradients, where the wave front is characterized by strong fluctuations (see Fig. 6.S3 and SI Section 7. (b) Our theory reproduces the observed trends of the treatment efficiency Q except for the highest positive convection speeds.

In our simulations, we use $K = 100$, which should lead to a correction to the velocity by almost 25%. Quantitative comparison between numerics and simulations reveals such correction. In shallow gradients with positive convection, where the population density and establishment probability profiles are effectively cut off at a characteristic position ξ^* (see eq. 6.S26), we compute the effective convection speed by comparing the cut-offs in simulated profiles with the numerical curves. The results are shown in Fig. 6.S3(d) and (h): the population density obtained from simulations at convection speed ν_{sim} has cut-offs positions corresponding to a numerical convection speed ν_{num} that is shifted up by a constant. For instance, even at $\nu_{\text{sim}} = 0$, we observe a cut-off consistent with a convection speed $\nu_{\text{num}} = 0.27$. The same shift is not visible in the apparent convection speeds obtained from the establishment profiles; in this case, $\nu_{\text{sim}} = \nu_{\text{num}}$, except for very high velocities, where $u(\xi)$ is entirely determined by the population density profile $c(\xi)$ (which deviates from the analytical prediction, see Fig. 6.S3c).

Despite these subtle deviations between our model and simulations, we expect good agreement as long as the population density is not too small; Since the establishment probability $u(x)$ is typically low where the wild-type density $c(x)$ is high and vice-versa, and the rate of adaptation R depends only on the product of $c(x)$ and $u(x)$, regions of small population density should not significantly impact the integral in most cases. Fig. 6.S4 shows that there is indeed good agreement between the rate of adaptation R, the total death rate B and the treatment efficiency Q obtained from simulations and from numerical evaluation of our model.

References

[1] D. T. Gillespie. A general method for numerically simulating the stochastic time evolution of coupled chemical reactions. *Journal of computational physics*, 22(4):403–434, 1976.

[2] D. T. Gillespie. Exact stochastic simulation of coupled chemical reactions. *The journal of physical chemistry*, 81(25):2340–2361, 1977.

[3] R. A. Fisher. The wave of advance of advantageous genes. *Annals of eugenics*, 7(4):355–369, 1937.

[4] K. A. Dahmen, D. R. Nelson, and N. M. Shnerb. Life and death near a windy oasis. *Journal of mathematical biology*, 41(1):1–23, 2000. doi: 10.1007/s002850000025.

[5] E. Brunet and B. Derrida. Shift in the velocity of a front due to a cutoff. *Physical Review E*, 56(3): 2597–2604, 1997.

7
Conclusion

This thesis has addressed the effects of ecology on evolutionary dynamics in a very simple model system: microbial colonies grown on solid agar surfaces. This model system allowed us to isolate the effects of spatial structure from other ecological interactions that would confound evolutionary dynamics in more complex system. As a reward, we were able to make quantitative sense of our measurements of typical population genetic observables.

In Chapter 2, we brought the Luria-Delbrück experiment into space by analyzing colonies grown from single cells: population sequencing and image analysis together with simple lattice simulations allowed us to show that neutral mutant clones in spatially structured populations can grow to large sizes much more often than would be expected from the classical well-mixed model. The accompanying Eden model simulations hint at an underlying universality that may make our results widely applicable to other spatially structured populations such as tumors. At a time where sequencing prices have dipped low enough for researchers to routinely perform large-scale, spatially resolved sequencing studies in solid tumors, a quantitative understanding of patterns of intra-tumor heterogeneity (ITH) has come within reach, but mathematical models often still ignore the spatial aspect of tumor growth and how it influences ITH. Our work here may serve as a starting point for explicitly spatial models of ITH; indeed, our scaling predictions for the clone size distribution of neutral mutations were recently applied to rationalize ITH in simulated tumors[1].

In Chapters 3 and 4, we investigated adaptation in microbial colonies. Using mixtures of wild type and mutants, we showed that adaptation from standing variation is much stronger in colonies than in well-mixed cultures. This is a direct result of the spatial growth of the colonies. We also showed that not all microbial

species are created equal when it comes to their evolutionary dynamics: even when population sizes and selective advantages are identical, different species can vary tremendously when it comes to their adaptive potential and the establishment probability of beneficial mutants. To explore these differences in more microscopic detail, we performed microscopic lineage tracking in growing colonies to show that the different (macroscopic) evolutionary dynamics can be understood from differences in dynamics at the microscopic scale. Varying microscopic parameters such as adhesion strength systematically, or even just measuring them accurately, is difficult, especially inside of microbial colonies. We therefore used biophysically explicit, agent-based models to show that nutrient uptake rate, cell shape, and anisotropic friction can all have a strong influence on the establishment probability of beneficial sectors. However, we found a mesoscopic parameter, the roughness of the colony front, which was predictive of the establishment probability; changing the microscopic parameters affected the establishment probability only because they altered the front roughness. This finding suggests a broader look at evolutionary dynamics in microbial colonies and biofilms: since microscopic details will in many cases be inaccessible, one should instead look for mesoscopic observables (such as front roughness) that can be predictive of certain aspects of the (macroscopic) evolutionary dynamics (see Fig. 7.1).

In Chapter 5, we studied the establishment of mutations with a fitness effect in heterogeneous environments. While we started with standing diversity to investigate the establishment process in Chapters 3 and 4, in Chapter 5, we used a model system for spontaneous mutations whose fitness effect we could easily tune experimentally. I want to highlight two findings that are especially important in the grand scope of this thesis: firstly, we had predicted in Chapter 3 that beneficial mutations would only be able to establish if they arose in the first cell layer in the growth layer. In agreement with this prediction, we found establishment probabilities on the order of 10^{-7} even for strongly beneficial mutations with $s \approx 20\%$, to be compared to an expected establishment probability of $2s \approx 40\%$ in a well-mixed population. Once a mutation established, however, its success relative to its conspecifics was astronomical: a single successful mutation could take over almost half the population over the course of only a few dozen generations. Thus, evolution in microbial colonies is an extremely noisy process, where most mutations are lost immediately, but a few lucky mutants can quickly rise to high frequency. When we grew colonies from single cells on rough surfaces, we made our second major finding: selection seemed to be almost entirely ineffectual in colonies grown on rough surfaces, where even strongly beneficial mutants established at neutral rates. Through extensive Eden simulations with environmental heterogeneity, we showed that the efficacy of selection is generically reduced by environmental disorder, which serves as an additional source of noise that selection must overcome.

An important next step is to extend the approach taken in this work to microbial biofilms with more complex colony morphologies, e.g., due to the secretion of extracellular polymeric substances, that may shape evolutionary dynamics in interesting ways. In particular, biofilms of *B. subtilis* grown on hard agar form

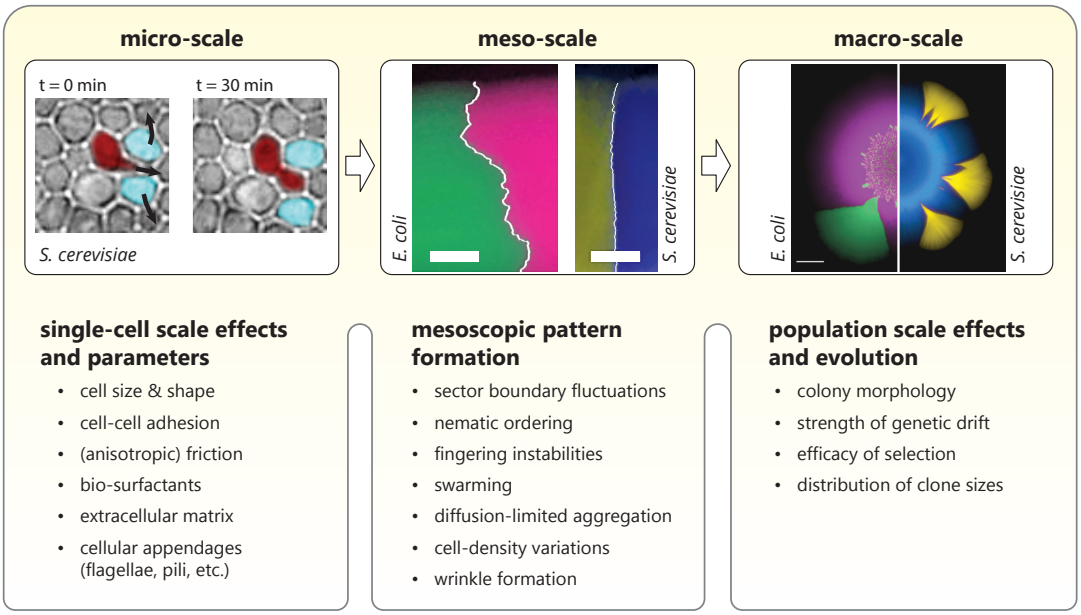

Figure 7.1: How can we understand evolutionary dynamics on the population level in complex systems such as biofilms without requiring knowledge of all microscopic details? In this thesis, we have shown that it can be possible to find mesoscopic observables that are predictive of macroscopic processes.

fascinating patterns: on high nutrient concentration media, they are encased in extracellular matrix, form wrinkles and have an overall rough exterior, while they have a feathered morphology in low nutrient conditions whose statistics are well described by diffusion-limited aggregation (DLA). This existing theoretical framework may help explain evolutionary dynamics in these biofilms in the same way that KPZ universality enabled analytical predictions in this thesis.

Finally, in Chapter 6, we investigated the effect of convection on the establishment of resistance mutations in antibiotic gradients using simulations and analytical theory. We showed that flow, which is an important ecological factor for many microbial communities such as the gut microbiome [2] or *V. cholerae* biofilms [3], can dramatically alter not only the population profiles of microbial population, but also have a strong impact on the fates of mutations arising in different places in the population. The population dynamics of microbial populations under flow conditions have recently been investigated in microfluidic devices [4], and it would be interesting to study evolutionary dynamics in similar experimental model systems.

What do the results in this thesis tell us about evolutionary dynamics in microbial biofilms and other spatially structured populations in the wild? To make progress toward answering this question, additional

complexities faced by natural biofilms can be added in one by one[5]. One example is adding time-varying growth conditions that can arise from seasons, tides or day-and-night cycles[6]. Such periodic growth conditions could be emulated in the laboratory by growing temperature-sensitive yeast strains at time-varying temperatures. In addition, while the evolution of resistance in spatial antibiotic gradients has been studied qualitatively[7], a truly quantitative understanding of the rate and mode of evolution in gradients and other forms of spatial heterogeneity is not yet achieved.

The life cycle of many microbial species includes periods of sessile growth in biofilms interspersed with migration periods. Whether microbial species evolve predominantly while they are in biofilms or swimming is currently unknown. For example, it is possible that beneficial variants can establish in the community much more easily if they arise in free-swimming microbes that subsequently settle to grow a biofilm, compared to if they arise within an existing biofilm, where they have to compete with their conspecifics. On the other hand, spatial structure can afford evolutionary avenues that are unavailable in swimming population. Answers to such questions will require a quantitative understanding of the rate and mode of evolution in both scenarios.

The matter is further complicated by the fact that the dominant form of biofilms in the wild and in the human host, e.g., dental plaque[8,9], consists in communities of many different species[10]. Interactions in multi-species biofilms can be synergistic, e.g., through the exchange of public goods, or antagonistic, through the competition for nutrients or actively through antimicrobial activity[11], and experiments have shown that ecological interactions can change rapidly in spatially structured communities[12]. While engineering microbial strains of the same species to cross-feed[13] or engage in active "chemical warfare"[14] can emulate multi-species ecological interactions for isolated study, the interactions between different species will be more multi-faceted. One reason for this is that evolution in multi-species communities need not rely on spontaneous mutations alone; bacteria can also evolve through the exchange of genetic material (horizontal gene transfer) by conjugation between bacteria or through bacteriophages. Both bacteria-bacteria and phage-bacteria interactions appear to be relatively limited in biofilms, potentially negatively impacting the efficacy of horizontal gene transfer, and thus slowing down evolution, in sessile communities[15–17]. To estimate the relative contributions to evolution in multi-species communities from swimming cells and biofilms requires the combination of quantitative insights about evolutionary dynamics and horizontal gene transfer in both growth modes.

Microbial biofilms are ubiquitous and crucial components of virtually all environments[18]. Studying their ecology and evolution is not only important for medical applications, such as combating drug resistance in *P. aeruginosa* biofilms in the lungs of cystic fibrosis patients[19] or preventing the contamination of implant infections[20]. Microbial biofilms also perform a number of ecological functions in the environment, and understanding their assembly and response to environmental change can help us predict the resilience of

macroscopic ecosystems[21,22]. In addition, multi-species biofilms are often the result of ecological succession, wherein primary consumers attach first and are later overgrown by secondary members of the biofilm[23,24]. Ecological successions also characterize the assembly of macroscopic eco-systems; for instance, grasses usually regrow before trees after a forest fire[25]. Unraveling general principles about the evolutionary dynamics in biofilms is thus a formidable task with far-reaching applications.

References

[1] Z. Ahmed and S. Gravel. Intratumor Heterogeneity and Circulating Tumor Cell Clusters. *bioRxiv*, 2018. doi: 10.1101/113480.

[2] J. Cremer, M. Arnoldini, and T. Hwa. Effect of water flow and chemical environment on microbiota growth and composition in the human colon. *Proceedings of the National Academy of Sciences*, 114 (25):6438–6443, 2017.

[3] K. Drescher, C. D. Nadell, H. A. Stone, N. S. Wingreen, and B. L. Bassler. Solutions to the Public Goods Dilemma in Bacterial Biofilms. *Current biology*, 24:1–6, dec 2014. doi: 10.1016/j.cub.2013.10.030.

[4] F. Tesser, J. C. Zeegers, H. J. Clercx, L. Brunsveld, and F. Toschi. Finite-size effects on bacterial population expansion under controlled flow conditions. *Scientific Reports*, 7:43903, 2017.

[5] S. Widder, R. J. Allen, T. Pfeiffer, T. P. Curtis, C. Wiuf, W. T. Sloan, O. X. Cordero, S. P. Brown, B. Momeni, W. Shou, et al. Challenges in microbial ecology: building predictive understanding of community function and dynamics. *The ISME journal*, 10(11):2557, 2016.

[6] I. Cvijović, B. H. Good, E. R. Jerison, and M. M. Desai. Fate of a mutation in a fluctuating environment. *Proceedings of the National Academy of Sciences*, 112(36):E5021–E5028, 2015.

[7] M. Baym, T. D. Lieberman, E. D. Kelsic, R. Chait, R. Gross, I. Yelin, and R. Kishony. Spatiotemporal microbial evolution on antibiotic landscapes. *Science*, 353(6304):1147 LP – 1151, 2016. doi: 10.1126/science.aag0822.

[8] P. E. Kolenbrander, R. J. Palmer Jr, S. Periasamy, and N. S. Jakubovics. Oral multispecies biofilm development and the key role of cell–cell distance. *Nature Reviews Microbiology*, 8(7):471, 2010.

[9] J. L. M. Welch, B. J. Rossetti, C. W. Rieken, F. E. Dewhirst, and G. G. Borisy. Biogeography of a human oral microbiome at the micron scale. *Proceedings of the National Academy of Sciences*, 113(6): E791–E800, 2016.

[10] S. Elias and E. Banin. Multi-species biofilms: living with friendly neighbors. *FEMS microbiology reviews*, 36(5):990–1004, 2012.

[11] C. D. Nadell, J. B. Xavier, and K. R. Foster. The sociobiology of biofilms. *FEMS Microbiology Reviews*, 33(1):206–224, 2009. doi: 10.1111/j.1574-6976.2008.00150.x.

[12] S. K. Hansen, P. B. Rainey, J. A. Haagensen, and S. Molin. Evolution of species interactions in a biofilm community. *Nature*, 445(7127):533, 2007.

[13] M. J. I. Mueller, B. I. Neugeboren, D. R. Nelson, and A. W. Murray. Genetic drift opposes mutualism during spatial population expansion. *Proceedings of the National Academy of Sciences*, 2013.

[14] M. F. Weber, G. Poxleitner, E. Hebisch, E. Frey, M. Opitz, and J. R. S. Interface. Chemical warfare and survival strategies in bacterial range expansions Chemical warfare and survival strategies in bacterial range expansions. *J. R. Soc. Interface*, 11:20140127, 2014.

[15] P. D. Freese, K. S. Korolev, J. I. Jiménez, and I. A. Chen. Genetic drift suppresses bacterial conjugation in spatially structured populations. *Biophysical journal*, 106(4):944–954, 2014.

[16] M. Simmons, K. Drescher, C. D. Nadell, and V. Bucci. Phage mobility is a core determinant of phage–bacteria coexistence in biofilms. *The ISME journal*, 2017.

[17] L. Vidakovic, P. K. Singh, R. Hartmann, C. D. Nadell, and K. Drescher. Dynamic biofilm architecture confers individual and collective mechanisms of viral protection. *Nature microbiology*, 3(1):26, 2018.

[18] W. B. Whitman, D. C. Coleman, and W. J. Wiebe. Prokaryotes: the unseen majority. *Proceedings of the National Academy of Sciences*, 95(12):6578–6583, 1998.

[19] T.-F. C. Mah and G. A. O'toole. Mechanisms of biofilm resistance to antimicrobial agents. *Trends in microbiology*, 9(1):34–39, 2001.

[20] M. E. Davey and G. A. O'toole. Microbial Biofilms: from Ecology to Molecular Genetics. *Microbiology and Molecular Biology Reviews*, 64(4):847–867, 2000. doi: 10.1128/MMBR.64.4.847-867.2000.

[21] F. S. Chapin, B. H. Walker, R. J. Hobbs, D. U. Hooper, J. H. Lawton, O. E. Sala, and D. Tilman. Biotic control over the functioning of ecosystems. *Science*, 277(5325):500–504, 1997.

[22] M. G. Van Der Heijden, R. D. Bardgett, and N. M. Van Straalen. The unseen majority: soil microbes as drivers of plant diversity and productivity in terrestrial ecosystems. *Ecology letters*, 11(3):296–310, 2008.

[23] N. Fierer, D. Nemergut, R. Knight, and J. M. Craine. Changes through time: integrating microorganisms into the study of succession. *Research in microbiology*, 161(8):635–642, 2010.

[24] M. S. Datta, E. Sliwerska, J. Gore, M. F. Polz, and O. X. Cordero. Microbial interactions lead to rapid micro-scale successions on model marine particles. *Nature communications*, 7:11965, 2016.

[25] J. H. Connell and R. O. Slatyer. Mechanisms of succession in natural communities and their role in community stability and organization. *The American Naturalist*, 111(982):1119–1144, 1977.

Appendix A
Growth and mechanics in yeast colonies

A.1 Introduction

In this Appendix, we characterize the growth of colonies of budding yeast (*S. cerevisiae*) at different glucose and agar concentration with two main goals: first, to compare our experimental results with the FKPP equation, see eq. (1.22) in the Introduction, i.e., we want to test whether the expansion speed v is proportional to the square root of the individual growth rate k,

$$v \sim \sqrt{k}. \tag{A.1}$$

Secondly, we want to estimate how nutrient gradients, from the front of the colony into the bulk, and mechanical pushing shape where cells grow in the colony.

A.2 Individual growth rates in liquid culture

We first measure individual growth rates of *S. cerevisiae* during exponential growth in YPD (20g/l peptone, 10g/l yeast extract) media with variable amounts of glucose (c_G =0.5, 2, 4, 7, 10, 20, 35, 50g/l). A clonal culture of the *S. cerevisiae* W303 lab strain yJHK111 was grown in YPD overnight, diluted 1:10 into fresh media and grown for another 2 hours. 50μl of this culture were inoculated into 5ml of YPD with different glucose concentrations in duplicate and grown shaken at 30°C. The optical density (OD) was measured every hour for 8 hours to determine cell density. The resulting growth curves are shown in Fig. A.1a. Fitting the growth curves with an exponential growth model $\mathrm{OD}(t) = \mathrm{OD}(0)2^{t/\tau}$ with a common initial density $\mathrm{OD}(0)$ for all culture, we obtain the per capita growth rates shown in Fig. A.1b. Exponential phase growth rates k are fitted by the Monod equation

$$k = k_{\max}\frac{c_G}{K + c_G}, \tag{A.2}$$

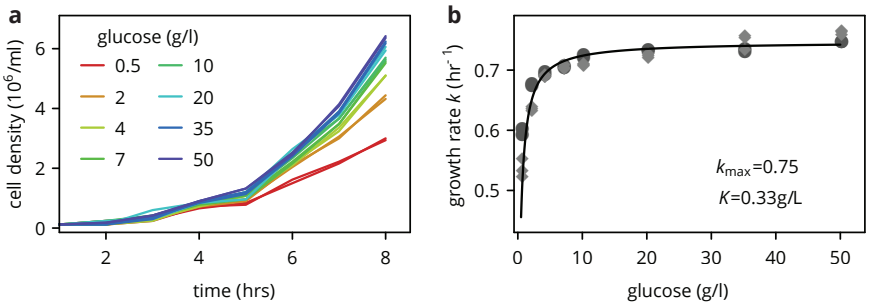

Figure A.1: Measuring growth rate in liquid culture. (a) Time traces of cell density, measured by optical density. (b) Growth rates at different glucose concentrations obtained by exponential fits to the curves in (a), fitted with the eq. (A.2) (black line). Circles and diamonds are from biological replicates.

a common model for microbial growth rates as a function of the concentration c_G of the substrate (here, glucose)[1]. K is a fit parameter corresponding to the glucose concentration where the cells reach half their maximal growth rate. We achieve a good fit with $k_{\max} = 0.74\text{hr}^{-1}$ and $K \approx 0.3\text{g/l}$.

A.3 Colony growth rates

To measure colony growth rates, we prepared a single batch of YP medium (YPD without glucose) with different agar concentration (c_A =1, 2, 4, 6, 8%), adding glucose after autoclaving to avoid any differences in nutrient concentrations except for different glucose concentration. For each set of parameters (c_G, c_A), we filled one 6 well plate with 5ml per well and inoculated 2μl of overnight culture into the middle of each well. Colonies were grown at 30°C for 5 days, with images taken every 24h with a Zeiss AxioZoom v16 microscope. Images were binarized and colony radii extracted using custom scripts in Mathematica.

For all agar concentrations, colony radii grew roughly linearly over time, such that we used linear fits over the first 4 days to extract radial growth rates. The results are shown in Fig. A.2a and b. As a function of glucose concentration c_G, the radial growth rate, or front speed v, exhibits roughly power-law scaling (a non-linear fit gives a best fit with $v \sim c_G^{1/4}$). Using the per capita growth rate k at a given glucose concentration, we also plot the front speed as a function of k, resulting in highly nonlinear curves that increase weakly with growth rate for small growth rates and sharply over a small range of growth rates near the maximal growth rate. Thus, our results show unequivocally that yeast colonies, at least for the strain and the procedure used here, are not Fisher waves in the sense of eq. (A.1).

The front speed also decreased with agar concentration (see legend in Fig. A.2b). Colonies grown on high agar concentration were thus smaller, but also noticeably taller (Fig. A.2c). Since a higher agar concentration increases the stiffness of the medium and potentially alters other physical properties, this suggest a significant

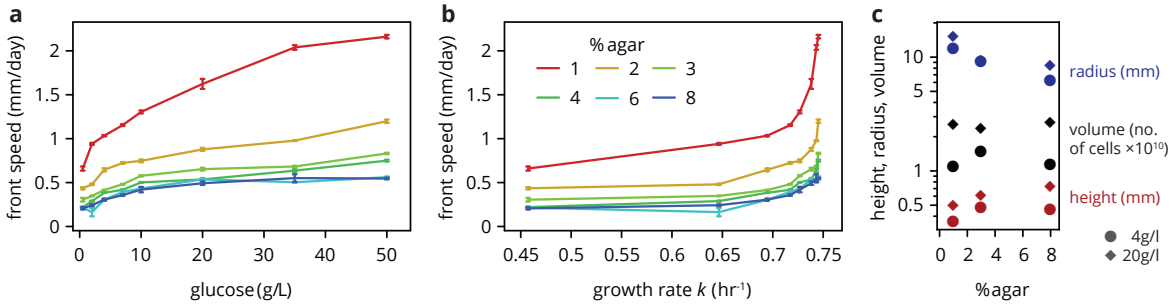

Figure A.2: (a, b) Radial growth rates, measured from daily images of colonies growing on plates containing varying concentrations of glucose and agar (see panel b for legend). For panel b, the growth rates in measured in liquid culture were used as an estimate for growth rates at the colony front. (c) Colonies grown on higher agar concentration are taller and less wide, but contain overall about the same amount of cells regardless of agar concentration.

role of mechanical effects in shaping colony growth.

A.4 Growth layer thickness

Beyond testing the Fisher wave model, we can characterize where cells grow in the colonies, as follows. Since the colony expansion is entirely caused by cell growth and division (as the cells are non-motile), we can express the front speed as the cumulative pushing of all cells behind the front. Nutrients diffuse into the agar occupied by the colony over time, giving rise to a nutrient concentration gradient that is maximal outside the colony and decreases inside the colony. Since we do not have direct access to the nutrient concentration profile in our experiments, we introduce a location-dependent growth rate $k(x)$, in cell diameters per unit time, depending on the distance from the colony front x, such that $x = 0$ corresponds to the front itself. We can model the front speed v of a colony of radius R as

$$v = \int_{-R}^{0} k(x)dx. \tag{A.3}$$

For our experiments, since the radial growth speed was constant in time, $k(x)$ must go to zero at some distance from the front that is roughly constant in time; otherwise, the colony would grow faster than linear in radius. We call the region where $k(x) > 0$ the growth layer. In the simplest case, cells inside the growth layer, i.e., $|x| < \lambda_G$, where we call λ_G the growth layer width, grow at the maximal rate $k(0)$, whereas those outside the growth layer, i.e., $|x| > \lambda_G$, do not grow at all because they do not have access to sufficient nutrients. This simplified picture is inspired by the finding above (Fig. A.1b) that cells grow at roughly their

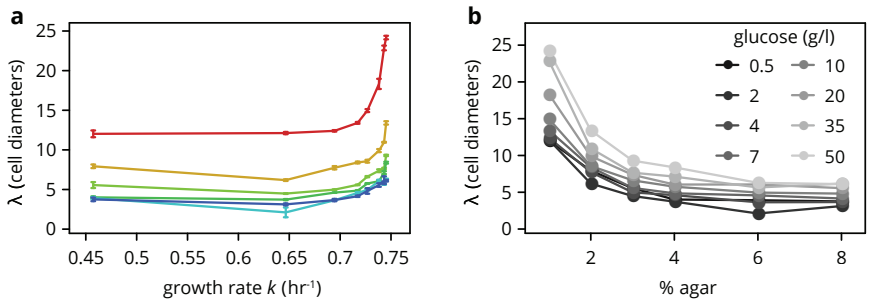

Figure A.3: The growth layer width λ, defined through $\lambda = vk$, as a function of per capita growth rate k (a) and agar concentration (b).

maximum growth rate until the nutrient concentration becomes very low, where the growth rate dips sharply. In this approximation, we may therefore measure the growth layer width in units of cell diameters, λ_G/a, directly as

$$\lambda_G/a = v/k(0) \tag{A.4}$$

We can generalize this picture by considering other shapes for $k(x)$ and express the front speed in terms of the growth rate $\langle k(x)\rangle_{\lambda_G}$ averaged over the growth layer as

$$v = a \int_{-\lambda_G}^{0} k(x)dx = a\lambda_G \langle k(x)\rangle_{\lambda_G} \tag{A.5}$$

As shown in Fig. A.3a, the growth layer width λ_G is roughly constant for low growth rates before it sharply ramps up near $k_{\max}$. A higher agar percentage in the media gives rise to a shorter growth layer (Fig. A.3b), for all glucose concentrations. This shows that the growth layer width does not solely depend on nutrient concentration as one would perhaps naively expect; instead, it is also modulated by the mechanical differences induced by different agar concentrations c_A.

A.5 Single-cell microscopy & PIV

We now examine the assumption that the growth layer can be approximated as a box of length λ_G within which all cells grow at the maximal growth rate. We can use eq. (A.5) to describe not only the local velocity at the front (the radial growth rate), but also the local speed $v(x)$ at a distance x behind the front by writing

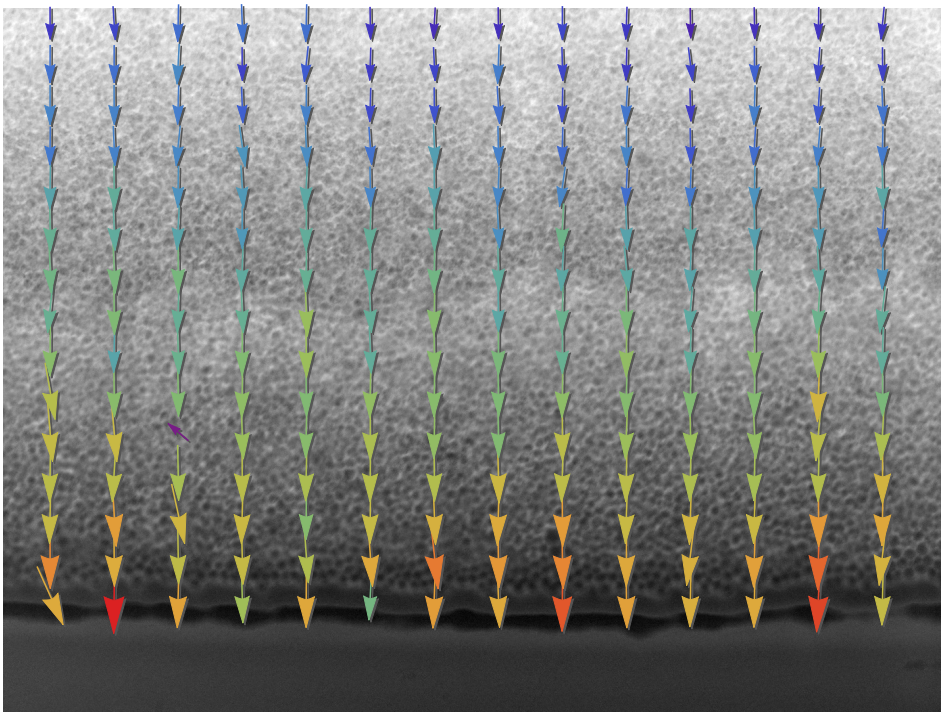

Figure A.4: Example for the result of particle image velocimetry (PIV) analysis of single-cell timelapse movies in yeast. Color and thickness of the arrows indicate the magnitude of the displacement between images (images taken every 2 minutes). Cells are about 5μm in diameter.

$$v(x) = a \int_{-\lambda_G}^{x} k(x)dx. \tag{A.6}$$

Thus, by measuring $dv(x)/dx$, we can have direct access to the growth rate at different positions in the population.

To do this experimentally, we took time lapse microscopy movies of growing yeast fronts at the single cell scale, grown for several hours on 1% agar at three glucose concentrations. The resulting movies were then analyzed with the particle image velocimetry (PIV) pipeline in ImageJ to extract local displacements between images[2], allowing us to measure $v(x)$ directly in growing yeast colonies. This analysis corresponds to an automated version of the manual cell tracking performed for Fig. 3.B9. An example of the PIV analysis for one growth condition is shown in Fig. A.4. For all glucose concentrations, the local speed is maximal at the front and decreases with distance x from the front (Fig. A.5, dots). Notably, the local speed decreases linearly with x; for the lowest glucose concentration, there is no change in the speed gradient until it vanishes

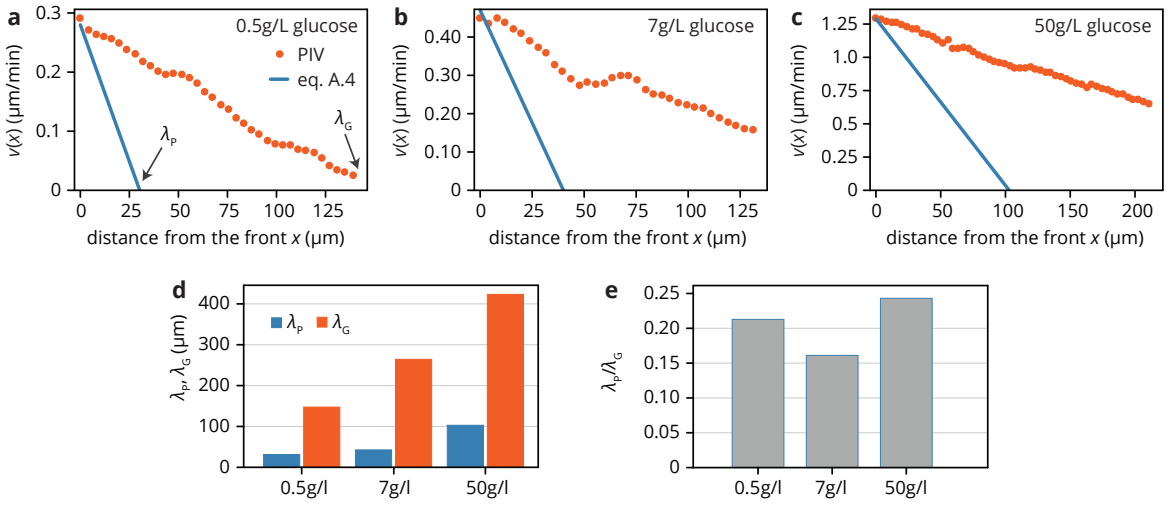

Figure A.5: Measuring the local speed in the colony growth layer via particle image velocimetry (PIV) unveils a disconnect between theory (lines) and experiment (dots), as cells grow and move much deeper into the population than expected naively from the front speed and per capita growth rate (a-c). The two length scales λ_G (Growth) and λ_P (Pushing) in (d) have a ratio that is consistent for different glucose concentrations, suggesting a mechanical relation between of the two length scales.

about 150μm behind the front. For higher glucose concentration, the local speed decreases linearly over the whole observable range, as well. From eq. (A.6), this implies that $k(x) \approx$ const. is a good assumption.

A.6 Interpretation and model

In Fig. A.5, we plotted as solid lines eq. (A.6) parametrized by the front speed $v(0)$ and the per capita growth rate at the front. There is clear disagreement between this theoretical prediction and the measured local speed. We found two different length scales: the width λ_G of the layer where cells grow, and the apparent growth layer width $\lambda_P = v(0)/k(0)$ expected if all cells within a distance λ_P contributed to pushing the colony expansion. Since the local speed decreases linearly with x and thus $k(x) \approx$ const., eq. (A.6) predicts that there should only be one length scale, but instead we find that the two length scales differ roughly by a factor of five in our colonies, consistent across glucose concentrations (Fig. A.5d). Since the front speed is the result of cells pushing from behind through growth and division, and we have directly observed where growth occurs, this must be because not all growing cells contribute to pushing the front forward. Indeed, some cells must contribute to growth in the third dimension, as mature colonies are several hundred microns tall (Fig. A.2c). The pushing fraction p of cells that contribute to the colony expansion is equal to the ratio λ_P/λ_G, around 15-20% in our experiments (Fig. A.5e). Hence, about 80% of all cell

division in the bottom layer of cells contribute to growth in height. That colonies are nevertheless wider than they are tall is presumably due to nutrient depletion in upper cell layers.

Our results suggest that out-of-plane growth is more prominent in colonies grown on high agar concentrations, leading to lower front speeds and taller colonies. Two factors may contribute to out-of-plane growth: first, the growth of new cells could be directed in such a way that some cells form buds that are directed out-of-plane and thus do not generate much in-plane stress. Secondly, friction with the agar surface combined with growth creates an in-plane stress profile inside the colony, with no stress directly at the front and increasing stress into the colony. This stress can be relieved by local "buckling", where individual cells are pushed out of the bottom layer if the stress surpasses a threshold stress[3].

These two factors make different qualitative predictions: if the direction of budding is random then out-of-plane growth should be equally prominent at all positions in the colony. Buckling, on the other hand, is more likely at higher stresses and since the stress profile inside the colony is increasing, this would imply that buckling is more prominent further away from the front. This would cause the local speed to depend nonlinearly on the distance from the front, which is at odds with our direct experimental observation. Thus, unless the buckling threshold is so low in yeast colonies that cells can be pushed out-of-plane by the small stresses created by the first few cell layers, we can rule out buckling as the major contributing factor to out-of-plane growth. Instead, cell growth to a large degree seems to be directed out-of-plane, or redirected through rotations of the cells, depending on the friction (viscous and potentially through active adhesion mechanisms) between cells and their neighbors, and between the cells and the agar surface[4,5]. The agar concentration could plausibly affect not only cell-agar friction, but also cell-cell adhesion: colonies on high agar concentration are noticeably "drier" and less macroscopically viscous when picked up with a pipet tip, presumably because the high osmotic pressure reduces the water content of the colony.

Colony growth depends on both the growth of cells and the generation and transmission of mechanical stresses. It seems plausible that the agar concentration c_A mostly impacts the mechanical component of colony growth, whereas the nutrient concentration c_G controls the growth of individual cells. This assumption would suggest that the local speed $v(x)$ factorizes into nutrient and mechanical contributions. Using the length scale λ_G and the pushing fraction p, we can then write the local speed $v(x)$ as

$$v(x) = \lambda_G k \left(1 - \frac{x}{\lambda_G}\right) \times p \approx v_G(c_G) \times p(c_A) \tag{A.7}$$

Eq. (A.7) implies if we normalize the front speed $v(0)$ as a function of agar concentration by the front speed at a reference glucose concentration (say, c_G =0.5g/l), the result should be roughly independent of agar concentration, since p cancels out. Likewise, dividing the front speed as a function of glucose concentration by the front speed at a reference agar concentration (say, c_A =1%), the result should be roughly independent of

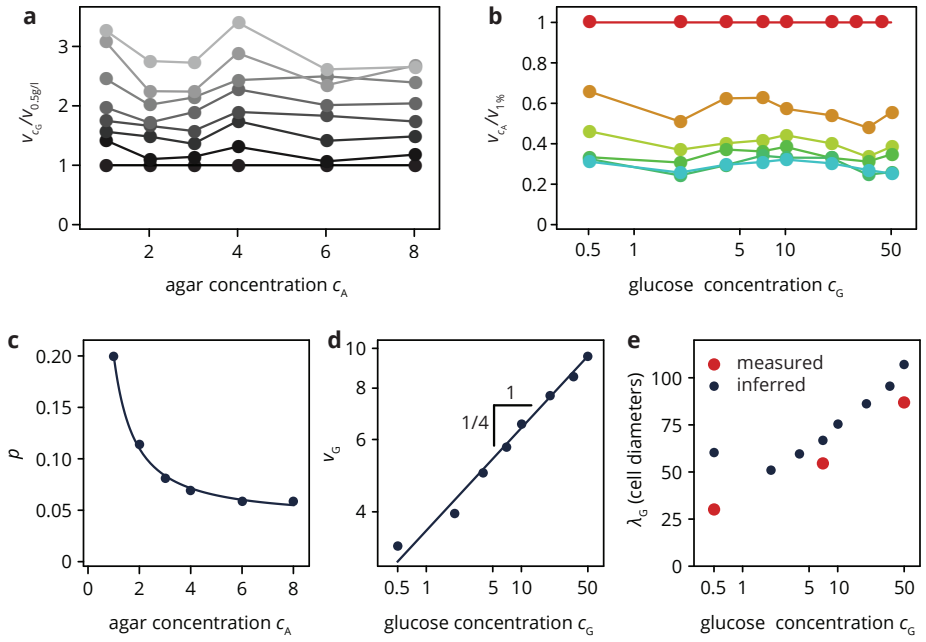

Figure A.6: (a/b) Normalizing the front speed as a function of the agar/glucose concentration by the front speed at the reference glucose/agar concentration (0.5g/l/1%), we obtain curves that are independent of the agar/glucose concentration, indicating that the front speed can be factorized into an agar and a glucose concentration-dependent part. (c, d) From (a) and (b), we can infer the pushing fraction p and v_G. (e) The resulting estimate for the layer width λ_G of growing cells agrees well with the direct observation via PIV.

glucose concentration, since v_G cancels out. This is indeed what we find in Fig. A.6a&b. Up to a numerical prefactor, the height of the lines corresponds to p and v_G, respectively, and we can estimate the prefactors for the case (1% agar, 0.5g/l glucose) from the microscopic observation in Fig. A.5. The results are shown in Fig. A.6c&d. The pushing fraction p decreases roughly as $c_A^{-5/4}$, while v_G increases with the glucose concentration as $c_G^{1/4}$. Using the per capita growth rates, we can also estimate the width of the layer of cell growth λ_G and compare to the value found directly via PIV in Fig. A.5. We find that our estimates overestimate the measured values for λ_G slightly compared with the direct observation (Fig. A.6e). The qualitative trend, however, is clear: a higher nutrient concentration is able to penetrate deeper into the colony, allowing for growth further from the front.

A.7 Discussion

In this Appendix, we have shown that the growth layer width depends both on glucose and agar concentration, i.e., it is set by a combination of resource gradients, which determine where cells grow, and mechanical cell-cell and cell-substrate interactions, which determine where the forces created by growth and division are directed. Our results suggest that these two effects are roughly independent: increasing the nutrient concentration allows for growth deeper into the populations, whereas increasing the agar concentration increases the propensity of growth forces being directed out of the plane of growth, thus contributing to taller colonies, at the expense of radial growth speed. The detailed reasons for this are so far unknown, as no direct measurements of the friction forces in yeast colonies on different substrates are available. Our results thus provide interesting future directions for further experimental work to measure the mechanical forces inside microbial colonies, but also for mathematical modeling of the nutrient concentration gradients in microbial colonies, which have so far only been studied for spherical aggregates[6], but not for two-dimensional populations on solid substrates.

References

[1] J. Monod. The growth of bacterial cultures. *Annual Reviews in Microbiology*, 3(1):371–394, 1949.

[2] J. Schindelin, I. Arganda-Carreras, E. Frise, V. Kaynig, M. Longair, T. Pietzsch, S. Preibisch, C. Rueden, S. Saalfeld, B. Schmid, et al. Fiji: an open-source platform for biological-image analysis. *Nature methods*, 9(7):676, 2012.

[3] M. A. Grant, B. Wacław, R. J. Allen, and P. Cicuta. The role of mechanical forces in the planar-to-bulk transition in growing escherichia coli microcolonies. *Journal of The Royal Society Interface*, 11 (97):20140400, 2014.

[4] T. B. Reynolds and G. R. Fink. Bakers' yeast, a model for fungal biofilm formation. *Science*, 291 (5505):878–881, 2001.

[5] K. J. Verstrepen and F. M. Klis. Flocculation, adhesion and biofilm formation in yeasts. *Molecular microbiology*, 60(1):5–15, 2006.

[6] M. O. Lavrentovich, J. H. Koschwanez, and D. R. Nelson. Nutrient shielding in clusters of cells. *Physical Review E*, 87(6):062703, jun 2013. doi: 10.1103/PhysRevE.87.062703.

Appendix B
Eden model with tunable line tension

B.1 Introduction

Experiments in yeast colonies suggest that the edge of some microbial colonies is characterized by a strong line tension that acts to keep the front straight and flatten out any curvature[1,2]. Since the boundaries between two clonal sectors in microbial colonies move normal to the front, how the front regulates its roughness and local curvature can have an impact in evolutionary dynamics in colonies. In the KPZ equation describing the height $h(x,t)$ of a rough interface, the effect of a line tension described by a term involving the local curvature $\kappa = \partial_x^2 h$ of the front, with a line tension parameter ν

$$\partial_t h = v + \frac{\lambda}{2}(\partial_x h)^2 + \nu \partial_x^2 h + \sqrt{D}\eta. \tag{B.1}$$

Through this work, we have simulated microbial colonies using the Eden model and have achieved good agreement between the model and experimental results. However, the Eden model has no parameter that would allow us to tune the strength of the line tension. In this Appendix, we present one possible way of incorporating a tunable line tension in the Eden model.

B.2 Simulation algorithm

To increase the relative importance of line tension in the Eden model, we need to modify the growth rate k of each filled site at the front by a factor $f(\kappa)$ that is proportional to the local curvature κ of the front. For simplicity, we choose $f(\kappa) = \nu\kappa$ where we call ν the line tension. The task is then to measure the local curvature in simulations. To do this, we count the number of filled lattice sites N in a neighborhood of radius R^* and compare it with the number of lattice sites N^* that would be filled if the interface was flat. To see that this algorithm measures local curvature, consider Fig. B.1. At the center point (black dot), we can fit a circle with radius r corresponding to the local radius of curvature. In a neighborhood around the

*For the simulations below, we use $R = 10$ as a good compromise between simulation speed and lattice artifacts.

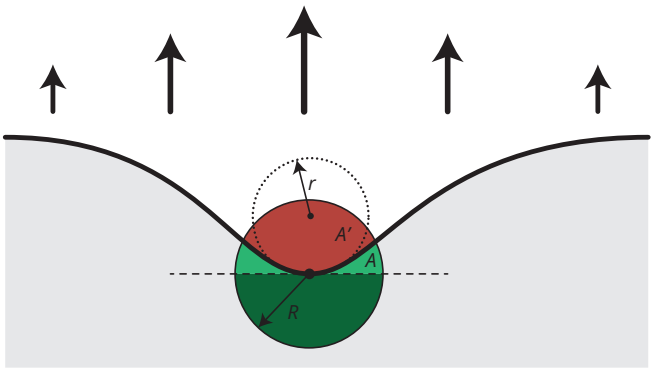

Figure B.1: Sketch of the simulation algorithm for finding local curvature. The number of filled sites in a circle of radius R is measured and compared to the expected number if the front was flat (dark green).

point of radius R (the "search radius"), the number N^* of filled sites in the flat case is simply $\pi R^2/2$. To compute the number of filled sites when the front is curved, we have to compute the area A. A simple but lengthy calculation gives $A = \pi R^2 - A' \approx \frac{R^3}{3r}$ in the limit of small curvature κ (large r), such that the ratio between filled sites in the curved and flat case becomes

$$\frac{N}{N^*} - 1 \propto \kappa. \tag{B.2}$$

Hence, to introduce a tunable line tension as in the KPZ equation, we must modify the local growth rate k according to

$$k_{\text{eff}} = k\,(1 + \nu\kappa) = k\left[1 + a\nu_{\text{sim}}\left(\frac{N}{N^*} - 1\right)\right], \tag{B.3}$$

where we have introduced the simulation parameter ν_{sim} and the fit parameter a to connect ν_{sim} to the measured line tension ν. In the following, we first examine the scaling of the resulting interfaces and determine the fit parameter a by comparing the interfaces to an analytically predicted front shape. Afterwards, we present three types of simulation familiar from previous chapter that allow for a direct examination of the effects of line tension on evolutionary dynamics.

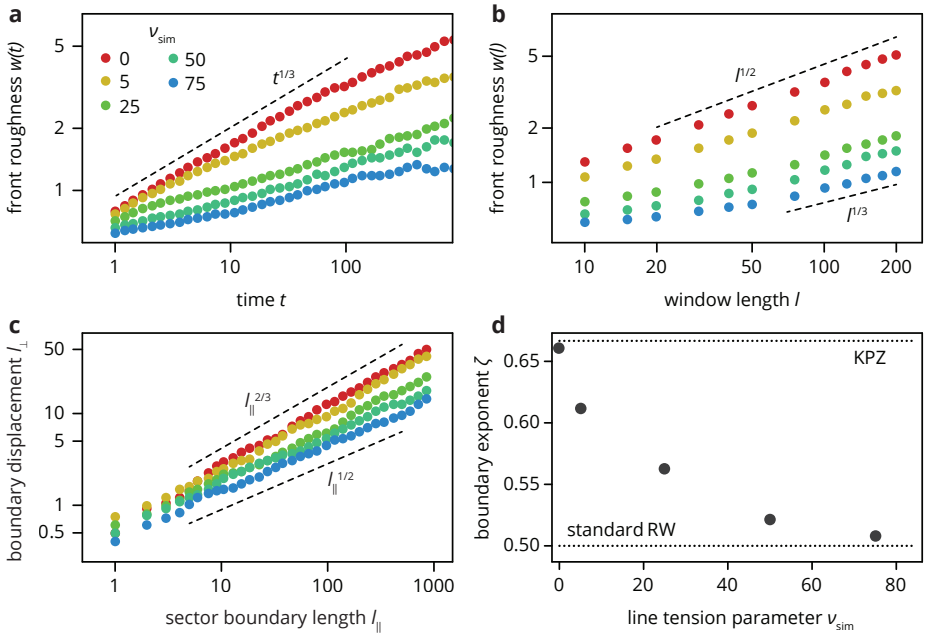

Figure B.2: Characterizing the interfaces created by the Eden model with tunable line tension. (a, b) As the line tension parameter ν_{sim} is increased, the population front becomes smoother, and deviates from the KPZ statistics observed without line tension, as explained in the main text. (c) The boundary between two sectors transitions from a KPZ-like superdiffusive random walk ($l_\perp \sim l_\parallel^\zeta$, $\zeta = 2/3$) in the standard Eden model without line tension to a standard (Brownian) random walk ($l_\perp \sim l_\parallel^{1/2}$) for strong line tension. The exponent takes values $1/2 < \zeta < 2/3$ for intermediate values of ν_{sim}.

B.3 Scaling of Eden interfaces with strong line tension

To determine the scaling properties of interfaces created by the Eden model with line tension, we grow Eden clusters starting from a line in a box of width $L = 250$ for different values of ν_{sim} and characterize the front roughness over time. As shown in Fig. B.2a, we recover the familiar KPZ scaling $t^{1/3}$ without additional line tension ($\nu_{\text{sim}} = 0$), while increasing line tension decreases the temporal exponent β. The scaling of the front roughness for different window lengths l also depends on the line tension (Fig. B.2b), decreasing from the KPZ value of $\alpha = 1/2$ to $\alpha \approx 0.3$ ($l^{1/3}$ is shown as a guide to the eye). Importantly, the overall roughness of the front decreased with increasing line tension.

Since the roughness of the boundary between neutral sectors depends on the roughness of the colony front (see, e.g., Chapter 3), we also simulated the wandering of sector boundaries for different line tensions and characterized the scaling of their lateral displacement $l_\perp$ as a function of the sector length $l_\parallel$ with the

exponent ζ ($\zeta = 2/3$ for the standard Eden model). The results are shown in Fig. B.2c&d: without addition line tension, we again recover the KPZ value $\zeta = 2/3$. For strong line tension, we obtain $\zeta = 1/2$, i.e., the sector boundaries become standard random walks. This is the expected result for colonies with a flat front. For intermediate values of ν_{sim}, the exponent ζ lies between the two theoretical values (Fig. B.2d).

In summary, we have demonstrated that Eden interfaces grown with additional line tension are smoother than in the standard Eden model without additional line tension. This impacts the strength and scaling of sector boundary fluctuations and can thus alter evolutionary dynamics through, e.g., the establishment probability of beneficial mutations, which depends explicitly on the scaling properties of the sector boundaries.

B.4 Tuning the model

To tune our model and compare our simulations with the deterministic KPZ equation in an analytically tractable geometry, we simulated one edge of a beneficial sector expanding into the slower growing wild type (see Fig. B.3a). Because of its selective advantage s, an established sectors is expected to grow at an angle $\approx \sqrt{2s}$ relative to the growth direction, while the wild type is flat on average. In the transition region, a crossover region arose, whose width depended on both s and the line tension ν. Without line tension, the transition would consist in a sharp kink. While increasing line tension should change the shape of the front in the transition region, we expected the front shape to be independent of ν far from the transition region.

To maintain the wedge shape, we need appropriate boundary conditions, i.e., we must fix the derivative of the front to keep the wedge at a constant angle at the left boundary of the simulation box. To do this, we increased the fitness of lattice sites at the boundary by a factor of $1 + \sqrt{(2+s)s}$ (see Ref. 3). This simulates the extra offspring that cells in the wedge would contribute if the system were larger. Since the interface must be flat (although tilted) at the boundary for a simulation box much bigger than the width of the crossover region, we enforce flatness at the boundary.

Solving the KPZ equation

We set up the deterministic KPZ equation with two types by writing

$$\partial_t h = [1 + s\Theta(x - l(t))] + \frac{1}{2}(\partial_x h)^2 + \nu \partial_x^2 h, \tag{B.4}$$

where $l(t)$ is the position of the moving sector boundary. Since the KPZ equation is rotationally invariant, we can rotate into a co-moving reference frame where $l(t) = 0$. In this reference frame, we can compute

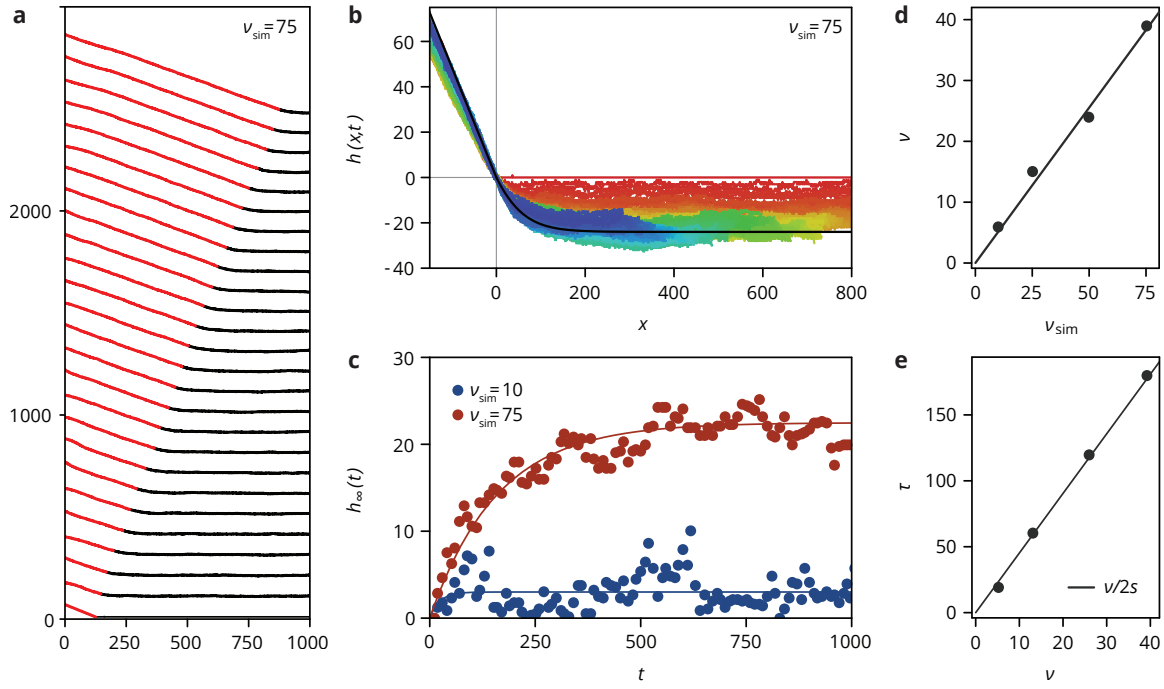

Figure B.3: (a) A mutant sector (red) invading the slow-growing wild-type population (black). Shown are traces of the front every 100 generations, simulated at $\nu_{\text{sim}} = 75$. (b) Shifting the front traces such that the mutant-wild type boundary is at (0,0), a crossover emerges over time. Using the parameter ν extracted from the front height $h(x \gg 0, t)$ far from the crossover via eq.s (B.7) and (B.8) in panel e gives an excellent fit of eq. (B.6) (black line) to the shifted front traces (b). Repeating the procedure for different ν_{sim}, we find the measured line tension ν as a function of the simulation parameter ν_{sim} (panel d), which shows the expected linear relationship. (e) The measured characteristic times τ plotted against the measured values of ν also shows a linear relationship, with a slope in excellent agreement with the theoretical prediction $\tau \sim \nu/2s$.

shape of the mutant sector as

$$\tilde{h}(\tilde{x}) = 2\nu \log\left[\cosh\left(\frac{\tilde{x}}{\sqrt{2\nu^2/s}}\right)\right], \tag{B.5}$$

which gives the crossover length scale $x_c = \sqrt{2\nu^2/s}$ between the mutants and wild type. Using this length scale and dimensional analysis of the KPZ equation, we can also estimate the characteristic time scale $\tau \sim x_c^2/\nu \sim \nu/2s$ over which the interface is deformed starting from a sharp wedge.

In the rotated frame, the interface between wild type and mutants is vertical at $\tilde{x} = 0$. In our simulation, however, the interface moves while the mutants are flat (at $x \to \infty$). Rotating by an angle $\theta_c = 2\pi -$

$\arccos(-\sqrt{2s})$ such that the mutant front line is flat at $x \to \infty$, but keeping the mutant-wild type interface at $(0, 0)$, we get the shifted mutant front line for from the origin as

$$h(x) = -\sqrt{2s}(1-s)x + \nu(1-s)\log\cosh\left[\frac{\sqrt{2s}}{\nu}x\right], \tag{B.6}$$

which can be used to fit the shape of the front to extract the line tension ν. For large x, we have $\log(\cosh[x]) \sim -\log 2 + x$, such that $h(x)$ saturates at the value

$$h_\infty = -\nu(1-s)\log 2. \tag{B.7}$$

Simulation results

We set the wild type (black in Fig. B.3a) to have a growth rate of 1 and the mutants (red) to have a growth rate advantage of $s = 0.1$ and simulated the population expansion for different values of ν_{sim}. To compare the resulting shapes with the theory, eq. (B.6), we shifted the fronts of different time points such that the boundary between wild type and mutants was at the origin (Fig. B.3b). While the wedge shape of the mutants stayed constant over time, the wild type fell behind the original front. For long times, the wild-type front approached a constant "lag" h_∞ far from the transition. The time traces of the wild-type lag are shown in Fig. B.3c for two values of ν, showing that a larger line tension parameter in the simulations created a stronger lag of the wild type. We parametrized the time traces of the lag by

$$h_\infty(t) = h_\infty\left(1 - e^{-t/\tau}\right), \tag{B.8}$$

where τ is the characteristic time scale over which the deformation establishes, introduced above. From h_∞, we computed ν via eq. (B.7) and found the expected proportionality between the simulation parameter ν_{sim} and the line tension ν extracted from the crossover shape in Fig. B.3d with the fit parameter $a \approx 0.5$. Plotting the characteristic time scale τ as a function of the measured line tension parameter ν, we found excellent agreement with the theoretical prediction $\tau = \nu/2s$ (Fig. B.3e).

B.5 Effects of line tension on evolutionary dynamics

Having established that line tension of varying strength can be efficiently implemented in a generalized Eden model, we can now examine how evolutionary dynamics is impacted by strong line tension. As alluded to in the introduction, we expect line tension to prevent strong curvature of the front, but as shown in Chapter 3, beneficial sectors bulge out of the wild-type population, and likewise, deleterious mutations are purged

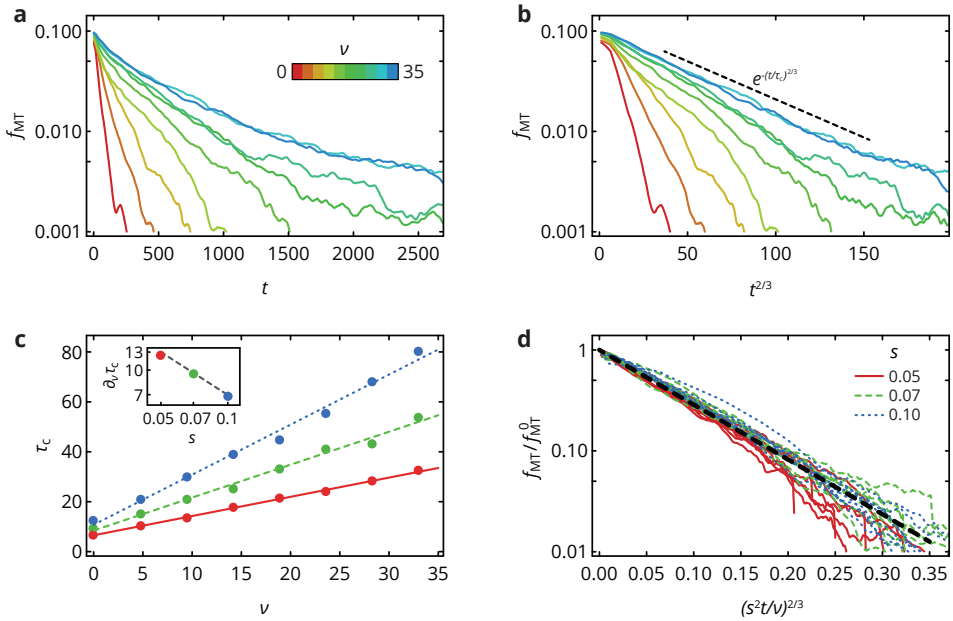

Figure B.4: a) Frequency f_{MT} of mutants with selective disadvantage s over time t. Increasing the line tension ν (see legend) slowed down the rate of decrease of f_{MT}. Here, $s = -0.07$. b) Same as panel a), but with time rescaled as $t^{2/3}$. The resulting curves are linear in a log-plot, indicating $\ln f_{\mathrm{MT}} \sim -(t/\tau_c)^{2/3}$ (dashed line). c) Fitting the curves in b), we measured the characteristic time of purging τ_c as a function of ν for different $s = 0.05,\ 0.07,\ 0.10$ from bottom to top. The slope of $\tau_c(\nu)$ scales as $s^{-4/3}$ (inset). d) Rescaling time as $t' = (s^2 t/\nu)^{2/3}$ and mutant frequency by the initial frequency f^0_{MT} collapsed all curves of f_{MT} onto a single master curve.

quickly because the surrounding wild type bulges out and invades the deleterious clone. Thus, if front curvature is suppressed by strong line tension, this may cause selection to act more slowly because fast growing mutants cannot invade as efficiently. On the other hand, strong line tension will reduce the roughness of the front, which generally increases the establishment probability of beneficial mutants according to the results in Chapter 4. In the following, we investigate how the purging of deleterious mutants from standing variation and the establishment of spontaneous beneficial mutations change when the line tension is increased.

Purging of deleterious mutations from standing variation

To study how deleterious mutants are removed from the population when line tension is strong, we started from a line composed of a mixture of 10% slower growing mutants with fitness disadvantage s in an otherwise wild-type population and followed the frequency f_{MT} of mutants over time (see Fig. B.4a) for different

values of the tension ν. The frequency of mutants decayed roughly exponentially over time, and increasing the line tension slowed the rate of purging by orders of magnitude. For instance, without line tension, the mutant fraction had decreased by a factor of 10 within about 50 generations, whereas over 1000 generations were needed for the same decrease with strong line tension.

A closer inspection of the frequency-vs-time curves shows that the decay of f_{MT} is not exactly exponential, but instead is well fitted by a stretched exponential

$$f_{\mathrm{MT}}(t) = f_{\mathrm{MT}}(0)e^{-(t/\tau_c)^{2/3}}. \tag{B.9}$$

We can make a semi-analytical argument to explain this stretched exponential. Consider first the dynamics of a single mutant sector in the random-walk picture described in Sec. 1.4.2. The frequency of the mutants is equivalent to the survival function $S(t)$ of a single mutant sector, multiplied by the initial number of sectors. The long-time limit of $S(t)$ for a standard random walk with a bias $v = 2\sqrt{2s}$ in a linear expansion is asymptotically given by[4]

$$S(t) \sim e^{-8st^2/\sigma^2(t)}, \tag{B.10}$$

where $\sigma(t)$ in eq. B.10 is the standard deviation of the sector boundary random walk. For a standard random walk, $\sigma(t) \sim t^{1/2}$, leading to an exponential decay of $S(t)$ over a characteristic time scale $\tau_c = 2D/s$. For a sector boundary in a population with a front described by the KPZ equation, however, we have $\sigma(t) \sim t^{2/3}$ (see Sec. 1.4.2). The stretched exponential form of the survival function is thus a direct result of the KPZ of the population front. We repeated the simulations for different values of s and found that the decay was faster for larger fitness disadvantages. By fitting the mutant fraction with eq. B.9 for different values of ν and s, we find the scaling

$$\tau_c \sim \nu^{3/2}s^{-2}, \tag{B.11}$$

which allowed us to collapse the data for all ν and s onto a single master curve described by eq. (B.9).

B.6 Establishment of beneficial mutations

If line tension can slow down the loss of deleterious mutants, what happens in the case of beneficial mutations? On the one hand, our results from deleterious mutations seem to predict that selection is weakened by surface tension. On the other hand, the interfaces and sector boundaries are less noisy for strong surface tension, which should increase the probability of establishment of beneficial sectors.

To test this, we simulated sector formation by starting from a single mutant in the center of a line of wild type and recorded the number of simulations where the mutant established into a sector. If the sector established, we also measured the width of the sector over time to understand the dynamics of establish-

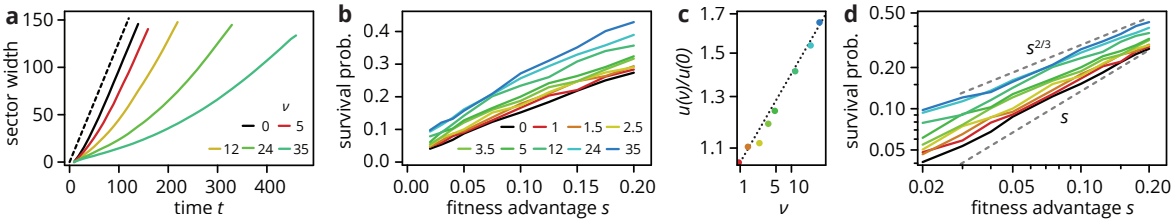

Figure B.5: Establishment of beneficial mutations in Eden model simulations with surface tension ν. (a) The expansion speed of establishing beneficial sectors approached its asymptotic value very slowly for strong line tension. (b) The establishment probability of beneficial sectors increased with the selective advantage s and the line tension ν. The increase of the establishment probability u with ν was relatively slow, increasing as $\nu^{0.13}$ (panel c), and its scaling with s changed from the theoretical value $u \sim s$ for the standard Eden model to an approximate scaling $u \sim s^{2/3}$ (panel d).

ment. The results are shown in Fig. B.5 for $s = 0.1$. Without additional line tension, the sector quickly reached its final lateral expansion speed $2\sqrt{2s}$ (black dashed line). As we increased the line tension ν, a long crossover region emerged before the final speed was reached. This crossover region could be very broad - for the largest line tensions we simulated, the sectors did not reach the final speed during the simulation time. The crossover was deterministic and a direct consequence of the increase line tension. Establishment, on the other hand, remained a stochastic process, although the probability of establishment was altered by the line tension ν. The establishment probability u increased with ν, although relatively weakly – we found a scaling $u(\nu)/u(0) \approx \nu^{0.13}$ (Fig. B.5c). The scaling of u with the selective advantage also appeared to be affected by line tension, as for the high line tensions we found $u \sim s^{2/3}$, whereas for small ν, we recovered the prediction $u \sim s$ (see Chapter 3).

B.7 Discussion

In this Appendix, we have introduced a mechanism for tuning the line tension in the Eden model. We showed that the interfaces created by our model are in excellent agreement with the deterministic KPZ equation. For increasing line tension, we found a higher establishment rate of beneficial mutations, although individual establishment events were delayed compared to the classical Eden model, and a decreased rate of purging of deleterious mutants from the front, in agreement with experiments[2]. This could have important consequences for other expanding cellular populations dominated by surface tension, such as tumors. By limiting the effectiveness of purifying selection, line tension may increase the chances of evolutionary rescue because deleterious mutants can remain in the population for a long time, which increases the probability of secondary beneficial mutations or environmental change that eliminates the selective disadvantage of the

mutants.

References

[1] B. Nguyen, A. Upadhyaya, A. van Oudenaarden, and M. P. Brenner. Elastic instability in growing yeast colonies. *Biophysical journal*, 86(5):2740–2747, 2004. doi: 10.1016/S0006-3495(04)74327-1.

[2] J. Kayser, C. Schreck, M. Gralka, D. Fusco, and O. Hallatschek. Collective motion conceals fitness differences in crowded cellular populations. *bioRxiv*, page 267286, 2018.

[3] K. S. Korolev, M. J. I. Müller, N. Karahan, A. W. Murray, O. Hallatschek, and D. R. Nelson. Selective sweeps in growing microbial colonies. *Physical biology*, 9(2):026008, jan 2012. doi: 10.1088/1478-3975/9/2/026008.

[4] S. Redner. *A guide to first-passage processes*. Cambridge University Press, 2001.